Summer 8-28-2013

In situ High Pressure and Temperature 13C NMR for the Study of Carbonation Reactions of CO2

James A. Surface
Washington University in St. Louis

WASHINGTON UNIVERSITY IN ST. LOUIS

Department of Chemistry

Sophia Hayes, Chair
Joseph Ackerman
John Bleeke
Mark Conradi
Dan Giammar
Liviu Mirica
Jill Pasteris
Philip Skemer

…

In situ High Pressure and Temperature ^{13}C NMR for the Study of Carbonation Reactions of CO_2

by

James Andrew Surface

A dissertation presented to the
Graduate School of Arts and Sciences
of Washington University in
partial fulfillment of the
requirements for the degree
of Doctor of Philosophy

August 2013

St. Louis, MO

Table of Contents

Acknowledgements

Sir Isaac Newton once wrote in a letter to Robert Hooke that, “If I have seen further it is by standing on the shoulders of giants.” I think I now finally understand what he was thinking and feeling when he wrote that. As I sit here and think about my graduate school experience I'm reminded of all of the people who have made it possible. I am reminded of my family who have supported me through this entire process; I am reminded of professors who have invested their time teaching me; I am reminded of my friends and fellow students who have worked hard beside me, helping me. Here I would like to take the opportunity to thank all of these people. I hope that I do not forget anyone.

First, I am foremost indebted to my wife, Sarah, who has been my biggest fan and confidant throughout my time in graduate school. I could not have completed graduate school without her encouragement, love, and faith in me. I have my son, James, to thank too. He kept late hours with me while I was studying and writing and he has always put a smile on my face even after the hardest day at work. There is also another little one on the way: he/she has reminded me of the thrill of being a father and the excitement that I have about teaching my children science one day.

I also want to acknowledge the hard work and dedication of my parents. Of all of my teachers, my Mom and Dad taught me the longest and the most. My Dad gave me my work ethic and the joy I have of working with my hands. Every morning I get up I think about all of those years he would get out of bed at 5 AM to go to work, no matter how he felt. My Mom gave me my interest in science and the world by teaching me to notice the details and to be curious about them. I cannot thank her enough for all of the endless hours she spent teaching me math, science,

and how to think. Whomever benefits from the rest of my career has my parents to thank for first inspiring me and patiently teaching me for all of those years.

There is also the rest of my family to thank. My twin sister, Emily, and brothers Timothy and David, were very supportive of my graduate school experience. They also were the ones that had to put up with my "scientific" experiments in grade school. My in-laws, Dave and Joanne Silvernail, were a constant source of wisdom and encouragement for me during graduate school. They really have believed in me and prayed for me through this process.

Next I have my best friend John Campbell to thank. John has been there through thick and thin with me since Freshman year of college. He has always lent a willing ear to my thoughts and rants and has constantly challenged me to think outside of the box, to be a better scientist.

I also owe a lot to my fellow Chemistry labmates. Jeremy Moore was the one student who knew what it was like to work in both chemistry and physics research groups at once. He was also a constant encouragement and pleasure to work with. I also really enjoyed the time he spent teaching me to throw a baseball correctly during lunch breaks, and his patience to teach me the finer attributes of baseball. There is also Erika Sesti, whose common sense and good advice have always been timely and extremely helpful. She has also been a really good friend to me and supporter through the whole process. She also loves baseball and refuses to leave voicemails as I do. Katie Wentz was a huge help early-on in the project with MAS. She and Jeremy patiently taught me how to spin a rotor. I owe a lot to the rest of the group as well: Dustin Wheeler, Zayd Ma, Sarah Mattler, Blake Hamman, and Matt Willmering, have all listened to my presentations and provided me with helpful feedback as well as challenging questions. I have really enjoyed the science conversations I have had with the people in the Hayes group. Traveling with them to

conferences is a blast as well.

I owe a lot to my Physics labmates too. David Shane was an inspiration to me. While he taught me the fine details of the home-built spectrometers in physics, he was always a willing help to troubleshoot problems and test ideas. Tim Ivancic, too, deserves recognition even though we only ever worked together for three days. His research advice my first three days in lab have been tremendously helpful my entire time in graduate school.

There is also the rest of the physics group to thank. Eric Sorte is a brilliant guy who has a real mind for science. He helped me in ennumerable ways to reapproach solutions to different science problems. He also was always up for hearing one of my lame science jokes. Sam Emery is one of the coolest guys in the physics lab. He was really helpful with suggestions for my imaging experiments and diffusion measurements. Bob Corey also helped me a lot with my research: he taught me some basic aspects of NMR pulse sequences and shares my interest in following the news.

I could not forget about Dan Giammar's research group in Engineering. Fei Wang, in particular, was a huge help in developing the pH model described in Chapter 4. She also helped me construct several of my high pressure experiments, helped me to interpret some of the data, and provided some of the reactant samples for later experiments.

I would be remiss if I didn't mention the key help of Andre D'Avignon and Jeff Kao for doing some of the solution NMR work, as well as Paul Carpenter for his help with pXRD.

The machinists in the machine shop in physics taught me a lot about machining metal and building things. Todd Hardt, Denny, and Tony were really helpful with constructing my high

pressure NMR probe as they machined the bulk of it. They were also always willing to help me find whatever part or metal piece I needed. I will miss them when it comes time to build things elsewhere.

I also would like to thank and acknowledge the hard work of the many undergrads and high school students that I had the pleasure of working with in my time here. John Beach was really helpful on the mineralization project (Chapter 6). He is the student who synthesized the hydromagnesite samples. Allison Brenner made an endless number of nesquehonite samples and played a pivotal role in identifying the contaminant mineral, northupite, in them. She also did a lot of excellent with with $CaCO_3$ synthesis that I was not able to include in this thesis. Louis Wang was the person who made the Dypingite sample studied in Chapter 6. He was the first to successfully make dypingite using a solution synthesis process. Yanzhe Zhu was also pivotal in getting the pH model (Chapter 4) to work and spent an entire summer working on it with me. Danny Corin was a huge help with spectral processing methods and wrote a lot of brilliant code that made processing data in bulk much easier. He also taught me a lot about computer programming. Ken Tharp helped me with the MAS setup on the 600 MHz magnet and obtained some of the first MAS data on the mineral dypingite. Daniel Martin worked on the calcium carbonate synthesis project (which is not discussed here).

Finally, I owe a lot to the people on my committee for both reading this thesis and for their constant advice through the years in my many committee meetings. Liviu Mirica is a brilliant chemist and gave me many excellent reaction ideas. I also really enjoyed working on the high pressure methane catalysts with him. John Bleeke taught me a lot about pXRD and NMR of inorganic structures. His organometallics class gave me a whole new perspective on inorganic

chemistry. Jill Pasteris was a huge help with learning Raman and interpreting some of the spectra. Phil Skemer also helped me a lot with sample preparation and basic geological science that I never learned in college. Dan Giammar's insight into my pH model and imaging experiments as well as his kind direction and detailed answers to my numerous questions helped to keep me on track and stay relevant with my research. Joe Ackerman taught me much of what I know about imaging and basic NMR. He was also my first advisor at Washington University and helped me get my graduate education off to a good start.

Finally last, but by far not least, I have my two advisors to thank. Mark Conradi and Sophia Hayes are both tireless advocates of science who have an inspirational passion for teaching and for NMR. Their excitement about research is contagious, and their patience with me as a developing scientist and wise counsel have made my graduate school experience quite wonderful. I owe all of the success of this project to them.

This project was funded in full by the Consortium for Clean Coal Utilization (CCCU). The CCCU operates under the umbrella of the International Center for Advanced Renewable Energy and Sustainability (I-CARES), located at Washington University in St. Louis. The primary financial sponsors of the CCCU are Arch Coal, Peabody Energy, and Ameren.

Chapter 1: Introduction

Carbon dioxide (CO_2) probably does not need any introduction as it is one of the most discussed chemicals of this century. It has been blamed for recent global warming trends[1] and acidification of the oceans,[2] and is continuing to be produced at record and still growing rates worldwide. Energy production, automobile exhaust, concrete manufacturing, and land use change are the primary producers of CO_2. Modern civilization simply cannot do without the processes that produce CO_2; nevertheless, the ever-increasing CO_2 levels are becoming a cause for concern.

There is no question that CO_2 levels are rising in the world today. The measured atmospheric CO_2 levels at the NOAA's Mauna Loa Observatory in Hawaii just surpassed a monthly average of 400 ppm, up from 310 ppm in 1958, when the observatory first started taking measurements.[3] The measurements at Mauna Loa are significant because the gas in the world's atmosphere is well-mixed. Increased CO_2 levels at the top of a mountain in the middle of the Pacific Ocean—far from power plants and continents of vegetation—indicate an increase in the average CO_2 levels in the world's atmosphere.

The rising atmospheric CO_2 concentration is thought to generate a number of different problems. While there may be some difficulty in ascertaining the global warming potential of CO_2 gas,[4] there are many other better understood negative effects of increasing CO_2 levels. These include ocean acidification[5,6] and probably most importantly, the effect on agriculture and plants.[7,8] These studies indicate that some crop plants are already beginning to show signs of

decreased crop yields due to the high levels of CO_2 and that if levels continue to rise crop production could be seriously affected.

A good question to ask is whether mankind is entirely responsible for this rise of CO_2 level in the atmosphere. The answer is *mostly* yes. Most researchers agree that one of the primary contributors of this increase is anthropogenic emissions and the amount of increase of CO_2 in the atmosphere does correlate with the amount of CO_2 released, minus the CO_2 that gets sequestered in land biomass and oceans. CO_2 is produced in massive quantities by mankind. Recent estimates state that some 8.6 Gt Carbon/yr is released into the atmosphere worldwide from energy production alone.[9]

The obvious problem is that there is no way CO_2 emissions are going to decrease globally in the near or even distant future. Its not going to end because modern civilization relies on energy sources that produce CO_2. In fact, there is a direct correlation between GDP growth and CO_2 production.[10] Economists systematically refer to charts of U.S. CO_2 emissions and show that dips in CO_2 emissions correspond to "dips" in the GDP. The better the economy the more CO_2 emitted into the atmosphere. This is why it is so hard to decrease CO_2 emissions and why no one has done it voluntarily: because the economy suffers when CO_2 production suffers.

Nevertheless, the worldwide concern over the longterm effects of high CO_2 emissions has led to a number of proposals that would at least curb an increase of CO_2 emissions in the future.[11] One such proposal is that of CO_2 geological sequestration.[12,13] Geological sequestration aims to take CO_2 and pressurize it and send it deep underground into deep saline reservoirs and aqueous mineral deposits where it will become trapped. Many different types of entrapment of CO_2 can occur under these conditions including simple physical entrapment (called stratigraphic

trapping), solubility entrapment (where CO_2 dissolves in the geological brine), residual entrapment (trapped in pore spaces and kept there by capillary pressure), and/or chemical entrapment (where it reacts with the rocks underground and turns into solid carbonates). Chemical trapping of CO_2 is widely considered the storage option with the most long-term security as the CO_2 is chemically changed into a thermodynamically stable solid carbonate. The process of chemical conversion of CO_2 into a metal carbonate also called mineralization or carbonation, is what the research described here addresses.

Mineralization of CO_2 occurs when CO_2 dissolves into and reacts with water to form aqueous bicarbonates and carbonates. This process is enhanced at high pressures (> 50 bar) and temperatures (> 50 °C). If there is a source of divalent metals (such as Mg^{2+}, Ca^{2+}, or Fe^{2+}) in the solution, these divalent metals will react with the bicarbonate and carbonate in the solution to form solid metal carbonates in the form of $MCO_{3(s)}$ where M is a divalent metal. In an aqueous environment formation of solid carbonates from CO_2 is one of the few thermodynamically favorable (spontaneous) reactions of CO_2.

Geological sequestration is a tantalizing option for mitigating CO_2 output as it has been preliminarily tested to be economically feasible (current estimates indicate that CO_2-sequestered power sources would increase electricity costs as little as 30%[14]) and possess a storage potential that could easily store the entirety of global CO_2 production be it that the infrastructure for capturing and transporting the CO_2 to these locations existed. Worldwide estimates for geological storage of CO_2 place current known global storage capacity at 100 trillion tons of CO_2, assuming complete mineralization.[15,16] This is enough for at least several hundred years of CO_2 sequestration at current global production.

Geological sequestration needs to be rigorously tested and shown to be safe *before* it is employed as large-scale method for CO_2 emission reduction. Because current geological sequestration proposals plan to put so much CO_2 underground, researchers need to make sure that the sequestered CO_2 will never make its way back up to the surface of the earth again. One need only read about the about the limnic eruption of Lake Nyos in Africa in 1986 to understand the destruction that could be caused by even moderate amounts of CO_2 leakage in a short amount of time from the earth.

The study of mineralization reactions of CO_2 has other benefits in addition to helping to evaluate the safety of geological sequestration proposals. Some researchers have proposed to sequester CO_2 above ground in chemical reaction chambers where solid carbonates are produced and subsequently used as building materials.[17] If this can be shown to work on a production level it could have very large implications for CO_2 sequestration.

Herein, I will describe the development of a novel tool and methodology for study of CO_2 mineralization reactions that will help researchers to better understand the chemistry of CO_2 carbonation reactions. As the mineralization reactions occur at high pressures (up to 250 bar) and high temperatures (up to 250 °C), studying these reactions can present certain challenges. Standard laboratory analytical instrumentation is not designed to study reactions under these conditions.

Here I will show that *in situ* ^{13}C nuclear magnetic resonance (NMR) can monitor progress of CO_2 mineralization reactions (Chapter 3) and that pH and other important experimental measurements can be obtained from this data (Chapter 4). I will further describe and demonstrate the ability to *image* pH during the progress of these reactions using ^{13}C NMR (Chapter 5). Lastly,

I will develop a methodology for identification of the solid carbonate products using various solid state NMR methods (Chapter 6).

It is my hope that the new tools and methodology developed here will be used in the future to help those in the field better understand and create new and efficient applications for the sequestration of CO_2 into metal carbonates.

Chapter 2: Experimental techniques

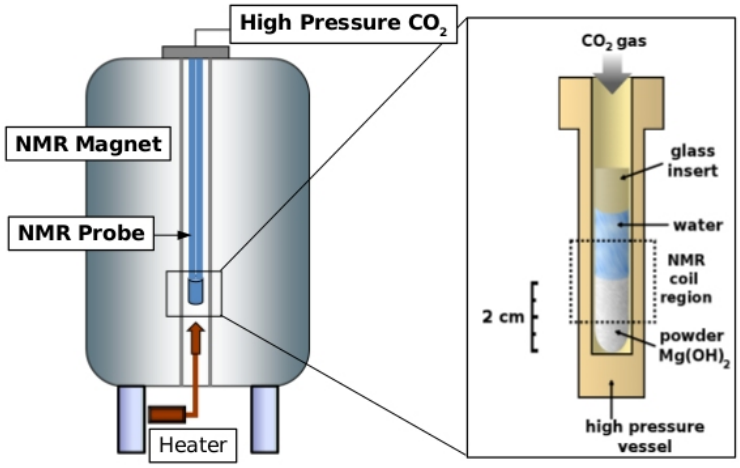

Figure 2.1: A sketch of the ^{13}C NMR probe and the high pressure zirconia reaction vessel designed in this project. It is has been used to measure ^{13}C NMR data up to 250 bar and 120 °C for up to 31 days at a time in the cryogenic magnet.

A. Introduction

Today there is a stunning number of analytical techniques available for chemists to use for product identification and quantification. Long gone are the days where the chemists had to make their identification based on what the compound was reactive with and what color and texture it had. With so many types of analytical techniques, scientific journals have begun requiring new compounds to be identified via two or more techniques. Each technique has a particular strength and/or weakness. Complementary techniques must be chosen where the strengths of one overcome the weaknesses of the other to not miss any key components of the sample.

In this research I have chosen to use three complementary analytical techniques: NMR (nuclear magnetic resonance spectroscopy), pXRD (powder X-ray diffraction), and Raman

spectroscopy. These three techniques all have strengths and weaknesses that are quite complementary. I will demonstrate in the upcoming chapters how they can be utilized together to provide in-depth insight into the physical and chemical dynamics of the products from high pressure and temperature reactions as well as provide full identification and quantification of those products.

In particular, the experiments described in this paper will also demonstrate the usefulness of *in situ* measurement. Most of the time scientists utilize analytical instruments to measure products *after* the reaction but, especially in highly complex reactions, it can be very difficult to piece together a story of what happened during the reaction based merely on the products after the fact. Not every detective is Sherlock Holmes. So *in situ* spectroscopy is born, where the chosen analytical device is modified so as to be able to make measurements under the conditions that the reaction needs. Sometimes this involves creating an elaborate and highly complicated instrumental setup. That is somewhat the case here.

The reactions I will be describing are high pressure and temperature carbonation reactions of CO_2. The conditions of such experiments are hardly amenable to conventional bench-top analysis methods (>50 bar and > 70 °C). And while *ex situ* methods have provided some valuable chemical insight into net products formed, they have failed in providing direct evidence for *how* the products form. So, many research groups have recently been working to develop new *in situ* analysis methods that can monitor high pressure and temperature carbonation reactions. These various groups have made much progress in modifying their instrumentation and acquiring data on these reactions using pXRD,[18–20] NMR,[21–26] spectrophotometry,[27,28] IR,[29] and Raman.[30,31] As expected, these *in situ* methods have provided much useful information about the mechanisms,

rates, and direct effects of changing reaction variables like pressure, temperature, and reactant concentrations.

After introducing pXRD and Raman and solid state MAS (magic angle spinning) NMR bench-top spectroscopic methods in this chapter, I will also introduce and describe the methods by which we have obtained high pressure and temperature ^{13}C NMR of carbonation reactions *in situ* at pressures as high as 250 bar and temperatures up to 120 °C.

B. Powder X-ray diffraction

X-rays are very high frequency electromagnetic waves and can be diffracted by any "grating" that has particles a few angstroms apart, i.e. on the order of the λ of the incoming radiation. Solid crystalline materials can act as such gratings, where the three dimensional structures of the materials diffract the X-rays according to how the crystals are organized.

pXRD was first discovered in in 1912 by Max von Laue when he realized that X-rays were diffracted by solid materials in a reproducible way that was unique to each solid sample exposed to the X-rays. It was only later that year that William Henry Bragg and William Lawrence Bragg (father and son) developed Bragg's law, which described in very basic terms how the perceived XRD peaks from a diffraction experiment resulted from the constructive interference of X-rays (Equation 2.1). They received the 1915 Nobel Prize in Physics for their accomplishment and remain the only father and son pair to have received the prize for the same work.

$$2d \sin(\theta) = n\lambda \quad (2.1)$$

where,

n is the order and is always an integer value

θ is the angle of incidence, which also equals the scattering angle

d is the interplanar distance between two identical crystalline planes

λ is the wavelength of the X-ray

The Bragg equation states that the constructive interference of X-rays by a crystalline sample occurs only under interdependent conditions of the angle of incidence of the X-ray beam with respect to specific atomic planes in the sample, the distance between the atomic planes, and the wavelength of the X-ray. The measurement requirements for a pXRD instrument are to be able to measure the angle of diffraction off of the sample, an X-ray detector capable of measuring numbers of photons of X-rays, and a highly filtered and monochromatic X-ray source (an array of X-ray wavelengths would blur the experiment and provide multiple simultaneous sets of pXRD patterns).

The basic sample requirement for pXRD analysis using instrument employed for all analyses in this paper, is that it be a powder with a particle size on the order of 5-20 μm. Typically about 0.1 grams of carbonate sample are needed to fill the pXRD slide for proper analysis. It is very important that each sample slide be loaded to the full and that the top surface of the powder be smoothed level with the top of the glass pXRD slide. Differences in levels or an uneven surface can cause error in the reported measurement of the angle of diffraction.

In cases where there is not enough powder to fill the XRD slide and it is acceptable to mix the experimental powder with another crystalline powder, co-mixing becomes a way to provide internal calibration of the sample peaks while also filling the volume of the slide. In cases where

I co-mixed powders, I typically added CaF_2 powder or Mg_2SiO_4 powders. The advantage to co-mixing with these powders is that neither has ^{13}C, ^{23}Na, or ^{1}H, so they do not interfere with the NMR spectra obtained from the samples. To reduce the amount of signal from the co-mixed powder in the spectrum, the slide can be filled halfway with the powder you do not want in the pXRD spectrum, and the last layer can be the sample you are most interested in. pXRD is most sensitive to the powder on the top of the slide. In most cases of co-mixing, the pXRD experiment did not detect the co-mixed powder.

In addition, to ensure that all pXRD patterns were accurately referenced, a standard of powdered silicon was run before each pXRD session and the instrument's angles were calibrated to the Si(111) reflection defined as 28.443 degrees 2θ. It takes 5 minutes to run this experiment, but it is very worthwhile. The instrument is used by many people and gets out of calibration easily.

pXRD spectrum analysis was completed using Jade Plus software and the combination of the PDF-4 and American Mineralogist XRD crystal databases. All pXRD figures were generated using the scientific plotting software Gnuplot. Where possible, the pXRD standard spectra were generated from published crystal .cif files using a crystallography program, Mercury v2.4.

All of the pXRD patterns in this paper and project were obtained on a Rigaku Geigerflex D-MAX/A diffractometer with Cu−Kα radiation at 35 kV and 35 mA. Typical pXRD experiments were obtained from 6°-60° degrees 2θ with 0.04 degree steps of 1 second intervals.

C. Raman spectroscopy

In 1923 Adolf Smekal first predicted that a small percentage of photons would scattered by

molecules would do so inelastically even though the only known scatter at the time was elastic.[32] It was some five years later that C.V. Raman was able to observe this scattering effect, for which he was given the 1930 Nobel Prize in Physics. It was a sensational discovery and had taken so long to be discovered because the effect occurs for only about 1 photon in every 10^5 to10^6 –or quite literally "one in a million." In fact, its quite amazing C.V. Raman ever saw the effect at all given the poor nature of the optical equipment he had to use. But he did—and he was able to accomplish this feat by focusing sunlight into an intense beam and shining it through a dust-free solution. Using this setup, he was able to measure the Raman scattering from some 60 different liquids which he reported in his original Nature article in 1928 on the matter.[33]

The Raman effect is a light scattering phenomenon that occurs when a photon collides with the electron cloud of a molecule, exciting it to a so-called "virtual state." The term "virtual state" is fancy language for a very short-lived (10^{-12} s) unstable energy state. This "virtual state" arises from a distortion of the electron cloud of the molecule due to the impinging electromagnetic field of the photon. The extent to which the molecular orbital can be distorted is referred to as its "polarizability," and the more polarizable a molecular is the stronger the photon's interaction with it. When the molecule relaxes back from its virtual energy state, it either returns to its original ground state (no change to the photon energy, elastic scatter, called Rayleigh scatter) or it relaxes to an energy level higher or lower than the original state (change in the photon energy, inelastic scatter). The specific difference in frequency between the higher or lower frequency scattered photon and the monochromatic source of light depends on the normal vibrational and rotational modes of the molecule scattering the light. The change in energy of the photon is always a function of the normal modes of the molecule scattering the light.

For the effect to be observable within a short time of gathering the signal, a large number of photons (intense light) of a highly-specific frequency (monochromatic) must be sent into the sample. The high intensity has greater success at distorting the electron clouds and also increases the small number of inelastic scattering events by mere feature of increasing the number of photons altogether.

Lasers are excellent sources of light for Raman experiments as they provide an intense and highly monochromatic light source. Mercury Arc lamps used to be the the light source of choice before the invention of the laser...but since the laser became available, Raman spectra can be collected in just a few seconds to a few minutes of time. Compare this to the original Raman spectra recorded which took hours to days to get any appreciable signal.

Raman spectroscopy is used here because Raman scattering is particularly efficient for crystalline carbonate solids[34] and because Raman works well in aqueous systems (water is a very weak Raman scattering medium and thus provides minimal distortion to spectral acquisition).[35] The study here is of both wet and dry carbonates so Raman spectroscopy is nicely fitted for these experiments.

Finally, in general, the Raman signal is stronger for symmetric stretches in a molecule than asymmetric ones (due to nuances in the selection rules). This means the asymmetric stretches that occur in a carbonate solid are typically very weak. As just mentioned, however, the symmetric CO_3 stretch is by far the strongest Raman signal in Raman spectra of carbonate-containing solids. The CO_3 symmetric stretch is also highly sensitive to its environment and has been shown to be highly indicative of the type of carbonate in a system.[34,36] The CO_3 symmetric stretch is also unaffected by the 50-100% ^{13}C labeling (because the carbon

atom is stationary during this stretching mode) allowing the Raman symmetric stretch wavenumber of the experimental sample to be directly compared to literature values from unlabeled compounds. The ^{13}C isotopic influence on the asymmetric Raman stretches is not easily calculated and therefore the experimental asymmetric stretches from ^{13}C-labeled samples cannot be easily compared to literature values. The CO_3 symmetric stretch is the primary peak utilized for Raman identification in this thesis for these reasons.

In nearly all cases in this paper, Raman analysis was done on 50-100% ^{13}C-labeled minerals and thus only the CO_3 symmetric stretches will be shown in the Raman data. In general, the other peaks in the spectrum were analyzed to ensure consistency with the crystalline assignment. In all cases (except where noted) Raman spectra were acquired using 20 scans of 1 second each.

The Raman instrument used to make the measurements in this paper is a HoloLab Series 5000 Laser Raman Microprobe (Kaiser Optical). The microprobe delivered a 532-nm laser beam from a frequency-doubled Nd:YAG laser through a 20× (except where noted) Leitz microscope objective (long-working-distance) with a 0.4 numerical aperture. This configuration delivered a maximum of 11 mW of laser power onto the sample; each spectrum had a resolution of about 3 cm^{-1} and was recorded from 100 to 4000 cm^{-1} with a reproducibility in peak position of 0.1 cm^{-1}. The sampled regions were about 5 μm in diameter and produced a penetration depth of a similar magnitude due to the highly scattering nature of the product crystals.

D. Nuclear magnetic resonance

NMR is a relatively young analytical technique. The first successful detection of magnetic moment didn occur until 1933 with the Stern and Gerlach experiment. Rabi was the first to

experimentally observe nuclear magnetic resonance four years later in 1937. But it was not until 1945 that the first NMR experiment was observed on bulk material by Purcell, Torey, and Pound[37–39] and the first ^{13}C NMR experiment didn't happen until 1957![40,41]

Here I will describe NMR in more detail than Raman and pXRD but will still gloss over many very important aspects of NMR. The purpose of this section is to provide basic definitions for the NMR terms I use throughout the rest of this thesis and to provide some basic fundamentals of the technique. If the reader is interested in a more detailed approach to learning basic NMR, I recommend Malcolm H. Levitt's book, *Spin Dynamics.*[42]

a. Introduction to NMR

All nuclei are made of particles that possess four important physical properties: mass, electric charge, magnetism, and spin.[42] Mass and electric charge are easy to understand because we see their direct effects in the macroscopic world. Objects with more mass are harder to pick up; drag your slippers across the carpet and touch a metal doorknob and you get shocked. But the other two properties, nuclear magnetism and spin, are harder to understand because they lack direct macroscopic analogues.

Both nuclear magnetism and spin are considered properties *intrinsic* to a nuclear particle. They are both also closely linked together through the magnetogyric ratio (Equation 2.2), which is unique for each element in the periodic table.

$$\hat{\mu} = \gamma \hat{I} \quad (2.2)$$

where,

$\hat{\mu}$ = quantum mechanical operator for magnetic moment

$\hat{I}$ = quantum mechanical operator for nuclear spin

γ = the constant that relates the magnetic moment and nuclear spin called the magnetogyric ratio

The consequence of Equation 2.2 is that the vectors representing spin and nuclear magnetic moments are either parallel ($\gamma>0$) or antiparallel ($\gamma<0$) meaning that as "as spin goes so does the magnetic moment." Their behaviors are closely intertwined and as such we often refer to either spin or magnetic moment almost interchangeably when describing aspects of NMR experiments (but they are not the same thing!).

The Pauli exclusion principle states that no two fermions (these include protons and neutrons) can have the same quantum state (includes spin state). The result is that a nucleus such as helium, which has two protons and neutrons, must have the spin states of each proton and neutron paired (and thus their magnet moments). A single helium atom, therefore, has no net magnetic moment or spin state because they are all paired, canceling each other out. The nuclear spin of the helium nucleus is then I = 0. However, in the case of hydrogen, where the nucleus consists of a single proton, there is no pairing and there can be a net magnetic moment and spin state for the hydrogen. The nuclear spin state is I = ½. The general rule is that a nucleus has net spin if it has an odd number of protons and/or an odd number of neutrons.

The hydrogen nucleus has net spin and therefore net magnetic moment but bulk hydrogen gas is not noticeably magnetic. Nor does it possess any net observable "spin" (whatever that would look like!). This is because spin and magnetic moment are vector quantities that are randomly

oriented in the absence of any external influences. A bulk set of randomly oriented vectors has no net vector magnitude, meaning that in bulk the net magnetic and spin effects are more-or-less canceled out.

Another way to think about this is that a nucleus of spin I has 2(I)+1 degenerate energy levels (in the hydrogen case for example, there are two degenerate energy states: 2(½) + 1 = 2). In bulk hydrogen, all of the energy levels are equally populated (because they are degenerate) and thus no net effect can be perceived in bulk because no one state has been "preferred." So the bulk effect of having a nonzero spin state and magnetic moment is still virtually zero unless there is something to *induce* spin orientation/lift the degeneracy of the energy levels.

As it turns out, there is a way to *induce* spin orientation/lift the degeneracy of the energy levels, but only partially. If a nucleus with a nonzero spin state is put in a magnetic field, its spin magnetic moment will *precess* around the axis of the magnetic field at a frequency linearly dependent on the strength of the magnetic field. This behavior only occurs because the spin angular momentum and the magnetic moment are so closely linked (Equation 2.2). The degeneracy of the energy states are also lifted when the nucleus is placed in a magnetic field. The difference between the new energy states is called the "Zeeman splitting" and is also linearly proportional to the strength of the magnetic field.

The frequency of spin precession in rad/s (ω) is the same number as the energy in rad/s (ω) separating the two energy states from Zeeman splitting and is defined in Equation 2.3. This frequency is called the "Larmor precession frequency."

$$\omega = -\gamma B_0 \quad (2.3)$$

where,

ω = Larmor precession frequency

γ = magnetogyric ratio

B_0 = magnetic field strength

Because the energy states are split, the lower energy level becomes selectively populated, but only by very little. The amount of preference for the lower energy state (i.e. spin polarization) is dependent upon the Boltzmann equation (Equation 2.4):

$$\frac{n_{ground}}{n_{excited}} = e^{\gamma \hbar B_0 / kT} \quad (2.4)$$

where,

n_{ground} is the number of nuclei in the ground state

$n_{excited}$ is the number of nuclei in the excited state

γ is the magnetogyric ratio of the atom

$\hbar$ is the reduced Planck constant (h), h/2π

B_0 is the strength of the magnetic field

k is the Boltzmann constant

T is the temperature

For hydrogen atoms in a magnetic field of 2.3 T and at room temperature spin polarization [polarization defined as $(n_{ground}-n_{excited})/(n_{grou\,d}+n_{excited})$ ratio] is only about 1.0000085 or just 8.5 ppm. For other nuclei, like carbon, the polarization is much, much worse as $\gamma_C/\gamma_H = 0.25$. The spin polarization in a 2.3 T magnet for ^{13}C is only 2.1 ppm (it's a wonder we see it at all!). The NMR experiment detects only the spins that are polarized, thus the vast majority of spins in the sample do nothing in an NMR experiment.

b. The NMR experiment

The NMR experiment is the process of detecting the polarized spins in the sample. This is usually accomplished by pulsing the sample with a radio frequency (RF) pulse at the same frequency as the Larmor frequency. Matching the frequency of the RF pulse with the Zeeman splitting energy allows energy to be transferred to the nuclei from the RF. The transferred energy "adjusts" or "flips" the net spin state in the sample on the basis of how much energy is transferred (power of the pulse). Once the spin states have been flipped, they will relax back to their original state by releasing the specific RF signal that they absorbed.

Another way of describing the NMR experiment is using the spin precession vector model. The RF pulse is an electromagnetic pulse that creates an oscillating magnetic field (called B_1) that "nutates" the net magnetic moment of the sample into a position perpendicular (90°) to the applied magnetic field (B_0). The magnitude of the pulse to position the net magnetic moment of the sample perpendicular to B_0 is called a 90° pulse. Once in the X-Y plane, the spins still precess around B_0, but the bulk magnetic moment vector is pointed perpendicular to the B_0. This creates a "massive" (compared to what they were generating before) oscillating magnetic field. The oscillatory components of the alternating magnetic field from the sample are specific to the *exact* frequencies of precession of each proton nucleus in the sample. The oscillating magnetic fields generate an oscillating electric current in a copper coil carefully placed nearby. This oscillating electrical current can be detected and recorded and processed as frequency spectra. The results of the NMR experiment are called "NMR spectra."

The NMR experiment is bound by two time limits: how often you can pulse the sample and how long you can perceive the NMR signal. These two time limits are dictated by the physical

dynamics of the sample (such as types of molecular motion and vibrations).

The first time limit, how often you can pulse, depends on how long it takes the sample to polarize. The rate constant of a sample's polarization is $1/T_1$ where T_1 is called the longitudinal relaxation time constant or spin-lattice relaxation time constant. T_1 is the time it takes for 63% of the polarization to be achieved by the spins and is the exponential time constant for the polarization process.

The second time limit, how long you can perceive the NMR signal, depends on how long the spins stay in synchronization after they are put 90° relative to B_0. It too has a rate constant which is $1/T_2$, where T_2 is called the transverse relaxation time constant. The time T_2 is the time it takes for 63% of the NMR signal to decay. In practice, however, field homogeneity of the magnet and other processes make the observable NMR signal die more quickly. This effect has another time constant that we use called T_2^* which is the "effective T_2" for the sample given the sample conditions.

T_2 is almost always shorter than T_1 because spins in the X-Y plane are sensitive to static and oscillating fields along any of the three cartesian coordinate axes and T_1 is not (T_1 is only sensitive to magnetic oscillation along X and Y axes). The absolute rule for T_2, however, is $T_2 < 2T_1$.

The signal that we observe from the NMR experiment is an oscillatory one that exponentially decays with time contant T_2^*. The NMR signal we collect is called the FID or free induction decay. Within that decaying signal are various frequency components based on the *exact* Larmor frequencies of types of hydrogen (for example) in the sample. The absolute frequencies of hydrogens vary from hydrogen to hydrogen type because of chemical shielding.

Shielding of the B_0 field occurs by the induced field from the electron clouds around the nucleus of the individual hydrogens. The more electron density around the nucleus, the greater the induced field is around the nucleus. The induced field is in the opposite direction of B_0, so the shielding partially (only slightly) cancels out B_0's effect at the nucleus. Thus, via Equation 2.2, the observed frequency is decreased as the net B_0 effect on the nucleus is decreased by the shielding. The change in frequency from the shielding of the electrons is called chemical shift and it is a very, very small effect relative to the Larmor frequency. The chemical shift is typically on the order of 10^{-6} of the Larmor frequency, which is why it is always written as *ppm* or parts per million. The ppm term is literally referring to "parts per million of the Larmor frequency".

Chemical shift is one of the reasons why the NMR experiment is so powerful. Specific frequencies in ^1H NMR data correlate to specific types of hydrogen atoms...so a CH_2 hydrogen has a different frequency or chemical shift than a CH_3 hydrogen and can be differentiated on that basis.

The specific frequencies are obtained by processing the time-domain FID into a frequency-domain spectrum. The FID is digitally collected in 2^n number of points so a fast fourier transform algorithm can be used to quickly separate the frequency components of the spectrum.

As the strength of the NMR signal is directly proportional to the number of polarized spins in the sample, NMR spectra are quantitative. The strength of an NMR signal in time is the initial height of the FID. In the transformed frequency spectrum, the strength of the NMR signal is the area of the peak. So quantitative data is obtained from NMR data by integrating the peaks in NMR spectra. Additionally, as long as all of the spins in a spectrum have fully recovered

between acquisition pulses, the peak-to-peak ratios obtained in a spectrum are fully quantitative. Relative integrations are often easier to obtain in an NMR experiment as the only restriction to obtain them is that the spins in the sample fully relax before pulsing them again. Correlating absolute concentration to NMR peak area can only be done with the use of a standard sample where the concentration of spins is known. Often, coil effects from changing the sample must also be taken into account when using NMR to quantitatively measure a sample.

c. Solid state NMR

Most NMR experiments, even to this day, are still done on a liquid. This is because the NMR of liquid species is easier to acquire and interpret than on solids. There are many reasons liquids are much easier to interpret. In short, the primary reason liquid spectra are fundamentally easier to obtain is because of the *fast motion (short correlation time)* of the molecules in the solution phase. The effect of this motion is to average out many complicating effects such as dipole-dipole interactions, where the dipole of one spin is able to couple with the dipole of another atom. Fast motion in solution also increases the length of T_2 such that $T_2=T_1$. This allows signal to be observed for longer period of time thus making the peaks in the frequency spectrum very narrow and easy to distinguish from others. Yet another effect from fast motion is that the chemical shift of a given type of nucleus is *averaged*. In general everything about solution-phase NMR narrows the lines and makes signals easier to interpret and understand.

But not everything is a liquid or can be observed in the liquid state. So if NMR data is needed on a solid sample the added effects of running NMR on a solid must be dealt with. Just as everything about a liquid solution narrows NMR lines, just about everything of a solid-state experiment broadens the lines. Solids have dipole-dipole interactions, short T_2 values, and

chemical shift anisotropies, and quite often have very long T_1's. (one of the solid carbonate samples I worked on had a T_1 value over 24 h!).

Some ways have been developed to get around the shortcomings of solid state NMR. Probably the biggest contribution to the field was the development of Magic Angle Spinning (MAS) where the solid sample is packed into a rotor and spun around an axis that is 54.74° relative to the B_0 axis (this angle is called the "magic angle" and is the angle of a body diagonal of a cube relative to any cube edge). Spinning around this axis at high frequencies (generally 1-15 kHz) " averages" all three cartesian coordinates of the solid sample and causes a number of wonderful things to happen. The chemical shift and dipole-dipole interactions are averaged, like in solution NMR, so CSA and dipole-dipole line broadening disappear, thereby significantly narrowing the lines. True T_2 does not necessarily change but T_2^* improves considerably as the physical rotation of the sample contributes to the perceived magnetic oscillation of the sample, artificially extending T_2^*. Spinning the sample essentially averages all anisotropic interactions in the sample. Finally, magnetic susceptibility effects go away when the sample is being spun at the magic angle.

So MAS solid state NMR enables the precise measurement of isotropic chemical shift and the ability to distinguish specific sites in a solid that in a static experiment are all blurred together. Considerable discussion and examples of these types of experiments will be discussed in Chapter 6.

E. High pressure *in situ* nuclear magnetic resonance

Typical NMR experiments are accomplished at room temperature and room pressure. Among

the key contributions of this thesis, however, are ^{13}C NMR measurements attained on a reacting system at high pressures and temperatures. In order to make these measurements a special NMR probe had to be designed and built to obtain NMR under these conditions. Some of the design requirements were that it had to fit in a widebore 354 MHz magnet (89 mm) whose magnetic field sweetspot is 64.39 cm from the top rim of the magnet. It also needed to be able to heat the sample to a temperature of 250 °C and pressurize it to 250 bar for up to several weeks. The pressure and temperature needed to be measured inside the reaction chamber and the sample needed to be easily removed, if needed, while still pressurized.

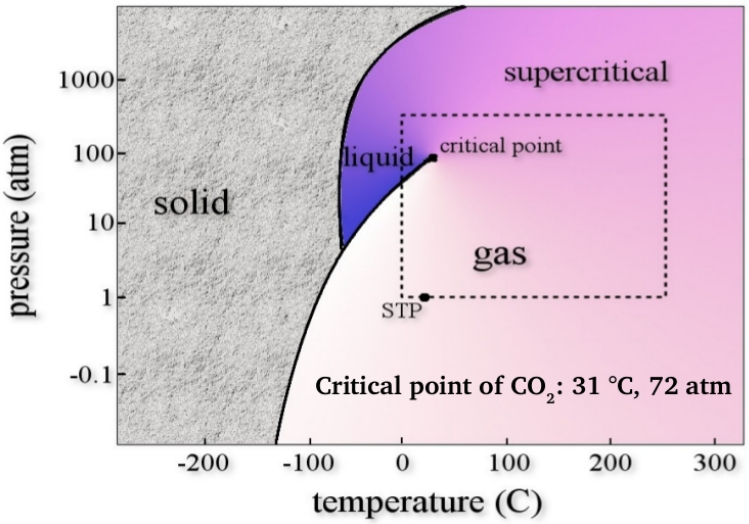

Figure 2.2: The phase diagram of CO_2. The dashed box indicates the pressure and temperature of the operating window of the probe (up to 250 bar and 250 °C).

a. Probe design

The high pressure NMR probe, is a top-loading NMR probe which means it is loaded from the top of the magnet and rests on the top rim of the bore of the magnet. The probe is constructed primarily from brass, but also contains stainless steel, aluminum, and copper. The NMR circuit is of a tank circuit design with an Alderman-Grant coil (more details below) specifically tuned to

89.066745 MHz (the frequency of the ^{13}C $CO_{2(g)}$ resonance in this magnet). Tuning of the circuit is accomplished by two non-magnetic 0.8-10 pF variable Polyflon capacitors connected in parallel. Matching of the circuit is accomplished by changing the impedance through tapping the circuit along a wire until it is matched to 50 Ω. The match cannot be changed once the circuit is assembled. Without further circuit modifications, the probe is capable of being tuned as low as 88.175 MHz and as high as 101.50 MHz. The ^{13}C resonance is purposely not in the middle of the tuning range so that other nuclei (such as ^{27}Al and ^{23}Na) are easily accessible.

The probe design makes use of both ends of the magnet's bore. The top of the magnet is where the probe is loaded and rests. The high pressure tubing and associated valves, tuning rods for the capacitors, thermocouple access, RF cables, and cooling tubes run through the top of the probe and down into the magnet. The heater, heating tube, and vent tube from the probe are at the bottom of the magnet. Heating and cooling are both accomplished by blowing heated and cooled air into the probe. The cool air is blown over the temperature-sensitive tuning capacitors in the NMR circuit and the hot air is blown into the “hotbox,” the heated portion of the probe, discussed in greater detail below.

The temperature of the probe is monitored in two locations via two Type K thermocouple wires. The first location is the hotbox, the heated zone of the probe. It was found in testing that monitoring the temperature of the hotbox was as good as monitoring the temperature within the high pressure vessel next to it (this was tested by heating the hotbox and monitoring its temperature with a thermocouple wire at the same time as monitoring the temperature inside of the high pressure vessel with another thermocouple wire). The second thermocouple wire monitors the temperature of the NMR circuitry in the cool zone of the probe. This is to make sure

the probe is properly cooling itself during operation and does not overheat or damage the Polyflon tuning capacitors (max operating temperature of 125 °C).

The pressure of the probe is monitored by a MSP-300 pressure transducer (0-2500 psig, 1-5 V, Measurement Specialties Inc.). It monitors the pressure seven feet away from the magnet and probe, at the other end of the small-volume (1/16" OD), high-pressure stainless steel tubing (HiP, Erie, Pennsylvania). The pressure transducer was calibrated using a glycerin-filled 0-2000 psi needle pressure gauge. This particular type of pressure transducer changes its output voltage linearly with respect to the pressure applied to it. A chart was made that converts the output voltage to pressure in bar.

The high pressures in the probe are created by cryogenic pressurization, where $CO_{2(g)}$ is frozen using liquid nitrogen in a stainless steel low-volume, thick-walled recollection vessel that can be completely submerged in LN_2 (see below figure). The low-volume recollection vessel is then closed off to the $CO_{2(g)}$ source and opened to the probe. The low volume recollection vessel is then heated with a hand-held hair dryer, and this causes the CO_2 to sublimate into gas. The restricted volume of the container causes the pressure to increase significantly. The pressure will rise until the CO_2 either liquefies (59.9 bar at 22 °C) or reaches equilibrium.

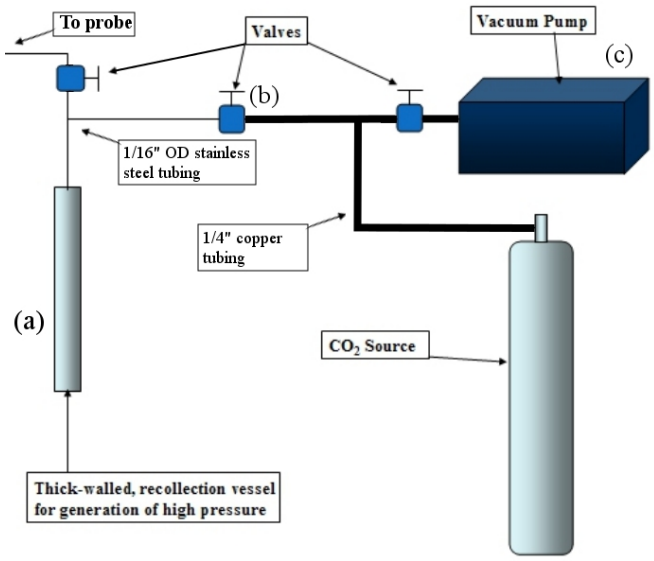

Figure 2.3: High pressures can be cryogenically achieved. Here, CO_2 is first frozen in a small-volume, thick-walled recollection vessel (a). Then valve (b) is closed and the recollection vessel is heated to sublimate the CO_2. Because of the now restricted volume, the pressure of the CO_2 increases dramatically. The vacuum pump (c) allows for pumping out of the system between uses and allows for cleaning of the probe of gas if necessary.

The probe has several key components to its design: the high-pressure reaction vessel, the Alderman-Grant coil, and the hotbox region. The schematic drawings for these detailed portions of the probe are included in Appendix B.

High-pressure reaction vessel

It was decided that the NMR coil would reside outside of the high pressure region of the probe to prevent the use of high pressure feedthroughs for the RF cable. The high-pressure reaction vessel then had to be built of a material that is non-conductive, has high tensile strength across a range of temperatures, contains no carbon, is unreactive to most chemicals, is impermeable to gas with 0% water retention, has virtually no thermal expansion, yet is moderately thermally conductive. The material we chose that meets all of these criteria is an

yttria-stabilized zirconia called AmZirOx 86 sold by AstroMet Inc. (Cincinnati, Ohio). AmZirOx 86 is 95% zirconia and 5% yttria and is ivory in color. It has the feel and weight of ivory as well. AstroMet not only made the material, but they also cast it to to approximate designed dimensions, grinding it to the final designed dimensions. A total of two high pressure vessels were designed and made, differing only in their lengths. A short one of 4" length was the first one to be designed and built. It is the piece that was used for all of the high pressure reaction data in this thesis. The long one is 5.5" in length and was designed for increased sample size and distancing of the RF coil region from the other metal portions of the probe. The long one has not yet been used in the project, but was designed with a zirconia filler plug (made of AmZirOx 86) to take up some of the headspace volume in the tube. The use of the same material allows its susceptibility to be matched to that of the vessel material, thereby decreasing its susceptibility effect on the magnetic homogeneity of the coil region. The design of these zirconia high pressure vessels allows them theoretically to be taken up to 400 °C at 400 bar—although the short one has only ever been taken as high as 150 °C and 250 bar (and not simultaneously).

RF coil

Several saddle coil designs were experimented with this probe. None of them had good RF homogeneities nor good B_1 field strength. The final design that had the best performance was a coil of a modified Alderman-Grant design.[43] The coil itself has a 0.7" inner diameter and is 1" in length (top to bottom) with two flat vertical copper strips (cut 1/4" wide) that connect a loop of thin copper strips (also cut 1/4" wide) at the bottom and two copper strips forming wings at the top. The bottom loop of the coil is a complete loop with no capacitors. The top wings of the coil are connected with high temperature non-magnetic capacitors which tune the coil to 89.066745

MHz. These capacitors do the job of the chip capacitors in Grant and Alderman's design. Also, there are two other differences with this design and the Grant and Alderman design. First, there is no inner ring on the inside the coil (so there is no e-field shielding). Second, the hot wire connects to the top of one of the vertical strips and the ground wire connects to the top of the other vertical strip. The hot and ground wires are the only form of support the coil has in the probe. Consult Appendix B for a drawing of the coil in the probe.

Heating the probe

The probe is heated and cooled with forced air. The cooling air is run through the hollow support rods of the probe, from the top down into the tank circuit of the probe. The heating is accomplished by running air through a glass tube with a heating filament in it. The heating filament is controlled through a platinum resistance thermometer and an Omega temperature controller. There are two safety features to the heater: there is a pressure switch attached to a "T" in the tubing *just before the heater.* When the air is on full flow through the probe a small back pressure is created by the air resistance of the probe. If the heating tubes were to pop off internally within the probe or anywhere between the heater and the probe or the heater and the air source in the wall, the back pressure would drop and the pressure switch would disengage the heater. This was tested multiple times by disconnecting the tube from the probe, the air source from the heater, etc, with the heater and air still running. The heater turned off each time. The pressure switch was calibrated for 1 psi. Any back pressure below that would cause the heater to be turned off. This safety feature is critical for long term experiments and has proven to be useful a number of different times.

Another pressure switch is connected to the building air system so that if the pressure in the

building air system drops below 60 psi the heater will turn off due to insufficient air flow through the probe. These safety features are essential to protect the heater, probe, and magnet. And they have been very useful multiple times due to building air failures and/or tube failures.

b. Probe performance

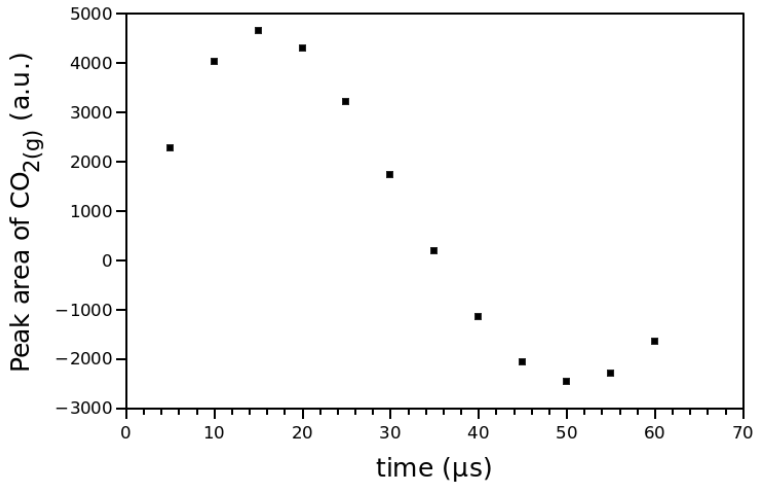

Figure 2.4: 90-time experiment nutation curve showing the performance of the Alderman-Grant coil design in the high pressure probe. Each point is the integrated $CO_{2(g)}$ gas peak. (Data: 20130422).

The Alderman-Grant coil design is very efficient. It has a Q-factor of 54 (FWHM of resonance is 89.825 MHz – 88.175 MHz). When it is run with 1 kW pulses it has a 90-time of 17.9 μs measured on $CO_{2(g)}$. The 90-times will fluctuate throughout a high pressure reaction due to changing ionic strength of the solution within the coil, but always stays less than 25 μs. Figure 2.4 shows the 90-time calibration curve.

As will be discussed a number of times in this thesis, the sheer size of the coil (1” in length) means that there is signal loss the more selective the pulse sequence. Comparing the absolute value of the amplitude of the 90° pulse to the 270° pulse shows that about 40% of the signal is lost. This is not necessarily spins within the coil, but the spins on the edge of the coil and just

outside of the coil. The selectivity of the coil can actually be an advantage in that the pulse sequences used can be tuned for location specificity within the sample as well as to avoid background signals in the probe.

As will be described in great detail in Chapter 5 of this thesis, some of the reactions studied in this probe can have very large pH gradients. The large pH gradients also mean a huge gradient of solution ionic strength—how many ions are in the solution. As the performance of the coil is only slightly affected by ionic strength, it does not matter much, except that the 90-time across the coil can vary. So care must be taken when measuring the 90-time *in situ.*

Early in the probe testing process I was trying to get the 90-time as short as possible by using different coil designs and amplifier powers. The record I obtained was on a brand new Alderman-Grant coil, on which I was able to measure a 90-time of 14.5 μs at 1 kW. The reported 90-time above is for a coil that is about two years old. Perpetual use in moist St. Louis air has caused the copper coil to oxidize, and the thin layer of oxidation does degrade the coil performance. After two years of use (and about 4800 h of reaction time) the 90-time has increased by 3.5 μs.

Pulsing at 1 kW can be very hard on the probe: arcing was actually a huge issue at the beginning. The coil was carefully built such that there were no sharp points in it (all solder was smooth). The biggest issue with arcing, however, was in the “hot wire” coming through its hole into the hotbox (see Appendix B). Three layers of teflon tubing were not enough to keep it from arcing into the grounded hotbox. So the hole was made much large than the wire (3/8”), and the wire was carefully covered in about 8 layers of carbon-free silicone tape to ensure that it was placed in the center of the hole and that the heat could not leave the hotbox. After this fix, the

probe no longer arced at 1 kW power.

c. *Probe calibration and testing using $^{13}CO_2$*

A series of experiments on the simple systems of $CO_{2(g)}$ and $CO_{2(aq)}$ at different temperatures and pressures were run to calibrate the probe's sensitivity and resolution as well as to understand its abilities to monitor long-term reactions and measure different aspects of the dynamics of the CO_2. These are reported briefly in this section.

T_1 of $CO_{2(g)}$ vs. pressure

The T_1 relaxation time constant of $CO_{2(g)}$ was measured at a variety of pressures at room temperature and compared to previously measured values by Kobayashi et. al.[44]

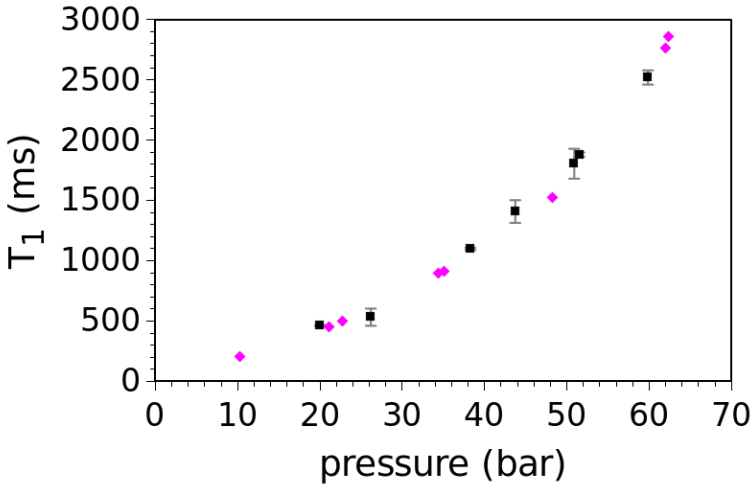

Figure 2.5: $CO_{2(g)}$ T_1 at various pressures at room temperature. The black squares with error bars are the results measured in the high pressure probe at 89.06 MHz. The pink diamonds are the values measured by Kobayashi et al. at 22.65 MHz.

The trend of increasing T_1 with increasing pressures indicates that the T_1 relaxation mechanism for $CO_{2(g)}$ is spin-rotation. The line is curved because of the Van der Waals (non-ideal) interactions of the CO_2 molecules. A plot of T_1 vs. density of the gas is a straight line.

Additionally, there is excellent agreement between the experimental measurement here at 89.06 MHz and those of Kobayashi et al. at 22.65 MHz (as seen in the figure above). This agreement is to be expected for a gas (which has a very short correlation time). The short correlation time gives the gas a nearly constant spectral density across a wide range of observation frequencies, meaning there is little observed field dependence of the T_1 relaxation time constant.

The dynamics of the $CO_{2(g)}$ can be probed by turning it into a liquid in the probe and observing what happens to its T_1 relaxation time constant. As the spin rotation mechanism for T_1 relaxation states, increased rate of molecular collisions increases T_1. Turning the gas into a liquid should therefore drastically increase the T_1 as the liquid is denser and has *many more* collisions per unit time. The condensing pressure of CO_2 at 22 °C is 60 bar (dashed line in following figure).

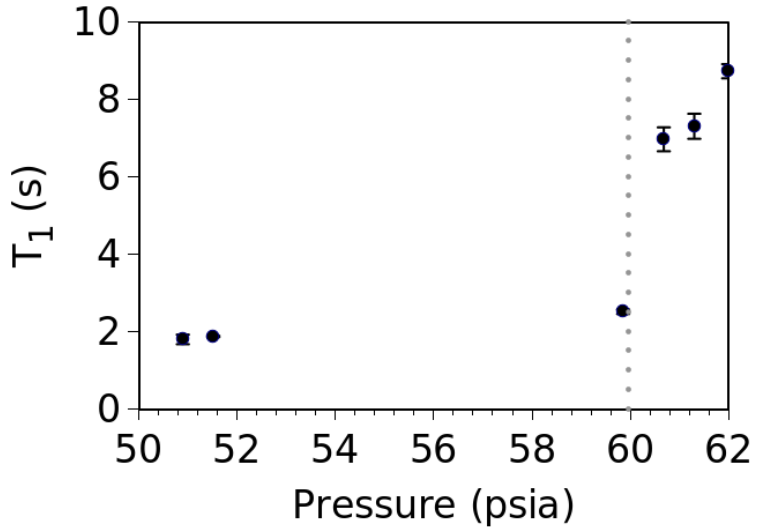

Figure 2.6: Condensation of CO_2 at 22 °C (60 bar, dashed line) is indicated in the T_1 relaxation time constant by a large discontinuity. The T_1 value continues to increase after condensing as the density of the $CO_{2(l)}$ increases. T_1 of CO_2 is actually a very good indicator of density.

Dissolution of CO_2 into water

If water is added to fill the coil, CO_2 dissolution can be monitored by watching the $CO_{2(aq)}$ signal increase in the solution with time. The following figure is from a CO_2 dissolution experiment and illustrates how the probe can deliver *relatively exact* measurements of absolute concentration. A spin counting technique was used to calibrate the probe's sensitivity to spins by measuring the signal from of $CO_{2(g)}$ known densities (calculated via the van der Waal's equation) at different pressures. The calibration was then used to estimate [CO_2] in water vs. time. The final concentration of [CO_2] in water at 48.9 bar was measured to be 0.86 M and the calculated equilibrium [CO_2] value in pure water for this pressure at 22 °C is 1.25 M (using Duan's model of CO_2 solubility, see Chapter 4). The difference between the calculated and experimental values is probably due to impurities in the water (St. Louis tap water was used) and changing of coil sensitivity due to the change of pH in the solution within the coil (the Alderman-Grant coil was not used in this experiment). The small vertical oscillations between experiments can be attributed to temperature changes in the room.

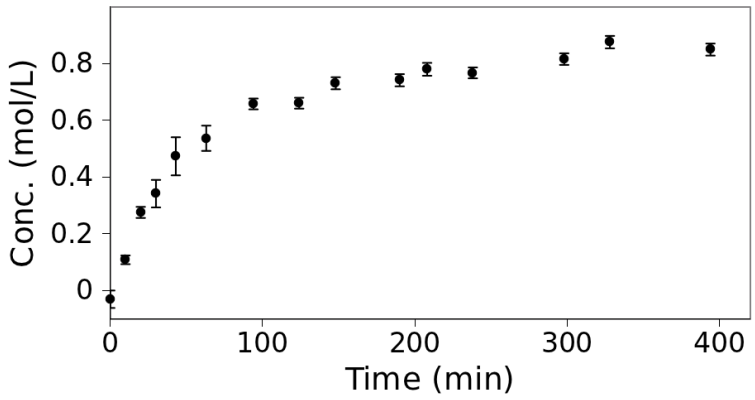

Figure 2.7: Dissolution of CO_2 in water vs. time.

The dissolution rate is much faster than what would be expected via a diffusion-only

mechanism (~24 h to reach equilibrium). The fast dissolution rate indicates that there is come kind of convection mechanism that occurs when CO_2 dissolves with H_2O. Perhaps a more dense phase of CO_2 is formed at the top of the H_2O and it then sinks, creating a convection current. ^{13}C NMR images of the dissolution event (using the imaging techniques discussed in Chapter 5) indicate that $CO_{2(aq)}$ fills up from the bottom of the vessel...something that could only appear to happen if there were dense layers "sinking" to the bottom of the tube.

The chemical shift of CO_2 and magnetic susceptibility effects

Throughout this thesis *in situ* ^{13}C NMR spectra will be referenced to the chemical shift of $CO_{2(aq)}$ as 126 ppm. This is well-documented in the literature[22,45,46] but has also been measured in two additional ways using the probe. The first way was to reference the $CO_{2(aq)}$ peak relative to acetone's ^{13}C CH_3 peak at 30.89 ppm, a reference that is nearly solvent-independent.[47] The second was to measure the difference in ppm between $CO_{2(aq)}$ and HCO_3^- in solution. The chemical shift of HCO_3^- is well documented and known to be 161.5 ppm.[46,48,49] In both cases the chemical shift of CO_2 was found to be 126 ppm. In addition, experiments in the probe where aqueous solutions containing $CO_{2(aq)}$ were heated up to 100 °C, the chemical shift of $CO_{2(aq)}$ did not change relative to the spectrometer frequency.

Using $CO_{2(aq)}$ as a chemical shift reference for the *in situ h*igh pressure ^{13}C NMR experiments is important because it does not involve the the addition of a chemical shift standard to the solution, thereby changing the chemistry of the reaction. Additionally, it makes referencing much easier in that magnetic susceptibility affects do not have to be taken into account, because the reference is in the same phase as the other species in the solution.

I found that the observed chemical shift of CO_2 in this probe changes by -2.6 ppm from $CO_{2(g)}$

to $CO_{2(aq)}$. This has been observed in a separate set of experiments. The first experiment measured the ^{13}C NMR frequency of neat $CO_{2(g)}$ in the high pressure probe. The second experiment measure the ^{13}C NMR frequency of $CO_{2(aq)}$ in a system of H_2O+CO_2. The observed difference between the frequencies of $CO_{2(g)}$ and $CO_{2(aq)}$ was -234 Hz and can be seen in Figure 2.8. Another experiment demonstrated tha the absolute ^{13}C NMR frequency of neat $CO_{2(g)}$ and sc-CO_2 does not change. These effects must be taken into account when referencing *in situ* spectra, as the sc-CO_2 peak (or $CO_{2(g)}$, depending on pressure and temperature) is present in addition to $CO_{2(aq)}$.

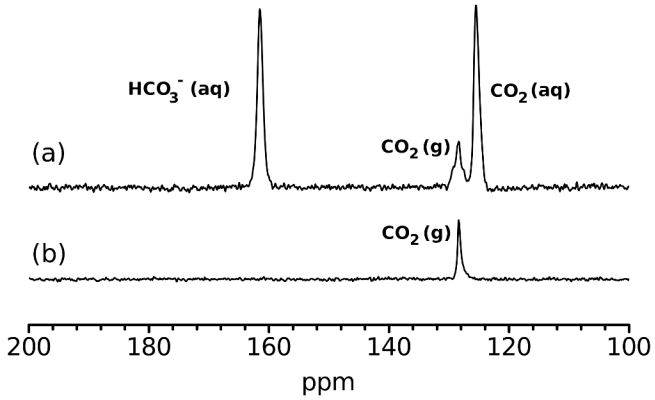

Figure 2.8: In situ spectrum of a carbonation reaction (a) vs. the spectrum of neat $CO_{2(g)}$ (b). The magnetic susceptibility effect of water is not small and care must be taken to avoid referencing to the wrong peak in situ.

The T_1 relaxation time constants of the $CO_{2(g)}$/sc-CO_2 peak and the $CO_{2(aq)}$ peak are further evidence that the peak assignments have been made correctly. The T_1 is quite short in the gaseous phase (1-3 s) while the T_1 is quite long in aqueous phases (20-40 s). The reason why the T_1 is longer in solution is because CO_2's dominant relaxation mechanism is spin rotation. The longer correlation time of the liquid makes spin rotation less efficient, thereby increasing T_1.

The chemical shift experiments and the T_1 experiments support the peak assignments made in

this work, but they fail to explain the cause of the -2.6 ppm difference in chemical shift. At least in part, magnetic susceptibility differences between the gas and the aqueous solution are probably a contributing factor. The negative change in frequency from the gaseous to the liquid state supports the magnetic susceptibility explanation. Nevertheless, in a ^{13}C NMR experiment where the coil is half-filled with water and pressurized with CO_2, the chemical shift difference between the $CO_{2(g)}$ and $CO_{2(aq)}$ still exists even though the geometry of $CO_{2(g)}$ on top of the $CO_{2(aq)}$ solution would not cause the susceptibility effect of increasing the $CO_{2(g)}$ frequency. In the end, I was never able to come up with a satisfying explanation for the differences in chemical shift observed between $CO_{2(g)}$ and $CO_{2(aq)}$.

Comments on S/N of the probe

It was found in practice that obtaining ^{13}C NMR spectra from any natural abundance ^{13}C-containing compound was quite difficult except in cases of very high density such as a pure solution of a carbon-containing material like ethanol. The probe does have a weak carbon background, however. If one were to do several thousand scans (tests were done at 4000) without the use of an echo, the carbon background would be quite visible. The background could not be eliminated even with thorough cleaning. To avoid background effects, and to decrease phase effects, Hahn echoes were used throughout this thesis. In addition 99% ^{13}C-labelled CO_2 was also used.

As you cannot alter the magnetogyric ratio to improve S/N of ^{13}C NMR spectra, the only way to improve S/N is to use 100 % labeled compounds. This provides ~100x more signal and also has the added benefit of shortening the T_1 relaxation times in carbonate solids (because of spin diffusion—this effect was measured, although it will not be discussed in this thesis). Labeling

improves the S/N considerably: you can see $^{13}CO_2$ gas shot-to-shot at just a few bar pressure in the high pressure probe described here. With the labeling you can also obtain a ^{13}C MAS NMR spectrum of a carbonate in one shot with a S/N greater than 500/1, and even see a complete static carbonate powder pattern in a single scan. Most of the spectra shown in this thesis are of partially (50-90%) or 99% labeled ^{13}C samples.

Other uses for the high pressure probe

The high pressure probe described here can be used any desired reaction at high pressure and temperature. If one were to exchange the coil, other types of NMR could be done. Although not described here, ^{27}Al, ^{1}H, and ^{69}Ga experiments have been done on this probe in addition to ^{13}C.

The probe has also been used to study high pressure and temperature reactions of methane (CH_4). While none of these work will be discussed here, the following figure shows a ^{13}C spectrum of methane gas at 65.29 bar. The $^{1}J_{H\text{-}C}$ couplings of 125 Hz can be clearly seen. This spectrum was taken with ^{13}C-natural abundant gas, so it also provides a benchmark for the probe's sensitivity. The T_1 of methane is very short (in the ms range), so the chosen recycle delay of 1 s was more than sufficient for attaining the following spectrum, which was acquired in 1000 scans.

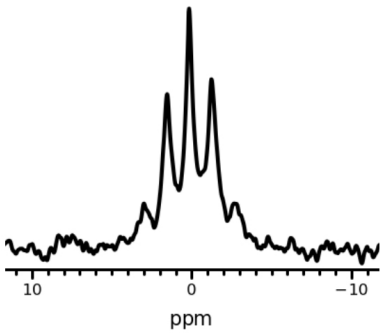

Figure 2.9: ^{13}C NMR spectrum of methane (CH_4) gas at 64.29 bar.

Chapter 3: *In situ* measurement of magnesium carbonate formation

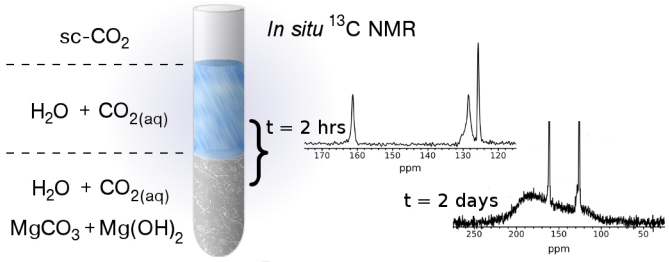

Figure 3.1: In situ [13]C NMR can monitor formation of magnesium carbonates in high pressure and temperature reactions.

A. Introduction

^{13}C NMR is a powerful technique for determining carbonate structure and can provide as much or more structural and phase information than either pXRD or Raman spectroscopy. ^{13}C MAS NMR is equally sensitive to both amorphous and highly crystalline compounds, unlike pXRD, which can only be used to analyze crystalline compounds. ^{13}C MAS NMR is also sensitive to all carbonates within a sample whereas back-scattered Raman can only detect species on the surface of carbonate particles. ^{13}C MAS NMR is also quantitative: one can determine relative amounts of carbonates in a sample by integrating the NMR peaks relative to each other, determining relative carbonate composition of a sample. All of these strengths make ^{13}C NMR an incredibly useful technique for studying solid carbonates.

^{13}C NMR carbonate analysis is not without its difficulties, however. Pure carbonate phases have very little physical motion at the frequencies we study them (the NMR frequencies we are able to use to study ^{13}C range from 50 to 150 MHz for ^{13}C), and as such have very poor spin relaxation properties.[21,50–52] As has already been discussed in Chapters 1 and 2, these poor

relaxation properties mean the samples can have excessive T_1 relaxation time constants and long T_1's mean the samples take a long time to polarize in the magnet, making it difficult to obtain quantitative spectra. To further complicate matters, ^{13}C is only 1.108% abundant. With a magnetogyric ratio that is roughly ¼ of hydrogen's, it has an NMR receptivity 1.7×10^{-4} that of hydrogen (receptivity $\propto \gamma^3 I(I+1)$, where I is the spin of the nucleus[53]). Thus, long relaxation times and poor polarization can make obtaining ^{13}C NMR spectra with good S/N very difficult.

Nevertheless, ^{13}C NMR has been shown to be useful in a number of ways to measure carbonate formation *in situ*[21,24] as well as to identify carbonate solids *ex situ* (see chapter 5).[21,25,50,51,54–56] Solid carbonates have a ^{13}C isotropic chemical shifts that range between 162 ppm and 175 ppm, where the lower range (162-167 ppm) is indicative of carbonate groups weakly associated with hydrogens (the hydrogens increase the chemical shielding of the carbon). Chemical shifts greater about 167 ppm or so are typically pure metal carbonates and are hydrogen-free (save a few exceptions, see Chapter 6 for more details). The differences in chemical shift from one pure metal carbonate to another are entirely due to the symmetry of the carbon site in the crystalline structure and the metal ion with which the carbonate group is associated.

In this chapter I will discuss the various *in situ* ^{13}C NMR measurements that I made on high pressure and temperature magnesium-containing mineral systems. Magnesium-containing minerals [periclase, MgO; brucite, $Mg(OH)_2$; and forsterite, Mg_2SiO_4] were chosen as the first mineral reactants to be studied because magnesium-containing minerals make up the bulk of sequestration minerals.[24,29,30,57–60] In particular, forsterite, the magnesium end-member of the mineral olivine ($Mg_XFe_{2-X}SiO_4$), has been studied extensively because olivine is the most

abundant mineral in the earth's upper mantle, has the fastest-reaction with CO_2 of any bulk mineral in the earth's upper mantle, and has the highest magnesium fraction of any naturally-occurring bulk sequestration target mineral.[61]

Forsterite has several complicating factors in its reaction with CO_2, however. First, it is a silicate-containing mineral, so its dissolution produces a concomitant release of silica into the surrounding solution, which ultimately precipitates as amorphous silica.[20,24,25,29,58] This silica can slow the kinetics of the dissolution of forsterite and even reprecipitate on the surface of the forsterite as passivating layers inhibiting its further dissolution.[59,62,63] Additionally, while forsterite does have the highest Mg content of any natural sequestration target mineral, it is still only 34.5% Mg by weight. Presumably higher Mg content in a mineral would speed the CO_2 sequestration process, as each gram dissolved would contain more Mg and thereby increase $[Mg^{2+}]$ in the solution at a faster rate. So two other minerals, periclase (MgO) and brucite $[Mg(OH)_2]$, were considered first. MgO is 60% Mg by weight and $Mg(OH)_2$ is 42% Mg by weight, both considerably higher in Mg than Mg_2SiO_4.

Sequestration reactions work best at elevated pressures and temperatures because the dissolution of the target minerals is enhanced by high temperatures and pressures (the higher the pressure of CO_2, the lower the pH of the solution; the lower the pH, the faster the dissolution of the mineral).[59,64] The dissolution of the mineral results in release of a large number of ions from the mineral (in the case of $Mg(OH)_2$, Mg^{2+} and OH^-, see Equation 3.2). These ions act to increase the pH of the solution, and the higher temperatures enhance diffusion and mixing of the reactants. Typical pressures and temperatures of proposed sequestration conditions range between 50 and 250 bar and 50-250 °C.[58,65,66] Most reactions above pressures and temperatures of

120 bar and 100 °C are not geologically relevant, as most candidate sequestration sites and reaction chambers have maximum pressures less than 120 bar and temperatures between 50 and 100 °C.[12,67–69]

a. Sequestration chemical reactions

The following chemical equations describe the generalized chemical reactions that occur on the minerals I consider in this chapter. Equation 3.1 shows the dissolution of $CO_{2(g)}$ into water. Though seemingly trivial, this step is very important and is often the most difficult portion to model in the chemical reactions, because knowing [CO_2] is very important to calculating the reactions correctly.

Additionally, as already experimentally shown in the previous chapter and described here in Equation 3.1, the dissolved CO_2 is in fact still CO_2–it does not become carbonic acid, H_2CO_3. Many, particularly in the biological community, like to refer to $CO_{2(aq)}$ as H_2CO_3. It is not.[70–73] Only about 0.4% of the CO_2 reacts with the water to form H_2CO_3 in solution, which is extremely unstable in solution and prefers to exist as $CO_{2(aq)}$ rather than $H_2CO_{3(aq)}$.[70,71,74] Some have attempted to find spectroscopic evidence for the existence of H_2CO_3 in solution, but no conclusive observations have ever been made that show H_2CO_3's presence in water.[45,46] However, attempts have been made using highly acidic and superacid solutions by me (unsuccessful) and others (also unsuccessful) to observe H_2CO_3.[74,75] Many theoretical papers have been written to calculate the most stable conformations of H_2CO_3 in solution, its vibrational properties, and its theoretical chemical shifts, but they don't necessarily agree on what the H_2CO_3's ^{13}C spectroscopic signature should look like.[73,74] Another generalized way of writing $CO_{2(aq)}$ that many chemists have adopted is $H_2CO_3^*$. This convention assumes that $H_2CO_3^* = CO_{2(aq)} + H_2O$

and is a nice way of showing that $CO_{2(aq)}$ has different reactivity than free CO_2. Here I use the term $CO_{2(aq)}$ because the ^{13}C chemical shift observed *in situ* is more closely related to $CO_{2(g)}$ than H_2CO_3's theoretical ^{13}C chemical shift.[74,75]

Finally, $CO_{2(aq)}$ also reacts with H_2O in a second way that is also pH-controlled. In the presence of enough alkalinity to consume the product H^+ (Equation 3.2), the reaction can produce a considerable amount of HCO_3^-, bicarbonate, or CO_3^{2-}, carbonate.

$$CO_{2(g)} \rightleftharpoons CO_{2(aq)} \quad (3.1)$$

$$CO_{2(aq)} + H_2O \rightleftharpoons HCO_3^- + H^+ \rightleftharpoons CO_3^{2-} + 2\ H^+ \quad (3.2)$$

$$MgO_{(s)} + 2H^+_{(aq)} \rightarrow Mg^{2+}_{(aq)} + H_2O \quad (3.3a)$$

$$Mg(OH)_{2(s)} + 2\ H^+ \rightarrow Mg^{2+}_{(aq)} + 2\ H_2O \quad (3.3b)$$

$$Mg_2SiO_4 + 4\ H^+ \rightarrow 2\ Mg^{2+}_{(aq)} + H_4SiO_4° \quad (3.3c)$$

The dissolution of the minerals, shown in Equations 3.3a-3.3c, raises the pH of the solution and competes with the dissolution of the CO_2 for control of the pH of the solution (dissolution of CO_2 lowers pH, while dissolution of mineral raises pH, as can be seen in Equations 3.1-3.3 by noting where H^+ is being produced or consumed). Once the $[Mg^{2+}]$ concentration is high enough and the right nucleation conditions exist, the Mg^{2+} ions will bond/react with the HCO_3^- ions to make $MgCO_3$-containing minerals (Equation 3.4).

$$Mg^{2+}_{(aq)} + HCO_3^-{}_{(aq)} \rightleftharpoons MgCO_{3(s)} + H^+_{(aq)} \quad (3.4)$$

Precipitation of the new magnesium carbonate mineral lowers the pH as mineral precipitation removes alkalinity from the solution. Precipitation happens only when the conditions are just right—that is, when conditions favor initial nucleation of the mineral and subsequent precipitation on that surface. Little is still understood about the minute details of the precipitation

process, and much of what we do "know" is from theory. Studies have shown that precipitation is a thermodynamically-driven process that can be manipulated by ionic strength, pressure, and the preexisting mineralogical surfaces.[57] They also show that the precipitation process can be very complicated and involve multiple precursor phases that form in solution before nucleation.[76] Here, I will not discuss any more details about precipitation mechanisms other than to note that the use of a measurement called "saturation index" (described in Chapter 4) helps to predict the probability of precipitation using the ion activity product (also described in Chapter 4).

As can be seen in Equations 3.1-3.4, there are two things that are needed for CO_2 sequestration reactions to occur: (1) a divalent cation source (such as Ca^{2+}, Fe^{2+}, or Mg^{2+}) and (2) lots of water. This chapter specifically deals with Mg^{2+} divalent cations, and all reactions are done with excess water. Carbonation reactions do occur, in a limited way, with minimal water (enough to have one or two monolayers of water on the mineral particles or in a humid environment), but they are typically slower and very inefficient. Several studies have attempted to understand the full relevance of water by pressurizing different minerals with CO_2 and varying amounts of water.[20,29,62,77,78] While they are interesting, they all more or less conclude the same thing: water is imperative for efficient carbon sequestration. And such results should not be surprising—CO_2 has only two oxygens, and carbonates have three. The third oxygen needs to come from somewhere, and in most cases it comes from water.[62]

b. Experimental details

Here we react three different minerals [MgO, $Mg(OH)_2$, and Mg_2SiO_4] with CO_2 at pressures and temperatures ranging from 80 to 120 bar and 70 to 100 °C within a high pressure yttria-stabilized zirconia vessel (see Chapter 2). The reactions range in length of time from 4

days to 31 days and are summarized in the reaction table at the end of this thesis, just before Appendix A. In total, 22 different high pressure reactions were run in the high pressure zirconia probe, only five of which will be discussed here.

Pressures and temperatures were carefully monitored throughout the duration of each experiment, and various *in situ* ^{13}C NMR experiments were obtained throughout the entire reaction time. ^{13}C NMR experiments ranged from simple Bloch decays (90-acquire experiments) to more complicated 16-step phase cycled Hahn echo sequences and saturation recovery T_1 sequences. The goals here were to watch the ^{13}C NMR signal evolve with time by monitoring the growth of the $MgCO_{3(s)}$ powder pattern and the ratio $[CO_2]/[HCO_3^-]$ by taking the ratio of the integrals of both the CO_2 and HCO_3^- ^{13}C NMR peaks.

The samples were prepared by filling a glass tube with water and a powdered mineral (usually in that order to ensure mineral pore space was saturated with water), and allowed to sit in the vessel overnight. Porosity of the mineral powders in the experiments described here ranged between 40 and 55% and were measured using a ^{13}C NMR spin counting technique. The amount of mineral added was typically just enough to fill the coil of the NMR probe, but occasionally only to partially fill the coil (to study the interface between the solution and the mineral). The water was always filled to the height of the coil or higher to ensure that the $CO_{2(g)}$ signal in the headspace of the pressure vessel was not detected by the coil. Figure 3.2 shows the different possible sample/coil configurations.

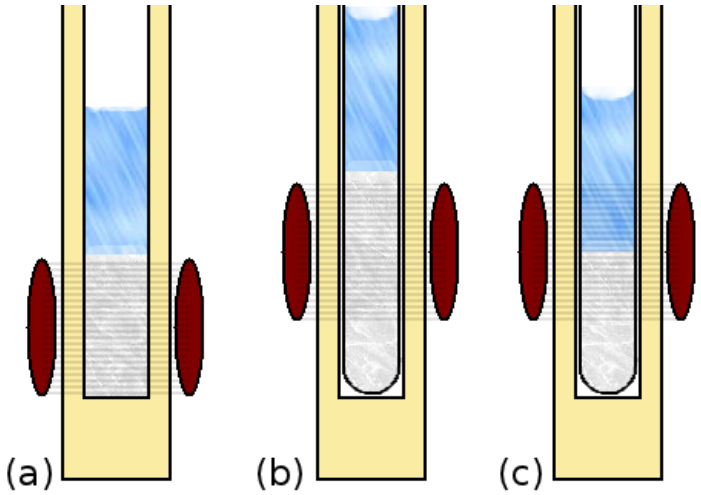

Figure 3.2: Three different coil/sample configurations for high pressure and temperature experiments. The brown ovals represent the two sides of the RF coil and the gray striped region between them represents the RF region of the coil. The coil is 1" tall. The blue region at top represents the solution on top of the sample, which is the gray matter in the bottom of the tube.

In Figure 3.2, position (a) was was tried at first because it used the least amount of mineral reactant. It was found that the bottom of the zirconia tube caused susceptibility issues that distorted the ^{13}C NMR lines in the spectrum that could not be corrected by shimming. Adjusting the RF coil to 1/2" above the bottom of the tube (b) reduced the susceptibility inhomogeneities caused by position of the the bottom of the tube within the "fixing range" of the shims. The downside is that almost twice the sample is required to completely fill the coil in position (b), but if the interface between the powdered solid and solution is to be studied, a half filled coil [position (c)] allows you to use less mineral reactant.

Additionally, a glass liner tube was added in position (b) and position (c) in Figure 3.2. The glass liner allowed for easy removal of the mineral product, as the glass liner prevented carbonate mineralization from occurring on the inside surface of the zirconia tube, which proved difficult to remove after the first reaction without the glass liner. The glass liner did not change

the ^{13}C linewidths by introducing any field inhomogeneities within detectable limits (25 Hz) so long as the RF coil was at least 1/2" above the bottom of the tube.

The height of water on top of the sample in Figure 3.2 was found to contribute greatly to the length of the reaction. This was because the sample was unstirred and the CO_2 had to diffuse and convect through the water layer to reach the mineral. The more water, the longer it took to see a $CO_{2(aq)}$ signal using the ^{13}C NMR coil. The length of diffusion time also affected the mineral products in that the $[CO_2]/[HCO_3^-]$ ratio slowly increased rather than suddenly increased, as occurred in the case of minimal water. Because the amount of water present matters in terms of pH and reaction rates, the molar ratio of mineral/H_2O will be provided for each reaction discussed.

In most cases, the particle sizes of the reactant minerals were 15 microns in their shortest dimension (determined by sieving and visibly confirmed through a microscope). A fine powder should increase the surface area of the reactant mineral and enable carbonate precipitation with less reaction time. The study of surface area and particle size effects on the CO_2 sequestration reactions will not be considered here.

Additionally, as mentioned earlier, the effects of water content can be very important. Here I use the convention of grams of mineral/liter of water to express the mineral/water ratio.

Finally, it is worth noting that both magnetic field strength[79] and extent of ^{13}C labeling[80] can affect the mineralization rates of different carbonate minerals. In the entirety of this thesis I assume that these effects are small and do not appreciably change the results presented.

B. MgO, Periclase

MgO, periclase, was chosen as the first reactant mineral to investigate because of its high magnesium content. Whereas several reactions were completed, here I will only show one called "R13", where 0.962 g of MgO was added to 3.240 g of H_2O (296.9 g mineral/L H_2O) in a glass liner tube that was then placed into the high pressure vessel and allowed to sit overnight so that it would settle. Once settled, the mineral filled the first 2.5 cm of the tube (from bottom, upwards) and the water level was 1 cm above the mineral/water surface. The reaction was run for 8 days at 95 °C. The pressure started at 96.0 bar and fell to 89.8 bar after 8 days of time. The pressure drop is due to the consumption of CO_2 during the reaction. A bolus of CO_2 is put on top of the solution at the beginning, as described in Chapter 2, and then the container is valved closed so that no more CO_2 is added through the duration of the experiment.

a. In situ ^{13}C NMR

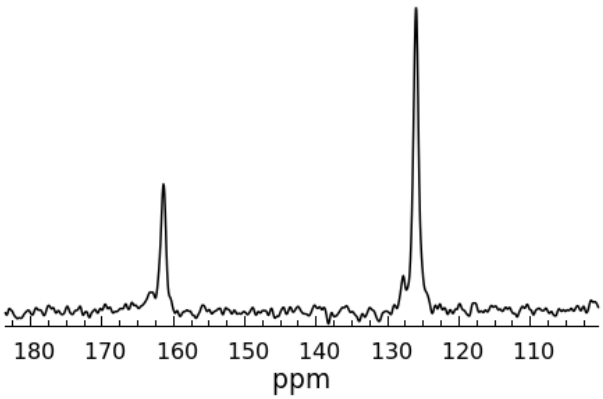

Figure 3.3: In situ ^{13}C NMR 1 h into reaction. 32 scans, 60s recycle delay. The HCO_3^- peak is at 161.5 ppm, and the $CO_{2(aq)}$ peak is at 126 ppm. A small sc-CO_2 peak can be seen at ~128 ppm.(Data: 642a, 20120320).

The reaction was begun and ^{13}C NMR acquisition began immediately thereafter. The first spectrum obtained, shown in Figure 3.3, shows two solution-phase peaks: $CO_{2(aq)}$ at 126 ppm and

HCO_3^- at 161.5 ppm. The $[CO_2]/[HCO_3^-]$ ratio here is 2.13, meaning that at the beginning of the reaction there is twice as much CO_2 as HCO_3^-. The appreciable bicarbonate this early in the reaction is indicative of somewhat fast mineral dissolution. The H^+ ions in the solution are being consumed by the very basic mineral, MgO (Equation 3.3a). Le Chatelier's principle states that if you remove one of the products, then the reaction will shift to make more, consuming more reactants. As HCO_3^- is not being consumed (at least not at the rate of H^+), there is still much of it in the solution. The rate of exchange between CO_2 and HCO_3^- is very fast (although slower than the NMR time regime (~10^{-3} s), which is why we see two peaks), such that any HCO_3^- lost is replaced within a few seconds (per known reaction rates at these temperatures[45,70,71,81–83]), because the loss of H^+ is driving the reaction. In other words, dissolution of the mineral is driving the reaction.

The ratios of $[CO_2]/[HCO_3^-]$, obtained by integrating the *in situ* ^{13}C NMR spectra during the 8 days during which the mineral was allowed to react with the CO_2, can be seen in Figure 3.4.

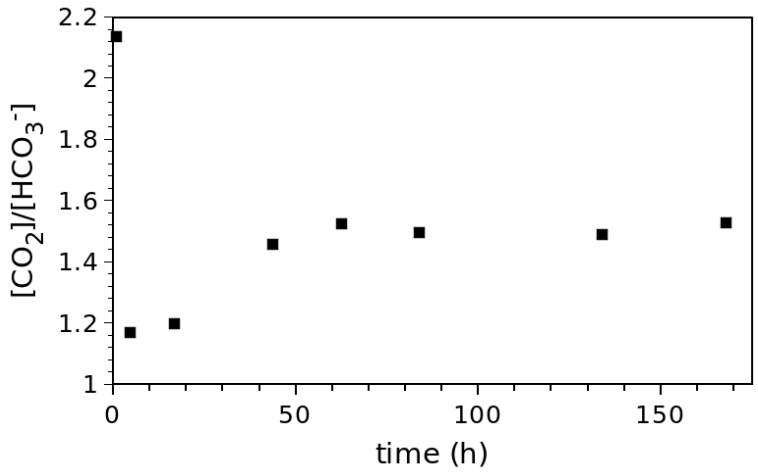

Figure 3.4: $[CO_2]/[HCO_3^-]$ ratios, obtained from in situ ^{13}C NMR data, for the reaction of MgO with CO_2 for the first 8 days of the reaction. (Data: R13).

The initial drop of the $[CO_2]/[HCO_3^-]$ ratio in the first three hours of the experiment indicates the pH of the solution is rising (so H^+ ions are being consumed). The drop is caused by the dissolution of the mineral. The trend, however, quickly reverses after the first 20 hours, wherein the $[CO_2]/[HCO_3^-]$ ratio begins to increase. The increase in the ratio does not mean that the MgO dissolution is finished, just that the carbonate precipitation is beginning to play a real role in removing the alkalinity of the solution and releasing H^+ ions into solution (Equation 3.4). Another important but smaller contributor to the increase of the ratio is a slowing of the mineral dissolution, such that the CO_2 dissolution rate is able to catch up with the mineral dissolution rate. As the solution is not being stirred, typical equilibration time for the CO_2 gas is around 12 h. The drop in ratio is much faster than that, however, indicating the speed with which the MgO dissolves at these high pressures and temperatures.

To show that carbonate precipitation is occurring during the later time periods (and contributing to the rise in the $[CO_2]/[HCO_3^-]$ ratio), the *in situ* ^{13}C NMR spectra are plotted in Figure 3.5 at four time intervals. The spectra shown in Figure 3.5 are focused on the baseline around the $CO_{2(aq)}$ and HCO_3^- signals to show the formation of the ^{13}C carbonate NMR powder pattern over time. The solid carbonate signal presents itself in a powder pattern because it represents a stationary solid, and represents a very large number of spins (because of the breadth of the pattern, the signal is spread out leading to less intensity than the narrow resonances). T_1 is very long for the mineral, so the area of the powder pattern relative to the narrower, solution-state resonances of the $CO_{2(aq)}$ and HCO_3^- is much smaller than it should be (spectra were not recorded at 5*T1, as required for quantitative comparisons).

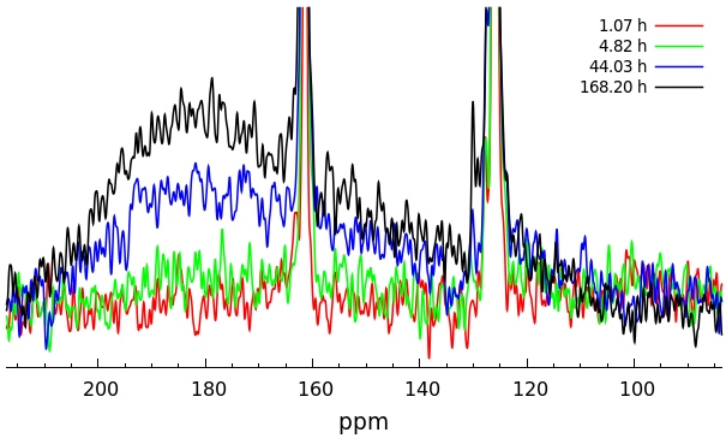

Figure 3.5: Formation of carbonate powder pattern in the sequestration reaction of CO_2 with MgO. The $CO_{2(aq)}$ signal is visible at 126 ppm and the HCO_3^- signal is at 161.5 ppm. The time at which each spectrum was obtained during the reaction is listed in the legend in the plot. These were acquired with a Bloch decay pulse sequence with a 60 s recycle delay and 32 scans each. (Data: R13 642a, 642f, 648a, 658a).

Because the spectra in Figure 3.5 were acquired with a Bloch decay pulse sequence, there are some first order phase distortions evident in the powder pattern of the spectrum from leftshifting of the time domain of the spectrum due to the long 90° acquisition pulse (30 μs) and about 7 μs of probe dead-time ("ring-down" time). Phase-cycled Hahn echoes are the best way to get rid of these problems and are used exclusively in later experiments.

After 8 days of reacting, the pressure vessel was cooled down to room temperature, and the CO_2 gas pressure was slowly decreased to atmospheric pressure (a process typically lasting two hours). The glass sample tube containing the product of the reaction was removed from the high pressure vessel, and a microspatula was inserted into the tube to ascertain the softness of the product material. It was found that about 1 cm into the sample was hard rock and the top portion was still viscous and liquid-like. The sample was then put into a vacuum chamber overnight for drying. No heat was used during this drying process as vacuum and heat combined can cause

some carbonate phases to convert to other carbonate phases.

b. Ex situ Raman analysis

The dried sample was removed from the tube by wrapping the tube in a paper towel and smashing it with a hammer. The glass shards were carefully removed from the sample. The bottom-half of the sample that was rock-like stayed intact during the glass breaking process, but the top portion of the sample was loose white powder. Several Raman spectra were run on both the bottom and top portions of the sample to confirm that the two reported spectra were indicative of the bulk of the sample. Figure 3.6(a) shows the spectrum from the top portion of the sample and 3.6(b) from the bottom of the sample. One clever portion to this experiment is that MgO is not Raman active; so any Raman signal indicates products formed as a result of the reaction.

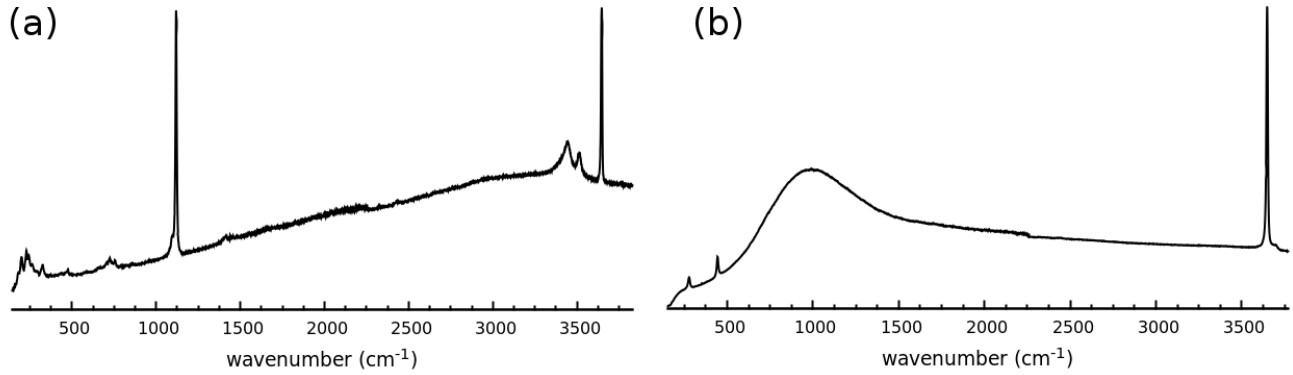

Figure 3.6: Raman spectra from the top (a) and bottom (b) of the sample tube. The divot at 2260 cm^{-1} in both spectra are an artifact from the instrument detector. The symmetric carbonate stretch can be seen in (a) at 1118.8 cm^{-1} but not in (b), indicating that carbonate formed in (a) and not in (b). (Data: R13 04122019, 04122022).

The very strong peak at 1118.8 cm^{-1} in Figure 3.6(a) is indicative of the symmetric stretch of the CO_3^{2-} group in the mineral hydromagnesite [4 $MgCO_3 \cdot Mg(OH)_2 \cdot 4H_2O$] and the small

shoulder at 1093.6 is indicative of the same symmetric stretch in the mineral magnesite ($MgCO_3$). Additionally, the two broad peaks between 3350 and 3550 cm^{-1} are indicative of mineral-bound water, and the very strong peak at ~3645 cm^{-1} is actually two peaks very close together, 3643.5 and 3647.5 cm^{-1}, which correspond to two different O-H stretches in the sample. The spectrum in Figure 3.6(b) lacks the hydromagnesite and magnesite peaks, but contains peaks consistent with the mineral brucite, $Mg(OH)_2$,[84] which formed under pressure.[85] The two peaks at 277.4 and 443.9 cm^{-1} correspond to the Raman-active $E_g(T)$ and $A_{1g}(T)$ modes, respectively, and match the reported peaks[85] of $Mg(OH)_2$ formed under pressure. Additionally, in the O-H stretch region there are two peaks: one shown very strong at 3648.2 cm^{-1} and another, a shoulder on that peak, that extends to 3698.3 cm^{-1}. Both are O-H stretches of $Mg(OH)_2$ and occur as multiple peaks because of effects on the mineral structure from being formed under pressure.[85] The very broad peak at ~1000 cm^{-1} is probably aqueous HCO_3^-.[30] Even though the sample was dried in a vacuum overnight, sample in the bottom of the tube was still quite moist (although not a slurry) and probably contained residual bicarbonate from trapped CO_2 that was not able to leave the solution due to the rise in pH from depressurization of the solution. The extra width of the peak is probably due to the HCO_3^- being in a thin layer of water on the mineral product (it is broader than aqueous HCO_3^- reported elsewhere[30,45]).

The results from the Raman spectra explain why the mineral reaction seemed to stabilize so quickly (after ~100 h) in Figure 3.4. It also explained the hardness of the mineral in the bottom portion of the reaction tube. MgO when heated in water converts to the mineral brucite (Equation 3.5):

$$MgO + H_2O \rightarrow Mg(OH)_2 \quad (3.5)$$

During the conversion into $Mg(OH)_2$, the individual particles fused together to become one solid "chunk" of $Mg(OH)_2$. The probable impermeability of this material prevented the CO_2 from reaching the rest of the mineral reactant below, and therefore only allowed carbonate mineral product to form in the top portion of the reaction tube.

c. Ex situ pXRD

The top and bottom portions of the sample were dry-ground using a mortar and pestle and loaded onto a slide for pXRD analysis to confirm the previous Raman assignments.

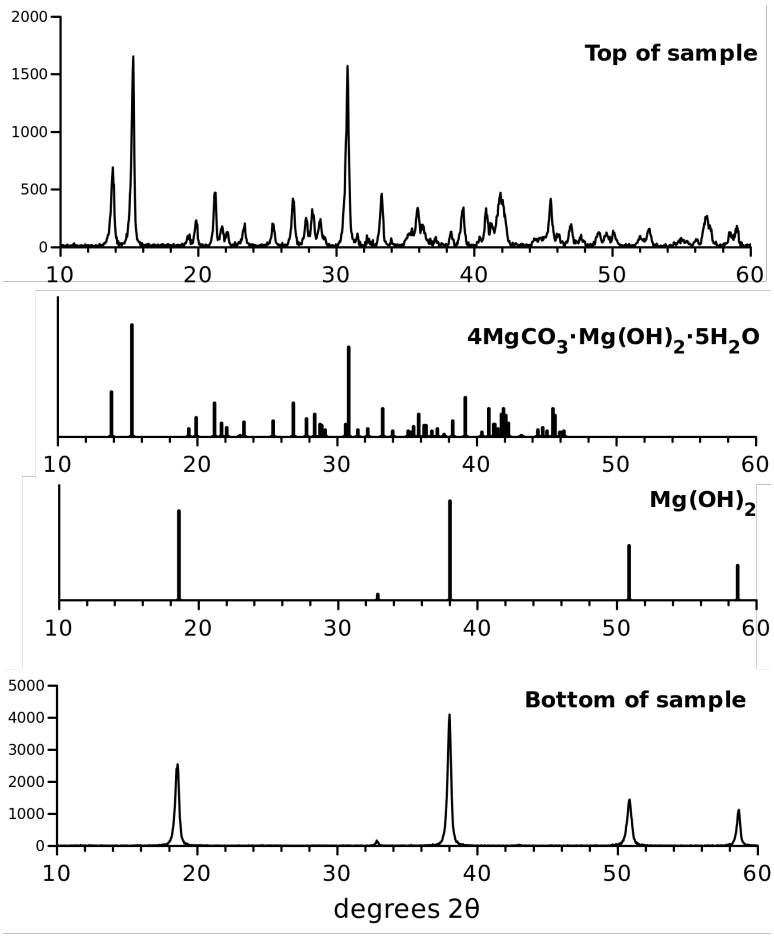

Figure 3.7: pXRD of the top and bottom of the sample as indicated. The mineral hydromagnesite, $4MgCO_3 \cdot Mg(OH)_2 \cdot 4H_2O$, is the dominant phase in the top and brucite, $Mg(OH)_2$, is the dominant phase in the bottom. In the middle of the figure, the hydromagnesite standard (PDF#00-025-0513(RDB)) only includes hydromagnesite peaks to 46 degrees 2θ. The brucite standard is PDF#00-007-0239(RDB). The y-axes are in arbitrary units, counts from the x-ray detector. (Data: R13 041212a, 041212b).

The pXRD results demonstrate that the top product is predominantly $4MgCO_3 \cdot Mg(OH)_2 \cdot 4H_2O$ (with no $MgCO_3$ detected). These reaction results are also supported in literature.[86] The pXRD results also confirm that the MgO is reacting to form pure $Mg(OH)_2$ in the bottom of the tube.

d. *Ex situ ^{13}C MAS NMR*

A portion of the top of the sample was packed into a MAS rotor, and a ^{13}C MAS NMR spectrum was obtained. This sample, like most of the samples discussed in this thesis, is 99% ^{13}C-labelled, which provides a factor of 100 S/N improvement over unlabeled compounds. This sample was spun at a rotational frequency of 5 kHz and allowed to magnetize for 30 minutes before a one-scan Bloch decay pulse sequence (with a 60° pulse) was recorded while simultaneously decoupling the ^{1}H channel with 15 kHz decoupling (only during signal acquisition).

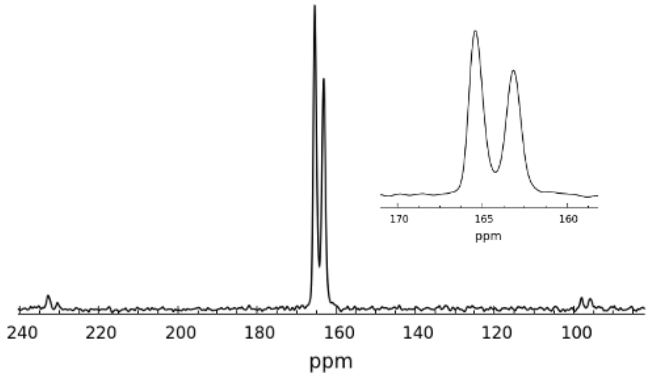

Figure 3.8: $^{13}C\{^{1}H\}$ MAS NMR spectrum (ν_r = 5 kHz) showing two well-defined peaks at 163.2 ppm (48.71 % area) and 165.4 ppm (51.29 % area). These two peaks are indicative of $4MgCO_3{\cdot}Mg(OH)_2{\cdot}4H_2O$, the mineral hydromagnesite. Spinning sidebands can be seen on both sides of the spectrum. The inset shows a close-up of the two peaks. (Data: 20130603-R13).

Figure 3.8 shows the $^{13}C\{^{1}H\}$ MAS NMR spectrum obtained on the top product of the sample. There is no $MgCO_3$ in this sample—just $4MgCO_3{\cdot}Mg(OH)_2{\cdot}4H_2O$. While $4MgCO_3{\cdot}Mg(OH)_2{\cdot}4H_2O$ will be discussed in greater detail in Chapter 6, it is important to note that two peaks of equal area are expected for $4MgCO_3{\cdot}Mg(OH)_2{\cdot}4H_2O$ based on how many inequivalent C's there are in the crystal structure. If the sample were fully relaxed, the peaks

should both have the same area, as they do (within 1%) in Figure 3.8. The peak at 163.16 ppm is consistently broader than the peak at 165.38 ppm, no matter where the ^{1}H decoupling frequency is in the proton spectrum. The reason is that there are actually two slightly different sites contributing to the peak. These two sites are likely the same crystallographically inequivalent site but are near a water that has some freedom to its position and/or actual motion within the crystal structure. More will be discussed about this multi-site description of hydromagnesite when $4MgCO_3 \cdot Mg(OH)_2 \cdot 4H_2O$ is fully elucidated in Chapter 6.

e. Conclusions about CO_2 reactions with MgO

Five different high pressure and temperature reactions were run on MgO at varying different temperatures, pressures, reaction length, and water content. All of them produced hydromagnesite ($4MgCO_3 \cdot Mg(OH)_2 \cdot 4H_2O$) selectively. Only a few Raman experiments showed any indication of $MgCO_3$ formation, and that only in very small amounts on only a few particles.

Furthermore, these experiments showed CO_2 and MgO to have high reactivity together. The XRD experiments showed there to be no MgO left in the top of the reaction tube, and on the basis of the *in situ* $[CO_2]/[HCO_3^-]$ ratios, the reaction progressed very rapidly. The rate observed here must be due to the high temperatures and pressures, as others have reported that MgO has essentially no reactivity with CO_2 at low partial pressures and low temperatures.[87–92]

These experiments demonstrate that MgO has apparent product selectivity for the mineral hydromagnesite ($4MgCO_3 \cdot Mg(OH)_2 \cdot 4H_2O$), at a wide array of temperatures (several experiments were run from 65 to 100 °C, and all products were selectively hydromagnesite). Nevertheless, use of MgO is not very practical for the sequestration of CO_2 in bulk, because it converts to impermeable blocks of $Mg(OH)_2$ that inhibit CO_2 from diffusing to the rest of the sample in any

reasonable amount of time.

C. $Mg(OH)_2$, Brucite

The second mineral studied was brucite, $Mg(OH)_2$. It was slated as an excellent candidate reaction mineral because it is so alkaline; when mixed with water, the pH of the resultant solution is >11, which is why a slurry of $Mg(OH)_2$ and water was sold under the name of Milk of Magnesia through the mid-20th century. Its high pH helped to ease heartburn by neutralizing the acid in the stomach (Milk of Magnesia is also a laxative—working as such because the osmotic force of the slurry solution draws fluids from your body into your intestine). The high pH of the solution was expected to convert most of the dissolved CO_2 into CO_3^{2-}, enhancing the rate of production of $MgCO_3$-containing minerals because of the high availability of CO_3^{2-}.

Furthermore, a great deal about the reaction of CO_2 with the mineral brucite, $Mg(OH)_2$, has been published.[21,64,77,88,91,93–97] This is largely because of its fast reaction rates, making it an ideal system for studying CO_2 sequestration. Whereas it is not present in any significant concentrations in the Earth's outer mantle for natural CO_2 sequestration, it has been proposed as a potential CO_2-scrubbing agent in an industrial setting.[93] It, like MgO, will likely not have any bulk CO_2 sequestration relevance, but understanding the fundamentals of its reaction with CO_2 is important for understanding CO_2 sequestration reactions because the reactive constituents of the mineral are the same as other target sequestration minerals. In addition, because of its fast reaction rates,[93] it makes an excellent test system for watching solid carbonate formation *in situ.*

As this system is so fast to react, it was used to explore a vast array of temperatures and pressures as well as water content. In total, nine high pressure and temperature experiments on

$Mg(OH)_2$, ranging in temperatures from 60 to 100 °C and pressures from 70 to 126 bar (see the reaction list at the end of this thesis, just before Appendix A). The shortest reaction probed was only 1 day and the longest one 31 days. I also probed several mineral/water ratios. The lowest ratio was 140.9 g $Mg(OH)_2$/L H_2O and the highest ratio was 742.1 g $Mg(OH)_2$/L H_2O. The different mineral/H_2O ratios were important to explore because the depth of water on top of the mineral affects rates of reaction and types of carbonate products. It controls the rates of reaction essentially by controlling how long it takes to diffuse the CO_2 through the solution to the mineral. It also appears to control the carbonate products by controlling how much water is actually available during the reaction—that is, if there is not much water at the top of the mineral, the dissolution of CO_2 into the solution can dehydrate the mineral, significantly lowering the pH.

Here I will show results from three different experiments of CO_2 with $Mg(OH)_2$. The first two will compare low water content (742.1 g $Mg(OH)_2$/L H_2O, ~0.1 cm of water on top of the mineral) to high water content (481.8 g $Mg(OH)_2$/L H_2O, 0.64 cm of water on top of the mineral). The small difference in water content does make a difference in the reaction rate and progress. I will refer to them as the "low water content" reaction, called "R15"; and "high water content" reaction, called "R19"; respectively. The third experiment, called R9, is a second high water content reaction that was performed to study the chemical products *ex situ* in great detail. Its mineral/water ratio was 281.53 g $Mg(OH)_2$/L H_2O.

a. In situ ^{13}C NMR

Figure 3.9 (a) and (b) shows a comparison of the low water content reaction system, R15, versus the high water content reaction, R19, respectively. Each reaction has two spectra taken at

two different time intervals: early in the reaction (pre-carbonate mineral formation, black lines) and later in the reaction (post-carbonate mineral formation, red lines).

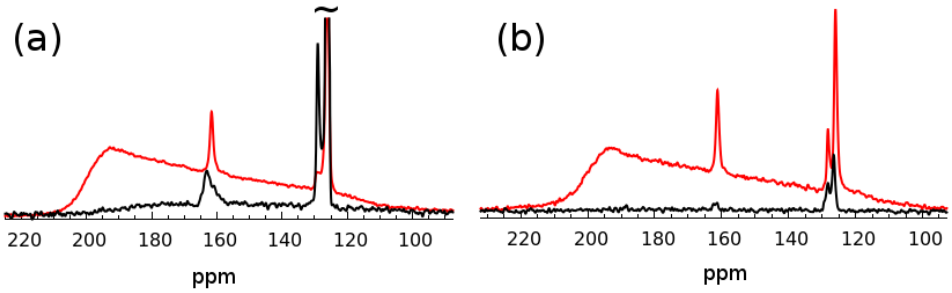

Figure 3.9: In situ static ^{13}C NMR of reaction with CO_2 and $Mg(OH)_2$ with low water content (a), R15, and high water content (b), R19. Early-time, before carbonate precipitation (black) is compared to late-time, after carbonate precipitation (red) during the reaction. For (a), black is 5 h and red is 105 h. For (b), black is 43 h and red is 234 h. (Data: (a)R15 661e,675c; (b)R19 1021b,1037b).

The spectra in Figure 3.9 outline the wealth of information that can be obtained by monitoring *in situ* ^{13}C NMR during carbonation reactions. For that reason the next couple of pages are devoted to fully explaining how they are interpreted.

First, the spectra in Figure 3.9a were both obtained in 128 scans with a 60 s recycle delay while the spectra in Figure 3.9b were both obtained using 256 scans and a 20 s recycle delay. Both sets of experiments used the same pulse sequence, a 16-step phase-cycled Hahn echo with a 100 μs τ delay. Both sets of experiments also are quantitative as the longest T_1 of the solution-phase species is on the order of just ~5 s at the temperature of these two reactions (81 °C). I used the Hahn echo sequence here and in the rest of the thesis because it selects for spins specifically within the NMR coil (it is more RF-selective than a 90-acquire sequence) and because it also allows acquisition of NMR FID's (free induction decays) that are free of the first-order phase effects from probe “ring down”.

The first observations to make about R15 and R19 in Figure 5.9 (a) and (b) are the noticeable differences between their early-time spectra. The $CO_{2(aq)}$ peak (126 ppm) is off-scale in (a) while in (b) it is very small, in comparison. Their $[CO_2]/[HCO_3^-]$ ratios are therefore very different, i.e., being ~25/1 in (a) and ~3.5/1 in (b). Also, despite the drastically different times into the reaction that the spectra were acquired [5 h into the reaction for (a) and 43 h for (b)], (a) at just 5 h already has mineral forming (see baseline distortion) and (b) still has a flat baseline at 43 h! Clearly, when there is less water to diffuse the CO_2 through as in (a), it takes less time to get large amounts of $CO_{2(aq)}$ into mineral. That resultant glut of $CO_{2(aq)}$ causes a huge drop in the pH and results in a higher $[CO_2]/[HCO_3^-]$ ratio at earlier times in the reaction. The rapid drop in pH also increases the rate of mineral dissolution, which in turn increases the rate of carbonate precipitation because the dissolution releases Mg^{2+}. Thus, intuitively, less H_2O bulk volume means faster carbonation because it takes less time for the overhead slug of CO_2 to get to the mineral and begin dissolving it.

You will also note that the difference in the way the two samples change with time. The sc-CO_2 peak at ~128 ppm in (a) *decreases in area* with time, whereas the sc-CO_2 peak in (b) appears to *roughly stay the same* or possibly even *increase a little.* This is a little more complicated to explain, because the sc-CO_2 peak is being detected from both the solution and the region between the glass insert tube and the high pressure zirconia vessel. Presumably in (a), the reaction with less water on top of the sample (R15), the slug of sc-CO_2 that entered the system caused an early-time dehydration of the top mineral region, meaning there were portions of the sample within the coil that experienced more CO_2 than water. A CO_2-rich zone often occurs when the two fluids (sc-CO_2 and H_2O) meet and have to mix together by diffusion and

convection.[20,62,78,98] Once the water and CO_2 remixed, causing the CO_2 within the coil to be fully hydrated, the chemical shift would return to 126 ppm. This, and the fact that some water is lost to the outside of the glass insert (decreasing the sc-CO_2 signal from between the glass tube and high pressure zirconia vessel), explains the loss of sc-CO_2 signal over time in (a). In (b), however, the situation shows that by the time the CO_2 reaches the mineral it is already $CO_{2(aq)}$. The mineral is probably never exposed to a solution phase that is more CO_2 than H_2O. In fact, the apparent slight increase in sc-CO_2 is attributable to the difference in match of the probe between the two times. This example illustrates why relative integrations between peaks in quantitative acquisitions is a more accurate measurement than direct quantitative integrations from acquisition to acquisition (see Chapter 2 for more details on the probe performance).

Other important points to make about R15 and R19, Figure 3.9 (a) and (b), are that the shapes of the HCO_3^- peaks are different as well in both their early-time acquisition and their late-time acquisition. Note the asymmetry of the HCO_3^- resonance in the early-time spectra (black) in (a) and (b). Both HCO_3^- resonances in (a) and (b) are noticeably broader (400 Hz and 200 Hz, respectively) in comparison to the HCO_3^- peaks at later times (90 Hz) and the concurrent $CO_{2(aq)}$ peaks at both early and late times (all 90 Hz as well). The fact that the $CO_{2(aq)}$ line is consistently 90 Hz in linewidth indicates that the line broadening of the HCO_3^- peak is not due to a magnetic field inhomogeneity but instead to an initial pH gradient caused by the mineral slowing the diffusion and convection of $CO_{2(aq)}$ from the top of the mineral to the bottom.

The HCO_3^- line broadens because the chemical shift of the HCO_3^- line is dependent on the relative amounts of HCO_3^- to CO_3^{2-} because of a very fast (much faster than the NMR time regime) equilibrium between them. If the pH shifts to values above 7, the chemical shift of the

observed HCO_3^- resonance will change with respect to the relative amount of the two species (see Chapter 4 for greater discussion on this). The $Mg(OH)_2$ solution had a pH > 11 before being pressurizing with CO_2. Therefore the first CO_2 molecules to make it into the powdered mineral domain would be converted into HCO_3^- and CO_3^{2-} and would stay in that state until more CO_2 gets there. The fact that there is a gradient in $CO_{2(aq)}$ across the sample caused by the obstructing mineral means that there is a gradient in pH, and the gradient in pH causes a series of chemical shifts (the line broadening) to appear for the HCO_3^- line. As will be described in great detail later, the dispersion of chemical shifts here indicate that the gradient could be as large as 4 or 5 units of pH across the short sample: ranging from 5 or 6 pH in the top of the tube to 10 pH in the bottom of the tube. Finally, that the line narrows with time indicates that the early gradient is only short-lived: eventually the $[CO_2]$ value equilibrates through the whole system and the initial pH gradient goes away.

While much has been said about Figure 3.9, there is still one more important point to be made about it. The spectra in Figure 3.9 indicate that both reactions are both precipitating similar carbonate product(s) (the lineshapes are both very similar between R15 and R19, Figure 3.9 (a) and (b)) and they also show that even the high water content system (b) is not free of the CO_2-saturation effect. In R19, Figure 3.9(b), the apparent chemical shift of $CO_{2(aq)}$ changes to a lower value between the early-time and late-time spectra (it shifts about -1 ppm). This is attributable to the mixing of the CO_2 and H_2O causing an initially less-dense CO_2-dominant phase, like in R15 (a), only to a lesser extent in R19 (b).

The $[CO_2]/[HCO_3^-]$ ratios were monitored using the *in situ* ^{13}C NMR for both high and low water content reactions (Figure 3.10). The ratios were measured taking the ratio of the integrals

of $CO_{2(aq)}$ and HCO_3^- peaks in each spectrum. The low water content reaction was only run for four days, whereas the high water content reaction was run for 31 days. The low water content reaction was meant to explore the early-time $[CO_2]/[HCO_3^-]$ ratios of the $Mg(OH)_2$ reaction (that is, before and during carbonate precipitation) with CO_2 in the limit, where CO_2 dissolution is as fast or faster than the mineral dissolution. The high water content reaction was meant to probe the long-term portion of the reaction, where the $[CO_2]/[HCO_3^-]$ ratio was observed after carbonate precipitation, that is, after most of (or even the entire) sample had reacted.

b. In situ $[CO_2]/[HCO_3^-]$ ratios

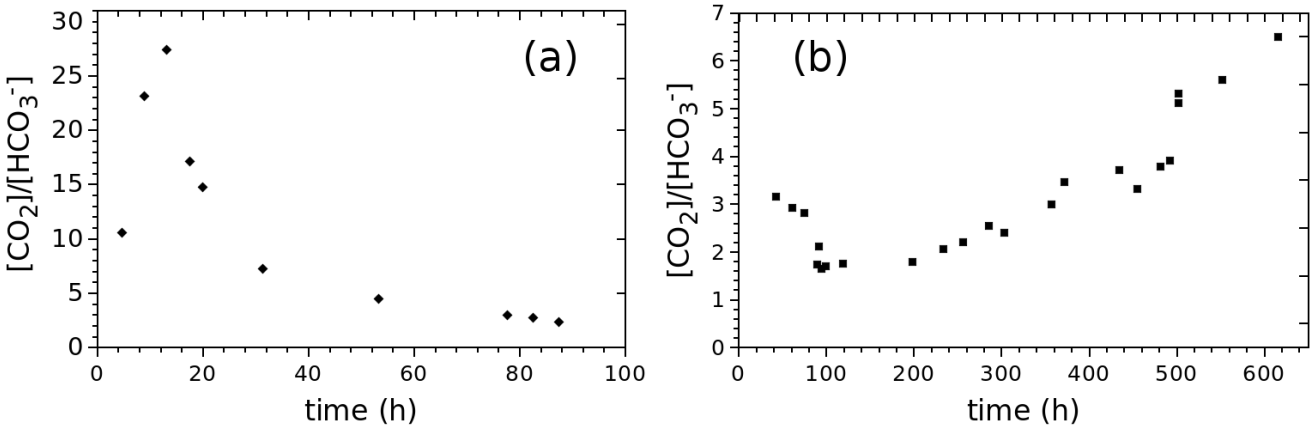

Figure 3.10: $[CO_2]/[HCO_3^-]$ ratio vs. time determined by ^{13}C NMR peak integration in low water content R15 (a) and high water content R19 (b) reactions of CO_2 with $Mg(OH)_2$. (Data: R15, R19).

In Figure 3.10(a), the $[CO_2]/[HCO_3^-]$ ratio increases in the first 15 h as the CO_2 is dissolving into the solution. At about 18 h, the ratio starts to decrease rapidly. This is due to the mineral dissolution raising the pH of the solution. After 25 h, the rate of decrease of the $[CO_2]/[HCO_3^-]$ ratio began to slow considerably. The decrase in the rate of change implies approaching equilibrium of the dissolution of CO_2, dissolution of the mineral, and carbonate precipitation. Presumably for long reaction times the ratio would begin to increase again as mineral dissolution

would be stopping and carbonate precipitation would be acting to remove the alkalinity from the solution, decreasing the pH and increasing the $[CO_2]/[HCO_3^-]$ ratio.

Figure 3.10(b) shows what happens with the mineral reaction over a long period of time. As (b) is the high water content reaction, $[CO_2]/[HCO_3^-]$ ratios could not be measured early in the experiment because the CO_2 and HCO_3^- signals were not strong enough to be integrable. From 20 h to 95 h the $[CO_2]/[HCO_3^-]$ ratio is decreasing similarly to (a). At 95 h, the ratio bottoms out and then the ratio stays relatively constant for the next 100 h. At 200 h, it slowly starts to increase, with some up and down fluctuations, for the next 400 h. The reaction was quenched at 600 h, but eventually the ratio should have leveled out at whatever the equilibrium value is for the system based on the headspace pressure of CO_2. Eventually no more carbonate mineral would be able to precipitate and the solution would just come to equilibrium with the CO_2 headspace gas pressure. The resulting ratio would be expected to be high (the pH should be low).

The fluctuations between 300 and 500 h could be caused by one or both of two possible mechanisms: (1) mineral regions/pores getting blocked/unblocked from CO_2 by carbonate precipitation and/or (2) the conversion of the carbonate precipitate converting into another phase that has different alkalinity. (1) is probable as $Mg(OH)_2$ is reacting so fast,[93] and it has already been shown that the CO_2 reaction can cause the mineral powder to fuse together by the precipitates in the MgO example. Clogs, afterall, are not uncommon in these types of reactions.[99–101] But (2) is also likely, where the precipitated carbonate converts into another type of carbonate. Carbonate conversions into other carbonates have been observed *in situ* by Kwak et al.[24] (using MAS NMR) in the Mg_2SiO_4 reacting system and by many others using various techniques (mostly XRD and Raman) in the form of pure mineral carbonates converting into

other mineral carbonates.[30,102–105] The transformation can happen by a process called "shrinkage transformation," where OH^{-f} and H_2O's are ejected from the crystal solid and the crystal changes its structure, or by another mechanism called "dissolution-precipitation solvent mediated transformation," where the carbonate mineral dissolves and reprecipitates as something else.[30] Here, the most likely mechanism is dissolution-precipitation given the relevant pressures and temperatures, but that is not to say that shrinkage cannot or does not play a role.

Figure 3.11 shows *in situ* ^{13}C NMR evidence of these carbonate conversions. The ^{13}C NMR spectra are probably best understood after reading Chapter 6. Essentially, each unique carbonate mineral has its own unique ^{13}C powder pattern that is contributed to by one or more magnetically-inequivalent ^{13}C spins within its unit cell. Each spin has its own isotropic chemical shift, chemical shift anisotropy, and biaxiality, all of which contribute to the overall observed powder pattern. As long as the composition of the carbonate product remains the same, the powder pattern will stay the same. Yet, when the composition changes, the powder pattern changes. Figure 3.11 shows how the carbonate pattern changed in the high water content reaction between 200 h and 300 h. While the observed changes in the powder patterns do not rigorously correspond to the fluctuations of the $[CO_2]/[HCO_3^-]$ ratios in Figure 3.10(b), the ratios are not likely to immediately respond to crystalline changes. This is because the ratios are the measured average of the whole sample—and not one specific region or another. Also, the ratios are still being affected by other carbonate precipitation and mineral dissolution processes in the rest of the sample.

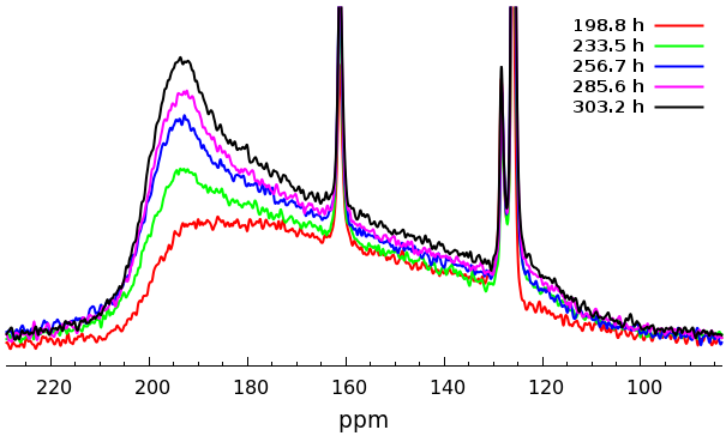

Figure 3.11: In situ ^{13}C NMR showing the powder pattern as it changes with time during the high water content mineral reaction. These spectra were taken between 198.9 and 303.2 h of the static reaction. (Data: 1036b, 1037b, 1038b, 1039b, 1040b).

Clearly carbonate mineral content (the peak area) is increasing with time in Figure 3.11, but the powder pattern shape is also changing with time. The change represents a conversion from one carbonate mineral to another {probably $4MgCO_3 \cdot Mg(OH)_2 \cdot (4,5,6,7,8)H_2O$, hydromagnesite/dypingite, to $MgCO_3$, magnesite} which occurs only after the $4MgCO_3 \cdot Mg(OH)_2 \cdot 4H_2O$ has first precipitated. The effect on the pH of the whole sample will not be realized until the majority of the carbonate has converted, affecting the entire mixture.

In conclusion, careful monitoring of peak linewidths, position (chemical shift), and relative and absolute integrals, gives the observer many details about the reacting system. Here, we have seen that the careful analysis yielded detailed results about the progress of the chemical reaction as well as dissolution of the $CO_{2(aq)}$ throughout the sample.

c. *Ex situ Raman spectroscopy*

The *ex situ* Raman experiments were meant to confirm the solid carbonate phases in the product. In these experiments I carefully removed the glass liner from the high pressure zirconia

vessel just after depressurizing it, and took it over to the Raman instrument in Earth and Planetary Sciences where Raman data were obtained on the product by focusing the laser through the glass liner. The advantage to obtaining the Raman spectrum through the glass liner is that the products are able to be analyzed without disturbing them, in their original location of precipitation, before being dried. A disadvantage, however, is that the tube and product/tube interface sometimes fluoresce. It is also difficult to get the same focus from location to location making it difficult to obtain quantitative spectra of the carbonate precipitation on the surface of the mineral from one superficial location to another in the tube. Therefore the spectra here are compared on the basis of whether a peak exists or not and on the relative areas of those peaks in each spectrum.

Figure 3.12 shows the Raman data from the high water content reaction of CO_2 with $Mg(OH)_2$. Each Raman spectrum was taken at a different location along the length of the tube, beginning with the top of the mineral. Only the C-O symmetric stretch region is shown in Figure 3.12 because the location of the symmetric stretch is indicative of the different type of carbonate mineral in the sample, and the position of the C-O symmetric stretch is independent of the ^{13}C isotope (these samples are 99% ^{13}C; the carbon atom remains at rest in the symmetric stretching mode, making the C-O stretch frequency isotope independent).[21,30,34]

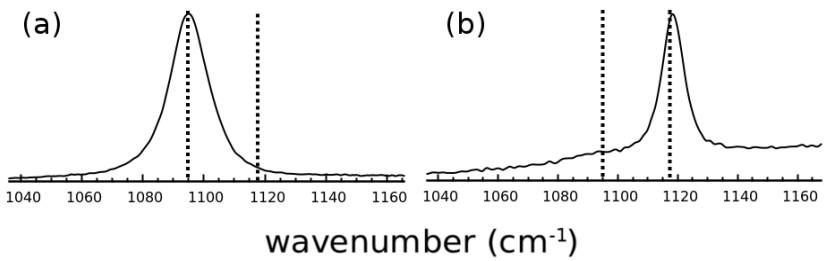

Figure 3.12: Raman spectra from (a) top of the sample (0.0 cm) and (b) deeper into the sample (-1.7 cm). Both y-axes have different scales so as to better compare the peaks. The dotted lines are indicative of the peak positions of the symmetric stretches of the minerals $MgCO_3$ (magnesite, 1094 cm^{-1}) and $4MgCO_3 \cdot Mg(OH)_2 \cdot 4H_2O$ (hydromagnesite, 1119 cm^{-1}), respectively.(Data: (a) 05223029 & (b) 05223032, R19).

Figure 3.12 demonstrates that there is spatial dependence of the carbonate precipitate in the sample. The peak at 1094 cm^{-1} is indicative of $MgCO_3$,[30,34] and the absence of other peaks in Figure 3.12(a) implies that the dominant mineral in the top of the sample is $MgCO_3$. Deeper into the sample, beginning around -1.6 cm into the sample, another peak at 1119 cm^{-1} (corresponding to the mineral hydromagnesite) appears concomitantly with the $MgCO_3$ peak, decreasing and then disappearing. At deeper locations (< -1.6 cm) within the sample the peak begins to shift to higher values, to 1120-1124 cm^{-1}. Figure 3.12(b) shows the Raman spectrum from -1.7 cm deep into the sample, and the $MgCO_3$ peak at 1094 cm^{-1} is completely gone. The new peak that was first seen at -1.6 cm deep into the sample has grown in and slightly shifted just above 1119 cm^{-1}. Literature indicates that 1119 cm^{-1} is indicative of the mineral $4MgCO_3 \cdot Mg(OH)_2 \cdot 4H_2O$, hydromagnesite,[30,31,34,102] and values just above that (1120-1124 cm^{-1}) for another mineral, $4MgCO_3 \cdot Mg(OH)_2 \cdot (5\text{-}8)H_2O$, dypingite.[36,95,106,107]

I first reported the spatial dependence of carbonate formation in the Journal of Environmental Sciences and Technology in the summer of 2012.[21] The article described an additional $Mg(OH)_2$ reaction (R9) that was also run with high water content (281.53 g $Mg(OH)_2$/L H_2O) but for only

2 days at 80 °C and 92-88 bar instead of the 31 days at 81 °C and 113-72 bar shown in Figure 3.12. The Raman data of this reaction, collected in a similar fashion as R19 in Figure 3.12, was the first to show this spatial dependence of carbonate precipitation. It is reproduced in Figure 3.13 and shows that the $MgCO_3$/$4MgCO_3{\cdot}Mg(OH)_2{\cdot}4H_2O$ conversion region occurs at considerably shorter distances into the sample (-0.25 cm) due to the much shorter reaction time. Figure 3.13 also shows the shifting of the $4MgCO_3{\cdot}Mg(OH)_2{\cdot}4H_2O$, hydromagnesite peak (1119 cm^{-1}) to higher values indicating the presence of $4MgCO_3{\cdot}Mg(OH)_2{\cdot}(5\text{-}8)H_2O$, dypingite.

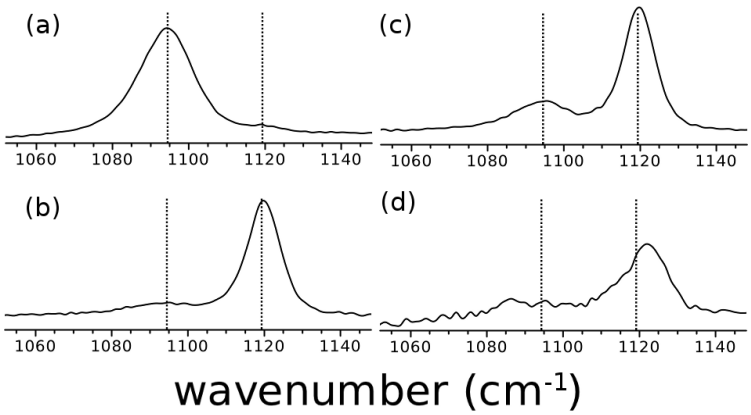

Figure 3.13: Raman spectra of the reaction products in the range of the characteristic CO_3^{2-} symmetric stretches, each taken at different points along the length of the sample tube: (a) at the solution/solid interface (0.0 cm), (b) -0.25 cm below the interface, (c) -0.5 cm, and (d) -0.6 cm. Spectra (b)−(d) were acquired using a 5× microscope objective, whereas spectrum (a) was acquired using a 20× objective. In addition, the y-axis in spectrum (d) has been expanded so as to better see the peaks. The lines at 1094 and 1119 cm^{-1} are guides to the eye for the locations of the magnesite and hydromagnesite/dypingite peaks, respectively.(Figure adapted with permission from Surface et. al. Copyright © 2013 American Chemical Society).

d. Ex situ pXRD

pXRD has been repeatedly used throughout this project to confirm Raman shift assignments and ^{13}C NMR chemical shift assignments. It is the one unambiguous method to confirm a crystal structure as no two crystal structures have the same pXRD patterns (likewise with Raman spectra). It is, however, only sensitive to moderately to well crystalline materials. Mesocrystalline and amorphous materials cannot be detected unambiguously by pXRD, unlike Raman and ^{13}C NMR. Raman spectra are sensitive to vibrations, that change to some degree based on the phase (for instance in CO_3^{2-}). ^{13}C NMR is sensitive to ^{13}C spins, which are there whether or not there is crystalline structure in the sample. pXRD, on the other hand, is only sensitive to *crystalline structures.* In the absence of crystal structure, there is no pXRD pattern.

Figure 3.14 shows a representative pXRD spectrum that confirms the existence of the different Mg-carbonate phases from the *in situ* reactions with $Mg(OH)_2$. This particular sample is the same material discussed in Figure 3.13, and is the product of the reaction of CO_2 with $Mg(OH)_2$ for 2 days at 80 °C and 92-88 bar.

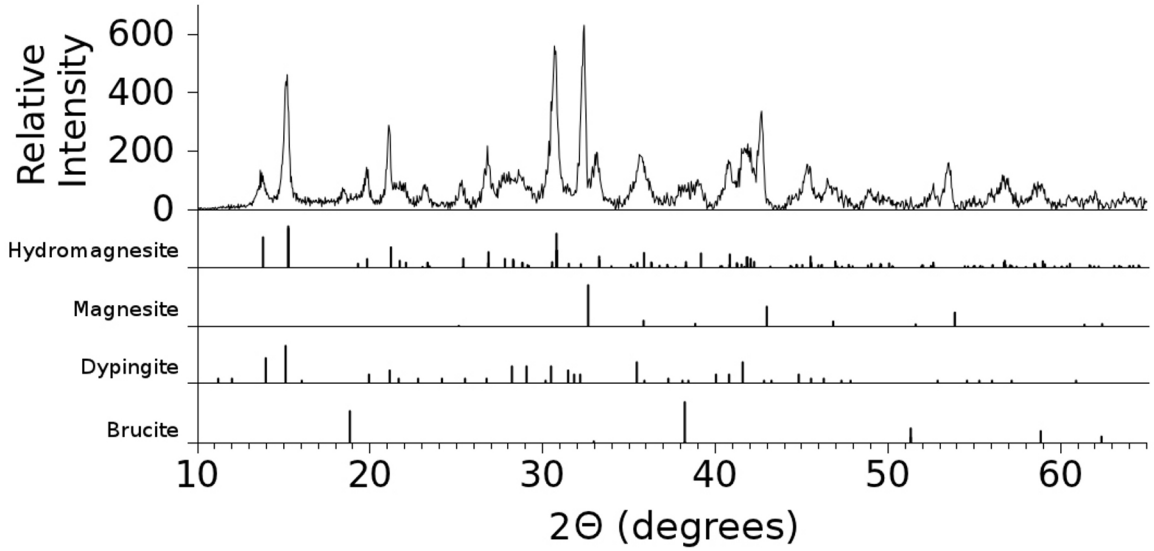

Figure 3.14: Powder X-ray diffraction pattern from the reaction product of CO_2 reacting with $Mg(OH)_2$, brucite. There are no detectable reflections remaining from the reactant $Mg(OH)_2$, indicating that it has all reacted. (Figure adapted with permission from Surface et. al. Copyright © 2013 American Chemical Society; Data: R9).

The pXRD results in Figure 3.14 indicate that within the limit of detection of pXRD, there is no reactant, $Mg(OH)_2$, remaining. Additionally, the reflections from $MgCO_3$ are slightly left-shifted (~1° 2θ) suggesting that some of the $MgCO_3$ unit cells have expanded. As pXRD is a time- and space-averaged measurement,[108] only some of the $MgCO_3$ crystals need be expanded to affect the pXRD pattern. The unit cell expansion in $MgCO_3$ is likely due to incomplete removal of water during the $4MgCO_3 \cdot Mg(OH)_2 \cdot 4H_2O$ to $MgCO_3$ transition[30] leading to partial hydration of some of the $MgCO_3$ unit cells. Lastly it is important to note that no $Mg(HCO_3)(OH) \cdot 2H_2O$,[31] nesquehonite, formed during the reaction, probably because the reaction temperature was too high.[102]

e. Ex situ ^{13}C MAS NMR

The products from the top of the mineral in the low and high water content reactions were

packed into rotors and spun at 5 kHz so that ^{1}H-decoupled ^{13}C MAS NMR spectra could be obtained. Both are shown in Figure 3.15.

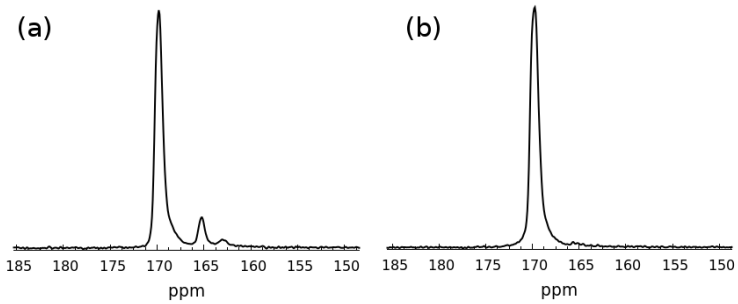

Figure 3.15: ^{1}H-decoupled ^{13}C MAS NMR of the top mineral layer of R15 (a) and R19 (b), low- and high-water content reactions respectively. The reaction is CO_2 with $Mg(OH)_2$ in an aqueous environment. (a) reacted for 4 days and (b) reacted for 31 days. (Data: 20130604-(a)R15,(b)R19)

The differences between Figure 3.15 (a) and (b) do not say much about the differences between the water content as the reaction times are so different. Nevertheless, both spectra suggest that the dominant product in the top layer of the product mineral is $MgCO_{3(s)}$ (169.74 ppm), in agreement with the Raman data. The two small peaks at 165.25 and 162.91 ppm [Figure 3.15(a)] are indicative of $4MgCO_3 \cdot Mg(OH)_2 \cdot 4H_2O$, hydromagnesite.

It can be very challenging to get high quality ^{13}C MAS NMR data from carbonate minerals. As the T_1's can be so long, I have found that single-shot experiments after long polarization times (> 30 m) for the 99% ^{13}C-labelled samples have been adequate to get quantitative spectra. I have also found that high precision shimming by adjusting the RT-shims while observing an aqueous solution of ethylene glycol using ^{13}C NMR allows high resolution spectra to be obtained with linewidths < 1 ppm. In most cases I was able to get the resolution of the MAS probe to be less than 50 Hz and on some days better than 20 Hz. When analyzing the ^{13}C MAS data, the lineshape of the adamantane line should always be taken into account. If it is very narrow and symmetric,

its linewidth can be considered as the field homogeneity of the magnet. As the sample is spinning at the magic angle, changes in susceptibility have no effect on the chemical shift. Therefore any line-broadening or line-splitting in the sample down to 20 Hz or so resolution must be a result of multiple chemical shifts or dynamics causing the line to broaden in the solid. In the following Figure 3.16, the ^{13}C linewidth measured from the ^{1}H-decoupled ^{13}C adamantane reference is 18 hz and is totally symmetric—so the lineshapes observed in Figure 3.15 are the result of actual chemical shift dispersion and not magnetic field inhomogeneities. A closer look at the magnesite peaks in Figure 3.15 reveals that the magnesite peak is composed of three unique lines as seen in Figure 3.16.

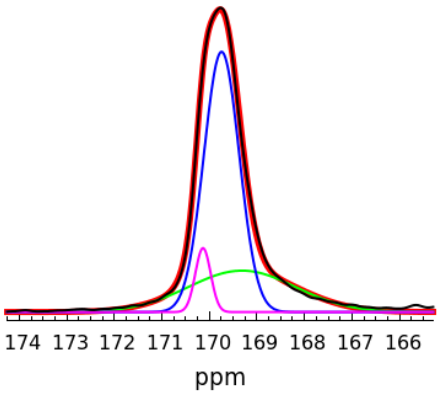

Figure 3.16: The $MgCO_{3(s)}$ line (black) and the sum of the three different lines composing it (red). The three comprising lines (blue, purple, and green) have chemical shifts of 169.3, 169.7, and 170.1 ppm, respectively. This particular data comes from Reaction (b), high water content.(Data: 20130603: R19)

Multiple lines for metal carbonate solids are not uncommon in ^{13}C MAS NMR as NMR is sensitive to both amorphous/mesocrystalline and crystalline compounds. As the pXRD suggested, various amounts of water can get caught in the crystal structure. The expanded crystal unit cell from partial removal of water probably causes a slightly higher chemical shift[21] and has

been observed in the singly-hydrated version of calcite, monohydrocalcite ($CaCO_3 \cdot H_2O$).[54] Additionally, mesocrystalline $MgCO_{3(s)}$ phases (partially crystalline) are also likely and would still be detected via ^{13}C NMR and would account for the small differences in chemical shift of the line. Analogous to amorphous versions of $CaCO_3$,[54] amorphous versions of $MgCO_3$ probably have a slightly lower chemical shift and a broader line. Thus, the narrow, smaller component of the $MgCO_{3(s)}$ line at 170.1 ppm in Figure 3.16 is probably from the partially-hydrated $MgCO_{3(s)}$ and the broader line at 169.3 ppm is probably from a mesocrystalline/amorphous phase of $MgCO_{3(s)}$. The peak at 169.7 ppm is the peak of crystalline $MgCO_{3(s)}$. Further analysis of the $MgCO_3$ MAS NMR will be discussed in Chapter 6.

The third reaction, reaction (c), that had similar *ex situ* ^{13}C MAS NMR results as reactions (a) and (b), just described. In the case of this reaction, I was able to obtain $^{13}C\{^1H\}$ MAS NMR data from two different vertical positions of the sample: the top layer of the reaction and the middle/bottom layer (from about 2 cm deep within sample). Figure 3.17 shows the results from the top and middle/bottom layer of the reaction.

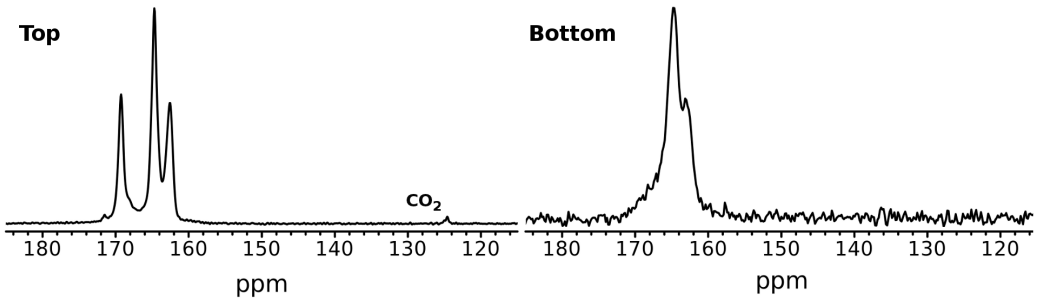

Figure 3.17: ^1H-decoupled ^{13}C MAS NMR that shows the differences between the top and bottom of the CO_2 reaction with $Mg(OH)_2$. There is a spatial dependence of the carbonates that are precipitated.(Figure adapted with permission from Surface et. al. Copyright © 2013 American Chemical Society; Data: R9).

In this case, the ^{13}C MAS NMR experiment was run soon enough after the sample was depressurized that some residual CO_2 could still be seen (Figure 3.17, "Top"). The top layer of this reaction showed similar results to the top layer of reaction (a), with the exception that the $4MgCO_3 \cdot Mg(OH)_2 \cdot (5\text{-}8)H_2O$ peaks (seen between 161 and 168 ppm in Figure 3.17) were stronger than the $MgCO_3$ peaks (~169.7 ppm). As this reaction, (c), was run for only 2 days, reaction (a) for 4 days, and reaction (b) for 31 days, it seems that the amount of $MgCO_{3(s)}$ product is dependent on length of reaction (i.e., more is made with more time). This is not surprising as $MgCO_{3(s)}$ here forms by first precipitating $4MgCO_3 \cdot Mg(OH)_2 \cdot (5\text{-}8)H_2O$ which then converts to $MgCO_{3(s)}$. One would also expect more $4MgCO_3 \cdot Mg(OH)_2 \cdot (5\text{-}8)H_2O$ at early times in the reaction and less at later times.

The "middle/bottom" spectrum in Figure 3.17 indicates that there is no detectable $MgCO_{3(s)}$ at layers deeper within the sample. The two peaks indicate that the $4MgCO_3 \cdot Mg(OH)_2 \cdot (5\text{-}8)H_2O$ crystals are both less crystalline (they are broader than in the "top" spectrum) as well as being the dominant phase deeper in the sample (there are no other peaks visible).

f. Conclusions about $Mg(OH)_2$ reactions with CO_2

The reaction of CO_2 with $Mg(OH)_2$ is both vigorous and rapid compared to literature-reported values of reactions of CO_2 with other minerals.[88,91,95] $Mg(OH)_2$ is a great system in which to study the carbonation reactions of CO_2 and has demonstrated several interesting facts about the system. First, free water content (the amount of water sitting on top of the mineral) affects the rate of mineralization and the magnitude and rate at which the $[CO_2]/[HCO_3^-]$ ratios change over time in the sample during the reaction. Second, the identity of the solid carbonate products of the reaction is spatially dependent on the depth relative to the mineral/solution interface. Third, the

longer the reaction is allowed to continue, the more $MgCO_{3(s)}$ is made and the greater the penetration depth of the carbonate precipitation within the mineral powder. Finally, three different analytical techniques (Raman, pXRD, and ^{13}C MAS NMR) are shown to be complementary as all agree on the identities of carbonate products as well as their relative ratios to each other, and to some extent, the depths these solid carbonates occur at in the sample.

The three complementary analytical techniques all have their strengths and weaknesses, however, which is why all three were applied instead of just one. Raman's small sampling size (a few grains of powder) allows high spatial resolution of the products within the sample using the symmetric carbonate stretch to identify different carbonate phases. pXRD's high sensitivity to crystal structure allows all of the pure mineral phases that are present in bulk to be detected unambiguously as each unique crystal makes a unique pXRD pattern. Finally, solid state ^{13}C MAS NMR is able to unambiguously detect the different carbonate minerals in all of their phases —amorphous as well as crystalline—in addition to quantitatively detecting the relative ratios of these carbonate solids in the sample.

D. Mg_2SiO_4, Forsterite

Here I will show some data from the reaction of CO_2 with synthetic Mg_2SiO_4, purchased from Alfa-Aesar. Like $Mg(OH)_2$, there is much previous work on the reaction of Mg_2SiO_4 with CO_2.[20,24–26,29,57–59,109] Here I will show the results of two different reactions, R20 and R14. The first reaction, R20, was meant to probe primarily *in situ* dynamics of the aqueous reaction of Mg_2SiO_4 with CO_2. $[CO_2]/[HCO_3^-]$ ratios were carefully probed during the reaction as was *in situ* formation of solid carbonates. This reaction had a mineral/H_2O ratio of 1338 g Mg_2SiO_4/L H_2O

and was allowed to react for 21 days from 120-105 bar at 80 °C (the pressure decreased with time due to consumption of CO_2). The second, R14, was meant to analyze the spatial dependence of the carbonate products, *ex situ, in* great detail. *Ex situ* data from R20 will be shown as well, but it was not taken with as detailed spatial resolution as R14. The *ex situ* analysis of R20 was merely meant to confirm that $MgCO_3$ was the only product. R14 was run for 10 days from 118-104 bar at 100 °C, thus 20 °C hotter than R20 and for only half the time.

a. In situ ^{13}C NMR

As in previous reactions, the $[CO_2]/[HCO_3^-]$ ratio was monitored for the entire length of the reaction to monitor the progress of the reaction. Figure 3.18 shows the $[CO_2]/[HCO_3^-]$ ratio determined by integrated the ^{13}C NMR peaks for the entire duration of R20, a reaction of Mg_2SiO_4 with CO_2.

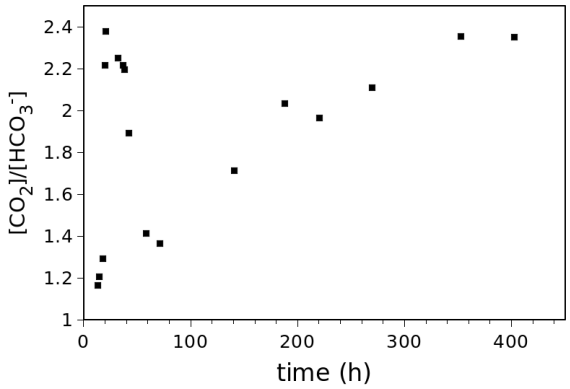

Figure 3.18: $[CO_2]/[HCO_3^-]$ ratios vs. time from static ^{13}C NMR in R20, a reaction of CO_2 with Mg_2SiO_4.(Data: R20).

Early in the reaction there is a marked increase of CO_2 indicating that CO_2 is dissolving into the solution containing the mineral. After 20 hours, the $[CO_2]/[HCO_3^-]$ ratio begins to decrease slowly, then rapidly. This indicates that the Mg_2SiO_4 dissolution rate overtook the CO_2 dissolution rate and the pH began to increase. The increased pH would also lead to solid

carbonate formation as it would increase the amount of $[CO_3^{2-}]$ in solution. Once the combined rate of CO_2 dissolution and carbonate mineral formation surpassed the rate of Mg_2SiO_4 mineral dissolution, the $[CO_2]/[HCO_3^-]$ ratio should begin to increase again, seen at about 100 h. From 100 h onwards, the rate of formation of solid carbonate appears to be relatively constant as the $[CO_2]/[HCO_3^-]$ ratio is steadily increasing and only appears to begin to level off at ~350 h.

The *in situ* ^{13}C NMR data of R20 at early times also indicates that there is a CO_2-rich aqueous phase (where H_2O is dissolved in CO_2 rather than CO_2 dissolved in H_2O) that forms in the sample as the initial plug of sc-CO_2 dissolves and reacts with the system. Figure 3.19 shows that the sc-CO_2 signal at ~128 ppm is very strong at 2.5 h and all but gone by 13 h. The remaining sc-CO_2 signal is from the sc-CO_2 that is stuck between the glass liner and high pressure vessel. The time lapse seen in Figure 3.19 also demonstrates that there is a concomitant increase of $CO_{2(aq)}$ and HCO_3^- as would be expected.

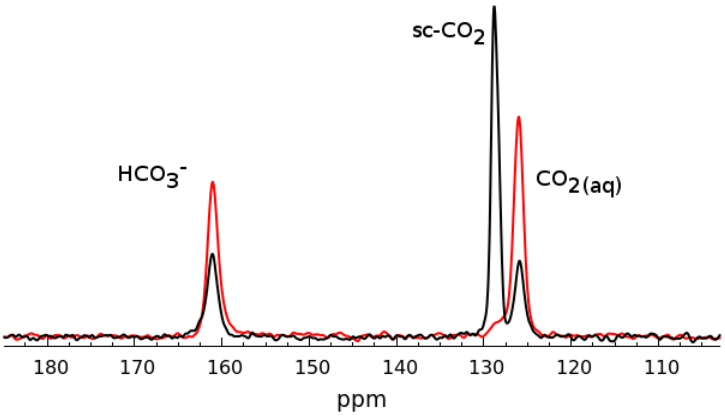

Figure 3.19: In situ ^{13}C NMR spectra acquired at 2.5 h (black) and 13 h (red) into reaction of CO_2 with Mg_2SiO_4 at 110 bar and 80 °C. (Data: R20- 1145,1150, 16-pc Hahn echo, 128 scans, 45s RD).

After a significant amount of time (403 h), the solid carbonate signal grows in similarly to

previous experiments with the exception that the lineshape of the solid carbonate did not change with time as it did in the $Mg(OH)_2$ reaction (see Figure 3.20). The lineshape grew in to the spectrum as a symmetric $MgCO_3$ powder pattern (see Chapter 6). This indicates that if the solid precipitate does form first as $4MgCO_3 \cdot Mg(OH)_2 \cdot (5\text{-}8)H_2O$, its subsequent conversion to $MgCO_3$ must be quick enough that its powder pattern is never able to be observed. This observation agrees with the lifetime of $4MgCO_3 \cdot Mg(OH)_2 \cdot (5\text{-}8)H_2O$ observed by Kwak et al. using ^{13}C HP-MAS NMR.[24] By the time the signal of the $4MgCO_3 \cdot Mg(OH)_2 \cdot (5\text{-}8)H_2O$ pattern could be observed, it already would have converted to $MgCO_{3(s)}$.

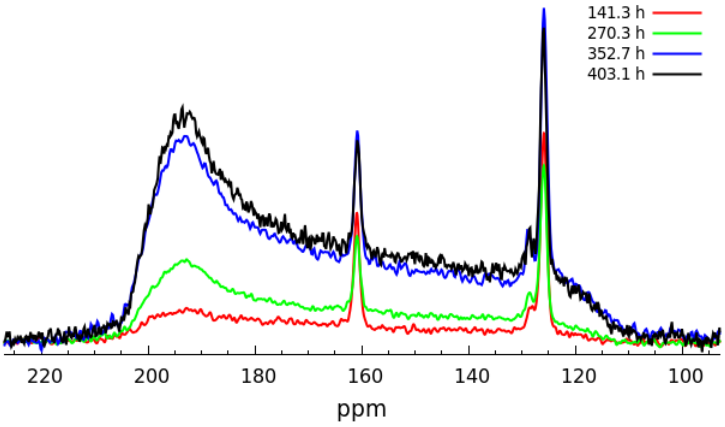

Figure 3.20: In situ ^{13}C NMR of R20, the reaction $Mg_2SiO_4 + CO_2$ at 141.3 h (red), 270.3 h (green), 352.7 h (blue), and 403.1 h (black). The solid carbonate powder pattern becomes the dominant signal in the sample, but does not change lineshape during the process, unlike the reaction of CO_2 with $Mg(OH)_2$. (Data: R20- 1194_c, 1215_c, 1228_c, 1236_c, 16-pc Hahn echo, 128 scans, 60 s RD).

b. *Ex situ Raman Spectroscopy*

Ex situ Raman spectroscopic data was acquired on the sample R20 and was found to be consistent with the more spatially-detailed analysis of another Mg_2SiO_4 reaction, R14, which will

be discussed here. The data from R14, the second reaction meant to probe the *ex situ* results of Mg_2SiO_4 reacting with CO_2, showed a dominant symmetric stretch for $MgCO_3$ at 1094 cm^{-1}. The point at which it was strongest was in the middle of the sample. And at no point was there a hydroxide peak in the ~3600 cm^{-1} region observed, indicating that no $4MgCO_3 \cdot Mg(OH)_2 \cdot (5\text{-}8)H_2O$ (hydromagnesite/dypingite mixtures) were formed. Figure 3.21 shows the region of 700-1150 cm^{-1}, where five Mg_2SiO_4 stretching and bending modes can be seen along with the single symmetric stretch of $MgCO_3$. The five Mg_2SiO_4 peaks are located at 825, 859, 883, 920, and 966 cm^{-1}, all of which are different Raman stretching and bending vibrations of the Si-O bonds where the three peaks at 825, 859, and 965 cm^{-1} correspond to the A_g stretches, 883 cm^{-1} to $B_{2g(xz)}$, and 920 cm^{-1} to $B_{3g(yz)}$.[110] The relative ratios are dependent on the average orientation of the Mg_2SiO_4 crystals in the laser beam of the Raman instrument. In some cases, considerable spectrum-to-spectrum differences in the Mg_2SiO_4 peaks can occur depending on where in the sample one is looking. Thus, the peaks cannot be usefully integrated unless the average orientation of the crystals are known.[110]

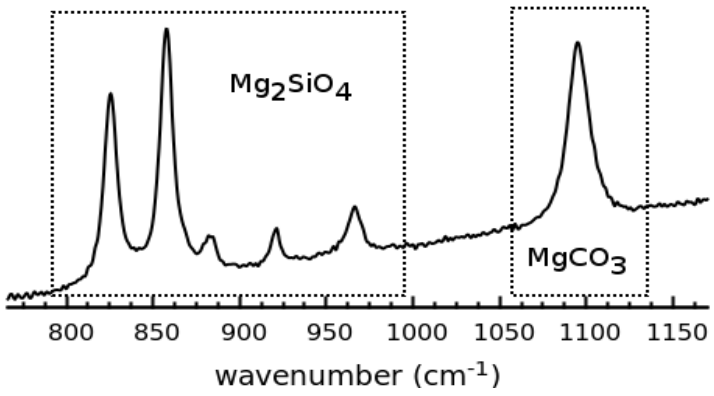

Figure 3.21: Raman spectrum showing the presence of both Mg_2SiO_4 and $MgCO_3$. (Data: 04122009, R14).

Many natural minerals are also known to fluoresce considerably, especially at the very high Raman wavenumber ranges (>3500 cm^{-1}). These broad peaks can sometimes be hundreds or thousands of times greater in amplitude than the sample peaks and can drown out all but the strongest Raman vibrations in the sample. Often samples containing Mg_2SiO_4 must be adjusted several times until the fluorescence has been minimized. Here, in Figure 3.21, the background fluorescence has been minimized but still can be seen in the strongly-sloping baseline which was deliberately not removed for the observation of this effect. The unseen portion of the spectrum, at values > 3000 cm^{-1}, contains discrete fluorescent peaks that are 50x stronger than the $MgCO_3$ symmetric carbonate stretch at 1094 cm^{-1} (data not shown).

c. Ex situ pXRD and ^{13}C MAS NMR

The purpose of the pXRD and ^{13}C MAS NMR experiments here are to confirm the spatial location of $MgCO_{3(s)}$ in the sample R14 as well as to confirm that $MgCO_3$ was the only carbonate phase formed in the entire sample. The sample R14 was divided into six portions, from top to bottom. Each of the six portions were loaded onto XRD slides for pXRD analysis and then MAS rotors for ^{13}C MAS NMR analysis. The sample-to-sample signal strength of the $MgCO_3$ phase in the sample was each scaled to the layer of sample with the most $MgCO_{3(s)}$ signal. The resultant relative signal magnitudes were charted vs. the respective sample depth in the reaction tube. The $MgCO_3$ signal strength from pXRD was calculated from the amplitudes obtained by a $MgCO_3$ pattern fit between 15 and 50° 2θ. The $MgCO_3$ signal strength from ^{13}C MAS NMR was obtained by numerical integration of the $MgCO_3$ line at 169.7 ppm.

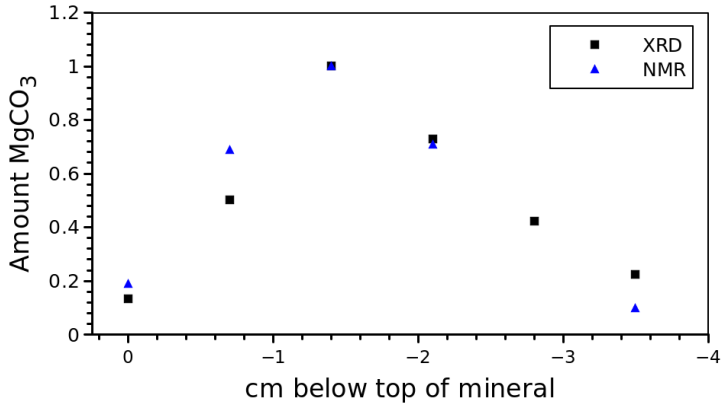

Figure 3.22: Spatial dependence of $MgCO_3$ precipitation in the reaction with Mg_2SiO_4. The y-axis has been scaled such that the maximum $MgCO_3$ reported is 1.0. The units are arbitrary as the MAS NMR measurements were made by integrating the narrow $MgCO_3$ peak and the XRD measurements by fitting the entire pXRD pattern. (Data: R14 XRD + NMR).

Figure 3.22 plots the relative quantities of $MgCO_3$ formation versus depth into the mineral sample, where 0 cm is the top of the mineral sample. Figure 3.22 also demonstrates that both analytical methods, NMR and pXRD, agree that the most $MgCO_3$ forms *below* the top surface of the mineral. In this case, the bulk of the $MgCO_3$ forms ~-1.4 cm below the surface of the mineral. In fact, the *least* amount of $MgCO_3$ forms at the surface of the mineral—and this was found to be the case for R20 also. The pXRD spectrum from -1.4 cm below the surface of the mineral, Figure 3.23, shows that there is still Mg_2SiO_4 present. It also shows that the $MgCO_3$ phase is very prominent and matches with the $MgCO_3$ crystalline standard, unlike in the previous $Mg(OH)_2$ experiment where crystal cell expansion had occurred leading to an imperfect fit.

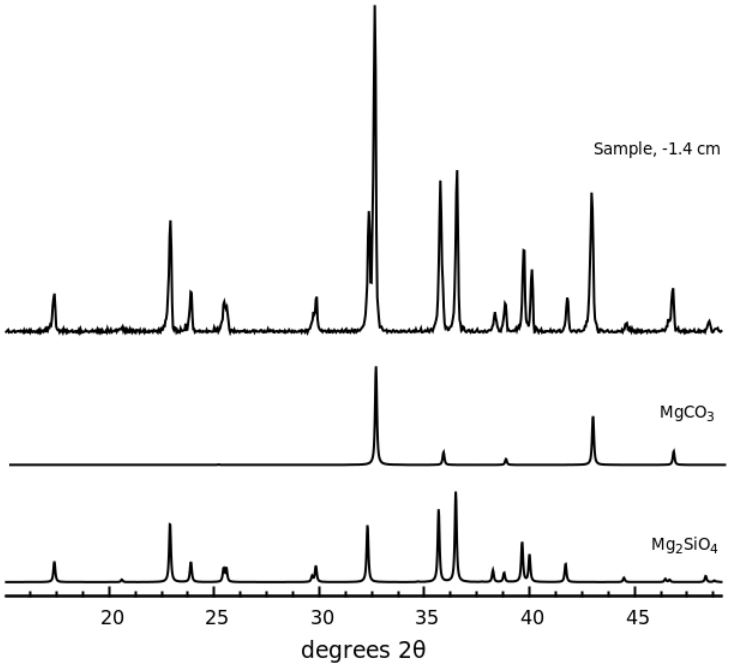

Figure 3.23: pXRD spectrum of the Mg_2SiO_4 sample from -1.4 cm deep into the sample. The dominant cyrstalline phase is $MgCO_3$, but there is still some Mg_2SiO_4 present. The $MgCO_3$ reflections are not shifted in this result. (Data: Surface041012a-R14middle(2); standards: AMCSD 0000389, 0009586).

The ^{13}C MAS NMR results shown in Figure 3.24 are similar to the previously-reported $MgCO_3$ peak, Figure 3.16, in that the "pure" $MgCO_3$-crystalline phase is probably a combination of three different $MgCO_3$ phases. The three different phases are most likely a pure $MgCO_3$ crystalline phase, a broad amorphous phase, and a H_2O- or OH-containing $MgCO_3$ phase. Unlike the $Mg(OH)_2$ reactions, however, Mg_2SiO_4 does not always yield a $MgCO_3$ line that has many phases. This feature will be discussed in greater detail in Chapter 6, where the formation of pure $MgCO_3$ (a single ^{13}C MAS NMR peak) was achieved by reacting the Mg_2SiO_4 sample for over 20 days.

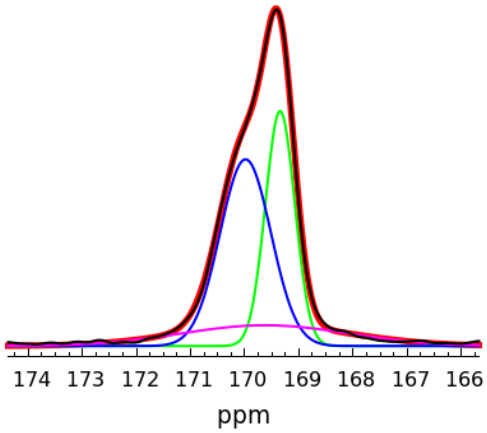

Figure 3.24: ^{13}C MAS NMR (v_r = 5kHz) of the sample from -1.4 cm deep into the sample. The only carbonate phase is $MgCO_{3(s)}$ (per pXRD), but there are three peaks in the ^{13}C NMR data that represent multiple $MgCO_3$-like carbonate phases at 169.35 ppm (green),169.62 ppm (purple), and 169.99 ppm (blue). (Data: r14middle2_040212).

Here in Figure 3.24, the same three peaks are observed in the $MgCO_3$ peak, indicating that multiple phases of $MgCO_3$ must form as the product, some with water/H's still trapped in the unit cell, and others that are amorphous or mesocrystalline.

d. Conclusions about Mg_2SiO_4 reactions with CO_2

Reactions with Mg_2SiO_4 are considerably slower than with $Mg(OH)_2$. They also yield, after similar reaction times and temperatures, pure $MgCO_3$ product, unlike the more basic mineral $Mg(OH)_2$, which yields a combination of $MgCO_3$ and $4MgCO_3 \cdot Mg(OH)_2 \cdot (5\text{-}8)H_2O$ (hydromagnesite and dypingite). The formation of the product $MgCO_3$ is also spatially dependent, precipitating at greater quantities deeper within the sample and the least at the top portion of the sample.

E. Conclusions

The carbonation reactions of CO_2 with MgO, $Mg(OH)_2$, and Mg_2SiO_4, have all been examined in great detail. All yielded some form of Mg-containing carbonate. All of the reactions exhibited spatial dependence in the formation of the carbonate products. The rates of the three reactions were all considerably different, and the use of *in situ*, high pressure and temperature ^{13}C NMR was successfully used to observe the progress of the reactions and the fate of CO_2 by examining the $[CO_2]/[HCO_3^-]$ ratios throughout the duration of the reactions. Finally, the use of three different *ex situ* spectroscopic techniques (Raman, pXRD, and ^{13}C MAS NMR), was demonstrated as an invaluable approach to identifying the products formed during the reaction.

An interesting comparison of the $Mg(OH)_2$ and Mg_2SiO_4 reactions can be found in their average $[CO_2]/[HCO_3^-]$ ratios. Surprisingly, the $Mg(OH)_2$ reactions exhibited an average $[CO_2]/[HCO_3^-]$ ratio (4 to 8) that was, in general, 3 to 4 times larger than the Mg_2SiO_4 reactions (2 to 4). This result is surprising because $Mg(OH)_2$ is the more basic and soluble of the two reactant minerals and would be expected to drive the pH of the reaction to higher values, thereby decreasing the average $[CO_2]/[HCO_3^-]$ ratio compared to the more acidic mineral, Mg_2SiO_4. However, the fact that the Mg_2SiO_4 reaction is more basic than the $Mg(OH)_2$ reaction shows how dependent the final reaction rate is on the *combination* of the rates of CO_2 dissolution, mineral dissolution, and carbonate precipitation. These three processes are what control the overall pH of the reaction. Where CO_2 dissolution is slowed, the net effect is for the pH to be higher. Where mineral dissolution is slowed, the net effect is for the pH to be lower. Where carbonate precipitation is slowed, the net effect is for the pH to be higher. Of course, it is probably impossible to attribute which process is primarily contributing to the change in a pH value as the

observed pH trend is a *combination of all three processes occurring simultaneously.* Nevertheless, if something is known about the progress of the reaction, one of the three processes will likely dominate: CO_2 dissolution should drive pH change early in a reaction while mineral dissolution and carbonate precipitation should drive the pH change later in a reaction.

Thus evaluating pH changes at different durations of the reaction can provide a method of understanding the progress of the reaction. Here, in the comparison of $Mg(OH)_2$ to Mg_2SiO_4, the pH is possibly lower in the Mg(OH)2 reaction because of fast CO_2 dissolution and carbonate precipitation. The stronger base increases the $[CO_3^{2-}]$ value in the solution increasing the rate of the carbonate precipitation, keeping the pH high. In the case of Mg_2SiO_4, the slower carbonate precipitation must increase the pH of the reaction system because the alkalinity (CO_3^{2-}) cannot leave the solution. That there is amorphous SiO_2 forming in the system is one of the likely culprits for slowing the carbonate precipitation; but the rate of the mineral dissolution may play some part in that as well. If the mineral dissolution is slow, it takes longer to get the concentration of Mg^{2+} high enough to cause precipitation of the carbonate phase which in turn increases the pH.

The spatial dependence of the products is also interesting and was not an entirely expected result. In any solid-state reaction, some spatial inhomogeneity is to be expected due to the restricted mobility of the solvent because of the solid phase, but here I have demonstrated a repeatable pattern in two different reaction systems. The spatial dependence of the products is likely due to a pH gradient being formed across the sample due to the mineral dissolution starting at the top of the mineral before the bottom because that is where the CO_2 arrives first. Particle size, porosity, and mineral permeability also likely play a role in this process and would be

interesting to explore in other additional reactions.

Altogether, the data presented here demonstrate the amount of insight *in situ* ^{13}C NMR can provide into CO_2 sequestration reactions with minerals. NMR provides a window into the reaction for rate analysis, product analysis, and the pH analysis (as I will demonstrate more fully in the next chapter). The fact that the reaction conditions are static (i.e. unmixed) is important because, as shown here, a non-mobile, unmixed system makes the products spatially dependent. I will explore the reasons for the spatial dependence in Chapter 5.

Chapter 4: In situ measurement of pH using ^{13}C NMR

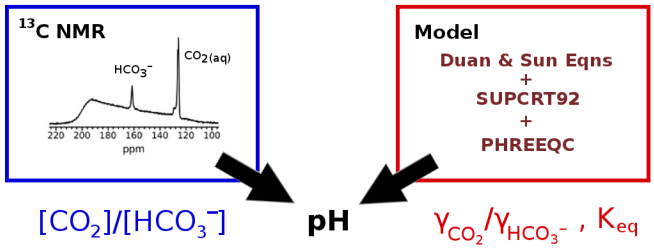

Figure 4.1: Measuring pH is possible by combining ^{13}C NMR data and output from a carefully constructed model.

A. Introduction to measuring pH using ^{13}C NMR

pH is probably the most important variable that can be measured in CO_2 sequestration reactions. This is because pH is a measurement of the activity of the hydrogen ion in solution (Equation 4.1). The activity of H^+ affects the solubility of CO_2 in water, CO_2's reactivity with water,[98,111–113] the solid carbonate phases that are thermodynamically accessible for precipitation,[21,114,115] and the rates of almost every chemical reaction that takes place during the mineral sequestration of CO_2 including mineral dissolution[96] and carbonate precipitation.[64] In short, pH is an excellent handle for interpreting the progress, reactivity, and fate of CO_2 in a high pressure reacting CO_2 sequestration system.[28,116]

$$\mathrm{pH} = -\log_{10}\{H^+\} \qquad (4.1)$$

where,

$$\{H^+\} = \gamma_H[H^+]$$

Traditional benchtop pH meters measure the activity, {}, of H^+ through direct potentiometry, where the activity of the H^+ ions change the electrical potential of a glass electrode. This highly accurate method works well only for specific conditions which are prescribed on the basis of the

type of glass cell and reference elements being used. Some common limitations of glass cells, however, include an inability to work at non-standard conditions (the glass electrodes are not able to withstand high pressures and provide erroneous readings at high and low temperatures) and the need to be standardized (tested on a solution of known pH) using several standard buffer solutions before making a reading. High pressure and temperature pH probes have been designed to circumvent some of the common issues with measuring pH at high pressures and temperatures, but use of these meter solutions remain tricky at best in day-to-day lab work and are so expensive as to discourage their use.[28,117,118] Rapid pressure changes can also break the high pressure pH probe element and instrument drift cannot be easily corrected with a standard buffer solution without depressurizing the sample (which changes the pH). Finally, there is also the issue that all pH measurement using an electrode requires physical contact with the system—which is a problem if one wants to measure the pH inside of a porous rock or a slurry without disturbing it.

Recently, Shao et al. described an approach to measure pH indirectly using pH sensitive chromophores that could be monitored using spectrophotometry.[28] This method is also very accurate but requires the presence of chromophores (in their case, bromophenol blue, or BPB) in the reaction solution to observe the changes in pH and is limited in its pH range. An additional difficulty with this method is that it requires optical access to the sample—so one is limited to measuring pH to portions of the sample that the instrument can "see". Using a so-called "simplified absorbance ratio method," they were able to generate $[H^+]$ values from their technique, from which they were able to calculate pH (or more exactly, pH_m, where "m" is molal, a way of calculating pH in terms of [H+] not {H+}...see Equation 4.5). While they did not

calculate $\{H^+\}$ values from their measurements, their paper is still very important because they introduce the concept of using an indirect method (measurement of a pH-sensitive chromophore) to calculate pH in high temperature and pressure sequestration reactions. Their paper also introduces the concept of combining multiple, already-existing geochemical calculation packages into one model to check experimental pH measurements and provide supporting calculations.

Another research paper that provided inspiration and a starting point for measuring pH from CO_2 dissolution into aqueous systems is a 1992 paper by Meyssami et al.[113] This paper played a crucial role in the development of the pH measurement method I describe here. In their paper, Meyssami et al. develop a simple model for calculating pH in terms of $\{H^+\}$ during CO_2 dissolution into aqueous solutions. This was the first paper I came across that presented a working pH model for CO_2 dissolution into aqueous solutions in as simple a way as it does. And this paper, coupled with Shao et. al.'s paper, are the single two most important papers that inspired the research I present in this chapter.

The approach I have taken to solve the pH-measurement problem at high CO_2 pressures and reaction temperatures is built upon the ideas that Shao et al. described in their paper. However, instead of using a chromophore with light as the indirect method of calculating $[H^+]$ like Shao et al., I use ^{13}C NMR to detect the $CO_{2(aq)}$ and bicarbonate that already exist in the reacting system from which $[H^+]$ can be calculated. This method works because the concentrations of CO_2 and HCO_3^- are pH dependent (Figure 4.2 and Equation 4.3). Using $[CO_2]/[HCO_3^-]$ ratios to calculate pH is an elegant solution to measuring pH because both CO_2 and HCO_3^- are already part of the reaction. No additional chemicals need be added to measure pH.

I have also used Shao et al.'s second major contribution, the concept of combining

pre-existing computational packages to create a model that provides supporting pH calculations. I constructed a model that combines several freely available computational packages to calculate activity coefficients and solve the equilibrium equations associated with the sequestration reaction(s). I also took this idea one step further. Rather than just comparing the calculations to experiment, i.e. using the calculations to "support" experimental results, I combined the calculations with the experiment in such a way that real pH (that is pH calculated using $\{H^+\}$ and not $[H^+]$) could be calculated from the experimental data.

To best understand how this works, it is good to have a picture of the reactions that are going on in a CO_2 sequestration reaction. Equations 4.2-4.4 describe the three major reaction steps in a typical sequestration reaction. The Mg^{2+} metal ions are representative of metal ions that would come from the dissolution of some mineral reactant, such as brucite or forsterite (see Chapter 3). Reactions (4.2)–(4.4) have been studied in high temperature and pressure vessels using various minerals as the magnesium source extensively by others.[58,65,88,93,95,119]

$$CO_{2(g)} \rightleftharpoons CO_{2(aq)} \qquad (4.2)$$

$$CO_{2(aq)} + H_2O \rightleftharpoons HCO_3^- + H^+ \rightleftharpoons CO_3^{2-} + 2H^+ \qquad (4.3)$$

$$Mg^{2+} + CO_3^{2-} \rightarrow MgCO_3 \qquad (4.4)$$

As described in Reaction 4.3, there are three aqueous carbon species that form in solution after $CO_{2(g)}$ dissolves in water: $CO_{2(aq)}$, HCO_3^-, and CO_3^{2-}. These three species have distinct ^{13}C NMR chemical shifts and spin relaxation properties.[23,45,46,74,120,121] Using the first equilibrium step ($CO_2 \rightleftharpoons HCO_3^-$) in Reaction 4.3, the pH_m under standard and ideal conditions can be calculated using the $[CO_2]/[HCO_3^-]$ ratio (obtained from the quantitative ^{13}C NMR intensities) and the standard pK_{a1} of 6.35[57] using Equation 4.5 (the subscript "1" in pK_{a1} refers to the first equilibrium

step, $CO_{2(aq)} + H_2O \rightleftharpoons HCO_3^- + H^+$). If the solution is dilute such that the ideal approximation can be made (where activity coefficients, γ, are equal to 1), $[CO_2]=[HCO_3^-]$ at pH of 6.35. (Note: here I have simplified this first equilibrium step and pK_{a1} as the combination of two reactions $CO_2 + H_2O \rightleftharpoons H_2CO_3$ and $H_2CO_3 \rightleftharpoons HCO_3^- + H^+$. The concentration of H_2CO_3 is negligible, allowing the two reactions to be combined[70,71]). At pH values decreasing from 6.35, CO_2 increasingly becomes the dominant species. Likewise, at increasing pH values above 6.35 (pK_{a1}), HCO_3^- increasingly dominates. As the pH further increases, CO_3^{2-} grows in relative concentration; at pH = 10.33 (pK_{a2}), $[HCO_3^-]=[CO_3^{2-}]$.

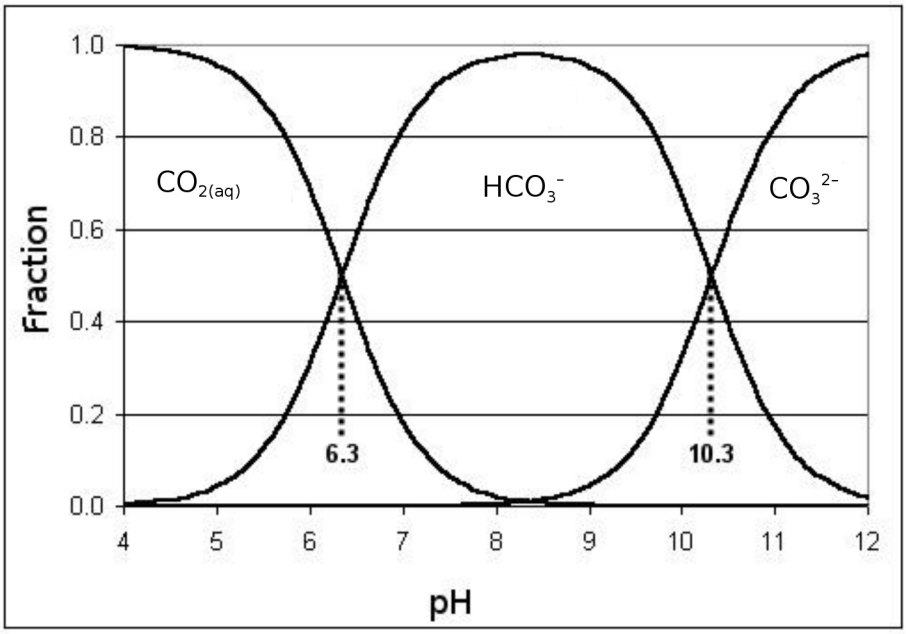

Figure 4.2: pH controls the ratios of CO_2/HCO_3^- and HCO_3^-/CO_3^{2-}. The points 6.3 and 10.3 are pK_{a1} and pK_{a2}, respectively.

The first of the two equilibrium steps in Equation 4.3 ($CO_{2(aq)} + H_2O \rightleftharpoons HCO_3^- + H^+$) is the most relevant equilibrium step to use for calculating pH as sequestration reactions almost always have a pH less than 8 (making $[CO_3^{2-}]$ vanishingly small). Under ideal conditions, one would calculate pH using Equation 4.5, where $pH_m \approx$ pH. As high pressure, sequestration reactions

deviate considerably from ideal conditions (concentrations of ions can exceed 1 M, and much greater than that in high salinity sequestration environments), another equation (Equation 4.6) needs to be used to account for the CO_2 and HCO_3^- activity coefficients not being equal to 1. Equation 4.6 differs from 4.5 in that it includes the activity coefficients. These activity coefficients are obtained from the calculation packages, which will be discussed in greater detail later in this chapter.

$$\mathrm{pH_m} = -\log_{10}\left(\mathrm{K_{a1}} \cdot \frac{[\mathrm{CO_2}]}{[\mathrm{HCO_3^-}]}\right) \quad (4.5)$$

$$\mathrm{pH} = -\log_{10}\left(\mathrm{K_{a1}} \cdot \frac{\gamma_{\mathrm{CO_2}}}{\gamma_{\mathrm{HCO_3^-}}} \cdot \frac{[\mathrm{CO_2}]}{[\mathrm{HCO_3^-}]}\right) \quad (4.6)$$

The high pressure NMR probe (described in Chapter 2), used to obtain the experimental $[CO_2]/[HCO_3^-]$ ratios, has been specifically designed to measure the ratios with great precision. It can detect any ^{13}C-containing gaseous, aqueous, or solid phases in its reaction chamber. The chamber is large enough to incorporate several grams of solid mineral reactant and can operate at temperatures up to 250 °C and pressures up to 400 bar. When properly shimmed, the probe has a spectral resolution on the order of 1 ppm or better, even with solid phases present, and can easily distinguish ^{13}C NMR signals of sc-CO_2 (~128 ppm), $CO_{2(aq)}$ (126 ppm), and HCO_3^- (161.5 ppm). If the T_1 relaxation times of the different ^{13}C-containing chemical species are known, the experiment can be set up to ensure the ^{13}C NMR spectra are quantitative. If one is very careful and uses a spin-counting technique, $[CO_2]$ and $[HCO_3^-]$ values can be calculated directly from the integrated ^{13}C NMR peaks. However, I have found it easier in practice to rely on calculations to provide $[CO_2]$ and use the quantitative ^{13}C NMR data to calculate $[CO_2]/[HCO_3^-]$ from which $[HCO_3^-]$ can be derived using the calculated value of $[CO_2]$.

The work discussed here is not the first to utilize ^{13}C NMR to measure $[CO_2]/[HCO_3^-]$ and $[HCO_3^-]/[CO_3^{2-}]$ ratios. Nor is it the first to extract pH values from the ^{13}C NMR data. Many other researchers have used ^{13}C NMR to monitor CO_2 dissolution and chemical equilibration with water,[23,45] CO_2 interaction with alkanolamine CO_2-sorbent solutions,[46] CO_2 production and consumption during formic acid dehydrogenation reactions for H_2 storage,[121] imaging of *in vivo* pH,[48] and exchange between CO_2 and HCO_3^- catalyzed by carbonic anhydrase *in vivo*.[122,123] ^{13}C NMR has proven very useful in a number of different research problems involving CO_2. And this research continues that tradition.

The work I describe here contributes to the CO_2 reaction and NMR communities by establishing a method to extract pH values from ^{13}C NMR experiments based on $\{H^+\}$, not $[H^+]$ like previous work. This is accomplished by combining ^{13}C NMR experimental data with a specially-constructed model (made of a combination of various freely-available, robust calculation packages). The calculated activity coefficients and solutions to the equilibrium equations based on the experimental conditions, make the calculation of $\{H^+\}$, and thus pH, possible from ^{13}C NMR data.

B. Development of a pH model

Equation 4.6 describes how the model and experimental data work together to derive the final pH of the solution. The model calculates K_{a1} and γ_{CO2}/ γ_{HCO3-} and the ^{13}C NMR measures $[CO_2]/[HCO_3^-]$. These values combined enable the measurement of pH. The model is made of a combination of freely-available computational packages namely, Duan and Sun's solubility equations (D&S equations),[112,124–127] SUPCRT92,[128] and PHREEQC.[129] The D&S equations are

used to calculate [CO_2] in reaction solution, given a certain amount of [Na^+] and [Mg^{2+}] in the solution. SUPCRT92 calculates equilibrium constant (K) values for all equilibrium reactions in a sequestration reaction based on temperature and pressure of the system. The calculated [CO_2] and K values are then passed to PHREEQC which simultaneously and recursively solve the equilibrium equations based on the constraining experimental [CO_2]/[HCO_3^-] ratios obtained from the ^{13}C NMR data. The model is pictorially presented in Figure 4.3.

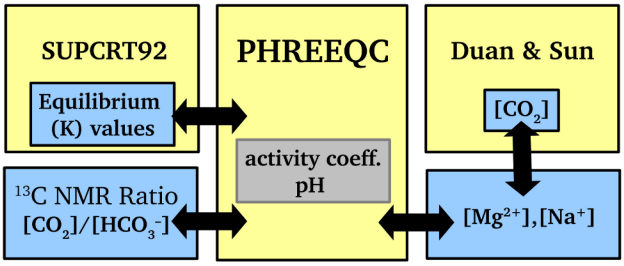

Figure 4.3: The model is comprised of several freely-available, robust calculation packages that recursively work together to solve the equilibrium equations, [CO_2], [Mg^{2+}], and [Na^+]. Yellow boxes represent the calculation packages and blue boxes represent values that are produced/used by the model. The gray box is what the combination of programs ultimately produce.

The D&S equations solve for [CO_2] in a way unlike most other programs, including default settings of PHREEQC. In the D&S equations, [CO_2] is determined by first solving for the chemical potential of CO_2 in the vapor phase (μ^v_{CO2}) above the solution by solving its equation of state (EOS).[130,131] The μ^v_{CO2} from the CO_2 EOS is set as the solution to the chemical potential of CO_2 in the aqueous phase ($\mu^v_{CO2} = \mu^l_{CO2}$), from which [$CO_2$] is calculated using the specific interaction model of Pitzer.[132] D&S have written their equations into a Windows executable program (co2-solubility.exe) which can be downloaded from their research group's website.[133] The executable is based directly on the equations they describe in their 2003 and 2006 papers.[112,127] Yanzhe Zhu, an undergraduate researcher in the Hayes group, and I checked the

output of the executable to make sure they were consistent with their papers by building the equations from their papers in MATLAB. The D&S CO_2 solubility equations are accurate within experimental limitations, which they describe in their 2003 paper as 7% for CO_2 solubility values.

SUPCRT92 solves for equilibrium constant (K) values at different temperatures and pressures for the the equilibrium equations in the reaction system (see Equations 4.2 and 4.3). SUPCRT92 also solves for the K values of the reactant mineral, such as $Mg(OH)_2$. SUPCRT92 is a software package written in 1992 and is only as good as the database (.dat file) of mineral data that is loaded in it. The program was written for geochemical modelers who needed quick access to thermodynamic data on different minerals and other geochemical reaction data on different systems. SUPCRT92 is designed "to calculate standard molal Gibbs free energies, enthalpies, entropies, volumes, and heat capacities of minerals, gases, aqueous species, and reactions as a function of temperature and pressure."[128] In our specific case, we chose the database dslop98.dat which was built in 1998 by the GEOPIG project (led by Dr. Everett Schock) while it was still at Washington University in St. Louis (GEOPIG is now at ASU). The database is assembled from data from ~30 different thermodynamic data publications on various minerals and chemicals related to geochemical reactions. The database is formulated by mineral name, chemical formula, reference, and a series of thermodynamic data including but not limited to $\Delta G°_f$, $\Delta H°_f$, $S°_{P,T}$, $V°_{P,T}$, and a series of P/T-independent coefficients for various analytical expressions describing how these values change as a function of temperature and pressure. The equations used within the program are described in great detail in the original SUPCRT92 paper.[128] And even though the dslop98.dat database was never published in a paper, it is an updated version of the

SPRONS92.dat database described in the paper and contains much of the same data but with additional minerals.

In the model presented here, I use PHREEQC (version 2.18.3) as the core calculation base for the model, taking inputs from D&S equations and SUPCRT92. PHREEQC is a geochemical modeling package capable of many functions including calculation of chemical speciation, saturation indices, kinetic modeling, and transport modeling. It has been designed for geochemical applications where gases/liquids are mixed together at high pressures and temperatures and react with solid minerals precipitating new minerals. Here I utilize its ability to solve multiple equilibrium problems simultaneously. I also use it for its ability to calculate activity coefficients using Pitzer's equations.[132] Here we use PHREEQC for a very specific set of functions (equilibrium calculation and activity coefficient calculation) leaving unused much of its capabilities. For instance, PHREEQC is capable of calculating [CO_2] and K values at different temperatures and pressures. I have not utilized these aspects of PHREEQC, however, because D&S equations are more accurate than PHREEQC for calculating [CO_2] and SUPCRT92 provides a more extensive database that works over a larger P/T range than PHREEQC. As described earlier, Shao et al. did an excellent job describing the advantages to combining different calculation packages to get better calculation results.[28] The idea is each calculation package has a strength and if you combine the strengths of different packages you get better calculation results.

Nevertheless, I think it is appropriate to provide more detailed justifications for using D&S and SUPCRT92 with PHREEQC here. The D&S equations use chemical potential matching ($\mu^{v}_{CO2} = \mu^{l}_{CO2}$), Pitzer's equations,[132] and an EOS[127,130,131] that incorporates non-ideal interactions of

gases at high pressures and temperatures (D&S uses fugacity of CO_2 when calculating chemical potential). PHREEQC uses the ideal gas equation (in version 2.18.3, the version I use here) and partial pressures instead of fugacities. It also does not use activity matching to determine $[CO_2]$. However, PHREEQC 3, the newest version as of this writing, uses the Peng-Robinson EOS[134] to calculate fugacity coefficients of CO_2 from the critical pressure and temperature of the gas. And even though I do not evaluate PHREEQC 3 here, D&S have already shown that their solubility model works better than the Peng-Robinson equations for calculating $[CO_2]$ across a large range of temperatures, pressures, and ion concentrations.[112] So D&S equations would still be needed with use of PHREEQC 3.

In addition to using D&S equations and SUPCRT92 with PHREEQC, I used the pitzer.dat thermodynamic database file for PHREEQC calculations instead of the default phreeqc.dat. This database file uses thermodynamic data derived from the Pitzer equations, which are more accurate at determining the energy of interaction between ions in a solution of elevated ion concentrations (> 0.5 M).

The model I develop here, comprised of these three different software packages, only works because the different software packages are allowed to communicate with each other recursively. For example, imagine trying to calculate how much CO_2 will dissolve in a solution of water with an unknown value of $[Na^+]$. NMR data can give you $[CO_2]/[HCO_3^-]$ and D&S can give you $[CO_2]$ (but only if you know $[Na^+]$, which you don't know). So the model solves the system by starting the D&S equations with the assumption that there is no Na^+ in the solution at all. The $[CO_2]$ value that D&S calculates is input into a spreadsheet which includes the charge balance equation, Equation 4.7, solving for a $[Na^+]$ value. This $[Na^+]$ value is then sent back to the D&S equations

to recalculate [CO_2]. After a new value of [CO_2] is found, the new value is sent back to the spreadsheet and Equation 4.7 to calculate a new [Na^+] value. This back-and-forth, recursive communication continues between D&S and the charge balance equation until convergence (the same value of [CO_2] is calculated two times in a row). The spreadsheet can be replaced with PHREEQC calculations, but it was found in practice that doing the charge balance step in a spreadsheet and then using PHREEQC to solve for pH after [Na^+] had been calculated was quicker and produced the same results. As the two software packages (D&S and PHREEQC) do not talk to each other by default, keeping track of their exchanged values in a spreadsheet is helpful. The spreadsheet and calculation steps will be described in greater detail later in this chapter and in Appendix A.

$$[Na^+] + 2[Mg^{2+}] + [H^+] = [HCO_3^-] + 2[CO_3^{2-}] + [OH^-] \quad (4.7)$$

PHREEQC has some unique calculation caveats which are described in detail in Appendix A. The most important two to mention here are that PHREEQC requires its input values for CO_2 to be presented in terms of activity, which is not known initially, and the activity values it calculates are MacInnes activities. The initial input in activities can be overcome by running calculations as [CO_2] initially then substituting with {CO_2} once γ_{CO2} is known. PHREEQC's use of MacInnes activity coefficients is important because MacInnes activities are scaled values based on the assumption that $\gamma_{KCl} = \gamma_{K+} = \gamma_{Cl-}$. The representation of these activities values only really matters in terms of comparing one calculation to another. If an activity coefficient value calculated in this document were compared to another literature value, one would want to make sure the same scaling conventions were used. Plummer et al. have a very helpful and detailed discussion on pg. 11 of a USGS report about justification for using MacInnes scaling factors in activity coefficient

calculations.[135]

The model I have described here will be used in a number of different ways in this chapter, depending on what calculations it is needed to do. Not every package contained within the model is used within every calculation.

C. Experimental validation of the pH model

Three sets of validation experiments will be described here. The first set of experiments called "pH meter experiments," makes solutions with high ionic strength (between 0.8-2.4) and tests the model's ability to predict pH values measured by a traditional benchtop pH meter. This test is crucially important because it tests the model's ability to calculate accurate activity coefficients at high ionic strengths.

The second set of experiments called "Liquids ^{13}C NMR of $NaHCO_3/Na_2CO_3$ solutions" was meant to repeat work done previously by Jakobsen et al.[46] and Morrow et al.[136] More of the $NaHCO_3/Na_2CO_3$ aqueous solution mixtures, like those used in the "pH meter experiments," were analyzed using high resolution liquids ^{13}C NMR. These experiments were designed to acquire a curve of $[HCO_3^-]/([HCO_3^-]+[CO_3^{2-}])$ vs. ^{13}C NMR chemical shift of the bicarbonate/carbonate peak in ^{13}C NMR (there is only one peak due to fast exchange, but its chemical shift is dependent on the ratio of $[HCO_3^-]/[CO_3^{2-}]$).[45,46,136] As per the previous research, a plot of the ratio vs. the chemical shift should be a straight line. This second set of experiments was important to complete because it calibrated the measurement of pH at high pH values using ^{13}C NMR as well as tested the model against systems that are well studied in literature.

The third and final set of validation experiments called "High pressure ^{13}C NMR experiments

of CO_2 in NaOH solutions," validate the model's CO_2 pressure and solubility calculations. In these experiments $CO_{2(g)}$ is pressurized over an NaOH-containing aqueous system. As pH could not be directly measured under these conditions, the model predicts $[CO_2]/[HCO_3^-]$ ratios for comparison to experimental $[CO_2]/[HCO_3^-]$ ratios obtained by ^{13}C NMR. The solutions being pressurized also have known amounts of $[Na^+]$ to which the model's $[Na^+]$ predictions can be compared. Accurate $[CO_2]/[HCO_3^-]$ ratios and $[Na^+]$ values indicate that the model can predict $[Na^+]$ and $[CO_2]$ values accurately at ionic strengths up to 1.04 (although the model is probably able to work at ionic strengths much higher than this, ionic strengths much higher than this start to become a problem for the NMR circuitry. See Chapters 2 & 3 for greater detail on this effect).

a. pH meter experiments

Eleven different solutions with different pH values were prepared by mixing different ratios of $NaHCO_3$ (Sigma-Aldrich) and Na_2CO_3 (Sigma-Aldrich) with a carbon molality of 0.80 in each solution at STP. The solutions varied in $NaHCO_3$ concentration from 0 to 0.8 molal in steps of 0.08 molal while the concentrations of Na_2CO_3 varied from 0.8 to 0 molal, thus making solutions with $[NaHCO_3]/[Na_2CO_3]$ ratios of 10/0, 9/1, 8/2, etc., to 0/10 and the ionic strengths vary from 0.8 to 2.4. The pH values of these solutions were immediately measured with a Fisher Scientific Accumet Electrode XL15 pH probe calibrated with standard solutions of 2.0, 4.0, 7.0, and 10.0 pH. Measurements were sufficiently fast that any exchange of CO_2 with the atmosphere would have a negligible effect on the measured pH.

The SUPCRT92 and PHREEQC packages were used in these validation calculations as CO_2 solubility was not considered here because of the "closed-system" assumption—that the partial pressure of CO_2 in the atmosphere is not in equilibrium with the $CO_{2(aq)}$ in the solution. Figure

4.4 shows the results of the model predictions based on initial [$NaHCO_3$] and [Na_2CO_3] concentrations with the experimental results.

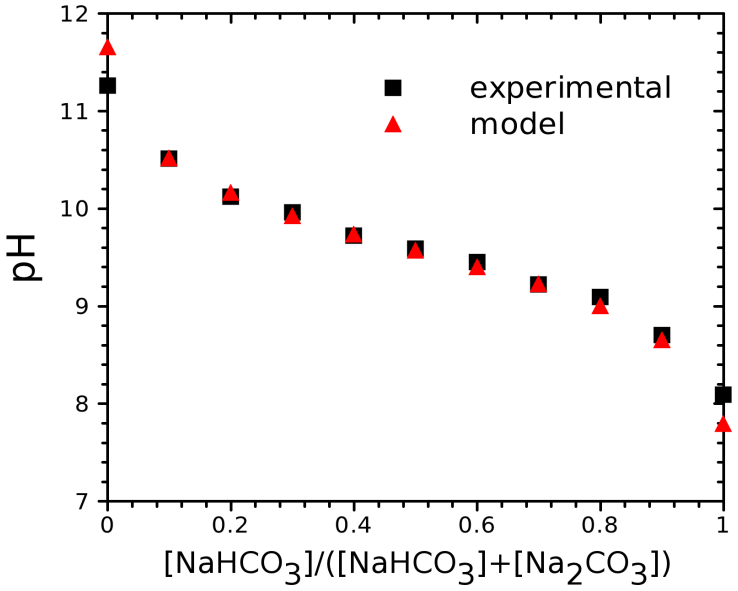

Figure 4.4: Comparison of calculated and measured pH vs. the molar fraction of bicarbonate/carbonate in solution.

The "titration curve" shown in Figure 4.4 is similar to previous experiments on bicarbonate/carbonate equilibrium[45,46,120,121,137] and Figure 4.1. Solutions with highest [CO_3^{2-}] concentration have highest pH values and solutions with highest [HCO_3^-] concentration have lowest pH values, all as expected. The differences between the experimental values and values from the model can be attributed to experimental error and have a difference of 0.1 pH units by average. Agreement is much better than the 0.1 pH unit average throughout the graph except for both endpoints, where only Na_2CO_3 or $NaHCO_3$ are added to the water. The reasons for this disagreement are unclear but it is interesting to note that the pH is changed towards the pK_{a2} value in both cases.

The agreement of the model pH predictions with the experimental values demonstrate that

the model is very capable of running accurate calculations at high ionic strengths, in this case, up to ionic strengths of 2.4.

Finally, the commercial program Geochemist's Workbench (GWB)[78] was used to predict pH for these solutions. The GWB results were compared to the model and found to be within 1% relative error (by comparing pH values). The similar results between GWB and the model are not surprising as both use Pitzer's equations[132] to calculate activity coefficients. The small differences between the two computational packages were accounted by comparison of the difference of significant digits used by both programs during the calculations.

b. Liquids ^{13}C NMR of $NaHCO_3/Na_2CO_3$ solutions

Similar to the previous experiment, a series of solutions were made with varying amounts of $NaHCO_3/Na_2CO_3$ ratios. These solutions were made by adding the solid powder to a liquids NMR tube to which a specific amount of water (in this case heavy water, or D_2O, was used for field locking in the high resolution ^{13}C NMR experiment) was added. The effect of the ionic strength of these solutions on the NMR circuit did not matter as the objective was to measure a chemical shift. Chemical shift was calculated from an internal reference that was added to the solution, Dioxane, set at 67.19 ppm.[47,138]

The ratio, $[HCO_3^-]/([HCO_3^-]+[CO_3^{2-}])$, was calculated from the experimental ^{13}C NMR chemical shift data by Equation 4.8, where $\delta_{HCO3-} = 161.5$ and $\delta_{CO32-} = 169.0$. The experimental ratios were compared to calculated equilibrium ratios, calculated identically as in the previous pH meter experiments, based on the initial amounts of $NaHCO_3$ and Na_2CO_3.

$$\left(\frac{[HCO_3^-]}{([HCO_3^-]+[CO_3^{2-}])}\right)_{exp} = 1 - \left(\frac{\left(\delta_{obs} - \delta_{HCO_3^-}\right)}{\left(\delta_{CO_3^{2-}} - \delta_{HCO_3^-}\right)}\right) \qquad (4.8)$$

The experimental ratios are plotted against the modeled ratios in Figure 4.5.

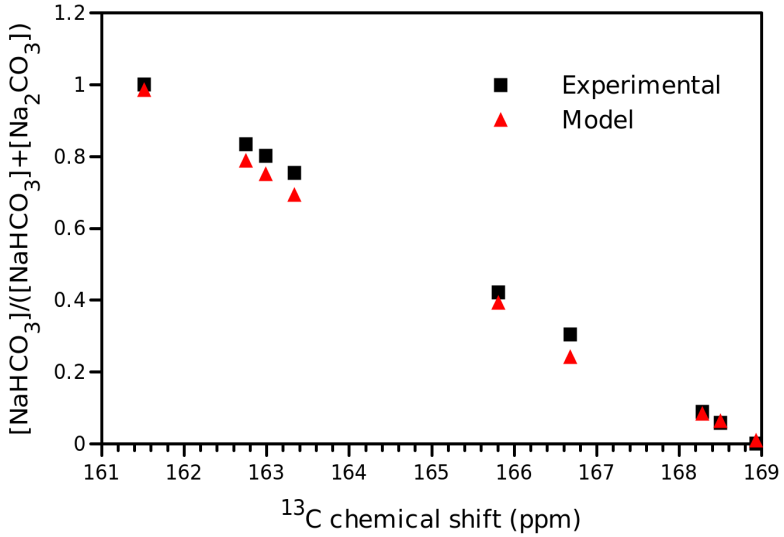

Figure 4.5: Experimental and calculated ratio of carbon as bicarbonate vs. ^{13}C chemical shift for several different solutions.

There is excellent agreement between the model and the experimental data at the ends of the graph. In addition, the ^{13}C NMR data (black boxes) present a straight line, which was as expected. The modeled data, however, diverges considerably from the experimental data in the middle of the plot, in some cases as much as 0.1 ratio units (corresponding, to a pH error close to 1 unit). The uneven sampling spacing was due to several experiments not working. In some tubes we were unable to obtain ^{13}C NMR signal altogether. In others, the ^{13}C chemical shift had large error. These errors were due in part to using contaminated NMR tubes in one case, poor mixing in another, and/or aging solutions. As I will show later, these solutions are not stable and eventually equilibrate with the atmosphere, causing an increase in pH. While the tubes in these

experiments were sealed, they were not airtight.

At first I thought the deviation of these points in the middle were due to some sort of experimental error, but after plotting the ^{13}C chemical shift data vs. calculated pH (Figure 4.6), and comparing it to the the literature values of Jakobsen et al.[46] it became apparent that the D_2O-dominant solution was shifting the pK_{a2} value. This has the affect of increasing the error in the middle of the line because that is the region that the NMR chemical shift will have the greatest change due to a change in $[HCO_3^-]/[CO_3^{2-}]$ ratios. D_2O does not change the *pure* chemical shift of HCO_3^- or CO_3^{2-}, just the equilibrium values between those two extrema, which is why the two lines coalesce at either end in Figure 4.5. In truth, Jakobsen et al. use some D_2O for field-locking (but sparing amounts) so the measured pK_{a2} of their curve is relatively unaffected by the deuterium from the true value that it should be.

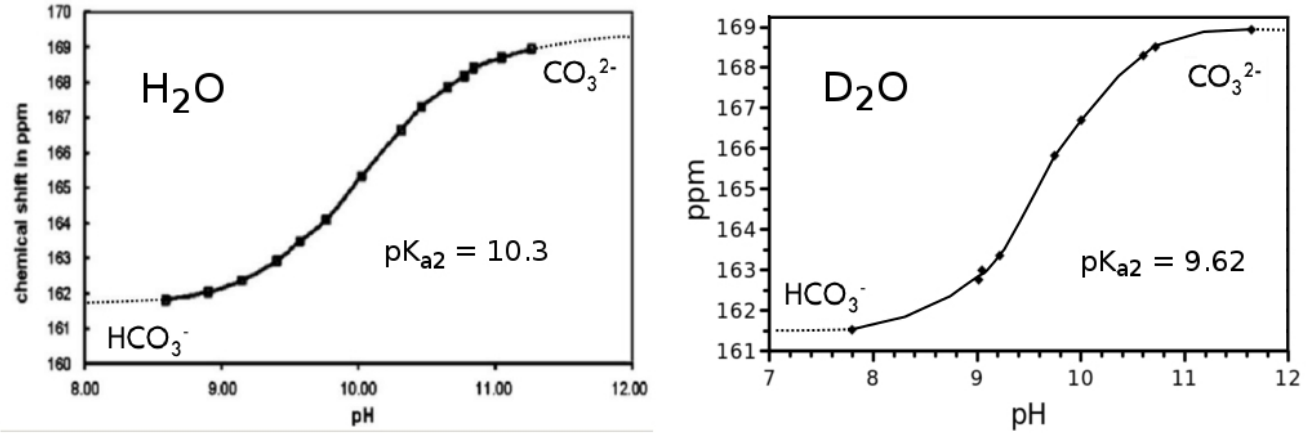

Figure 4.6: pH of solution vs. ^{13}C chemical shift in H_2O-dominant and D_2O-dominant solutions. H_2O curve adapted with permission from Jakobsen et. al. Copyright © 2005 American Chemical Society.

To confirm that the difference between the experimental values here and Jakobsen's research were real, three solutions were made that had different D_2O/H_2O compositions but identical

chemical composition (9/1, Na_2CO_3/$NaHCO_3$): 100%, 50%, and 25% D_2O by mass. Identical solutions showed chemical shift differences of 168.13 ppm (100% D_2O), 168.03 ppm (75% D_2O), and 167.80 ppm (25% D_2O). The experiment showed a depression of the observed chemical shift for the same chemical composition, showing a depression of pK_{a2}. Deuterium is known to have a isotopic effect in reactions across a wide range of pH values.[139] This effect usually (but not always) decreases the K value as the forward kinetic rate constant is decreased relative to the reverse rate constant because the deuterium is roughly twice the mass of hydrogen and slows the rate of exchange.[140–142]

In addition, several solutions were monitored for chemical shift change over time. In all cases, chemical shift increased with time, indicating that $CO_{2(aq)}$ was escaping the system (equilibrating with the atmosphere) causing the pH to increase. In general these effects were only able to be seen in solutions with pH's between 7 and 9, where the composition was mostly $NaHCO_3$. Their changes in pH were not equal, which can be attributed to their different handling, quality of capping, and time spun in the NMR magnet. In the most extreme case, a solution starting initially as $NaHCO_3$ and water started at 161.5 ppm (100% $NaHCO_3$, $[CO_3^{2-}]/[HCO_3^-]=0$) and after one month had drifted to 164.4 ppm ($[CO_3^{2-}]/[HCO_3^-]=4/6$).

Finally, the pH calculations show that in samples with pH < 8, the $[CO_2]$ in the solution should be high enough to detect with ^{13}C NMR (~0.01 m for the aqueous solution with only $NaHCO_3$ added). However, the $CO_{2(aq)}$ peak was never detected, even when 99% ^{13}C-labelled $NaHCO_3$ was dissolved in D_2O. This is probably due to the fact that CO_2 has a very long T_1 in room temperature solution (~30 s). Even though the recycle delay was extended up to several minutes, the S/N of the bicarbonate peak was high enough to be able to resolve a peak ~2% of its

area, as the [CO_2] peak should have been. This could also be from the the use of a pulse that was shorter than a 90° pulse because the highly ionic solution partially dematched the probe.

Despite the depressing effect of D_2O on the pK_{a2}, these ^{13}C liquids NMR experiments show that the pH model and NMR data work well together. It also shows that the model can accurately predict [HCO_3^-]/[CO_3^{2-}] ratios (and from that, pH) for solutions of high ionic strength and at pH values from 7 to 12.

c. High pressure ^{13}C NMR of CO_2 in NaOH solutions.

Three different solutions of varying ionic strength were prepared by diluting three aliquots from a standard NaOH solution made by mixing NaOH pellets (Alfa Aesar, 98% purity) with deionized water. The three diluted solutions were 0.0948, 0.288, and 1.041 molal NaOH. Approximately 2 mL of each aliquot was pressurized with $^{13}CO_2$ in the high pressure NMR apparatus described in detail in Chapter 2. Each aliquot was allowed to equilibrate for ~12 hrs at each different CO_2 pressure before the [CO_2]/[HCO_3^-] ratios were measured by ^{13}C NMR. These experiments were designed to test the model's ability to calculate [CO_2] at different pressures by predicting [CO_2]/[HCO_3^-] ratios and [Na^+] values at different pressures in the three solutions.

Before each solution was pressurized with CO_2, a modest vacuum was applied to the solution (0.1 bar) to allow for removal of most of the air in the headspace of the pressure chamber. Each solution was allowed to equilibrate at each pressure reported was allowed to equilibrate overnight (~12 hrs) without being stirred. As previously described in Chapter 2, this equilibration time is enough to achieve equilibrium for most experiments.

Whereas the alkalinity came from $NaHCO_3$ and Na_2CO_3 in all previous experiments in this

chapter, here the alkalinity comes from the NaOH. Thus, all inorganic carbon in the solution comes from CO_2 in these experiments—not from any initial $NaHCO_3$ or Na_2CO_3 in the solution. These experiments use ^{13}C NMR to explore the pH range of 3 to 7 and thus the $CO_2 \rightleftharpoons HCO_3^-$ equilibrium (first equilibrium in Equation 4.3), unlike the previous liquids ^{13}C NMR experiments (second set of experiments) that explored the 7-12 pH region. Ionic strengths in these samples are as high as 1.04.

As described in the liquids ^{13}C NMR section, the ^{13}C T_1 of the carbon in CO_2 is quite long in solution. As the dominant relaxation mechanism for CO_2 is spin rotation relaxation, infusion into water considerably lengthens the T_1 of the CO_2. At room temperature, the T_1 of the CO_2 at 89.06 MHz is around 20 seconds.[21] So, to ensure that the $[CO_2]/[HCO_3^-]$ ratios in these pressurized solutions were quantitative, a 5 minute recycle delay was used between scans. In addition, 16-step phase-cycled Hahn echoes with a τ delay time of 100 μs were used for all $[CO_2]/[HCO_3^-]$ ratio acquisitions to separate the 7 μs probe ringdown and the NMR signal to ensure there was no first-order phase effects in the signal and to limit the spins observed to those entirely within the coil (Hahn echoes are more spin selective than a Bloch decay pulse sequence because they only refocus spins that are within the coil).

Figure 4.7 shows the $[CO_2]/[HCO_3^-]$ ratio results (points) obtained at the different pressures in the three different samples. The model predictions (curves) are closely aligned with the data and were generated using the known $[Na^+]$ values as described in Appendix A. The largest disagreement is in the 1.041 m data set (at low CO_2 pressure, 7.19 bar) and is a $[CO_2]/[HCO_3^-]$ ratio difference of 0.09 (0.19 model ratio vs. 0.10 experimental ratio) which corresponds to 0.3 pH units in error (using Equation 4.6). The largest disagreement in the 0.0948 m data set (43.21

bar data point) was a $[CO_2]/[HCO_3^-]$ ratio difference of -1.68 (11.99 model ratio – 13.68 experimental ratio), corresponding to a difference of -0.05 pH units error (using Equation 4.6). The average model agreement with the experimental data corresponds to +/- 0.1 pH units overall. The experimental error of the $[CO_2]/[HCO_3^-]$ ratios from S/N in the ^{13}C NMR experiments is smaller than the size of the data points in the graph.

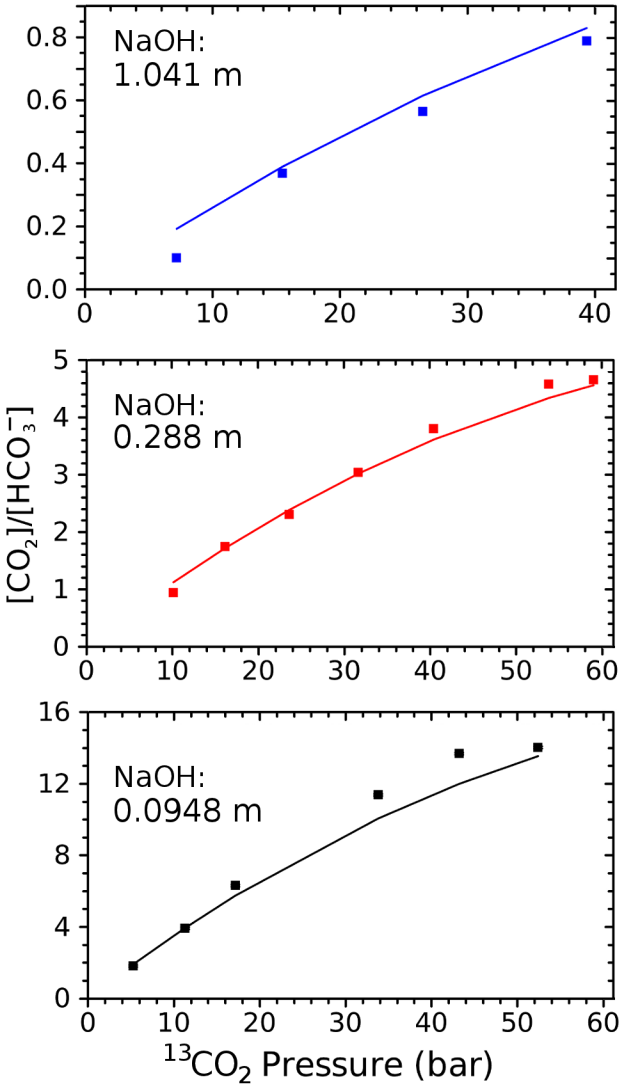

Figure 4.7: Experimentally measured $[CO_2]/[HCO_3^-]$ ratios from high pressure ^{13}C NMR (square symbols) and predicted values (curves) at three concentrations of NaOH as a function of CO_2 pressure.

After testing for agreement between predicted and measured $[CO_2]/[HCO_3^-]$ ratios, the data and model predictions were combined to see if the known $[Na^+]$ concentration could be calculated accurately. These calculations would demonstrate the feasibility of calculating pH values for these solutions in the absence of knowing $[Na^+]$ explicitly and were completed using recursive calculations between D&S equations, the charge balance equation (Equation 4.7), and PHREEQC as described in Appendix A. $[Na^+]$ must be known to calculate the correct CO_2 solubility and activity coefficients. The results of these $[Na^+]$ calculations are in Figure 4.8.

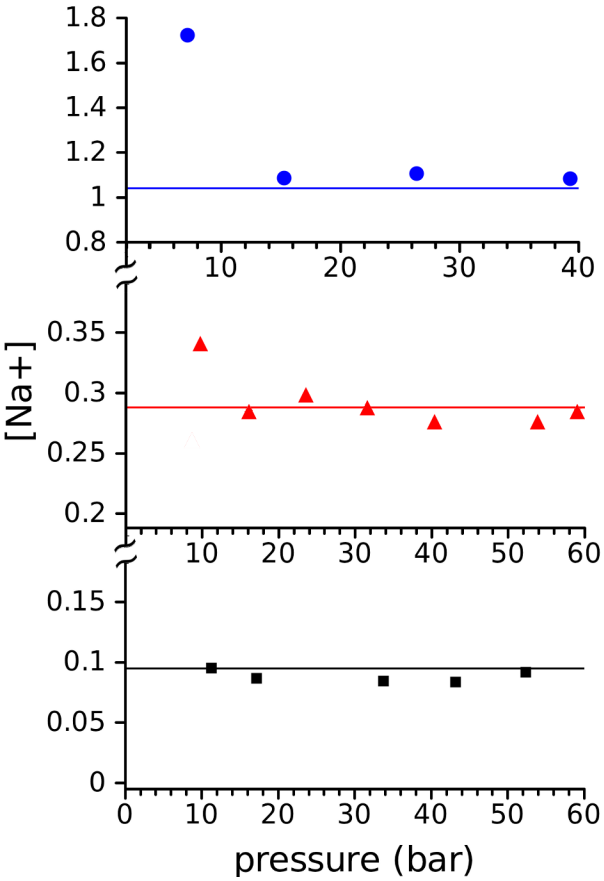

Figure 4.8: $[Na^+]$ estimations from ^{13}C NMR data using the experimentally-obtained $[CO_2]/[HCO_3^-]$ ratios and the model. The solutions are 1.041 m (blue circles, top), 0.288 m (red triangles, middle), and 0.0948 m (black squares, bottom). The solid lines are the actual solution concentration of $[Na^+]$ in each of the solutions.

The significant deviations of the [Na^+] calculations in the first points of the 1.041 m and 0.288 m data are most likely from the lack of equilibrium between with the CO_2 gas above it. The solutions were allowed to equilibrate for 12 hrs at each pressure, but CO_2 dissolution can take as long as 18 hrs depending on the initial pressure of the CO_2 gas, the temperature of the probe, and whether there is already CO_2 in the solution (see information on CO_2 dissolution into water in Chapter 2). The concentration of NaOH also plays a role in the dissolution kinetics and has been described in great detail elsewhere.[143] All of the other data points had a [Na^+] concentration deviation from the real values less than the 7% precision ascribed to the D&S solubility equations, which represent the limit of precision for the model.[112]

Finally, the calculated pH values of the three NaOH solutions at different equilibrium pressures were compared with the experimentally determined [CO_2]/[HCO_3^-] ratios measured by ^{13}C NMR. For each solution, the pH results were calculated with and without the addition of the activity coefficients. That is, for each set of data, pH was calculated using Equation 4.5 (ideal approximation) and then Equation 4.6 (use of activity coefficients). This comparison was to show how much of an effect the addition of the activity coefficients was having on the pH calculations. The deviation in pH between the two methods becomes greater with increasing ionic strength, up to just over a half of a pH unit in the 1.041 m solution, confirming that activity coefficients are needed to calculate an accurate pH value at these ionic strengths and conditions.

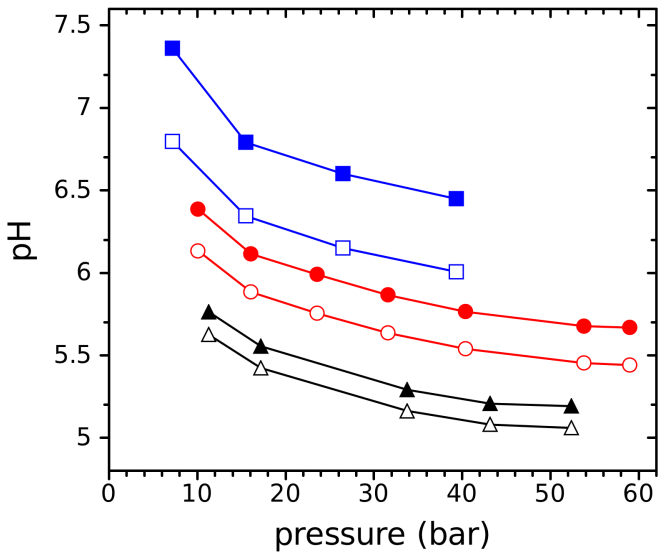

Figure 4.9: pH titrations of all three NaOH solution experiments. Measured pH results without (filled symbols) and with (hollow symbols) the calculated activity coefficient corrections. The three different solutions are 0.095 m (black triangles), 0.288 m (red circles), and 1.041 m (blue squares). The lines are provided as guides to the eye.

Figure 4.9 shows the depression of pH in each solution as the CO_2 pressure was increased. It also shows the increasing differences between the ideal approximation and incorporation of the activity coefficients to calculate pH values as $[Na^+]$ concentration is increased (increasing ionic strength). The ideal approximation, then, works best at low ionic strengths and therefore cannot be used in carbon sequestration-like conditions. At high ionic strengths, it is critical for activity to be included.

D. Application of pH model: measuring pH during a CO_2 sequestration reaction

Now that I have fully validated the pH model and shown how it can be combined with ^{13}C NMR data to produce accurate pH values that are based on $\{H^+\}$, I will apply the model to a real reacting sequestration system. Here I will show data from the short reaction of $Mg(OH)_2$

discussed in Chapter 3, where CO_2 was reacted with $Mg(OH)_2$ in water for 4 days at 107 bar and 81 °C (Figure 3.10a).

As described earlier, the measured $[CO_2]/[HCO_3^-]$ ratios from Figure 3.10a were input into the model, and a series of $[Mg^{2+}]$ values were calculated using the recursion technique between D&S's CO_2 solubility equations and charge balance for each time point. The calculated $[Mg^{2+}]$ values vs. time are shown in Figure 4.10.

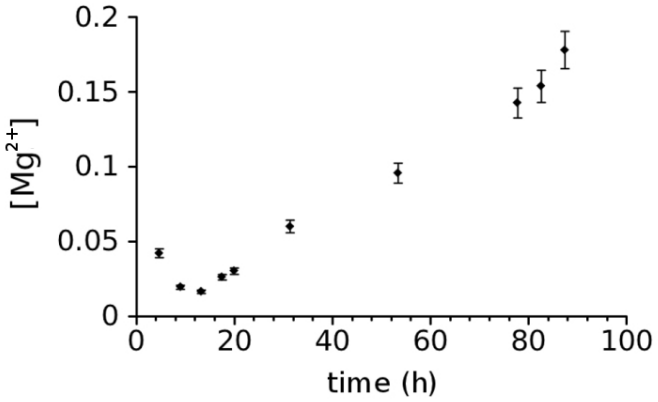

Figure 4.10: Estimated $[Mg^{2+}]$ values vs. time in the sample, obtained by charge balance restricted by the $[CO_2]/[HCO_3^-]$ ratios. The error bars represent 7% relative error as estimated from the $[Na^+]$ experiments and the limitations of D&S's solubility model.

The initial decrease in the $[Mg^{2+}]$ is non-intuitive. The $[Mg^{2+}]$ calculation uses recursion between the charge balance equation and the D&S equations, and the initial decrease may be an artifact of that calculation. The $[Mg^{2+}]$ value is allowed to float freely to fulfill the charge balancing needs of the reaction as it progresses. Every CO_2 molecule that reacts with water forms HCO_3^- and H^+. As H^+ is consumed by dissolving the mineral, Mg^{2+} is released into the solution, captured by the calculation to keep the system electrically neutral. It is possible that there are

other ways for the solution to stay electrically neutral, keeping the $[Mg^{2+}]$ constant, such as impurities in the solution. This model does not consider those other possibilities, however. An approximate value of $[Mg^{2+}]$ is all that is needed to calculate an activity coefficient. Nevertheless, if the initial decrease of $[Mg^{2+}]$ is real, then $[Mg^{2+}]$ is almost certainly being sequestered in a reaction with CO_3^{2-} or HCO_3^- and either precipitating as an amorphous or crystalline phase or existing as a polymer precursor[76] in the solution.

When the $[CO_2]/[HCO_3^-]$ ratios are plugged into the model along with the activity coefficients, pH values based on $\{H^+\}$ can be calculated. Figure 4.11 shows the pH results generated from the model and data. The figure shows how they are increasingly dependent on the activity coefficients as the dissolution of the mineral continues and the $[Mg^{2+}]$ value increases. The difference between the pH calculated by $[H^+]$ (without activity coefficients) and $\{H^+\}$ (with activity coefficients) gets larger as the reaction continues and its behavior becomes increasingly non-ideal. After ~90 h of reaction, the difference between the two pH values is already 0.5 pH units—demonstrating the importance of using this method for measuring pH in the reaction. At higher pressures and longer reaction times, the system can become even more non-ideal.

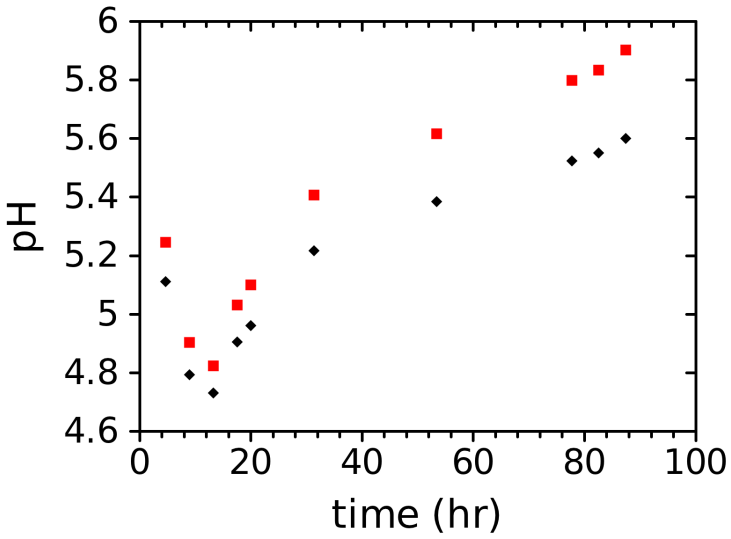

Figure 4.11: pH calculated from measurements made without (red) and with (black) activity coefficients as a function of time within the reaction.

The model can generate other parameters through PHREEQC other than pH values. It can also generate something called saturation indices for different minerals. The saturaction index, a metric used to describe and predict mineral dissolution and precipitation, can quantify what is thermodynamically favorable to precipitate in the sample. The saturation index is described in Equation 4.9 and defines the degree to which a solution is super-saturated with respect to the mineral of interest, in this case, $MgCO_3$.

$$\mathrm{SI} = \log_{10}\frac{Q}{K_{sp}} = \log_{10}\frac{\{\mathrm{Mg}^{2+}\}\{\mathrm{CO}_3^{2-}\}}{K_{sp}} \quad (4.9)$$

where,

Q = ion activity product

K_{sp} = solubility product, equilibrium constant for $MgCO_3$ dissolution

Precipitation can only occur when the solution is super-saturated with respect to the mineral of interest (i.e. based on thermodynamics) and the extent to which the mineral does precipitate, once saturation is reached, is dependent on the precipitation mechanism (kinetics). The kinetics

can be dependent on pressure, ionic strength of solution, and preexisting mineralogical surfaces on the basis of the system being studied.[57]

I will not consider any more details of the different possible precipitation mechanisms as they are beyond the scope of this thesis. I will, however, refer to and use saturation indices as a way of understanding the probability of precipitation of minerals.

In Figure 4.12, the saturation indices for different Mg-containing minerals have been calculated using the model during the first 100 hours of the reaction with CO_2, based on the aforementioned pH and [Mg^{2+}] values. Here the $MgCO_3$ saturation index starts above zero since [Mg^{2+}] is high, which is further evidence for early $MgCO_3$ precipitation. The latter would cause the decrease in the [Mg^{2+}] values at early times in the reaction, described earlier.

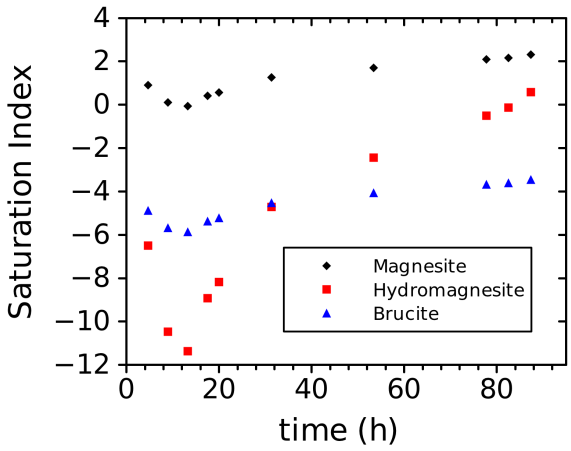

Figure 4.12: Calculated saturation index (dimensionless) for three different minerals ($MgCO_3$, $4MgCO_3{\cdot}Mg(OH)_2{\cdot}5H_2O$, $Mg(OH)_2$) vs. reaction time.

Figure 4.12 shows that $MgCO_3$ remains the thermodynamically preferred phase for precipitation the entire time of reaction, although the saturation index of $4MgCO_3{\cdot}Mg(OH)_2{\cdot}5H_2O$ (hydromagnesite) dramatically increases throughout the entire reaction.

The reactant mineral, $Mg(OH)_2$ (brucite), keeps a negative saturation index, indicating that throughout the entire reaction it will never precipitate out of solution, just dissolve.

It is important to realize that these ^{13}C NMRmeasurements are made by averaging the conditions of the entire NMR coil region of the sample, which represents the *first* 2.5 cm of powdered mineral in the reaction tube. If there is a gradient of conditions (as indicated by the spatial dependence of the formed carbonate products in Chapter 3), there will be a gradient of saturation indices. Hydromagnesite was detected as a product in this reaction (see Chapter 3), but only in deeper portions of the sample (towards the bottom and/or outside of the NMR coil region). Hydromagnesite could have formed there either because the precipitation of $MgCO_3$ was kinetically limited (had to form hydromagnesite first, then convert) or because the saturation index of hydromagnesite was above 0.0 (or above the critical saturation index value) in the deeper portions of the sample (something that the averaging of the first 2.5 cm of the sample would not be able to catch). The saturation indices calculated here are consistent with the *ex situ* results, described in Chapter 3.

E. Conclusions

Here I have demonstrated how the combination of a pH model and experimental ^{13}C NMR data allows the measurement and calculation of a vast array of important experimental variables for CO_2 sequestration reactions, including pH, $[Mg^{2+}]$, activity coefficients, equilibrium constants, and saturation indices applicable to CO_2 sequestration reactions. These values would not be possible to obtain either empirically from the NMR data alone or by the modeling alone. This combination of experimental measurements and calculation provides data that greatly aids

the understanding of high pressure, high temperature CO_2 sequestration reactions to help determine dominant processes in the reacting system.

Through a series of three validation experiments (pH meter experiments, ^{13}C liquids NMR, and ^{13}C NMR of CO_2-pressurized pressure NaOH solutions), I was able to demonstrate that the model works very well to predict the pH and $[CO_2]/[HCO_3^-]$ values at high ionic strengths (up to 2.4) given known quantities of ionic species in solution. The pH meter experiments demonstrate that the model can accurately calculate activity coefficients in solutions of high ionic strengths, which are known to be challenging, as it predicted pH values with a precision better than 0.1 pH units. The NaOH solution experiments show that the model can accurately predict $[CO_2]$ values and can further use that data to accurately predict $[HCO_3^-]$, $[Na^+]$, and $[Mg^{2+}]$ values from which the model can then calculate activity coefficients. Using the resulting activity coefficients, real pH values can then be obtained.

In situ ^{13}C NMR provides the additional tools needed for the measurement of pH in aqueous reactions involving CO_2, far removed from ideal conditions (low ionic strengths and standard temperature and pressure). This methodology is relevant to a wide variety of fields including carbonate chemical production and CO_2 capture methods. NMR is a readily-available analytical tool for these purposes, and the combination of readily-available models and experimental data shows promise for researchers across many disciplines to adopt these methods.

Chapter 5: In situ 1D pH imaging

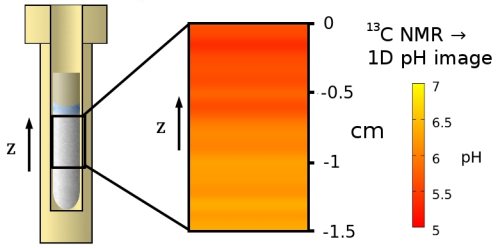

Figure 5.1: In situ ^{13}C NMR can measure the pH gradient across a sample of a wet slurry of powder mineral reacting with sc-CO_2 during a sequestration reaction at high pressures and temperatures.

A. Introduction

Chapter 4 describes in great detail the importance of being able to measure pH during a sequestration reaction. pH provides a wealth of information on the reaction progress and likelihood of carbonate mineral precipitation in terms of the saturation index. In this chapter I seek to use pH to further describe the spatial dependence of carbonate products as well as to confirm, by direct measurement, the already-proposed existence of a pH gradient in CO_2 sequestration reactions with solid minerals.[21,144]

a. Observed Ex situ spatial dependence

As already described in Chapter 3, when a wet slurry of powdered mineral (such as $Mg(OH)_2$ or Mg_2SiO_4) is pressurized with CO_2 and heated, it reacts with the CO_2 to form solid carbonates in a spatially dependent manner. The solid carbonate product(s) form in different amounts along the length of the sample, exhibiting a reproducible depth dependency given the same temperatures, pressures, mineral grain sizes, etc.

The depth dependence of carbonate products was a great puzzle as one would expect the CO_2

to mix (albeit, rather slowly) with the rest of the sample forming one carbonate product in equal amounts along the Z-axis of the sample. Given that the porosity of the powdered mineral is around 50% (measured by ^{13}C NMR spin counting), the CO_2 diffusion through the sample should not be very limited as the CO_2 should be relatively free to mix with the entire powdered sample. But that is not what happens. In the case of the $Mg(OH)_2$ reaction system, several different carbonate products form: $MgCO_3$ predominantly at the top (0 to -1 cm), with $4MgCO_3 \cdot Mg(OH)_2 \cdot 5H_2O$ (hydromagnesite) slightly deeper (-1 to -2 cm), and $4MgCO_3 \cdot Mg(OH)_2 \cdot (6\text{-}8)H_2O$ (dypingite) even deeper (-2 to -4 cm). In the case of the Mg_2SiO_4 reaction system, only one mineral, $MgCO_3$ (magnesite), forms but its extent of formation is extremely dependent on depth. The top layer of the Mg_2SiO_4 has the least amount of $MgCO_3$ precipitate in the entire sample, with the middle layers of the mineral powder (1.4 cm deep into the sample) having the most $MgCO_3$.

Almost certainly the reason for the spatial dependence of the mineral is that there is a gradient of reaction conditions across the sample. The different reaction conditions across the length of the sample probably involve different $[Mg^{2+}]$ values and thus saturation index values—meaning that different minerals have different likelihoods of precipitating depending on their position in the sample. When the CO_2 plume initially reaches the mineral sample, the top layer of the mineral sees the CO_2 first, before the rest of the mineral sample, and consequently begins reaction with the CO_2 before the rest of the mineral. Assuming that the initial dissolution rate is close to the rate of CO_2 introduction into the powdered mineral, the mineral dissolution will cause a $[Mg^{2+}]$ bias across the sample, with a disproportionate amount at the top of the mineral slurry. Depending, of course, on the saturation indices and whether the conditions are favorable

for carbonate precipitation at the top layer of the mineral, carbonate precipitation can also begin, decreasing the [Mg^{2+}] values.

The point is that the rate of CO_2 introduction into the mineral slurry (controlled by diffusion and convection currents in the sample), the rate of mineral dissolution, and the rate of carbonate precipitation, can, in principle, create a moderate to strong Mg^{2+} gradient across the sample. The gradient of [Mg^{2+}] implies a gradient of other ions in the solution, including H^+, HCO_3^-, and CO_3^{2-}. An H^+ gradient is a pH gradient and could be observed *in situ* by a depth-dependent [CO_2]/ [HCO_3^-] ratio.

b. Observed in situ spatial dependence

Spatial dependence of carbonate products are not the only evidence for pH gradients. In an effort to speed up the mineralization process to observe a carbonate powder pattern, I added a pellet of NaOH to an aqueous MgO reaction with CO_2 at 104 bar and 90 °C that ran for two weeks. I then observed $CO_3^{2-}{}_{(aq)}$ and $HCO_3^-{}_{(aq)}$ simultaneously in the sample via ^{13}C NMR. The equilibrium between $CO_3^{2-}{}_{(aq)}$ and $HCO_3^-{}_{(aq)}$ is faster than the NMR time regime and therefore should only present one peak with a chemical shift that is based on the [HCO_3^-]/[CO_3^{2-}] ratio (see Chapter 4). It is impossible to observe both peaks at the same time with ^{13}C NMR unless there are two regions of the sample that have two different pH values. Presumably, adding NaOH to the MgO reaction with CO_2 increased the pH to high enough values in portions of the sample that CO_3^{2-} *could* exist. The NaOH changed the overall pH of the system enough so that the gradient's effects could be observed in the pH dependent chemical shift of HCO_3^-/CO_3^{2-}.

Both the HCO_3^- peak (161.5 ppm) and CO_3^{2-} peak (168.8 ppm) were observed early (as the CO_2 dissolved into the water and immediately converted into CO_3^{2-}) as well as after two weeks

time. Figure 5.2 shows three spectra that were acquired a day into the reaction. The three spectra were all acquired using 16-step phase cycled Hahn echoes with a 120 s RD (so spectra are spatially limited to spins within the coil and are fully quantitative). The coil was positioned so that it was focused on the MgO mineral at the top of the sample for the 0 cm position, -0.675 cm into the sample for the second experiment, and -1.27 cm deep into the sample for the third experiment. The change in the shows a simple image by way of spectra at different locations within the sample where there is more $CO_{2(aq)}$ at the top of the sample than $CO_3^{2-}{}_{(aq)}$ and more CO_3^{2-} at the bottom of the sample than $CO_{2(aq)}$.

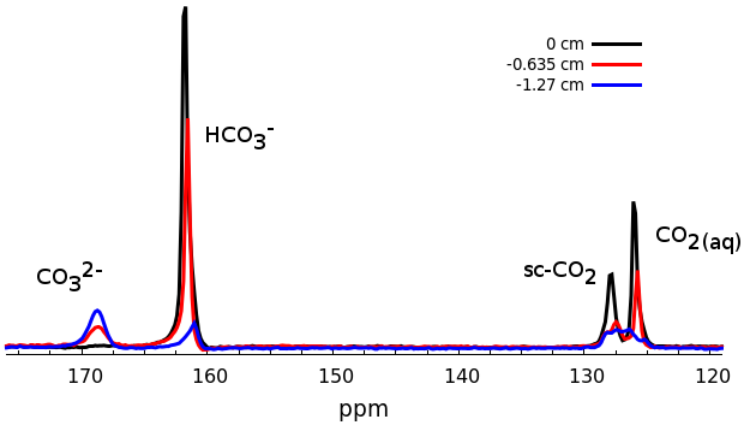

Figure 5.2: Three spectra observed from three different locations in the MgO + NaOH + $CO_{2(aq)}$ reaction along the length of the sample tube: top (0 cm), middle (-0.635 cm), and bottom (-1.27 cm). (Data: R5 94,96,98).

As the coil is moved to observe increasingly deeper portions of the sample, the $CO_3^{2-}{}_{(aq)}$ peak increases in strength. Likewise both the $HCO_3^{-}{}_{(aq)}$ and $CO_{2(aq)}$ peaks decrease in strength, indicating a shift in the pH to lower values deeper within the sample. This observed pH gradient must be very massive in this sample. Regions where CO_2 exists in almost equal amounts to $HCO_3^{-}{}_{(aq)}$ must have a pH value in the range of 6-7 (black spectrum Figure 5.2). The pH value

where CO_3^{2-} is dominant must be greater than 10. The pH gradient here is on the order of 4 units of pH across the entire sample tube!

There are two other important notes about Figure 5.2 to be made. First, the powder pattern did form during the reaction but was small compared to the solution peaks in the spectra shown. Second, the lineshape of the CO_2 peaks drastically changes with depth into the sample. Recall that the sc-CO_2 peak is at ~128 ppm relative to $CO_{2(aq)}$ at 126 ppm because of its difference in magnetic susceptibility. When the coil is at 0 cm, the bottom of it is 1.27 cm above the bottom of the glass tube and bottom of the zirconia high pressure vessel. As the coil is moved down towards the bottom of the vessel, the magnetic homogeneity of the volume between the glass liner and high pressure vessel gets worse because of the round bottom of the glass liner. The change in homogeneity increasingly distorts the sc-CO_2 line (~128 ppm), and the $CO_{2(aq)}$ line (126 ppm) all but vanishes as there is not much in the bottom of the tube (the pH is very high).

The *ex situ* and *in situ* evidence all point toward the existence of a pH gradient during reactions with CO_2 and a mineral. And it appears that the gradient can be driven by a number of factors: rate of dissolution of CO_2, rate of mineral dissolution, and rate of carbonate precipitation. The pH gradient will form, change, stretch, and even vanish based on the individual rates and progress of all three reaction steps. Herein I develop the methodology for measuring the spatial $[CO_2]/[HCO_3^-]$ ratios (from which spatial pH can be obtained) along the z-axis of the reaction tube while the reaction is occurring.

B. Experimental details

a. Introduction to simple 1D imaging techniques

NMR is extremely well-suited for measuring spatial variations across a sample. The principles of using NMR to *image* a sample is called MRI (magnetic resonance imaging) and is a highly-developed field being used everyday by medical professionals to image the human body. MRI works essentially by applying a known magnetic field gradient across the sample causing the observed spin frequency to be a function of space, because the observed NMR spin frequency depend on the strength of the magnetic field (Equations 5.1 and 5.2).

$$\nu_0 = \gamma B_0 \quad (5.1)$$

$$\Delta\nu_0 = \gamma \Delta B_0 \quad (5.2)$$

where, ν_0 is the frequency of spin precession

γ is the magnetogyric ratio of the nucleus (fundamental constant)

B_0 is the strength of the magnetic field

Per Equation 5.2, the the frequency of the spins will be a dispersion of values if the magnetic field is a dispersion of values. And if the dispersion of magnetic field values is linear, the spin frequencies will vary linearly in proportion to their position in the magnetic field gradient (or space). Thus the location of the spin in space is "encoded" in its frequency. In addition, the intensity of the signal at each frequency is proportional to the number of spins precessing at that frequency. So a 1D NMR spectrum acquired in the presence of a linear magnetic field gradient creates a 1D projection of spin density across the sample.

A simple example of this frequency encoding principle can be seen when I obtain a ^{13}C NMR spectrum of free $CO_{2(g)}$ at 50 bar with and without a magnetic field gradient (Figure 5.3).

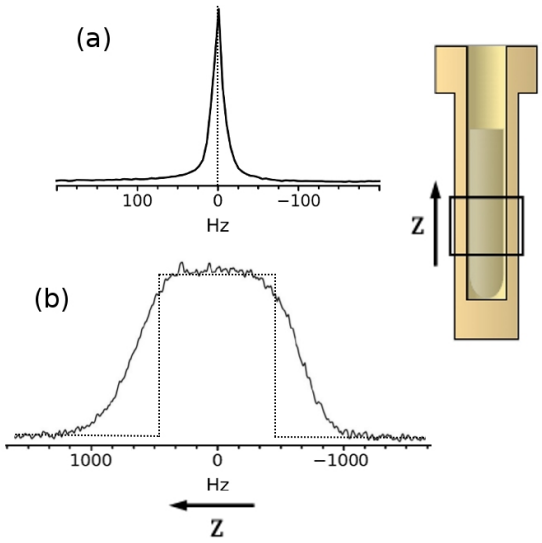

Figure 5.3: $CO_{2(g)}$ (52 bar) without gradient on (a) and with the gradient on (b). The image is limited by the size of the coil, and the direction of Z is dependent on the sign of the gradient. The dashed lines show the ideal shapes of the NMR signal given a linear gradient. (Data: 04262011-shim, #378).

Figure 5.3(a) illustrates that in the absence of purposeful magnetic field gradients, the observed $CO_{2(g)}$ linewidth is very narrow (20 hz, 0.22 ppm). It would be a single frequency (see dotted line) if there were no magnetic field inhomogeneities in the probe. When the Z_1 magnetic field gradient is turned on, the line broadens to become a width in the frequency domain that is a function of the magnetic field gradient strength and the length of the sample space. The ideal shape is a rectangle, but as sample extends outside of the coil and as the coil picks up spins outside of itself, there is a "fall off" of signal from the edges of the coil, which is a function of how far the B_1 field "sees" outside of the coil (and this "fall off" is not necessarily linear with distance as the magnetic field homogeneity drops decisively outside of the large 2.5 cm NMR coil). In addition, if the sample is situated exactly in the middle of the pivot point of the Z_1 field gradient, it will broaden symmetrically, as seen in the Figure 5.3.

Stronger Z_1 field strengths increase the linewidth of the signal while weaker Z_1 field strengths narrow the signal. Additionally, the strength of the Z_1 field is measured in gauss/cm, or more practically Hz/cm, and can be tuned to achieve the desired resolution for the image. "Resolution" here means smallest distinguishable unit of space that can be deciphered in the absence of any magnetic field gradient. The resolution is typically the full width at half maximum (FWHM) of a peak in the absence of a linear Z_1 gradient and represents the smallest Hz width observable given the magnetic inhomogeneties of the probe. Typical *in situ* FWHM values are on the order of 1 ppm (~90 Hz), so if the image has, lets say, 10 "distinguishable units of signal" across the length of the coil, a linear gradient must be applied that broadens the line 900 Hz. Stronger Z_1 field strengths increase the resolution of the image because more FWHM values can fit into the broader line. Nevertheless, there is a price to pay for increased resolution: stronger Z_1 field strengths also weaken the S/N as the number of spins per Hz value is less at higher gradient strengths. So the Z_1 field strength must be tuned to achieve the needed balance of resolution and S/N. The maximum Z_1 field strength achievable in the setup used for the images in this paper is 4.0 gauss/cm (4225 hz/cm). Typical gradient strengths used for the experiments reported here are 1.0 gauss/cm (1125 hz/cm). This gradient strength provides the needed balance between resolution and S/N for *in situ* experiments.

One dimensional imaging is relatively simple experiment because it only involves the acquisition of signal in the presence of a linear magnetic field gradient. Figure 5.4 (a) shows the imaging of the water/air interface (meniscus) using $^{13}CO_2$ and the imaging of the interface between two solutions, cyclooctane and water.

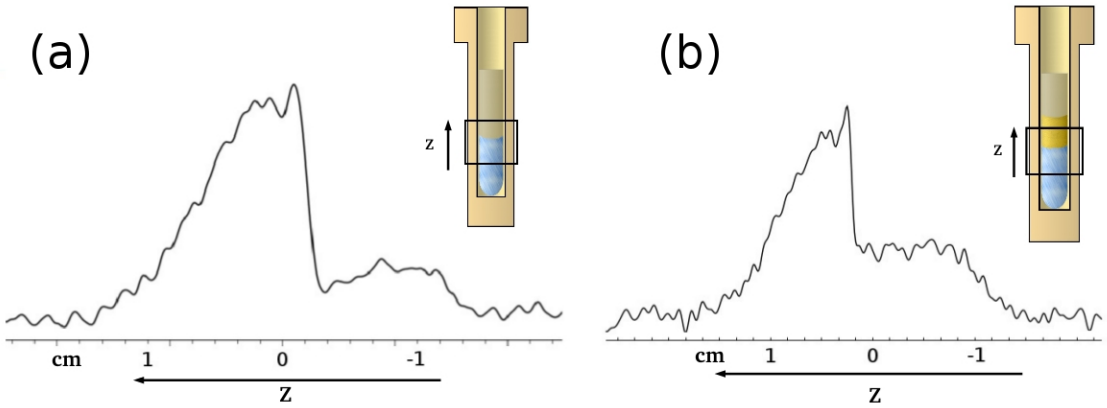

Figure 5.4: Imaging the miniscus of water (a) and the solution interface between two immiscible solutions, cyclooctane and water, (b). These images show the approximate ^{13}C spin density along the z-axis and form effective 1D images of the samples. (Data: #161-22072011, JS5-999c)

In Figure 5.4, the x-axis units have been converted into cm from hz, using the gradient field strength for each of the images: (a) 2836 Hz/cm (2.6 gauss/cm) and (b) 1549 Hz/cm (1.4 gauss/cm). The drastic vertical change of signal approximately in the middle of the image in (b) is sharper than in (a) because the interface between the cyclooctane and water is virtually flat (no miniscus) whereas the water/CO_2 gas has a meniscus with much curvature in the glass tube. This "smooths" the sharp line that would otherwise exist for the interface between the two phases. It is worth noting that imaging is a good method for determining solubility of CO_2 in any solution as the ratio of two heights of either side of the partition in the image is essentially the Ostwald solubility coefficient.[145] Figure 5.4's spectra are only semi-quantitative, however, as the recycle delay was 60 s in both experiments (a) and (b). The T_1 constant for $CO_{2(aq)}$ is 25.9 ± 0.77 s at room temperature (and is relatively independent of pressure), so the 60 s recycle delay is only ~2T_1 which means we are only recovering about 84% of the signal in the aqueous phase. (The T_1 of CO_2 in cyclooctane is the same as in water, within experimental error, so the ratio in (b) is actually very close to quantitative because there is no disparity between the T_1's of the two sides

of the image).

b. Details of Z-storage Imaging pulse sequence

When running imaging experiments it is important to know two values very well: where you are in the sample and the strength of the magnetic field gradient. Without them, an "image" is like a map without a legend (no scale) and no city names (no indication of where the objects are on the map). Here, the gradient strengths were determined by moving the probe a precise distance vertically through the magnetic field gradient through a number of different linear gradient strengths. The change in frequency of the ^{13}C NMR signal between the two probe positions over the set distance between the two positions provided the gradient strength in units of Hz/cm. These were back-calculated to produce the field strength in gauss/cm based on the magnetogyric ratio of ^{13}C and the change of frequency.

Position, on the other hand, typically involves putting a sample of known dimensions into the coil. This "phantom" sample should be quick and easy to load so as to get a position reference quickly, if needed (typically one needs to take a position reference in this setup for each new coil used: sample-to-sample changes were not found to effect its observed position). One such candidate phantom sample is the water meniscus example discussed in the previous paragraphs. The location of the meniscus in the H_2O meniscus experiment in Figure 5.4(a) unambiguously provides a strong location reference mark. The downside to this experiment, however, is the time it takes for the CO_2 to dissolve into the solution (several hours) and the fact that every time CO_2 is dissolved in water, some of it is inevitably lost. So, to determine sample position precisely, a small teflon ring was carefully machined to fit inside of a glass liner for the high pressure zirconia tube. This was placed at precise locations within the coil and images were attained of the

sample with the teflon disk in place. The precise width of the teflon disk could be measured using this method and its known physical location calibrated the experiments for position. Figure 15.4 shows a sample spectrum containing the teflon disc. The disc had a hole drilled into the middle of it which allowed gas to pass through it to the other side, so as to not affect its position. The gas within the hole can be seen as the signal density in the middle of the hole.

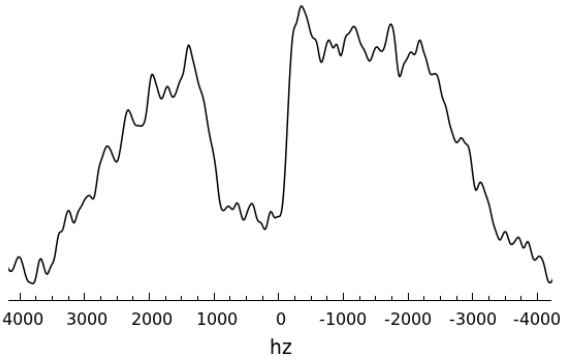

Figure 5.5: ^{13}C NMR 1D image of the profile of a teflon ring carefully fixed in the high pressure vessel. The location of the teflon ring was measured so as to be a reference for location in the image. (Data: 20121002).

When imaging the teflon disk, the higher gradient settings for the Z_1 gradients had to be used to get rid of the magnetic susceptibility effects (appearing as spikes on the edges of the teflon disk) in the 1D image. These are caused in images when two substances of very different magnetic susceptibilities interface. The small magnetic field inhomogeneities cause the spins near it to all report a similar frequency and "appear" to be very close to the surface of the solid. In these experiments, gradients greater than 3 gauss/cm were able to remove the susceptibility spikes, providing a smooth image, as seen in Figure 5.5.

The NMR pulse length and type of sequence also affect the shape of the image. As the coil is nearly 2.5 cm in vertical length, it is quite large compared to most NMR coils but quite small

compared to virtually any MRI coil. The RF in the coil is quite homogeneous, but the RF homogeneity falls off from its edges to its outside (see Figure 5.3). Figure 5.6 (a) demonstrates how the shape of the image $CO_{2(g)}$ at 61 bar changes with respect to the length of the pulse in a single pulse sequence (a "pulse-and-acquire" sequence). Figure 5.6 (b) shows how the the acquired image is "sharper" due to higher selectivity in a Hahn echo pulse sequence over the single pulse sequence.

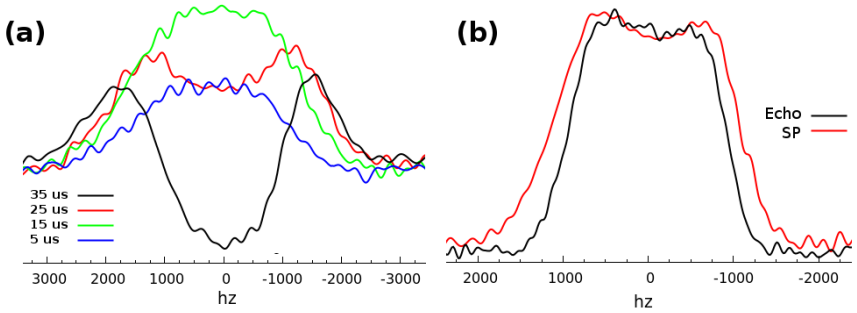

Figure 5.6: The 1D image of $CO_{2(g)}$ at 62 bar changes with respect to the excitation pulse length for single-pulse (SP) aquisitions (a) and choice of pulse sequence (b). (Data: (a)20120223-601, (b)20130422-1277,1279).

Imaging pH requires imaging both the $CO_{2(aq)}$ and HCO_3^- signals. While they do not have to be measured simultaneously (one could selectively excite $CO_{2(aq)}$ then HCO_3^-), it is preferable to measure them simultaneously as *in situ* imaging experiments can take several hours to obtain a good image. If it takes four hours of signal averaging to obtain a good image of $CO_{2(aq)}$, another four hours to get the HCO_3^- signal is hardly practical and could even introduce experimental error as the HCO_3^- signal could be different in the second four hours than it was in the first due to reaction progress.

Figure 5.7 shows the approach I took to image the $CO_{2(aq)}$ and HCO_3^- peaks simultaneously. To select both peaks at the same time, gradient strength was chosen that broadens both lines as

much as they can be broadened without overlapping. The gradient strength chosen for most *in situ* imaging experiments was 1.0 gauss/cm (1125 Hz/cm). $CO_{2(aq)}$ and HCO_3^- are 35.5 ppm apart which is 3161 Hz at 89.066 MHz. As the NMR coil is 2.5 cm in length, the signal would be ~2812 Hz wide, which would bring both signals very close to each other, but not overlapping, as simulated in Figure 5.7.

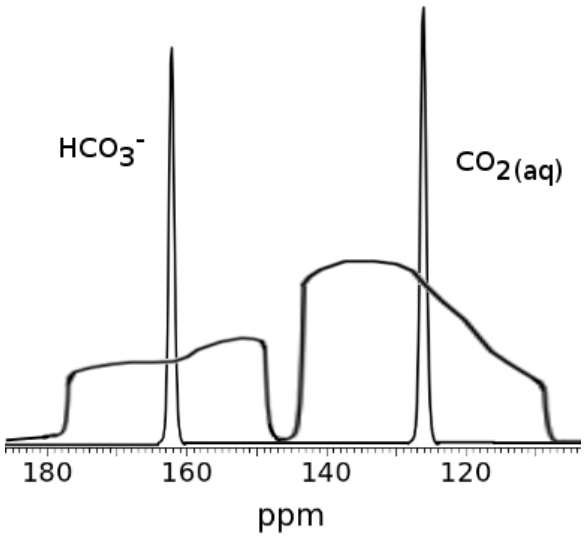

Figure 5.7: A simulation of imaging two NMR signals ($CO_{2(aq)}$ and HCO_3^-) simultaneously in a gradient condition. The narrow lines represent the NMR signals in the absence of a gradient. The broad lines are, ideally, what the image should look like if the gradient strength and number of scans are set correctly. (Data: simulation).

The gradient inhomogeneities due to the mineral/water interface are small (on the order of 1 ppm or 90 Hz) within the sample, thus the gradient strength is strong enough to be able to ignore those effects in the image. It is very convenient that $CO_{2(aq)}$ and HCO_3^- are 35.5 ppm apart.

Once the two signals are obtained, they are carefully mathematically overlapped (they are not visually placed on top of each other) by shifting the HCO_3^- image 3161.5 Hz lower. Once

overlapped, the 0 Hz frequency location is adjusted to the pre-determined location of the top of the sample and then the ratio of the two signals can be obtained spatially across the length of the sample, where 0 Hz is defined as the top. The overlapping process is illustrated in Figure 5.8.

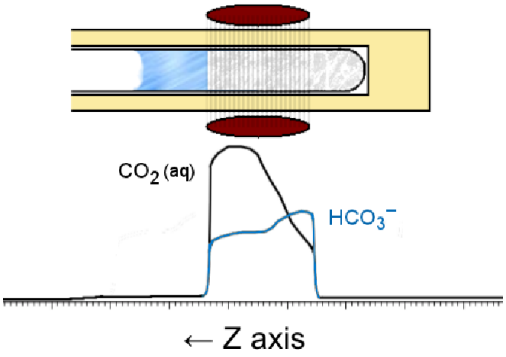

Figure 5.8: A cross section of the high pressure NMR reaction vessel and NMR coil region placed on its side to show how the imaging data correlates to the physical sample. (Data: simulation).

Most of the imaging experiments in this project used a 16-step phase-cycled Hahn echo acquisition with a 100 μs τ value for acquisition of the signal. The probe has a 7 μs deadtime after a pulse, so the echo separates the signal from the ringdown of the probe. As the 90° pulses are typically quite long (18 μs), using an echo allows obtaining the full FID rather than only the portion following the pulse. Proper leftshifting of the echo so that a complete FID is recovered makes an image completely free of first order phase effects. This is very important as first order phase effects can institute error into the imaging measurements, especially if the first order phasing errors affect one peak unequally from the other.

It is also important to note here that spectral distortions in the image that affect both the $CO_{2(aq)}$ and HCO_3^- lines equally do not matter. As the ratio of the $CO_{2(aq)}$ and HCO_3^- signals along the Z-axis are the values being sought, lineshape distortions from B_1 inhomogeneities and magnetic susceptibilities within the sample change the absolute magnitude of the $CO_{2(aq)}$ and

HCO_3^- signals, but not their ratios. This facet of the experiment is particularly nice!

As has already been shown, reaction progress is made evident by strong solid state NMR signals from the solid carbonate products. These signals present themselves weakly at first but grow to be the dominant signals in the sample. The simple pulse-and-acquire imaging experiments are no longer able to image the $CO_{2(aq)}$ and HCO_3^- signals as the carbonate product signal is so prominent and will mix with the images, distorting them. The solution to imaging in the presence of carbonate solid is a pulse sequence that is able to filter out the solid carbonate signal on the basis of its typically longer T_1 values and shorter T_2 values. By shortening the recycle delay to 10-60 s, the solid carbonate NMR signal is truncated because its T_1 is typically in the 1-10 minute range at high temperatures. Extending the echo time of the echo acquisition also selectively kills the solid-state signal because the T_2 of the solid carbonate is so short. A proof-of-concept experiment shown in Figure 5.9 demonstrates how the T_1/T_2 filtering works in a sample that is pressurized with $^{13}CO_2$ (13 bar) and contains ^{13}C-labelled carbonate mineral.

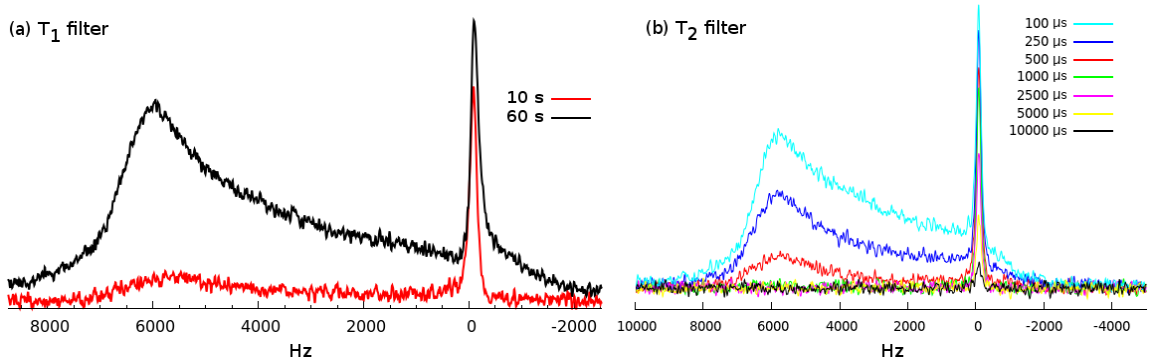

Figure 5.9: $CO_{2(g)}$ pressurized (13 bar) on top of a ^{13}C-labelled Mg-Carbonate sample. Both shortening of the recycle delay (a) and of the echo time in an echo acquisition (b) decreases the magnitude of the solid carbonate signal. (Data: (a) 852c,853; (b) 20120907-T2).

The T_1 of the particular solid carbonate sample in Figure 5.9 is ~20 s (although some ^{13}C-labelled samples can be minutes long) and the T_1 of the $CO_{2(g)}$ is ~0.5 s at 13 bar and 22 °C.

Shortening the recycle delay in Figure 5.9(a) to 10 s severely but not completely decreases the signal. The area of the $CO_{2(g)}$ peak does not appreciably change as the 10 s recycle delay is still $20\times T_1$.

The T_2 value of the $CO_{2(g)}$ should approximately equal its T_1 value of 0.5 s. However, when measured here using a CPMG echo train it is approximately 3.9 ms due to the rapid diffusion of the gas. The T_2 of the carbonate solid is 0.24 ms, much shorter than the $CO_{2(g)}$. When the τ value for the Hahn echo is extended to 1 ms, the carbonate signal is completely gone but the $CO_{2(g)}$ signal is only 76.8% of its original area. The decrease of CO_2 signal here is due to the rapid diffusion of the gas;[44] in solution its diffusion is much slower,[146] so the loss of signal is much less than the 23.2% observed here.

Finally, application of the T_2 filter must be done with the magnetic field gradient off. This means the gradient must be able to be "snapped on" after the T_2 filter has been applied but before signal acquisition. This requirement posed a huge problem because the gradient coil is situated outside of the high pressure probe which contains much metal (copper and brass, see Chapter 2). The fluctuating magnetic field from the gradient pulse generated eddy currents throughout the probe. The eddy currents prevented a stable, linear magnetic field gradient from being established for 25 ms slowing the effective slew rate (rate of rise of the gradient) of the probe. Generally, one wants the slew rate of the gradient to be on the order of a pulse length, and certainly shorter than T_2^* of the NMR signal. 25 ms is well out of the range of the solid signal in the probe (which is okay) but unfortunately also out of the range of the liquid signals as well.

To fix the problem of eddy currents I used a method that has long been in use in the Conradi group and was suggested by Dr. Conradi: Z-storage. The principle of Z-storage is to first do all

the filter/prep pulses on the spins with the gradient off. After the preparatory pulses are over, the spins are returned to the Z-axis of the rotating frame by another pulse (the returning of the spins to the Z-axis is why it is called "Z-storage"). The gradient can be turned on during the Z-storage time, and long after the effects of eddy currents are gone acquisition pulse(s) can be sent to the probe like a normal NMR experiment.[147] This scheme for magnetization storage allows the spin states to have a lifetime on the order of T_1.[148] As only 25 ms (50 ms for the strongest gradient strengths) of storage time was needed, the T_1 lifetime limitation (~1s for $CO_{2(g)}$ and 26 s for $CO_{2(aq)}$ in this system) was considerably more than needed. Figure 5.10 describes the Z-storage imaging pulse sequence.

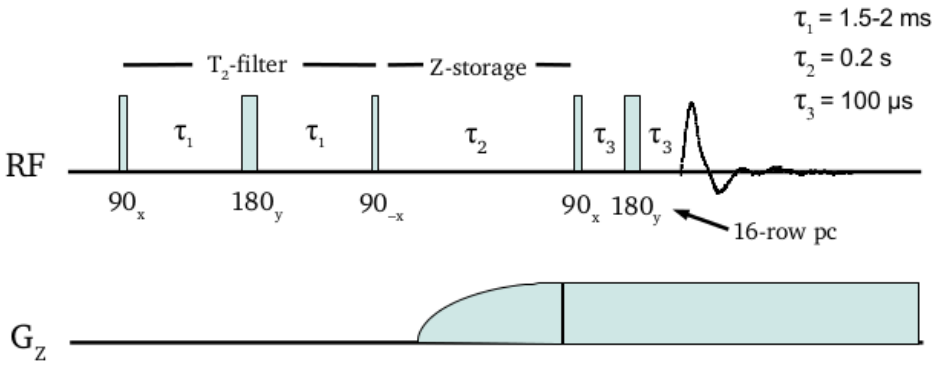

Figure 5.10: Illustration of the Z-storage imaging pulse sequence used for image acquisition. It is a combination of a T_1 and T_2 filter, Z-storage, and Hahn echo readout. The three tau values determine the various properties of the sequence: τ_1 is the T_2 filter time, τ_2 is the Z-storage time, and τ_3 is the echo time for the Hahn echo readout.

The three τ values in Figure 5.10, as well as the recycle delay (not shown) together control the results of the entire pulse sequence. τ_1, the length of time of the T_2 filter, must be long enough to kill the solid carbonate signal. Figure 5.9(b) shows that the T_2 of the solid carbonate powder pattern is on the order of 0.24 ms, so complete removal of the signal could be

accomplished with a 1 ms τ_1 time. In practice I have had to use T_2 filter times as long as 2 ms to completely remove the solid carbonate signal. Some solid carbonate powder patterns have surprisingly long T_2 values (upwards to 0.5-0.75 ms) probably due to the high order of some of the crystals comprising the sample. In truth, the crystal structure's intrinsic ^{13}C-^{13}C distance probably factors into the T_2 values as well (spin diffusion).

The τ_2 value is the time of Z-storage. This needs to be long enough to outlast any eddy currents in the probe. As the eddy currents are dependent on the gradient field strength, the strongest gradient strengths (4 gauss/cm) achievable in this setup require about 50 ms of storage time. In practice I have successfully used 100-200 ms to completely avoid the eddy current problem at all gradient field strengths. But, by experimental validation, any Z-storage time value between 40 – 500 ms produce identical results given similar reaction conditions and T_1 values and accurate pulses.

The τ_3 value is the τ-time of the acquisition echo. An echo must be used to avoid first order phase effects from loss of the early time of the FID due to pulse length and ring down of the probe. The echo must be phase-cycled through a 16-step table to avoid any spurious phase effects of FID bleed-through from the original 90-pulse and effects from pulse imperfections and DC-offset. A 16-step phase-cycled table must be used as anything less (2-step, 4-step, and 8-step, which were all tried) are all inadequate and result in spurious phase effects in the FID. While the T_2-filter and Z-storage pulses were not phase-cycled due to spectrometer limitations, phase cycling them would likely provide additional S/N enhancement as well as eliminate other spurious frequency-dependent phase effects found for certain T_2-filter values at certain frequencies off-resonance. These spurious frequency-dependent phase effects were noticed to be

"dip" and "dampening" effects on the edges of the image lines dependent only on the τ_1 value and relative location of the carrier frequency to the $CO_{2(aq)}$ and HCO_3^- imaging lines. The spurious frequency-dependent phase effects were independent of τ_2 and τ_3 values. To ensure that the images shown here were free of these spurious phase effects, the pulse sequence was tested on neat $CO_{2(g)}$ at high pressures using the same settings that were used during the *in situ* experiments.

c. Quantifying and identifying sources of signal loss in the Z-storage pulse sequence

The Z-storage imaging pulse sequence seen in Figure 5.10 is a very robust pulse sequence. If proper values for the three τ values, 90° pulse length, and recycle delay are selected based on the known parameters of the reaction system, the sequence will effectively filter and image the system very accurately. However, with so many variables to adjust, all of which are important, it is very easy to have some of the variables set wrong and the sequence to not perform as expected. Sometimes the τ_1 value can be too short and solid signal leaks through. The good news is that if this happens, the primary leakage point is another 1500 Hz higher in frequency than the bicarbonate signal, where the portion of the solid carbonate signal powder pattern is strongest. It appears as a "hump" that increases with strength the more inefficient the T_2-filtering step. Because of the way the experiment is setup, small solid carbonate leakage does not cause any issues with the imaging, because the solid carbonate signal does not overlap the HCO_3^- image during minor leaks. In fact, at later reaction times leaks are very difficult to avoid because the number of solid carbonate spins can get up to 100x that of the HCO_3^- and CO_2 spins together. If the filtering is only 99% efficient, the 1% leakage can be visible, but again, not overlapping the

bicarb image unless the leakage is particularly bad. Additionally, if the T_1 filtering step (controlled by the recycle delay) is not working as it should, the leaking solid carbonate signal can appear out of phase with the rest of the spectrum.

One would think that average T_1 recycle delays of 20-60 s and T_2 filtering steps of 1-2 ms would be more than adequate to filter out all solid carbonate signals. Sometimes it is not. Some of the solid carbonate patterns observed *in situ* have T_1 values less than 10 s at 100 °C—which means a recycle delay of 20 s has a filtering efficiency of only 14%. τ_1 times, too, sometimes have to be surprisingly long—in excess of 2.5 ms—to filter out the remaining signal. From reaction to reaction the T_1 and T_2 of the solids can vary considerably. Temperature has been found to be a very large determining factor for T_1 of the solution and solid phase ^{13}C spins, but a direct determination of the relationship of the T_1 values has never been made because of random sample-to-sample variations (probably because of paramagnetic impurity differences from sample to sample). T_2 of the solid seems to vary wildly from sample to sample too, and is probably determined by the local dynamics of the sample based on the crystallization purity and amount of present paramagnetic impurities.

The Z-storage pulse sequence shown in Figure 5.10 is also extremely selective, but it is important to understand *why* it is selective. The fact that there are 5 pulses before the signal is acquired, means the spins that are seen in the acquisition FID are only those that are in the very-RF-homogeneous portion of the coil. RF inhomogeneity and pulse lengths are the two largest source of signal loss in the Z-storage pulse sequence. If the pulses are set correctly, diffusion can never play a role in signal loss in this pulse sequence. However, if the pulse length is not set correctly the pulse will not fully Z-store the spins. Incorrectly Z-stored spins are subject

to signal loss from diffusion when the gradient turns on, and the effect on the signal can be disastrous. It is important to have some order-of-magnitude understanding for the different sources of signal loss in the Z-storage pulse sequence.

First, lets take the cumulative effect of incorrectly-set pulse lengths. Imagine, for example, that the 90-time is off by 1 us (for a 90-time of 18 us). This inaccuracy corresponds to a little over 0.5% signal loss *per pulse*. Over five pulses that are of incorrect lengths, the 0.5% can cumulatively add up and with the addition of RF inhomogeneity and the echo placement shifting due to the different pulse lengths, 5-10% of the signal could be lost by the end of the pulse sequence.

Incorrect pulse lengths do more than change the echoes and magnetization on the XY plane of the rotating frame, they also incorrectly Z-store the spins, as previously mentioned. Essentially, whatever spins are not perfectly returned to the Z-axis before the gradient is turned on will be lost to diffusion or mostly lost to diffusion. For neat $CO_{2(g)}$ at room temperature and 52 bar, the diffusion coefficient is about 1.3×10^{-3} cm^2/s.[44] Using the equation developed by Stejskal-Tanner[149–153] that defines magnetization loss due to diffusion in a magnetic gradient, any spin not returned to the Z-axis in a 1 gauss/cm gradient will have lost 99.7% of its original signal magnitude after a 50 ms z-storage time. The example of neat $CO_{2(g)}$ here is the worst-case scenario in terms of diffusion (CO_2 diffuses much slower in aqueous systems). The diffusion coefficient of $CO_{2(aq)}$ is essentially that of water,[146,154–156] thus water can be used as the approximation for the CO_2 diffusion coefficient at higher temperatures to get an idea of signal loss due to diffusion in the Z-storage sequence. At 100 °C neat water's diffusion coefficient is 8.6×10^{-5} cm^2/s,[157,158] two orders of magnitude smaller than for $CO_{2(g)}$. In this case, 30% of the signal

not correctly Z-stored would be lost during a 50 ms Z-storage time—so diffusion can still play a part in the Z-storage sequence if the experiment does not correctly Z-store the spins.

Loss of $CO_{2(aq)}$ signal due to diffusion in an *in situ* experiment, can be deciphered from other types of signal loss in the changing of the overall $[CO_2]/[HCO_3^-]$ ratio observed in the image data compared to the identical pulse sequence results but without the gradient turned on. This is because bicarbonate has a diffusion coefficient in water that is just over half that of CO_2 in water across a large temperature range.[146,159] This effect has been observed in some imaging data where the spins are allowed to dephase on the X-Y plane too long in the gradient. The CO_2 signal is selectively killed at twice the rate of the HCO_3^- signal.

Experimental results for a the Z-storage sequence with carefully-set pulse lengths, show that the overall efficiency from the Z-storage experiment in neat $CO_{2(g)}$ at 52 bar is 58% with the gradient on and 59% with the gradient off (compared to 90-acquire data at the same conditions). So, little to no signal is lost due to diffusion when the pulse lengths are set. It is all RF-homogeneity. Note that the Stejskal-Tanner equation states that the 100 μs acquisition echo would have less than 0.1% signal loss in a gradient strength of 1 gauss/cm from diffusion. It is experimentally true too: diffusion does not affect the signal strength during the average τ_3 values used here (50-500 us), even in the worse case diffusion scenario (neat $CO_{2(g)}$).

The takeaway message from all of this discussion is that the largest single contributor to signal loss in Z-storage experiments are RF-selectivity (from the RF inhomogeneities of the coil) from all of the multiple pulses. Diffusion does not play a role so long as the pulse lengths are set correctly. The selectivity decreases the linear field-of-view from 2.5 cm (the length of the coil) to 1.5 cm, which, given the cylindrical nature of the coil, is 60% of the volume of the sample within

the coil. You will recall that the reported loss of magnetization difference between a 90-acquire experiment and Z-storage was 58%.

d. Z-storage pulse sequence tests to ensure proper function

Finally, I have found that the best way to make sure the Z-storage pulse sequence is working correctly *in situ* is to always run a 16-step phase cycled Hahn echo sequence with a long τ time (1-2 ms—which kills the solid signal) with the same number of scans as a Z-storage sequence without the gradient turned on. Comparison of the absolute areas of the $CO_{2(aq)}$ and HCO_3^- signals between the Hahn echo and Z-storage sequence should yield an absolute difference in area of no more than 30% signal loss and the $[CO_2]/[HCO_3^-]$ ratios of all three experiments (Hahn echo, Z-storage without gradient, and Z-storage with gradient) should all be, within S/N error, the same. If these two conditions are not met, the pulse lengths or other settings of the pulse sequence are set incorrectly or the probe/spectrometer/gradients are not working correctly.

e. Other imaging methods

There are several other imaging methods that I tried to use to obtain spatial $[CO_2]/[HCO_3^-]$ ratios apart from the solid carbonate signal. They are important to mention here because I think they provide some perspective on how simple yet elegant the Z-storage imaging sequence is. These three techniques in principle should all work just as well as Z-storage imaging but have added difficulties that prevented their successful use. They also were all more complicated than the Z-storage imaging sequence.

First, we considered traditional imaging methods[160] where I made great efforts to increase the slew rate of the gradient shim pulses. Modifying a few parts of the probe showed that the only

way to accomplish removal of most of the eddy currents would have been to remove as much metal as possible from around the sample chamber and move the gradient coil as close to the sample as possible. It was determined that it would not be worth the money and effort to get rid of the necessary amount of metal in the probe to accomplish this feat, namely because most plastics would not have the temperature resilience of the metal and would produce a carbon background that the NMR coil would pick up. The NMR coil itself is also a source of the eddy current—the Alderman-Grant coil design has the metal/ceramic capacitors that tune it to the right frequency *on* the coil as well as large copper strips that form the inductors in the circuit. These large strips and capacitors would still act as partial shielding to the gradient pulse—so increasing the gradient coil proximity to the sample tube still would not get rid of all of the eddy currents without also changing the coil design, which was not an option. This particular coil design is the most efficient, high-performance coil I was able to build of the numerous prototypes tested...so changing it to a less efficient design to get rid of the eddy currents was not an option.

A second method for imaging is using a pulse sequence similar to Frydman et al.'s VACSY (variable-angle correlation spectroscopy in solid-state nuclear magnetic resonance) experiment.[161–163] This experiment would take multiple 1D ^{13}C NMR spectra at different gradient strengths instead of different rotor angles, as in the VACSY experiment. The different 1D spectra would then be projected onto a grid at different angles determined on the basis of the gradient strength. After interpolating the missing data points from the existing ones on the grid, a 2D fourier transform of the dataset would produce a 2D plot whose axes are chemical shift and position (respectively) within the sample. Such an experiment would have essentially obtained different 1D projections along the length of the sample. After a thorough investigation of the

method and working through the mathematics behind VACSY, I decided not to pursue this method for imaging. The primary reason was the amount of time the experiment would take: 5-10x longer than the Z-storage technique as an individual 1D spectrum would have to be obtained for each spatial point in space. In addition, the interpolation reconstruction methods are known to be tricky and often riddled with phase distortion artifacts that can be very difficult to get rid of.[162,163]

Finally, the last imaging option I call "selective inversion imaging" or "spin selection" and involved pulsing the sample such that the $CO_{2(aq)}$ and HCO_3^- ^{13}C peaks would be 180° out of phase and could be stored along the Z-axis in opposite directions (one pointing up and the other down). This selective inversion allowed *just* the narrow solution-phase $CO_{2(aq)}$ and HCO_3^- peaks to be selected for imaging and would allow the solid carbonate signal to dephase and disappear, similar to the T_2 filter discussed above. The difference between this experiment and the Z-storage image sequence is that the $CO_{2(aq)}$ spins and HCO_3^- spins would be Z-stored *with opposite phases.* The opposite phases essentially phase encode the signals allowing for stronger gradients to be used (yes, gradients of strength that actually cause the signals to mix on the frequency spectrum). In the Z-storage imaging sequence, the gradients can never be turned so high that the signals run together, but the signals in the spin selection sequence are phase encoded so it does not matter. If they mix, they can be extracted. So there is no upper bound on resolution with this sequence. But there are bounds to it.

The selective inversion imaging experiment was actually performed extensively on several samples but had poor overall performance due to two major issues. First, the experiment's selectivity is based on chemical shift not T_2, so any solid carbonate spins that had the same

chemical shift as the narrow peaks are selected too and cause amplitude bias in the resulting image...thus it does not work very well for filtering out carbonate solid signal effects directly on the imaged peaks of HCO_3^- and CO_2. Second, it assumes that the $CO_{2(aq)}$ and HCO_3^- spins do not exchange within the time limit of T_1. Unfortunately they do, so signal is lost to the spin exchange phenomenon and disables any quantitative $[CO_2]/[HCO_3^-]$ ratio-determining measurement at high temperatures (where exchange is faster).

C. In situ 1D pH images from ^{13}C NMR

Now that I have worked through most of the important details of the Z-storage imaging sequence, I can now describe and show what the Z-storage imaging sequence can do when used properly. Here I will show and discuss some *in situ* 1D pH images obtained on two different samples: $Mg(OH)_2$ reacted with CO_2 in water at 81 °C and 113 bar; and Mg_2SiO_4 reacted with CO_2 in water at 80 °C and 120 bar. The $Mg(OH)_2$ reaction is the same "long" reaction discussed in Chapter 3. The *in situ* pH images were obtained in the data-gaps (between the points) of Figure 3.10(b). The Mg_2SiO_4 reaction is also the same reaction discussed in Chapter 3. The *ex situ* Raman, pXRD, and MAS NMR results that showed spatial dependence for both reactions should be recalled and compared to these pH images. The results from these analytical methods show that there is carbonate product formation dependence that correlates to the observed *in situ* pH trends. The results demonstrate this correlation inasmuch depth as the imaging method can achieve given NMR coil size, RF-selectivity, and magnetic "sweet-spot" size limitations.

a. $Mg(OH)_2$ reaction

The reaction of CO_2 and $Mg(OH)_2$ is very rapid. Of all of the mineral samples studied, it

forms solid carbonate ^{13}C NMR powder patterns fastest (in 1-2 days time), as described in great detail in Chapter 3. The fast carbonate precipitation actually makes it difficult to obtain a pH image of the sample—not because the solid carbonate powder pattern is in the way (the T_2 filter in the Z-storage imaging takes care of that) but because the carbonate formation blocks the diffusion of more CO_2 and HCO_3^- into the sample. The time needed for signal averaging to bring the S/N of the image to high enough values for quantitative imaging is too long when the signal is too weak.

Figure 5.11 shows two *in situ* ^{13}C NMR spectra obtained by the Z-storage imaging pulse sequence, but one with the gradient off (black) and the other with the gradient on (red). The relatively poor S/N of the image gives some indication of how difficult it can be to measure the $[CO_2]/[HCO_3^-]$ spatially using ^{13}C imaging. The spectrum was attained in 4 h with 320 scans after 356 h (14.8 d) of reaction. Earlier images could likely be obtained if the reaction were a low-water content reaction where the CO_2 dissolution was faster than the mineral dissolution.

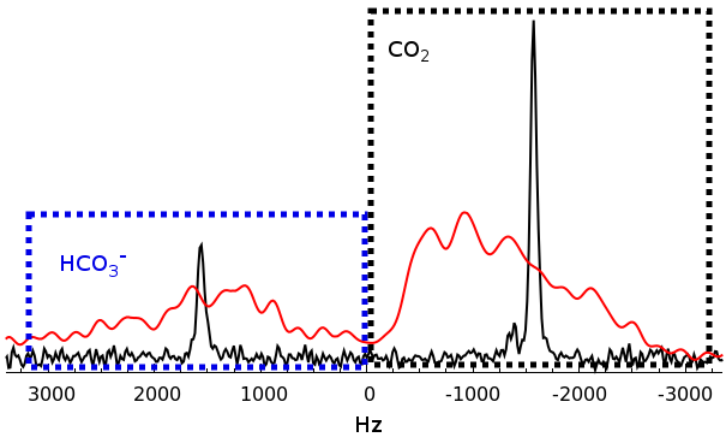

*Figure 5.11: Z-storage experiment without (black spectrum) and with (red spectrum) a Z_1 gradient for imaging the Z-axis profile of the sample. The black dotted box indicates the region of CO_2 ^{13}C spins and the blue dotted box indicates the region of HCO_3^- ^{13}C spins. (Data: 1043*zstorage).*

The dotted boxes in Figure 5.11 indicate the maximum resolution attainable without merging the two NMR signals together. The red image data in the background of the figure shows how the two spatial images of the two spins are separated by their chemical shift. These two signals are mathematically overlapped based on their difference in chemical shift (161.5-126=35.5 ppm), both of which can be seen in the Z-storage experiment without the gradient pulses, shown as the black spectrum. The small sc-CO_2 signal is essentially washed out by the turning on of the gradient in the Z-storage experiment as it is a gas and has a high diffusion coefficient.

Finally, there is a strong solid carbonate signal in the sample at the point the spectrum in Figure 5.11 was taken. To demonstrate how effective the T_1/T_2 filtering is at removing the solid signal for imaging purposes, Figure 5.12 shows a simple 16-step phase cycle Hahn echo acquisition taken just before the Z-storage imaging experiment was acquired (red spectrum). The exact Z-storage experiment, with the gradients turned off, was run as the black spectrum. There is no sign of any solid carbonate signal: the T_1/T_2 filter combination has removed all of it.

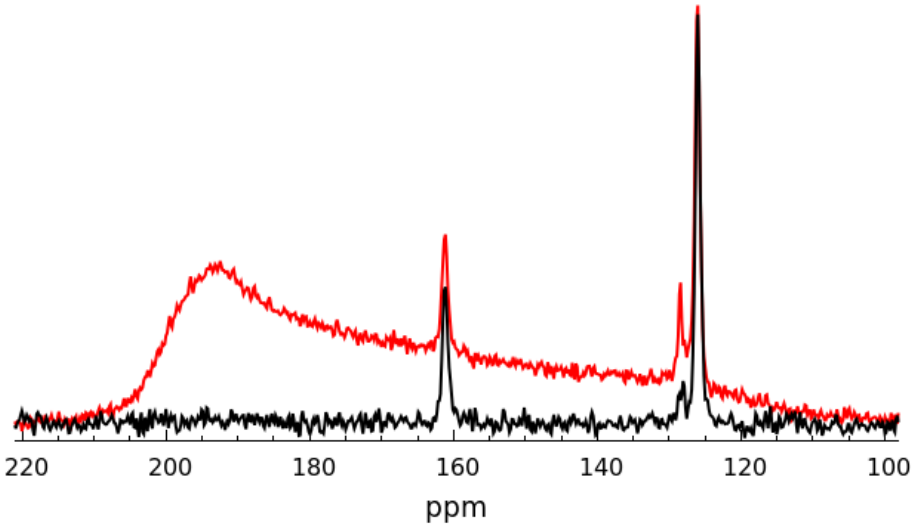

Figure 5.12: The T_1/T_2 filtering turned off (red spectrum) and turned on (black spectrum). It is capable of removing all of the solid carbonate signal so that imaging of the solution signals can be performed. (Data: 1043b, 1043c).

When the gradient is turned on and the two spatial images of $CO_{2(aq)}$ and HCO_3^- from Figure 5.11 are combined, the spectrum looks like Figure 5.13. The $[CO_2]/[HCO_3^-]$ ratio is derived by dividing the height of the CO_2 peak by the height of the HCO_3^- peak at each position along the axis. Figure 5.13 also shows the "waviness" of the image. This waviness is caused by two effects: an oscillation of the magnetic susceptibility throughout the sample due to small density differences and the RF B_1 inhomogeneity caused by the sample. In a single NMR experiment both the CO_2 and HCO_3^- signals have the same oscillations in the same positions with the same phase, indicating that they are not from random noise. They can be smoothed with a boxcar filter which changes each point to the average of itself and its nearby points around each individual point along the distance of the sample without changing the pH data. The existence of this "waviness" does decrease the image's effective resolution to on the order of 0.1 cm.

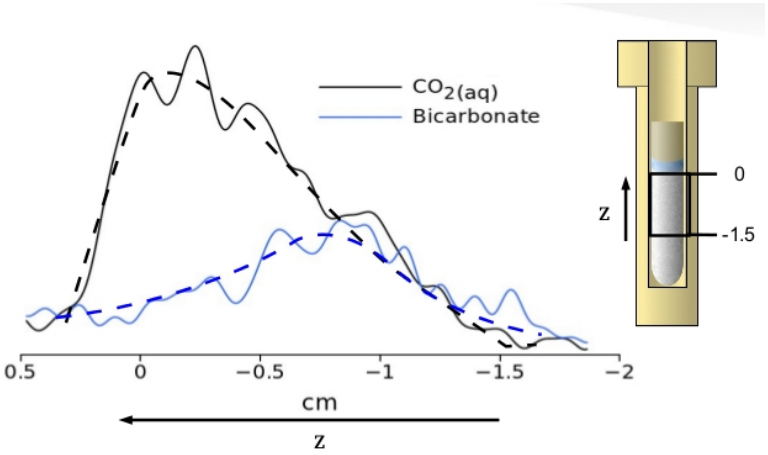

Figure 5.13: Z-storage image of $CO_{2(aq)}$ (black) and HCO_3^- (blue). The x-axis has been converted from Hz to cm. The dashed lines are a guide to the eyes to see the spin density trend. (Data: 1043).

The ratios were taken for each point along the z-axis and, using Equation 4.5, they were converted into spatial pH_m values using K values calculated by SUPCRT92 at 81 °C. In theory it is possible to use the pH model described in Chapter 4 to calculate the real pH at each point across the sample, but that would very computationally intensive and would have to calculate the spatial $[Mg^{2+}]$ values through thousands of computational iterations. It is better, in my opinion, to use the model to calculate a "pH adjustment factor," based on the progression of the reaction and the difference between the average pH_m and pH values across the entire sample. The adjustment factor should, according to calculations from Chapter 4, get the measurement within 0.1-0.2 pH unit accuracy across the imaged length of the sample. If higher precision is needed than that, the heavy computational approach would need to be used to calculate spatial $[Mg^{2+}]$ for the length of the tube. The pH adjustment factor here is about -.35 pH units.

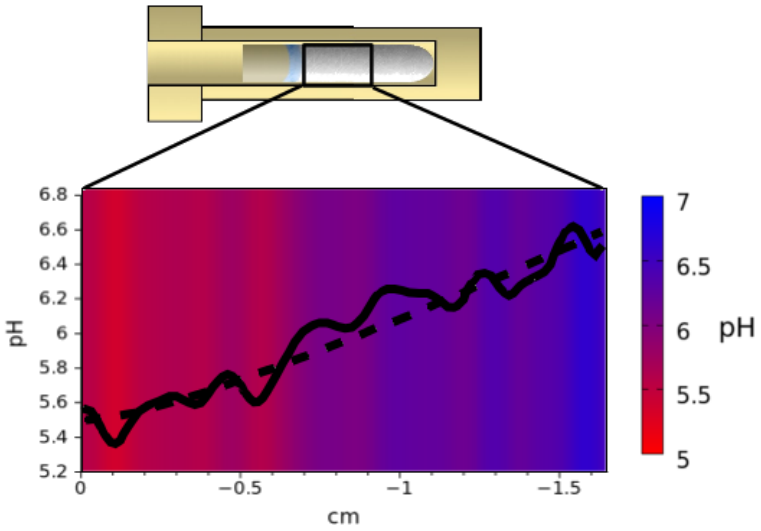

*Figure 5.14: 1D pH image of $Mg(OH)_2$ reaction with CO_2 after 356 h. The dotted line is a guide to the eyes. (Data: 1043h*zstorage).*

Figure 5.14 shows the pH image of the sample. The pH values have also been heatmapped into the background of the graph to give a better visual sense of how the pH changes throughout the sample. The "bands" in the heatmap are from the susceptibility oscillations just described. The first 1.5 cm of the sample show a pH gradient that is approximately 1 pH unit in magnitude. Presumably, the pH keeps rising at greater distances into the sample beyond what the imaging technique is able to detect.

Furthermore, the *ex situ* analysis of this reaction from Chapter 3 revealed that the reaction of CO_2 and $Mg(OH)_2$ form a gradient of carbonate products. $MgCO_3$ is the dominant product at the top of the mineral slurry, with $4MgCO_3{\cdot}Mg(OH)_2{\cdot}5H_2O$ (hydromagnesite) at the middle, and $4MgCO_3{\cdot}Mg(OH)_2{\cdot}6\text{-}8H_2O$ (dypingite) at the bottom. The spatial trend had been confirmed with *ex situ* pXRD, Raman, and ^{13}C MAS NMR, and presumed to exist because of a pH gradient. Figure 5.14 confirms the existence of this gradient but also confirms details on the reaction mechanism in that the spatial products measured through *ex situ* techniques do not necessarily correlate with the measured pH image.

$MgCO_3$, for instance, cannot precipitate at low pH values (this will be discussed further in the next section).[116] Yet, the pH measured at the top of the reaction tube where the $MgCO_3$ is found to precipitate is low. An explanation for this seeming disagreement is that the gradient recorded in the image indicates progress of reaction. That is, as the $Mg(OH)_2$ mineral is so fast to react with the CO_2 it forms $MgCO_3$ through the known metastable intermediates (dypingite ($4MgCO_3 \cdot Mg(OH)_2 \cdot 6\text{-}8H_2O$) → hydromagnesite ($4MgCO_3 \cdot Mg(OH)_2 \cdot 5H_2O$) → magnesite ($MgCO_3$)), and once the final product forms, the pH drops. *Ex situ* evidence indicates that the top layer of the mineral is completely reacted (there is no detectable $Mg(OH)_2$ remaining) and the pH image data supports this observation. Once the mineral is completely reacted, the pH drops. The only way to confirm this is to obtain a pH image at earlier times within the $Mg(OH)_2$ reaction with CO_2...But that has not been possible to date because the $Mg(OH)_2$ mineral is so fast to react that there is very little $CO_{2(aq)}$ and HCO_3^- signal to image, until the reaction has progressed for a considerable amount of time.

b. Mg_2SiO_4 reaction

The Mg_2SiO_4 set of imaging experiments was performed on the reaction of water-saturated Mg_2SiO_4 with CO_2 at 80 °C and 120 bar. As Mg_2SiO_4 reacts with CO_2 slower than $Mg(OH)_2$, the CO_2 does more diffusing through the sample than reacting at early reaction times, increasing the observed solution signal at earlier reaction times allowing an image to be obtained as early as a few hours into the experiment. Additionally, as there is no solid carbonate formation early in the reaction, the Z-storage imaging sequence is not needed to filter it out. So another way to enable imaging experiments earlier in the experiment is to use a 16-step phase cycled Hahn echo in the presence of a static gradient to acquire the images. The Hahn echo has less RF-selectivity than

the Z-storage pulse sequence and results in more overall signal (Hahn echoes have 86% signal efficiency in this coil compared to the 58% efficiency already discussed for the Z-storage sequence—the difference is 2-pulse selectivity versus 5-pulse selectivity). Thus increased solution signal and choosing a less RF-selective experiment enables imaging at earlier times within the sample. Here I will show and discuss images attained at 20.1 h, 47.8 h, 125.2 h, and 392 h (Figure 5.15a-d). Finally, as mentioned in the introduction to this section, this particular Mg_2SiO_4 reaction is the same long Mg_2SiO_4 reaction (R20) discussed in Chapter 3—so comparison of the average $[CO_2]/[HCO_3^-]$ ratios with time shown in Figure 3.18 is helpful to develop a better understanding of how these reactions work. Additionally, while R14 (discussed in Chapter 3) was run at different conditions for a different amount of time, the *ex situ* spatial data shown in Figure 3.22 are helpful to compare to the pH imaging data discussed here.

Figure 5.15 (a) and (b) were acquired using a 16-step phase cycled Hahn echo pulse sequence in the presence of a static gradient with a recycle delay of (a) 10 s and (b) 20 s (all solution species had T_1's less than 2 s) in 512 scans. (c) and (d) were acquired using the Z-storage imaging pulse sequence. (c) was acquired using τ_1= 1500 μs, τ_2= 500 ms, and τ_3= 100 μs with a 60 s recycle delay (the T_1's of the solution species had increased to about 10 s). (d) was acquired using τ_1= 2000 μs, τ_2= 100 ms, and τ_3= 100 μs also with a 60 s recycle delay. The τ_1 time had to be lengthened between (c) and (d) because of solid carbonate signal leakage. As the recycle delays in both (c) and (d) were long to compensate for the lengthened T_1's of the solution phase species, the T_2 filter (controlled by τ_1) had to be used to compensate for decreased T_1 filtering.

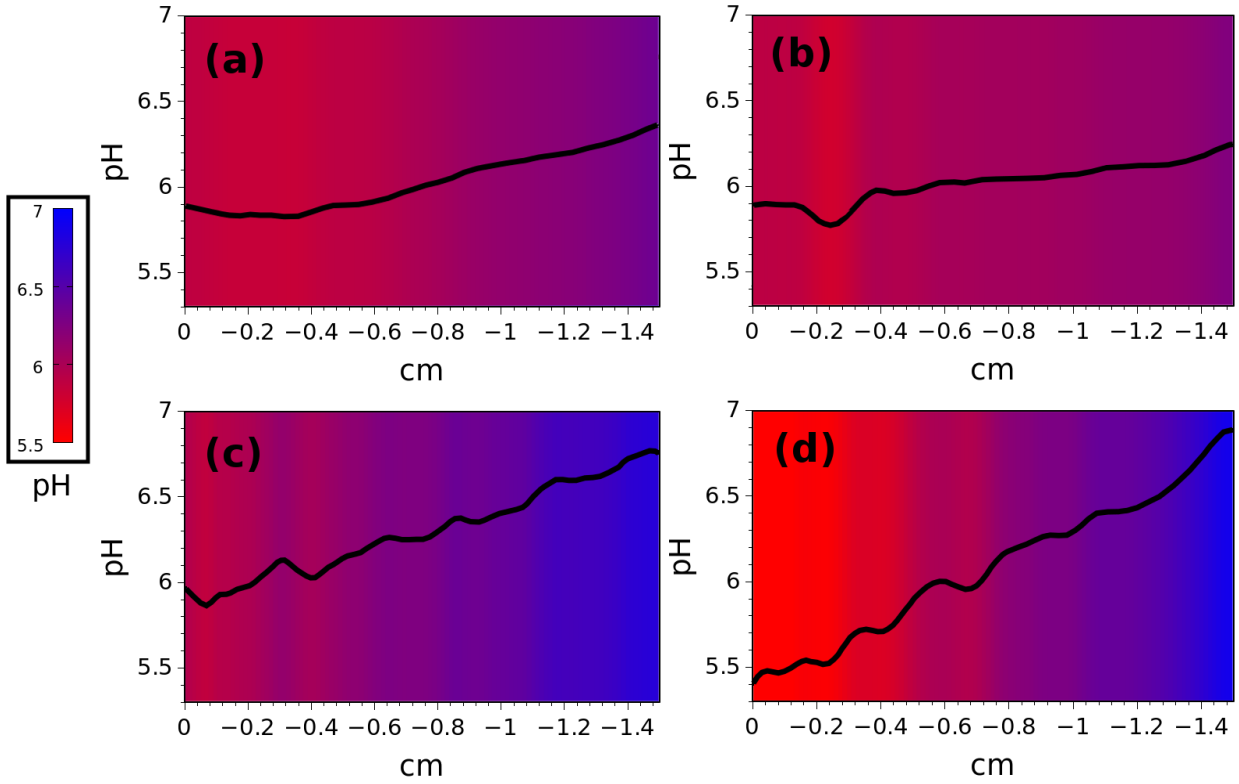

Figure 5.15: Four pH images acquired at (a) 20.2 h, (b) 47.8 h, (c) 125.2 h, and (d) 392.0 h. (a) and (b) were acquired using a less RF-selective 16-step phase cycled Hahn echo pulse sequence. (c) and (d) were acquired using the Z-storage imaging technique. All were smoothed with a 100 Hz (0.09 cm) boxcar filter. The gradient strength for all four images was 1124.8 Hz/cm (1.05 gauss/cm). (Data: 1152, 1162, 1186, 1234).

In Figure 5.15 (a), 20.2 h into the reaction, the CO_2 has already infiltrated most of the mineral but the "slug" of CO_2 that Figure 3.18 indicates entered the mineral appears to be "backing up" at the top of the mineral. By 47.2 h (b) the "backed up" CO_2 signal has mostly dissipated, leaving just a small area of decreased pH but having lowered the pH of deeper parts of the sample. (a) and (b) appear to be dominated by the dissolution process, where the major changes in the system are due to the dissolution physics of CO_2. By 125.2 h, the dissolution of the Mg_2SiO_4 mineral and precipitation of solid carbonates appear to have taken over controlling the progress of the reaction. A pH gradient has begun to form across the sample and the overall pH across the

sample has been increased (due to mineral dissolution). Also, other NMR experiments indicate that solid carbonates had already begun to form by 125.2 h, but as the pH is still rising in the sample the overall dominating reaction must still be dissolution of the Mg_2SiO_4 mineral. By 392.0 h, the gradient has increased in magnitude and the top portion of the mineral shows a large decrease in pH. Presumably the carbonate mineral precipitation has begun to control the progress of the reaction. Figure 3.22 indicates that the most solid carbonate formation happened at -1.5 cm into the sample. As the carbonate precipitation occurred in the layers between -0.5 and -1.5, the pH in that region would begin to drop. But the pH at the very top of the tube should drop even more as more CO_2 dissolve into the solution to replace that which was consumed making solid carbonates.

The extreme pH oscillations and gradients of this reaction indicate that pH at the top of the mineral is always held to a much lower value than the rest of the sample, which should inhibit formation of any carbonate mineral. Detailed *ex situ* analysis from R14, discussed in Chapter 3, also indicate that this is the case. It is well known that $MgCO_3$ only forms at higher pH values.[104,164–166] In fact, the ideal pH value for $MgCO_3$ precipitation is in the high 7's of the pH range and at pH values below ~6.5 magnesite is very slow to precipitate (both at P_{CO2} values in the 50-100 bar range), if at all.[116] Additionally, Figure 3.22 also shows a decrease in magnesite formation at values deeper than -1.5 cm (outside of the imaging region). The decrease is less likely due to pH gradients again, as the pH at the bottom of the tube should be very high due to Mg_2SiO_4 dissolution. The decrease is probably due to an inability to get CO_2 through the powdered mineral and carbonate precipitate making the CO_3^{2-} the limiting reagent in $MgCO_3$ precipitation at lower portions of the tube. Thus, a tapering off of $MgCO_3$ product in the bottom

of the tube is not due to pH limitations—it is most likely due to limited bicarbonate and carbonate for precipitation.

The gradient in Figure 5.15(d) has a magnitude of nearly 1.5 pH units across a very short distance (1.5 cm). In the interest of being thorough I have included the raw NMR data for this gradient so that the reader can see what the NMR data behind the pH image looks like.

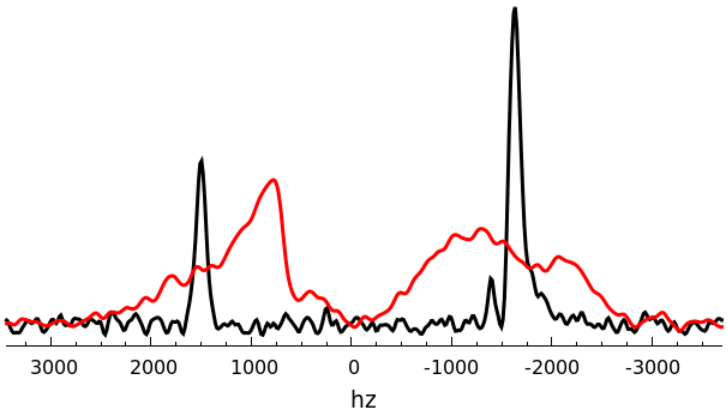

Figure 5.16: ^{13}C in situ NMR from the Z-storage pulse sequence with gradient off (black) and gradient on (red). The individual concentration gradients of $[CO_2]$ and $[HCO_3^-]$ can be clearly seen in the red data, where the gradient is turned on. Note that the imaged data was acquired in more scans so that the S/N would be the same as the spectrum with the gradient off. Also, recall that for each lineshape, higher frequency is higher on the Z-axis. (Data: 1233,1234).

Using the method already described, the $[CO_2]$ and $[HCO_3^-]$ values along the Z-axis are extracted from the NMR data and the X-axis is converted from Hz to cm using the gradient strength. For the NMR imaging data shown in Figures 5.15(d) and 5.16, the relative $[CO_2]$ and $[HCO_3^-]$ values are shown, form which the $[CO_2]/[HCO_3^-]$ ratios are extracted.

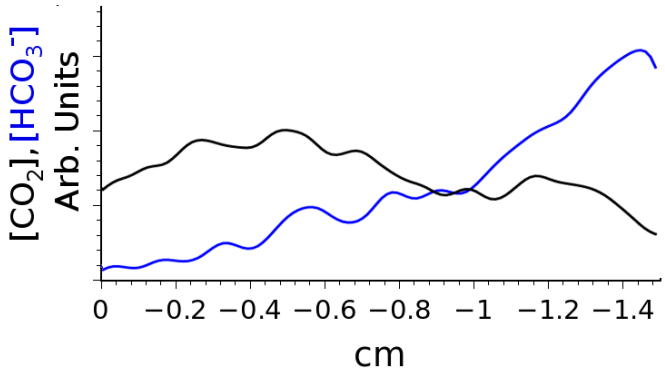

Figure 5.17: The spatial [CO_2] (black) and [HCO_3^-] (blue) values extracted from the image in Figure 5.16. The CO_2 is clearly the dominating signal at the top of the tube, while bicarb is the dominating signal at the bottom.

The oscillations seen in Figure 5.17 are from the RF field inhomogeneities. Both images have oscillations in approximately in the same location. For the most part, the oscillations cancel each other out as it is the ratio of the two lines that is extracted from this data to calculate pH. RF field inhomogeneities and other lineshape effects do not affect the pH image so long as both the CO_2 and HCO_3^- images are both equally affected.

D. Conclusions

Here I have shown the development and application of a new technique, high pressure and temperature ^{13}C NMR imaging. A new pulse sequence was developed to accomplish both spectral filtering and imaging in the presence of large eddy currents and free of the effects of diffusion. In addition I have shown and discussed the pH images that were measured on two different reactions of CO_2 with $Mg(OH)_2$ and Mg_2SiO_4. The images have been shown to record large pH gradients that were predicted based on *ex situ* observations of previous reactions. The pH images obtained also have been correlated to *ex situ* observations to show that the pH images have practical application in predicting what solid carbonates will form, where they will form in

the sample, and the method by which they form.

The practical applications of these experiments are that during the reaction of CO_2 with solid minerals in an aqueous solution very large pH gradients form. These pH gradients can indicate both the progress of the reaction (as shown in the case of the $Mg(OH)_2$ reaction), as well as where the products will form (as shown in the case of the Mg_2SiO_4 reaction). Overall, these pH measurements will be a valuable resource to the community of scientists who are trying to understand and model the spatial aspects of high pressure and temperature CO_2 reactions with minerals in water. The chemistry of the molecules and the physics of their interaction with the multiple phases present in the samples make for a very difficult reaction to understand and predict the formed products.

Chapter 6: Synthesis and characterization of metastable hydroxy-hydrated magnesium carbonates

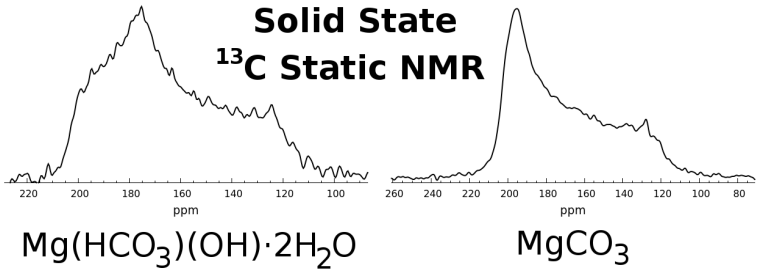

Figure 6.1: Solid state static ^{13}C NMR can differentiate between different magnesium carbonate solids based on the shape of the powder pattern. (Data: JS7-2, R12).

A. Introduction

The experiments described in this chapter aim to develop an analytical methodology for quantitative analysis of magnesium-containing carbonates using ^{13}C NMR. As has been shown in Chapter 3, many of the carbonation reactions produce *mixtures* of magnesium carbonates. In principle these mixtures could be quantitatively elucidated using ^{13}C NMR, but to do so requires a detailed spectroscopic knowledge of the pure components of the mixture. A great deal of work has been published on solid state ^{13}C NMR of metal carbonates,[51,54,55,167,168] some of which includes specifically the magnesium carbonate species discussed here.[24,25,167] However, there is little agreement on specific chemical shift values, relative peak areas, and even in some cases, the number of peaks. The differences are likely due to purity of the carbonate samples that were analyzed by the different research groups and varying NMR experiment parameters or methods. Additionally, most of the literature published on the subject neither include static ^{13}C NMR lineshapes [50,52,169] nor relaxation properties of the carbonates—two critical pieces of information

needed to identify carbonate products *in situ* and to measure mixtures of carbonate products quantitatively *ex situ*.

Therefore, this chapter will discuss the synthesis methods we developed to make the pure versions of four target magnesium-containing carbonate phases. This chapter will also discuss the subsequent analysis of these pure phases in detail using Raman, pXRD, and ^{13}C NMR to confirm the purity and identity of the phases. Finally, a complete solid state ^{13}C NMR workup including T_1 relaxation data, CP-MAS (cross polarization during magic angle spinning) data, chemical shifts, and quantitative peak areas and linewidths will be shown for these phases so that their identification can be unambiguously achieved exclusively with ^{13}C NMR alone in the future.

a. Origin of metastable hydroxy-hydrated magnesium carbonates

When CO_2 reacts with different magnesium-containing minerals it can form one or more of several Mg-containing hydroxy-hydrated carbonate mineral products even though $MgCO_3$ is by far the most thermodynamically stable magnesium-containing carbonate.[30,164] The reasons these other carbonates form is because of the small size of the Mg^{2+} ion. Magnesium's small size and high charge leads to a high charge density which, in turn, attracts the dipole moment of water molecules quite strongly. The water molecules form two very tight layers of hydration around the ion, effectively protecting it from reacting with anything in solution unless something is able to remove some of the waters.[170,171]

The waters of hydration make it more energetically favorable to precipitate magnesium carbonate minerals that contain H_2O (hence the term, hydrated) and/or OH's (hence the term, hydroxy-hydrated) than to form anhydrous $MgCO_3$. These hydroxy-hydrated magnesium

carbonates that form are “kinetically trapped” on the thermodynamically-favorable reaction pathway to $MgCO_3$. Their kinetically trapped states can be stable for a very, very long time, given that enough energy to eject water from its crystal structure and the kinetic route to be able to do it are never available. But because they are not the most stable form and can readily convert given the right conditions, they have been given the name “metastable magnesium carbonates”.[164]

In the reaction systems discussed here (> 25 °C and 50-120 bar), the kinetically favorable metastable magnesium carbonates are nesquehonite [$Mg(OH)(HCO_3)\cdot 2H_2O$],[172,173] dypingite [$4MgCO_3\cdot Mg(OH)_2\cdot 5\text{-}8H_2O$],[36,106,107] and hydromagnesite [$4MgCO_3\cdot Mg(OH)_2\cdot 4H_2O$],[174–176] listed in decreasing order of hydration. These minerals have been well characterized via Raman[31,34,36,177] and pXRD[106,178–180] and all, with the exception of dypingite, have known crystal structures. They are also known to convert into one another from more hydrated states (nesquehonite) to less hydrated states (hydromagnesite) or from hydromagnesite to magnesite, the dehydrated form.[31,102,104,181]

The specific magnesium carbonate formed in a sequestration reaction is dependent on the conditions of the sample such as pressure, temperature, and local ionic strength of the solution.[30,57,64,105,115,182] In general, nesquehonite is known to form as the predominant magnesium carbonate in any solution with high concentrations of Mg^{2+} and high HCO_3^- and CO_3^{2-} at temperatures less than 40 °C.[30] At temperatures higher than 40 °C, dypingite and hydromagnesite are the preferred products.[57,104,105] In general, anhydrous $MgCO_3$ will not form directly (that is, without first forming hydromagnesite then converting to $MgCO_3$) at temperatures below 120 °C and elevated CO_2 pressures (>100 bar, meaning high carbon concentration in solution).[30,166] The

carbonate products are also dependent on the reactant mineral (as has been demonstrated in Chapter 3) and the presence of other ions in the solution.[57,114,116]

b. Static ^{13}C NMR of solid carbonates

As I showed in Chapter 3, static *in situ* ^{13}C NMR data of a solid metal carbonate produces broad chemical shift anisotropy (CSA) "powder patterns" that possess a unique shape for each unique metal carbonate. Typically the lineshapes are very different from carbonate to carbonate, as in the case of the magnesium carbonate "nesquehonite" and the magnesium carbonate "magnesite," pictured at the beginning of this chapter in Figure 6.1. At other times, lineshapes can be very similar if the two carbonates have similar electronic environments around the carbons.

The static ^{13}C NMR signals of the solid carbonates are broad because the ^{13}C atoms are locked into a crystalline structure of other atoms and unable to experience isotropic motion. Isotropic motion is why liquid and gas NMR resonances are narrow: rapid isotropic motion averages the chemical shielding (shielding of the magnetic field by the local electronic environment) around each individual carbon spin. Shielding arises from the electrons in the molecular orbitals circulating around the nucleus (being stimulated by the field of the NMR magnet) generating another small magnetic field called the "induced field." This induced field alters slightly the strong magnetic field from the NMR magnet and results in a slight deviation around the nucleus, changing the net local magnetic field that the nucleus "feels" and thus its observed chemical shift. The shielding effect is typically very small compared to the magnetic field strength ($\sim 10^{-4} \cdot B_0$) and is measured in units of ppm, "parts per million," relative to another reference nucleus (chemical shift, δ, where increasing δ means less shielding) or relative to the

frequency that a "bare" nucleus would have in that magnetic field (called chemical shielding, σ, where increasing σ means increased shielding), free of any electronic perturbation. Here I use the chemical shift convention (δ) describing the location of resonances in an NMR spectrum.

Chemical shift is a three-dimensional effect on the nucleus which is typically described using a 3×3 matrix called the chemical shift tensor. The chemical shift that the nucleus experiences is dependent on orientation of the nucleus and tensor with respect to the magnetic field. Isotropic motion, as in a liquid, averages the chemical shift to one specific value for each magnetically inequivalent carbon (magnetic equivalence is defined as any two spins not related by translation or inversion symmetry operations[183]). This average chemical shift on each magnetically inequivalent spin is called, "isotropic chemical shift." However, in the absence of isotropic motion (such as in a crystalline solid), each carbon will experience a chemical shift based on its individual orientation with the magnetic field and its chemical shift tensor. The carbons in a given amount of solid crystalline powder will have an array of orientations, some orientations being more statistically likely than others, meaning that each magnetically inequivalent carbon will have an array of interactions with the magnetic field. Thus, the "spread" of chemical shifts in a powder pattern is controlled by the properties of the chemical shift tensor, and the height at each location in the powder pattern is determined by the number of spins at each orientation that produces that specific chemical shift.

There is a mathematical convention to describing the "spread" of chemical shift values for a powder pattern as well as some other notable line characteristics. The mathematical convention is based on defining three principal axes X, Y, and Z for each magnetically inequivalent carbon. These axes are orthogonal to each other and are defined where the magnetic field is parallel to

the induced magnetic field on the nucleus from the chemical shift tensor. Each nucleus has its own three unique axes upon which its chemical shift tensor is based. When one of the three principal axes is lined up with the magnetic field, it produces a so-called "principal value" chemical shift, based on the fact that the B_0 field is aligned with the induced field. These principal values are called δ_{XX}, δ_{YY}, and δ_{ZZ} and the components along the diagonal of the the 3×3 chemical shift tensor (the other off-diagonal tensor elements are equal to zero).

This discussion now leads us to the mathematical formulation of isotropic chemical shift (δ^{iso}, Equation 6.1), chemical shift anisotropy (δ^{aniso}, Equation 6.2), and biaxiality (η, Equation 6.3)—the three components that define the shape of a solid state NMR powder pattern of a spin ½ nucleus (like ^{13}C).

$$\delta^{iso} = \frac{1}{3}(\delta_{XX} + \delta_{YY} + \delta_{ZZ}) \qquad (6.1)$$

$$\delta^{aniso} = \delta_{ZZ} - \delta^{iso} \qquad (6.2)$$

$$\eta = \frac{\delta_{YY} - \delta_{XX}}{\delta^{aniso}} \qquad (6.3)$$

Note that the biaxiality, η, by definition will be a value between 0 and 1. Also, the values of δ_{XX}, δ_{YY}, and δ_{ZZ} correspond to characteristic positions in the lineshape of the pattern (see Figure 6.2). They are assigned to their positions based on their proximity to the isotropic chemical shift, δ^{iso}, Equation 6.4:

$$|\delta_{ZZ} - \delta^{iso}| \geq |\delta_{XX} - \delta^{iso}| \geq |\delta_{YY} - \delta^{iso}| \qquad (6.4)$$

In other words, Equation 6.4 states that δ_{ZZ} is always the farthest away from δ^{iso}, which is just the center of mass of pattern (Figure 6.2).

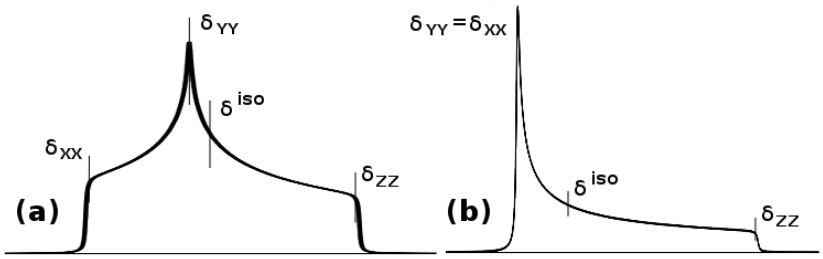

Figure 6.2: Simulated powder patterns of two different kinds of carbonates. (a) has a biaxiality of 0.7 while (b) has a biaxiality of 0.0. (Data: simulation).

Figure 6.2 pictorially illustrates the different properties of the powder pattern. Some important notes about the values are that biaxiality, η, is *never* negative. If δ_{YY} were to flip to the other side of δ^{iso} in (a), the anisotropy δ^{aniso} would change sign, not the biaxiality. Here the anisotropies of both patterns are negative by convention of Equation 6.2. Patterns with $\eta = 0$, like (b) in Figure 6.2, are called "axially symmetric" (like the D_{3h} symmetry of the isolated CO_3^{2-} anion) or uniaxial patterns because the tensor is symmetric at all orthogonal angles with respect to the principal Z-axis. In cases where $\eta = 1$, these patterns are called biaxial patterns and the δ_{ZZ} and δ_{XX} values cannot be unambiguously assigned. Patterns ranging between $\eta = 0$ and $\eta = 1$ are all called "axially assymetric" because none of their principal values are equal (the chemical shift tensor is different in every three dimensional direction).

Metal carbonates almost always have $\eta < 0.5$, meaning that they are all nearly uniaxial. This is because the CO_3 in the carbonate structure is trigonal planar. The Z-principal axis of the ^{13}C chemical shift tensor runs perpendicular to the plane of the C-O bonds of the carbonate. In cases where there is nothing to perturb the symmetry of the X and Y axes, patterns are axially symmetric. However, when perturbation does occur of the X and Y principal axes, the biaxiality increases to a non-zero number. Typical perturbations of the X and Y principal axes are

associations of hydrogens with the oxygens on the carbonate structure, such as hydrogen bonding. Take the case of Figure 6.1, for instance, where I compare the powder patterns of nesquehonite [$Mg(HCO_3)(OH)\cdot 2H_2O$] and magnesite ($MgCO_3$). Nesquehonite has a hydrogen associated with the carbonate structure, making it asymmetric and no longer uniaxial. $MgCO_3$, on the other hand, *should** have no hydrogens in it and therefore is totally symmetric, or uniaxial. (*In practice this is not true. See the section on $MgCO_3$ of this chapter).

Here I will describe the synthesis and characterization of each of the metastable hydroxy-hydrated magnesium carbonate minerals in the reactions we have studied thus far. They have been synthesized in their pure versions by various students that have worked with me in my time at Washington University, including Allison Brenner, Louis Wang, John Beach, and Yanzhe Zhu (see acknowledgements at the beginning of this thesis).

B. Nesquehonite, $Mg(HCO_3)(OH)\cdot 2H_2O$

Nesquehonite, known as $Mg(HCO_3)(OH)\cdot 2H_2O$ or $MgCO_3\cdot 3H_2O$, has been reproducibly made through many different synthetic methods.[173,184] While it does not form at the high temperatures of the *in situ* reactions discussed in Chapter 3 (the temperature is too high for its formation), it can form in the products *after* the reaction is completed if it is allowed to sit wet at room temperature. Nesquehonite occurs in pretty, needle-like crystals (elongated habits), and they typically form pointed in multiple directions around a sphere—much like a person with a "bad hair day." Nesquehonite's crystals are very easy to recognize under a microscope.[31,173] Finally it important to note that all of the several published nesuqhonite crystal structures[178,185] (amcsd 0009432, 0014644) agree on its structure. It is a member of the $P2_1/n$ space group and

has one crystallographically unique carbon. Crystallographically unique atoms are magnetically inequivalent as the rule for crystallographically unique atoms is that they cannot be related by translation or inversion symmetry operations. This means the ^{13}C MAS NMR spectrum of nesquehonite should have one isotropic chemical shift.

a. Synthesis

Two different samples of nesquehonite were made. The first, Sample A, was made by by adding 0.1555 g of 99% ^{13}C-labelled $NaHCO_3$ to a pre-made solution of 0.1889 g $MgCl_2$ in 2.15 mL of DI water. As $MgCl_2$ exothermically dissolves, the mixture of $MgCl_2$ and DI water was allowed to cool for at least 10 minutes before mixing so that the solution was at room temperature (21 °C) when the $NaHCO_{3(s)}$ was added. After the $NaHCO_3$ was added to the solution, it was stirred for one minute then allowed to sit for 3 days at room temperature in a sealed glass beaker. After that time, it was filtered and placed in a vacuum oven overnight at room temperature. The product crystals were lightly ground with a mortar and pestle before being loaded into a MAS NMR rotor and then a pXRD slide for pXRD and Raman analysis.

The second sample, Sample B, was designed to be a highly pure sample of nesquehonite by minimizing the Na in the reaction and with multiple washings to get rid of excess NaCl by-product. It was made by mixing 0.1456 g of 99% ^{13}C-labelled $NaHCO_3$ with a pre-made room temperature solution of 0.164 g of $MgCl_2$ in 3.25 mL of DI water. After mixing the $NaHCO_3$ while stirring the solution for one minute, the sample was allowed to sit for three days at room temperature in a sealed glass beaker. After that time, it was filtered and put into a vacuum oven at 40 °C for 10 minutes. The powder was then allowed to air dry overnight. It was then re-rinsed with DI water and filtered and replaced in the vacuum oven at 40 °C for ten more

minutes and allowed to air dry overnight.

b. Analysis

One day after drying, Sample A was analyzed via ^{13}C MAS NMR. As expected from the crystal structure there was a single ^{13}C peak representing the one magnetically inequivalent carbon (Figure 6.3a). However, after 2 weeks of sitting in the rotor at room temperature, the ^{13}C MAS NMR spectra was obtained again and there was a second peak that had appeared in the spectrum (Figure 6.3a).

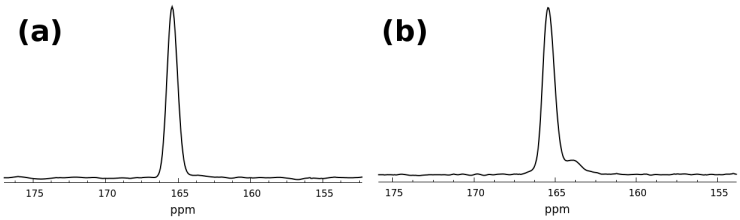

Figure 6.3: $^{13}C\{^{1}H\}$ MAS NMR of Sample A at v_r=5 kHz (a) 1 day after synthesis and (b) two weeks after synthesis. The nesquehonite peak in both (a) and (b) is 165.41 ppm. The second peak in (b) is located at 164.01 ppm. (Data:ALB19 20130213; (b) 201303328).

The ^{13}C T_1 relaxation time constants was measured using a saturation recovery T_1 sequence. The T_1 of the nesquehonite peak at 165.4 ppm was 32.8 +/- 0.5 s and the T_1 of the second ^{13}C peak at 164.0 ppm was 87.5 +/- 5.3 s. The large difference between their T_1 values indicate a large difference in crystalline properties and that the second carbon is probably an additional crystalline phase and not part of the nesquehonite crystal structure.

The sample was unpacked and loaded onto a glass slide for Raman spectroscopic analysis. The Raman spectrum showed that there was a second stretch at 1114 cm^{-1} (Figure 6.4, appears as a shoulder on the dominant nesquehonite stretch):

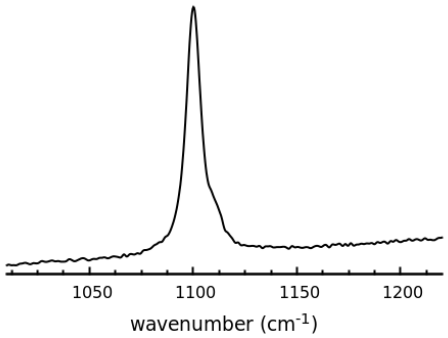

Figure 6.4: Raman of the nesquehonite crystals (Sample A) with an additional phase. The strong peak at 1100 cm^{-1} is the CO_3 symmetric stretch for nesquehonite, and the peak at 1114 cm^{-1} is from the additional carbonate phase. (Data: ALB19 02273013).

The new stretch at 1114 cm^{-1} corresponds is in the CO_3 symmetric stretch region, agreeing with the ^{13}C NMR data that the new phase is probably an additional carbonate phase. The close proximity of the new phase's ^{13}C NMR peak to the nesquehonite ^{13}C NMR peak and the close proximity of its Raman symmetric stretch suggest that the phase is an additional carbonate phase. Other asymmetric stretches in the Raman spectrum were not analyzed as the ^{13}C-labelling adjusts their positions from reference values. The sample was then loaded onto pXRD slide for diffraction analysis.

The pXRD experiment confirmed the presence of nesquehonite, although it was preferentially oriented (excessive grinding for pXRD preparation was avoided as it was originally thought that this grinding could contribute to a phase change of the nesquehonite—although we have never found any evidence for this effect since these experiments). The mineral halite, or NaCl, was also found to be present in the sample as a by-product of the synthesis. All of the remaining peaks matched that of a rare mineral called northupite, $Na_3Mg(CO_3)_2Cl$, with the exceptions of four small peaks located at 15.29°, 18.22°, 24.05°, and 24.37° 2θ. As the symmetric stretch at 1114 cm^{-1} reported in the Raman spectrum agrees with the previously

reported symmetric stretch for the mineral northupite,[186] the extra pXRD peaks could be from extra waters distorting the northupite crystal structure, further supported by the fact that I was able to cross polarize (^{1}H-^{13}C) the peak at 164.01 ppm from the broad ^{1}H resonance in the sample, suggesting close proximity of a proton, not present in northupite's chemical formula. Finally, the mineral northupite is known to have only one crystallographically unique carbon[187] which is consistent with the results of the ^{13}C MAS NMR data in that only one additional resonance is seen alongside nesquehonite's single ^{13}C resonance.

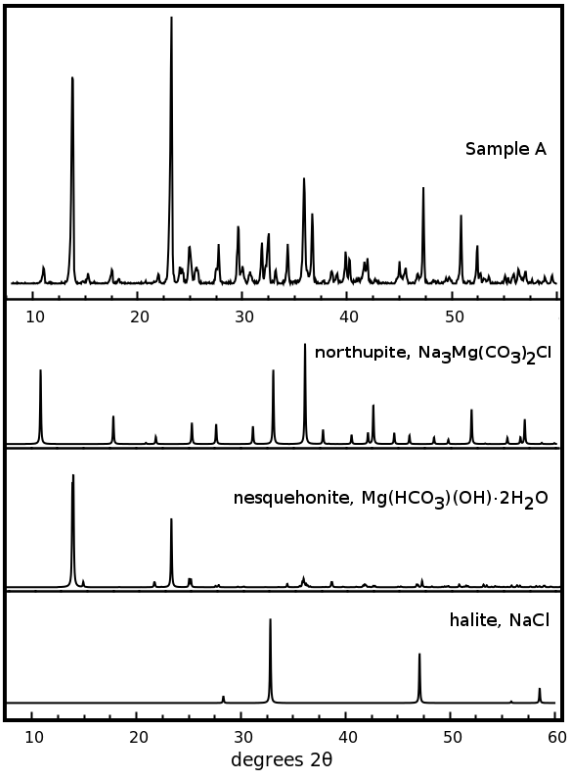

Figure 6.5: pXRD of Sample A. All of the peaks for nesquehonite were in the sample (although with preferential orientation). Most of the remaining peaks matched with halite and another mineral called northupite. (Data: ALB19, 02272013).

To further substantiate the northupite identification assignment to the second crystalline

phase, ^{23}Na MAS NMR was obtained to confirm the existence of an additional ^{23}Na NMR peak, distinct from that of NaCl. Figure 6.6a shows that there were two peaks present in Sample A: a symmetric peak at 6.65 ppm, in agreement with the known ^{23}Na chemical shift of NaCl,[188,189] and another symmetric peak at -0.57 ppm. All ^{23}Na NMR were referenced to a 1 M NaCl solution = 0 ppm. According to the solved structure of northupite,[187] there is one crystallographically unique Na, and the placement of the other atoms around it in its structure is totally symmetric—suggesting that little to no quadrupolar splitting should be expected of the ^{23}Na NMR lineshape from the mineral (in other words, a totally symmetric line could represent the presence of northupite). A saturation recovery T_1 pulse sequence was also run, and the T_1 of NaCl was found to be 13.6 s +/-2.6 s, again in agreement with previous literature.[190] However, the T_1 of the second ^{23}Na peak at -0.59 ppm was found to be in the millisecond range, considerably shorter than that of NaCl.

^{23}Na NMR was obtained for the crystalline solids $NaHCO_3$ and Na_2CO_3 to confirm that the ^{23}Na chemical shift at -0.59 ppm was in the expected chemical shift range of Na-carbonates (Figure 6.7).[191,192]

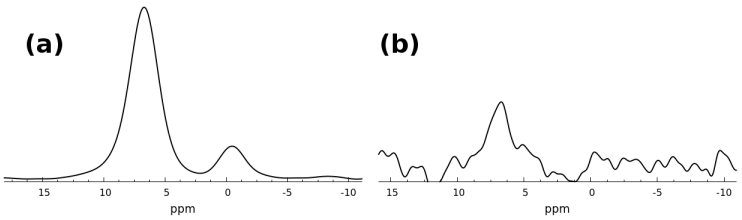

Figure 6.6: ^{23}Na MAS NMR (5kHz) of (a) Sample A two weeks after synthesis and (b) Sample B. NaCl(s) can be seen at 6.65 ppm in both spectra, although considerably less in (b) than in (a) as can be seen by the S/N comparison of the spectra. Sample A has a second peak at -0.57 ppm which is not present in Sample B. (a) had a 1s recycle delay while (b) had a 60 s recycle delay. (Data: (a) 20130404 ALB19 1sRD, (b) 20130405 JS7-2 60s RD).

^{23}Na NMR was also obtained on Sample B, shown in Figure 6.6b, to demonstrate the decreased NaCl content from the multiple washings. Sample B was also found by ^{23}Na MAS NMR to have none of the northupite phase as there was no peak at -0.59 ppm. A short recycle delay was used in Figure 6.6 (a) of one second to selectively decrease the slowly relaxing $NaCl_{(s)}$ signal relative to the fast relaxing ^{23}Na signal at -0.59 ppm. The longer recycle delay was used in Figure 6.6 b to enhance the sensitivity to detect the sparing amounts of $NaCl_{(s)}$ expected in the sample.

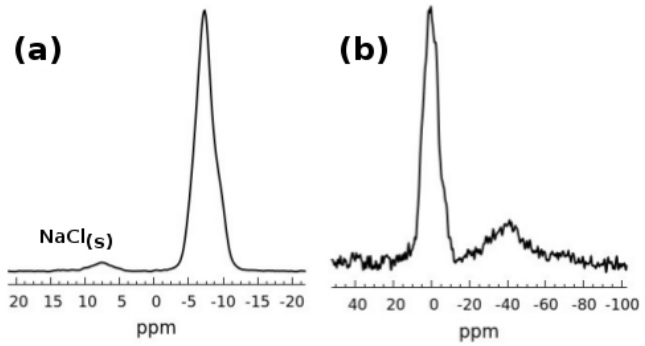

Figure 6.7: ^{23}Na MAS NMR spectra of (a) $NaHCO_3$ and (b) Na_2CO_3. The ^{23}Na NMR northupite peak in the nesquehonite sample is in the chemical shift range of sodium carbonates per (a) and (b). (Data: 20130405).

The ^{23}Na MAS NMR of $NaHCO_3$ (nahcolite) obtained from Sigma-Aldrich shows that there are minor amounts of NaCl(s) impurity in it. The spectrum also shows that there is one magnetically inequivalent ^{23}Na signal and that it is slightly asymmetric in shape. This observation agrees with the known details of the nahcolite crystal structure.[193] Na_2CO_3 (natrite) has more than one crystallographically unique Na site as previously shown by XRD and ^{23}Na MAS NMR.[191,192]

As Sample B was shown to be free of the assigned Na-impurity northupite, static and MAS ^{13}C NMR data were obtained on the pure nesquehonite sample (Figure 6.8). $^{13}C\{^1H\}$ MAS NMR

and static NMR of pure nesquehonite are shown in Fig. 6.8:

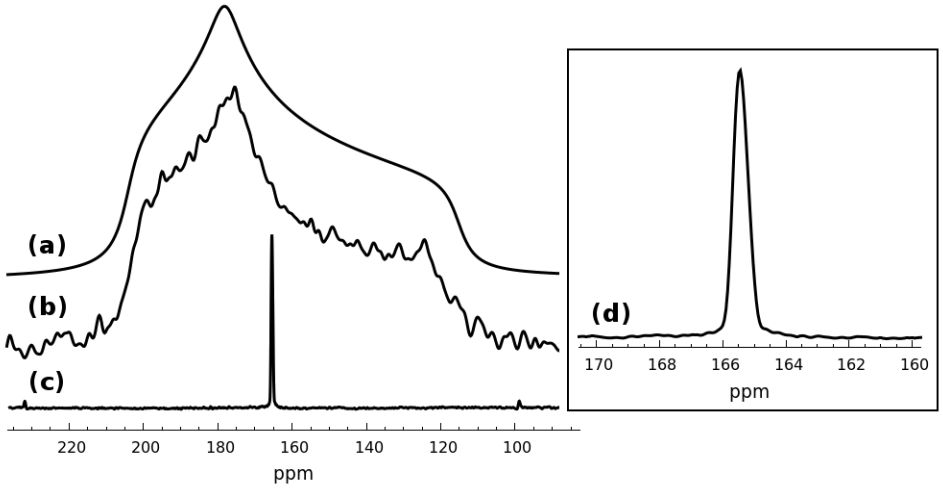

Figure 6.8: Powder pattern fit (a) for the static $^{13}C\{^{1}H\}$ NMR spectrum of pure nesquehonite (b). $^{13}C\{^{1}H\}$ MAS NMR (ν_r = 5 kHz) narrowed the powder pattern to show a single, well-defined peak at 165.42 ppm (c). The inset (d) is a closeup of the single peak of nesquehonite. (Data: JS7-2 20130312).

The isotropic ^{13}C chemical shift (δ^{iso}) for pure nesquehonite was found to be 165.42 ppm, relative to adamantane's C-H peak at 29.45 ppm.[194] The biaxiality (η) for nesquehonite was measured by a powder pattern fit to be 0.51 and the chemical shift anisotropy (δ^{aniso})=-50.64 ppm.

Additionaly pXRD (not shown here) confirmed that Sample B was nesquehonite. Raman (data also not shown here) additionally confirmed that Sample B was nesquehonite in that it had a strong symmetric C-O stretch for CO_3 at 1100 cm^{-1} and a OH stretch at 3554 cm^{-1}.[31,177] The ^{13}C T_1 of the Sample B nesquehonite peak was 35.67 +/- 0.89 s (about half of the length of the T_1 from Sample A). The peak's cross-polarization properties was also probed using a ^{1}H-^{13}C CPMAS experiment to obtain a CPMAS curve in Fig. 6.9. The T_{IS} value was found to be 1.12 +/- 0.04 ms, and the $T_{1\rho}$ to be quite long at 58.0 +/- 5.2 ms. The uncharacteristically-long $T_{1\rho}$ value suggests that there is little motion of the closest hydrogen in the crystalline unit cell,[195,196] and

that supports the suggestion that the more correct molecular formula for nesquehonite is $Mg(HCO_3)(OH)\cdot 2H_2O$ and not $MgCO_3\cdot 3H_2O$.[31] A hydrogen bound to a carbonate group is expected to have less range of motion than to a crystalline water and would therefore move less.

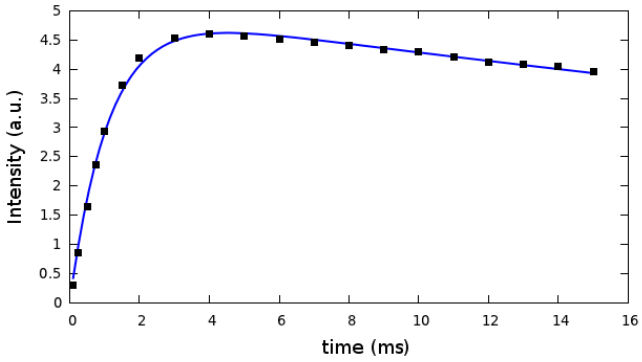

Figure 6.9: CP-MAS curve of the ^{13}C peak of nesquehonite. (Data: JS7-2 20130313).

c. Conclusions

There are only two known previous reports of ^{13}C NMR of nesquehonite,[25,26] and they both include the impurity identified here as the mineral northupite. Here I report a complete ^{13}C NMR dataset of pure nesquehonite and note that traditional synthesis methods and natural reactions that form metastable hydroxy-hydrated magnesium carbonate minerals can also co-precipitate phases that include sodium in high salinity environments. These extra Na-phases can be identified with ^{13}C and ^{23}Na NMR. Additionally, ^{23}Na MAS NMR is capable of probing the amount of NaCl impurity in the sample.

C. Dypingite, $4MgCO_3\cdot Mg(OH)_2\cdot(5\text{-}8)H_2O$

Dypingite, $4MgCO_3\cdot Mg(OH)_2\cdot(5\text{-}8)H_2O$, is a mineral originally discovered in the Dypingdal serpentine-magnesite deposit in Snarum, Norway by Gunnar Raade in 1970.[106] It was originally

published as containing either 5 or 6 H_2O's in its crystaline structure, but a publication three years later claimed that it in fact had 8 H2O's in its crystal structure, based on analysis of deposits of the supposedly same mineral found in Yoshikawa, Japan.[180] Some eleven years later, Canterford et. al wrote a paper analyzing the properties of these minerals and claimed that dypingite had 5 H_2O's in its crystal structure while noting that there were many other minerals with higher hydration values that appeared similar to dypingite in both XRD and visual analysis.[107] Nevertheless, subsequent research concludes that "dypingite" can have 5 or more waters: here I use the convention of many others that dypingite is any hydroxy-hydrated magnesium carbonate with 5 or more waters.[86,94,95,104,115] Its structure is unsolved but has a unique pXRD spectrum (which remains one of the few ways to unambiguously identify it). The pXRD of dypingite is only different from the well-known mineral, hydromagnesite, in that its lowest pXRD reflection is 5.8° 2θ, and its primary reflection is at 10.6° 2θ, unlike hydromagnesite's. Dypingite is most typically found in low temperature environments and probably exists in its "pure phase" with a dispersion of waters of crystallization—making it difficult to make in its "pure" form as no one seems to know what that is. It is not only found in only a couple of mineral deposits around the world, but a research group in Canada just recently found that dypingite is preferentially induced biologically by a group of cyanobacteria in Atlin, Canada.[197] Also more recently dypingite has been shown to exist as a phase transformation in the Mg-CO_2-H_2O reaction system.[104] Finally, our group and one other have published that it forms as one of the several magnesium carbonate products from the reaction of CO_2 with $Mg(OH)_2$.[21] Here we design a solution from which dypingite will selectively precipitate for the purposes of doing ^{13}C NMR analysis on a pure version of dypingite.

a. Synthesis

As hydromagnesite, a supposed slightly less-hydrated version of dypingite, forms from heating nesquehonite in an aqueous solution,[102] it was thought that a version of dypingite could be kinetically trapped by synthesizing a form of nesquehonite then heating it for a specific amount of time. Here we were able to make dypingite by mixing 0.2210 g of ^{13}C-labelled $NaHCO_3$ (Aldrich, 98% purity) into a pre-made and room temperature solution of 0.2509 $MgCl_2$ (Alfa Aesar, 99% purity) dissolved in 3.25 mL of DI water. This solution was allowed to sit unstirred at room temperature for 24 h then was heated at 62 °C for 48 h and then 72 °C for 24 h. The sample was then filtered and dried under vacuum at room temperature for 24h.

b. Analysis

pXRD and Raman were acquired on the synthetic product to confirm that it was consistent with the published pXRD and Raman data on it. The pXRD and Raman data obtained from this sample can be seen in Figure 6.10.

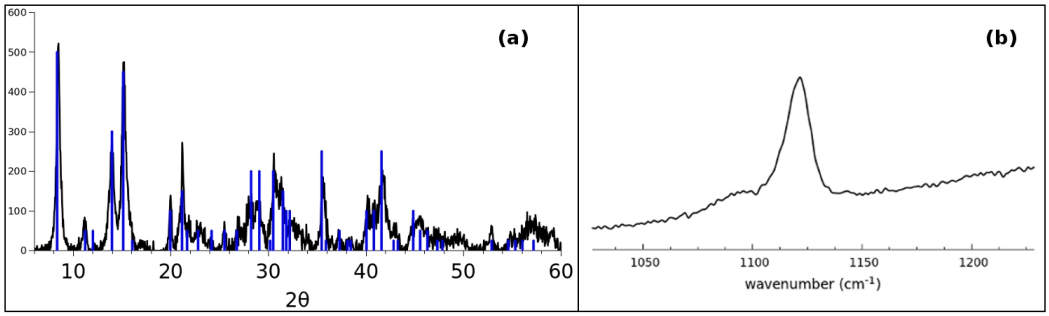

Figure 6.10: pXRD (a) and Raman data from the CO_3 symmetric stretch region (b) of the dypingite product. The stick pattern superimposed on the pXRD data is from Raade's original paper (PDF#00-023-1218). (Data: (a) LW26 20130308, (b) LW26 20130227).

The data in Figure 6.10 indicate good agreement with previously published pXRD data[106] and with previously published Raman data.[36] Here, again, only the symmetric stretch region of the

Raman spectrum is shown because it is one of the few regions of the Raman spectrum that can be quantitatively compared to literature results because of the ^{13}C labeling. Here the CO_3 symmetric stretch is at 1121 cm^{-1}, and the OH stretch (not shown) is at 3645 cm^{-1} (the OH stretch is indicative of hydroxylation in the sample). There is a broad shoulder at ~1094 cm^{-1} indicating the possibility of some carbonate impurity in the product.

Solid state ^{13}C NMR was performed on the product (Figure 6.11).

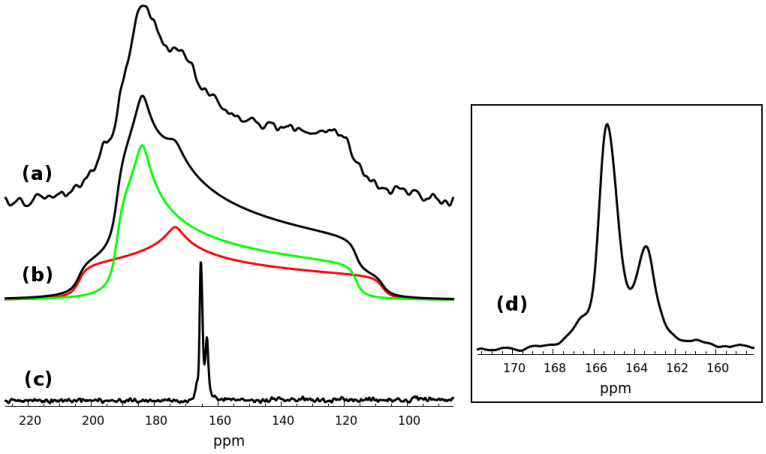

Figure 6.11: Solid state ^{13}C NMR of dypingite. (a) static, (b) fit to the static powder pattern, and (c) MAS NMR (ν_r = 5 kHz) and (d) which is a close-up view of (c). (Data: LW26, 20130305).

The solid state ^{13}C NMR data demonstrates that dypingite has two dominant ^{13}C sites whose isotropic chemical shifts are 165.3 and 163.5 ppm. The static ^{13}C NMR spectrum therefore is a superposition of two powder patterns, one from each of its two isotropic peaks. The δ^{aniso} and η values for the 165.3 peak are -47.3 ppm and 0.17, respectively. The δ^{aniso} and η values for the 163.5 ppm peak are -53.9 ppm and 0.57, respectively. Both were measured from the fit in Figure 6.11b. As can be seen in Figure 6.11d, there is also another peak/shoulder at 166.7 ppm which I assign to another carbonate phase impurity as previous reports have well-substantiated claims that dypingite's ^{13}C MAS NMR spectrum has two unequal peaks in these approximate

positions.[21,25] This NMR spectrum is quantitative so the ratios of the peaks can be measured to see the ratio of carbons in each site. Here the peak at 165.3 ppm is 60.7% of the area of the dypingite spectrum while the peak at 163.5 ppm is the remaining 39.3% (these areas come from fits of Figure 6.11d where the shoulder at 166.7 ppm was not included in the area calculations). This spectrum suggests that there are 6 carbons of site 165.3 ppm for every 4 carbons of site 163.5 ppm, or a 3/2 ratio. Additional samples of dypingite not discussed here but checked by pXRD for purity, however, have ratios that range from 75/25 to nearly 60/40 in the 165 ppm/163 ppm peak ratio. While I was never able to obtain conclusive proof of this, I think the ^{13}C NMR MAS data collected on other samples (not shown) demonstrate that the ratio of the two peaks of dypingite indicate the hydration state of the dypingite sample. The larger the ratio of the 165.3/163.5 peaks, the higher the hydration state. ^{13}C NMR data of nesquehonite's conversion into dypingite (also not shown here) show that the nesquehonite peak at 165.4 ppm will shift slightly to the dypingite peak's location of 165.3 ppm and then the second site at 163.48 ppm will grow in. Eventually it will be $\cdot 5H_2O$ dypingite, which, given more energy, will convert into the well-known $\cdot 4H_2O$ species, hydromagnesite, where the 165 ppm/163 ppm peak ratio is 1/1.

The shoulder at 166.70 ppm in Figure 6.11d may be an additional carbonate phase that is mesocrystalline and therefore does not show up in the pXRD diffraction pattern. The Raman spectrum may indicate the presence of another carbonate phase, but it is unclear. ^{23}Na MAS NMR (not shown) revealed that there were more sodium phases than just NaCl in the sample. There were two additional, small and symmetric ^{23}Na peaks at -0.8 ppm and -7.3 ppm ^{23}Na chemical shift range. These chemical shift ranges are consistent with Na-containing carbonates and are a strong indication that there was Na-carbonate impurities in the sample. While this was

the purest sample we were able to make using this aqueous synthesis method, we are very confident based on previous literature that these the dominant peaks at 165.3 and 163.4 ppm are the two peaks of the dypingite carbonate species.[20,25] Previous work by our group also identified these two peaks with a similar 165 ppm/163 ppm ratio in a Na-free high pressure reaction with CO_2 and $Mg(OH)_2$ in a sample whose Raman and pXRD signatures were also consistent with that of published dypingite.[21]

Additional ^{13}C parameters were explored for this dypingite sample. A saturation recovery T_1 experiment measured the T_1 relaxation time constants of the two dypingite peaks at 165.31 ppm and 163.5 ppm which were 104.2 +/- 5.8 s and 106.8 +/- 5.4 s, respectively. The longer T_1 time than the previous nesquehonite sample merely indicates that the crystals are probably of higher purity. It is interesting that less hydration per carbonate group in the crystalline unit has led to an increase in the T_1, perhaps water motion in the molecule contributes to crystalline dynamics that favor shorter T_1's.

The sample was also ^{1}H-^{13}C cross-polarized in a CPMAS experiment that determined each peak's T_{IS} and $T_{1\rho}$ values. The 165.3 ppm peak was found to have a T_{IS} of 0.489 +/- 0.01 ms and a $T_{1\rho}$ of 4.8 +/- 0.1 ms. The 163.5 ppm peak was found to have a T_{IS} value of 0.6 +/- 0.04 ms and a $T_{1\rho}$ value of 3.7 +/- 0.2 ms. The shorter $T_{1\rho}$ indicates that there is increased molecular motion compared to nesquehonite in the ~3 kHz range (the value of the spin-locking B_1 field in this CPMAS experiment). Figure 6.12 shows the CP-curve measured for the two dypingite resonances.

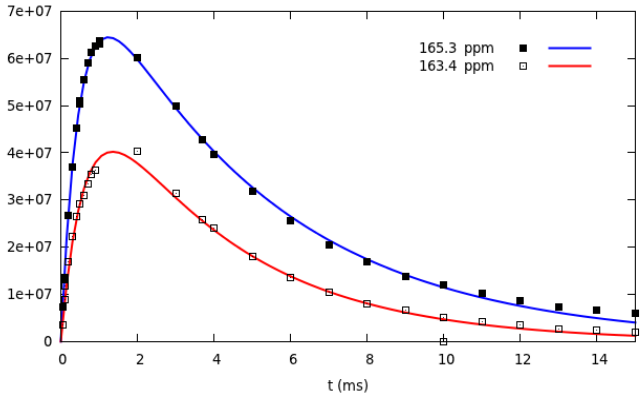

Figure 6.12: ^{13}C NMR CP curves of peak intensity (y-axis) vs. contact time (x-axis) for the 165.3 ppm peak (solid squares) and 163.4 ppm peak (hollow squares) of dypingite. The lines are the fits of the CP-curves. (Data: LW26 20121217).

c. *Conclusions*

Here we have developed a synthesis method for making the mineral dypingite. The product was evaluated by pXRD and Raman to confirm its phase and then fully characterized using several solid-state ^{13}C NMR techniques. The results indicate that it is very difficult to make pure dypingite and that its amount of hydration probably varies from sample to sample. Dypingite is considerably different spectroscopically from the previous mineral nesquehonite. The in-depth analysis allows for unambiguous characterization using ^{13}C static or MAS NMR.

D. Hydromagnesite, $4MgCO_3 \cdot Mg(OH)_2 \cdot 4H_2O$

Hydromagnesite is a reasonably well-known and chracterized basic magnesium carbonate mineral. It is also the least-hydrated of the known metastable hydroxy-hydrated carbonate minerals[164] and has been experimentally shown to be a product or an intermediate in reactions of CO_2 with other minerals containing magnesium.[21,24,57,86,93,102,104] It is manufactured commercially as a fire retardant[198,199] and is found naturally all over the world and even on the planet

Mars.[200–202] Additionally, it is quite stable up to temperatures of 250 °C[203] and often forms in the place of magnesite ($MgCO_3$), preceding magnesite, or along with magnesite as a mixed carbonate precipitate.[86,104,204]

a. Synthesis

0.2450g of $MgCl_2$ was added to 8 mL of DI water. After the solution cooled, 0.1065 g (0.08 g of which was 99% ^{13}C-labelled) was added to the solution and mixed for 1 minute at room temperature before being placed in the oven at 92 °C for 4 days. The sample was filtered and placed in a room temperature vacuum for 24 h until completely dry.

b. Analysis

After the sample was removed from the vacuum chamber, it was lightly dry-ground and evaluated with pXRD and Raman. The pXRD peaks (not shown) matched the literature values for hydromagnesite and demonstrated that the sample was not preferentially oriented.[174,175] Raman analysis (not shown) was also consistent with hydromagnesite, matching previously reported spectra for hydromagnesite (a C-O symmetric stretch for CO_3 symmetric stretch at 1118 cm^{-1} and an OH stretch at 3646 cm^{-1}).[31]

The sample was then packed into a MAS NMR rotor and ^{23}Na MAS NMR was run to see if any sodium impurities existed (data not shown). Only some residual $NaCl_{(s)}$ signal was observed with no additional ^{23}Na peaks. A full workup of static and MAS ^{13}C NMR was then obtained.

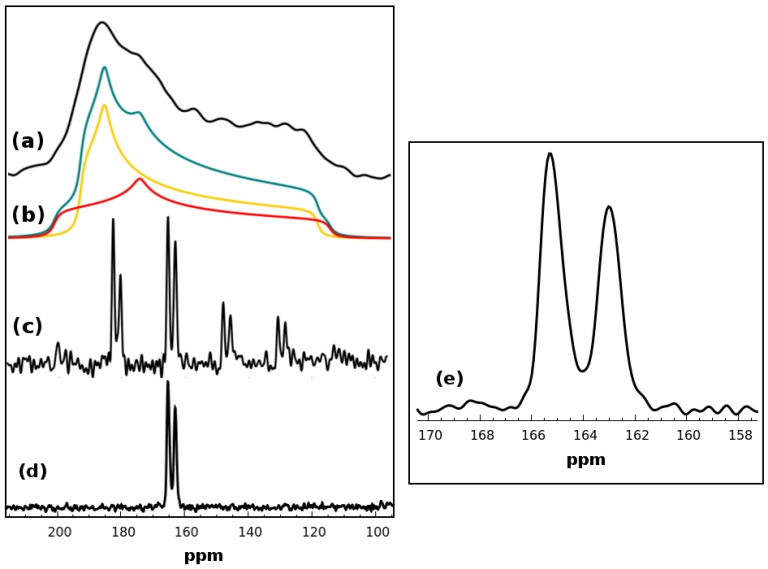

Figure 6.13: Solid state $^{13}C\{^1H\}$ NMR of hydromagnesite (a) static, (b) powder pattern fit, (c) MAS (ν_r =1.3 kHz), (d) MAS (ν_r = 5 kHz), and (e) closeup of (d). (Data: JB1, (a)20130306, (c) & (d) 20130304).

The solved crystal structure of hydromagnesite indicates that there should be two crystallographically unique carbons in the hydromagnesite crystal structure. This means there should be two unique ^{13}C peaks of equal area. The ^{13}C MAS NMR data of pure hydromagnesite in Figures 6.13e and the previously-discussed Figure 3.8 both indicate that there are two ^{13}C NMR peaks: at 165.2 ppm and 163.0 ppm for Figure 6.13; 165.4 ppm and 163.2 ppm for Figure 3.8. Both peaks are of unequal height, but their fitted integrals indicate that they are both the same areas within experimental error. A fit of the spectrum in Figure 6.13e has the peak at 165.2 ppm being 51.78% of the overall spectral area while the peak at 163.0 ppm is 48.22%. Therefore the ^{13}C NMR data is consistent with the quantitative expectation of a 1:1 ratio of the two peaks.

A "slow-spin" $^{13}C\{^1H\}$ experiment was performed on the sample to map out the CSA of both peaks in support of the shapes of the two CSA's already fitted in Figure 6.13b. The "slow spin" experiment allows the powder patterns of both peaks to be mapped by their spinning sideband

magnitudes. Such experiments are commonly done to elucidate the shape of two overlapping powder patterns.[205,206] The two peaks have magnitudes across the spectrum that one would expect from the two powder patterns fitted for them. The fitted peaks (Figure 6.13b) provided δ^{aniso} and η values of 0.16 and -47.39 ppm (165.2 ppm) and 0.55 and -49.06 ppm (163.0 ppm), respectively. These values are very close to dypingite and indicate that the electronic environment around the two carbon sites is very similar for both minerals. Furthermore, the CSA and biaxiality assignments are consistent with another slow-spin experiment performed on hydromagnesite elsewhere, confirming the synthesis.[167]

The T_1 time constants for both peaks were the same (like dypingite's two peaks), within experimental error: 156.56 +/- 7.4 s (165.4 ppm) and 156.0 +/- 5.6 s (163.0 ppm). The T_1 trend relative to the amount of hydration continues as hydromagnesite's T_1's are longer than dypingite's (a more hydrated species than hydromagnesite). In fact, $T_{1N}<T_{1D}<T_{1H}$, where N=nesquehonite, D=dypingite, and H=hydromagnesite. This trend indicates that water may play a role in the dynamics of the crystalline unit cell that helps the ^{13}C nuclei to relax in the magnetic field.

The CP-curve experiments revealed why the second peak at 163.0 ppm is shorter and broader than the peak at 165.4 (Figure 6.14): the peak at 163.0 ppm is actually a series of two or more chemical shifts.

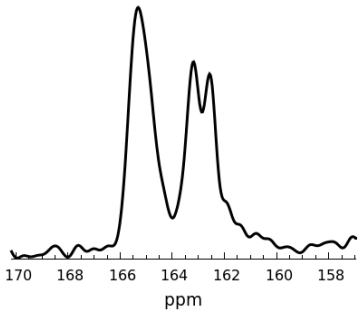

Figure 6.14: ^{1}H-^{13}C CPMAS of the hydromagnesite spectrum with a 250 μs contact time. The peak at 163.0 ppm splits into two peaks at 163.1 ppm and 162.5 ppm. (Data: JB1, 20130220 250u [16 scans, 3 s RD]).

The T_{IS} and $T_{1\rho}$ values for the peaks were T_{IS}(165.4 ppm) = 0.59 +/- 0.03 ms, $T_{1\rho}$(165.4 ppm) = 7.05 +/- 0.320 ms, T_{IS}(163.1 ppm) = 0.75 +/- 0.09 ms, $T_{1\rho}$(163.1 ppm) = 3.54 +/- 0.35 ms, and finally T_{IS}(162.5 ppm) = 0.38 +/- 0.04 ms, $T_{1\rho}$(162.5 ppm) = 8.000 +/- 0.56 ms. Clearly there is a small chemical shift dispersion due to two slightly different sites of the 163.0 ppm peak. The fact that the T_{IS} values are so different indicates that about half of the ^{13}C's are closer to a proton than the other half. As their ^{13}C T_1's are the same, the only way to resolve these two sites was by CPMAS.

c. Conclusions

A simple synthesis for the hydroxy-hydrated magnesium carbonate, hydromagnesite, was developed and a thorough ^{13}C NMR analysis was completed for the pure mineral. This mineral has two unique sites (as predicted crystallographically) but one of the sites has a dispersion of symmetry based on different distance relationships with hydrogens within the crystal. There is little spectroscopic difference between hydromagnesite and dypingite except in their relative peak areas (hydromagnesite's two peaks are defined as 1:1 but dypingite's is 6:4). Furthermore, within experimental error, the chemical shift of hydromagnesite and dypingite were found to be

roughly the same. This differs from previous claims.[24,25]

E. Magnesite, $MgCO_3$

Magnesite, $MgCO_3$, is extremely difficult to make in its pure form at temperatures <150 °C and pressures <150 bar. As outlined in the beginning of this chapter, it is very difficult to remove the water molecules that tightly adhere to the Mg^{2+} ion. In practice, $MgCO_3$ is only known to form under high pressure, high alkalinity, and/or high temperatures and usually only after long periods of time.[21,26,104,114,164–166] There are ways to make it at atmospheric pressure (but this method involves high temperatures),[165] and magnesite has also been reportedly made at low temperatures (but this method involves high pressures).[26]

Here I will discuss a method used to make magnesite and some of the preliminary high resolution ^{13}C NMR characterization of the $MgCO_{3(s)}$.

a. Synthesis

We have made magnesite for solid state ^{13}C NMR characterization using a high pressure and temperature method by reacting CO_2 with the mineral forsterite, Mg_2SiO_4, in an aqueous solution. This reaction has already been shown to selectively produce $MgCO_3$ in Chapter 3. Here I analyze the products obtained from the reactions R12 and R20 (see table of reactions at end of thesis).

Sample R12 was prepared by adding 1.598 g of Mg_2SiO_4 powder into 2.774 mL of DI water. The mineral was reacted with $CO_{2(g)}$ in a static, unstirred environment from 110-102 bar for 8 days at 90 °C. Likewise, Sample R20 was prepared by adding 2.498 g of Mg_2SiO_4 powder to 1.87 mL of DI water. It was reacted at 80 °C for 21 days. After both reactions were depressurized

and cooled to room temperature, they were removed and dried in a vacuum chamber for 24 h. The dried powder from each was then removed and a portion of the samplefrom the top of the reactor to -0.5 cm into the sample was separated and examined via Raman and pXRD before being packed into a MAS rotor for solid state ^{13}C NMR analysis.

b. Analysis

Figure 6.15 shows the pXRD data obtained from both R12 and R20 samples. They both show the presence of just two phases: forsterite and magnesite. As forsterite does not have carbon in it, it is not considered as an impurity in the ^{13}C NMR analysis of $MgCO_3$ as ^{13}C NMR is only sensitive to the presence of ^{13}C and thus does not detect the forsterite in the sample. Furthermore, the presence of silicate mineral has not been found to affect the crystalline structure of $MgCO_{3(s)}$ or the resultant relevance of ^{13}C NMR data from it.

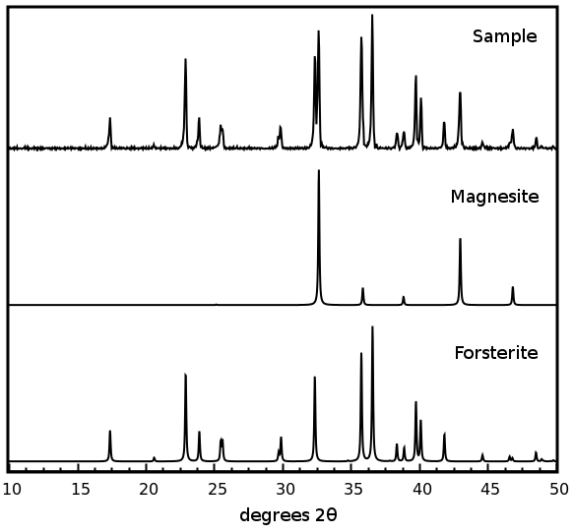

Figure 6.15: pXRD of R12 and R20 products along with the pXRD standards for forsterite and magnesite. (Data: R12-middle,).

Solid state ^{13}C NMR analysis of the R12 product is shown in Figure 6.16 where the static powder pattern for magnesite and fit to the spectrum can be seen. The fitted pattern has a δ^{aniso}

value of -54.5 ppm (+/- 0.07) and a η value of 0.135 (+/- 0.001).

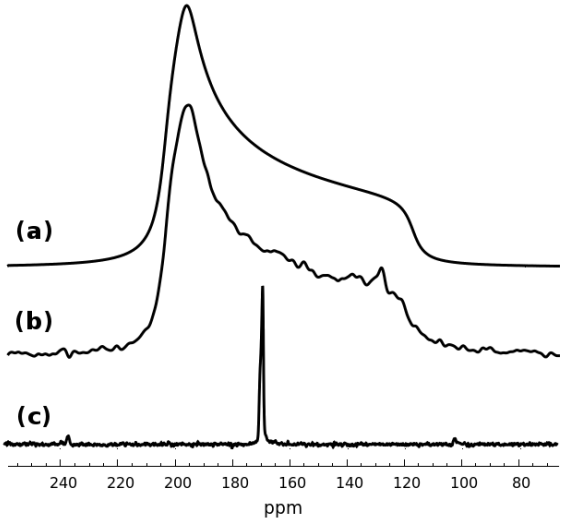

Figure 6.16: Solid state $^{13}C\{^1H\}$ NMR of pure magnesite, $MgCO_3$. (a) fit of powder pattern (b). ^{13}C MAS NMR narrows the line to a single peak in (c). (Data: R12-middle).

A close-up examination of the single peak in Figure 6.16c revealed that it was in fact not a single peak, but a combination of two different peaks. The two peaks can be seen in Figure 6.17.

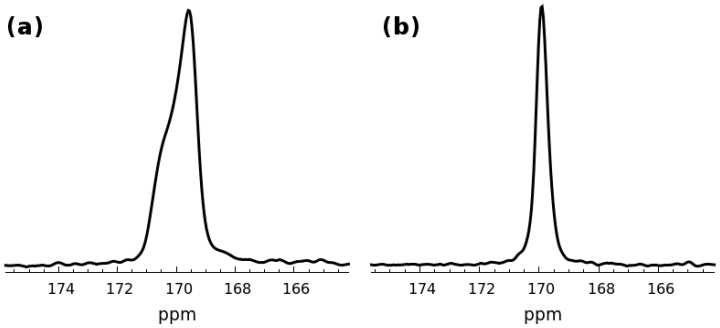

Figure 6.17: $^{13}C\{^1H\}$ MAS NMR of the magnesite product from R12 (a) and R20 (b). (Data: (a)R12middlebottom_040212[];(b)R20-middle 20130507[1 scan, 30 m RD]).

Analysis of the NMR spectra in Figure 6.17 showed that R12 had two peaks: 169.54 ppm (0.57 ppm linewidth) and 170.22 ppm (1.08 ppm linewidth). R20 had just one peak at 169.91 ppm (0.46 ppm linewidth). The R12 results are consistent with *ex situ* ^{13}C MAS results from previous reactions

producing $MgCO_3$ products (see Figures 3.16 and 3.24). There is a very, very small chemical shift dispersion (in terms of solid state NMR spectra) of the chemical shift of $MgCO_3$—but a significant one: the linewidth of $^{13}C\{^1H\}$ adamantane is some 18 Hz for these experiments. Raman data indicates that all of the phases are $MgCO_3$. pXRD data for the $MgCO_3$ phase is occasionally shifted (see Figure 3.14) and occasionally not (see Figure 3.23). Here, the pXRD of R12 and R20 are neither shifted—both pXRD experiments indicate an unshifted $MgCO_3$ phase. ^1H-^{13}C CP data is also seemingly ambiguous: both R12 and R20 $MgCO_3$ peaks can be cross polarized. However, the S/N is not very good, and the peak shape is heavily distorted. It seems likely that OH, H_2O, and/or HCO_3^- units are trapped in the $MgCO_3$ crystalline lattice, and these species are likely in locations where they playing some role in distorting the crystal structure slightly—just enough to cause some chemical shift dispersion in the high resolution ^{13}C NMR spectra. The dispersion of peaks seen here explains why literature has reported uncertainty in the chemical shift peaks for magnesite somewhere between 169 and 170.5 ppm.[21,24,25,51]

R20, on the other hand, was different from R12, and previous experiments in that it had only one peak. Of all of the Mg_2SiO_4 reactions run, R20 was synthesized the longest. The narrow line indicates that a longer reaction caused a more pure product to form—but the small differences in pressure and temperature may also have played a role in the synthesis. The powder pattern of R20 possessed the same fitted line parameters as R12 with no observed differences in the shape, anisotropy, etc. This implies that the different chemical shifts observed in the R12 sample and others are all Magnesite signals with just enough electronic environment difference to perturb the isotropic chemical shift and not the anisotropy.

c. Conclusions

$MgCO_3$ is a tricky mineral to make in pure form. The data shown here indicates that it probably is not made in its pure form in natural circumstances; $MgCO_3$ likely has some OH^-, H_2O, and/or HCO_3^- units trapped in its crystalline structure. Nevertheless, the ^{13}C NMR static and MAS spectra reveal a unique and highly characteristic lineshape and chemical shift that enable its characterization NMR.

F. Conclusions

The work presented in this chapter is important in a number ways. First, I have demonstrated that pure (or just relatively pure, in the case of dypingite) hydroxy-hydrated minerals can be obtained by relatively simple crystallizations in a beaker. The identity of the carbonate products can be controlled merely by controlling the concentrations of Mg^{2+} and CO_3^{2-} in the solution and the temperature.

In the case of the mineral nesquehonite, an important correction to literature has been made.Where it was previously thought that the mineral nesquehonite had two peaks in its ^{13}C NMR spectrum, [24,25] it has been shown that the second peak was an impurity from having too high of a concentration of sodium in the reactants and not enough washes at the end of the product. The ^{13}C NMR evidence supports the claim that the molecular formula $Mg(HCO_3)(OH)\cdot 2H_2O$ is more correct than the oft-published formula $MgCO_3\cdot 3H_2O$.[31] The ^{13}C NMR data is more consistent with a bicarbonate unit present in the crystalline structure than for a straight carbonate. This also makes sense in terms of the conditions that nesquehonite precipitates, moderate temperatures and pH.

Spectroscopically, it has been shown that dypingite is very much like hydromagnesite. The only way to distinguish the two apart via ^{13}C NMR is perform quantitative ^{13}C NMR and integrate the ratios of the peaks. In reaction products, proof of dypingite's presence can be shown merely by integrating the two hydromagnesite/dypingite peaks and taking their ratios. If their integrals are not 1:1, dypingite is present in the sample. Of the three papers published with hydromagnesite ^{13}C MAS NMR spectra, the two hydromagnesite peaks are not equal in area indicating that they do not have pure hydromagnesite as their hydromagnesite standard.[24,25,167]

Furthermore, it was shown that the biaxaility (η) of a powder pattern is indicative of the asymmetry around the carbonate unit in a unit cell. The more $MgCO_3$-like the crystal, the smaller the biaxiality parameter (the more symmetric the CO_3 site in the crystal structure). In the case of dypingite and hydromagnesite, there are two sites one that are more magnesite-like (CO_3) and the other that is more nesquehonite like (HCO_3). The shape of the powder pattern is dictated by how strong the perturbation of the CO_3 group's chemical shift tensor.

The fact that the $MgCO_3$ powder pattern does not have a biaxiality of 0 actually indicates that there is likely some of the CO_3 groups still weakly associated with an H. Similar results have been noted in calcite using ^{1}H-^{13}C CP-MAS NMR.[55]

Lastly, further evidence to support the idea that there are OH, H_2O, and/or HCO_3 groups stuck in the $MgCO_3$ crystal lattice is shown in the detailed peak analysis of the ^{13}C MAS NMR spectra of R12 and R20. Careful shimming of the probe revealed two different ^{13}C sites in the $MgCO_3$ peak indicating that there is at least two types of conditions in which the $MgCO_3$ may exist.

Measurement of the T_1 relaxation constants has been important to setting the bounds needed

to do quantitative NMR. The T_1's presented in this chapter indicate that the combination of crystalline purity, H_2O content, and amount of ^{13}C-labeling of a sample appear to contribute to the sample's relaxation properties. Quantitative ^{13}C NMR can only be obtained on metastable hydroxy-hydrated magnesium carbonates if the recycle delays are set to long times (in the range of 10 m or longer).

And finally, in conclusion, these experiments demonstrate that Na-content in the reaction solution can play a large role in the products that form, despite the high solubility of Na. The Na- and Mg- containing carbonate species can be detected via ^{23}Na NMR. $NaCl_{(s)}$ content from the reaction can also be detected with high sensitivity to determine amount of NaCl impurity. These experiments have large application for the concrete industry who often try to minimize NaCl content in their carbonate products. Altogether, solid state ^{13}C NMR is a very powerful technique that can quantitatively determine the relative abundances of different carbonate-bearing phases of a sample.

Chapter 7: Conclusions and future work

A. Conclusions

The research I have described in this thesis has demonstrated the diverse capabilities of nuclear magnetic resonance as an analytical technique. There is a vast amount of relevant information the technique can provide when used to study a reaction *in situ* and the carbonate products from the reaction *ex situ*.

Here I have shown *in situ* ^{13}C NMR measurements of CO_2 reacting with three different minerals and have shown that the fate of CO_2 can be monitored as the reaction progresses by observing solid metal carbonates form. I have also shown that ^{13}C NMR can report on the overall progress of the reaction by tracking $[CO_2]/[HCO_3^-]$ values over time. The details of these experiments were described in Chapter 3.

In addition to using high pressure and temperature ^{13}C NMR to monitor reactions *in situ* I have further showed in Chapter 4 that *real* pH values can be attained from the NMR data by combining the data with a carefully constructed pH model. This overcomes a major problem in the field: measuring accurate pH values at high pressures and temperatures during carbonation reactions.

Chapter 5 further demonstrated that pH can be *imaged* in a sample using ^{13}C NMR. There I worked through the details of setting up the imaging experiment and then showed some *in situ* imaging results obtained from two different high pressure and temperature reactions. The pH images were used to help explain the spatial dependence of product formation in the reaction chamber. The pH images also demonstrate that pH gradients *do form* in reactions of CO_2 with

minerals and that they can be *quite large over short distances.* Formation of pH gradients during CO_2 injection are important to consider in mineralization reactions as the gradients can contribute or take away considerably from the mineralization efficiency.

Finally, in Chapter 6, I reported the synthesis of a set of 99% ^{13}C-labelled metal carbonate product minerals made in pure or mostly pure form for full analysis using ^{13}C NMR and other *ex situ* techniques. The resultant ^{13}C NMR data from these pure forms of the minerals can now be used as standards for both *in situ* and *ex situ* ^{13}C NMR analysis and have solved several inaccuracies about ^{13}C NMR of these minerals in literature.

The project has successfully achieved the original goal set out for it: to "develop a unique set of spectroscopic tools to study the fate of CO_2 via NMR for CCS (Carbon Capture and Sequestration)," (2010 CCCU proposal).

B. Future work

The work I have described in this thesis is almost entirely about development of both a technique and a methodology for studying carbonation reactions. In my opinion, one of the most exciting portions of the research still lies ahead: applying the tool and methodology to other sequestration reactions, using the tool to work with other researchers in the field to solve difficult mineralization problems.

There are also a number of interesting questions that this tool and methodology could address next. One such area is studying the effect of NaCl on these reactions. True geological sequestration reactions have high concentrations and it has been shown in Chapter 6 that Na plays a large role in the carbonate products that precipitate. There is relatively little to no analysis

of the Na-containing carbonate precipitation in literature. There is also virtually no data in literature on the NMR properties of these minerals. This is an exciting area to explore both *in situ* and *ex situ.* ^{23}Na NMR is a reasonably sensitive technique and the high pressure NMR probe discussed in Chapter 2 has been built to also take ^{23}Na NMR data *in situ* without any needed modifications (one need only turn the tuning rod, adjust the NMR circuit to the ^{23}Na frequency at 93.68 MHz). *In situ* ^{23}Na NMR data may reveal regions of the sample that are being desalinated from mineralization. *Ex situ* ^{23}Na NMR data will reveal what types of Na-containing carbonates are forming and their relative stabilities can be evaluated and considered in the sequestration environment.

A further exciting area to explore is the study of CO_2 reaction with Al-containing minerals. The high pressure probe can also be tuned to obtain ^{27}Al NMR data without any modifications, meaning that in a single reaction [Na^+], [Al^{3+}], [Al^{2+}], [HCO_3^-], and [CO_2] could be analyzed *in situ*. *Ex situ* ^{27}Al analysis may reveal other Al-containing carbonates that are being formed during the reaction that were previously not thought to be made. The minerals dawsonite ($NaAlCO_3(OH)_2$) and anorthite ($CaAl_2Si_2O_8$) may be good candidate minerals for these future studies.

Finally, it would be interesting to obtain pH images as a function of both water content and mineral powder size to further elucidate the factors that control the formation of the massive pH gradients observed in the experiments described in Chapters 3 and 5.

The future is bright; I am excited to hear about where this project will go next.

Table of Reactions

This table of reactions specifies reaction details of all of the high pressure reactions that were run in the high pressure NMR probe that were discussed in this thesis. The pressure range represents the starting pressure and ending pressures. The pressure changed because the closed reaction system used CO_2 during the reaction.

Rxn	Rxn Type	Solid Mass	Soln Mass	Rxn Length	T range	P range
R9	$Mg(OH)_2$	0.761g	2.703g	2 days	80 °C	92.9-88.1 bar
R12	Mg_2SiO_4	1.598 g	2.774 g	8 days	90 °C	110-102 bar
R13	MgO	0.962 g	3.240 g	8 days	~95 °C	96-89.8 bar
R14	Mg_2SiO_4	2.170 g	3.041 g	10 days	100 °C	118-104 bar
R15	$Mg(OH)_2$	1.151 g	1.551 g	4 days	80 °C	107-105 bar
R19	$Mg(OH)_2$	1.02 g	2.117 g	32 days	81 °C	113-72 bar
R20	Mg_2SiO_4	2.498 g	1.867 g	21 days	80 °C	120-105 bar

Appendix A. Chemical reaction modeling using Duan & Sun's solubility equations, SUPCRT92, and PHREEQC.

A. Duan & Sun CO_2 Solubility calculation

The following [CO2] solubility calculation is for the sample JS1 pressurized at 39.35 bar. JS1 contains 1.04 molal NaOH and was at 22 °C=295.15 K. This [CO_2] solubility data was calculated using the known molality of NaOH. D&S can also be used with charge balance equations recursively (see Equation 4.7) for calculation of [Na^+] when it is not known (for more information on this, see Chapter 4 and section b of Appendix A).

co2-solubility.exe

```
------------------CO2SOLUBILITY---------------------
    This program is to calculate the solubility of CO2
    in pure water, aqueous NaCl solution or seawater type
     of brine  based on the solubility model developed by
     Duan and Sun (2003, Chemical Geology, 193, p257-271)
-----------------------------------------------------
  T-P-X range of this model: 273-533 K, 0-2000 bar, 0-4.5 m NaCl
  Unit---T: K, P(total): bar, mNaCl: mol/kg, mCO2: mol/kg
-----------------------------------------------------
Function 1: Calculate CO2 solubility in pure water or in  aqueous NaCl
solution

Function 2: Calculate CO2 solubility in seawater
Function 3: Calculate CO2 solubility in Brines containing Na+, K+, Mg2+, Ca2+,
Cl-, SO42-
Please enter 1 or 2 or 3 to select function
3
Please enter temperature(K) and pressure(bar)
295.15 39.35
Please enter the molality of ions in Brines in order:
  Na+, K+, Mg2+, Ca2+, Cl-, SO42-
1.04 0 0 0 0 0

**********************RESULT*****************************
      T(K)        P(bar)      mCO2(m)
     295.150      39.3500        .8622
Pause - Please enter a blank line (to continue) or a DOS command.
```

B. SUPCRT92 Calculations

Detailed step-by-step directions for using the command line program SUPCRT92 are contained on page 927 in Johnson et al.'s original research article.[128] As the original SUPCRT92 program was released before the dslop98 database was written, a few modifications to the instructions must be made. The following describes notes on the different steps in the article to specify specifics about each step I used in generating the K values.

Step 1.0: A negative response must be used and dSLOP98.dat needs to be input.
Step 2.0: Specify “3”...forces SUPCRT92 to build a new reaction file.
Step 2.3: Specify “1” as the solution is one-phase.
Step 2.4: Specify “2” forces calculations to be done in terms of temperature (°C) and pressure (bar).
Step 2.7: A negative response should be given, forcing the temperature and pressure to be independent variables.
Step 2.8: Specify “2” forces tables to be constructed in an isothermal fashion.
Step 2.9: Specify “1” forces calculations to be done in uniform increments.
Step 2.11: Enter min, max, and increment for P or T. Example: T25,100,25 makes temperature go from 25 to 100 °C in steps of 25 °C.
Step 2.19: Specify “y” to save parameters as a file.
Step 2.20: Enter appropriate filename. Write it down elsewhere so you know what look for after the calculation is done.
Step 3.0: Specify “2” to build a new reaction file.
Step 3.2: Specify number of reactions to be processed (if calculation K values for multiple reactions, specify the number of reactions here).
Step 3.3: Enter an appropriate title for the reaction file. Also write this one down so you know what to look for later.
Step 3.4: use “-” signs for reactants and positive numbers for products. Make sure reactions are balanced. Specify phase names as per the dSLOP98.dat database (you can open dSLOP98.dat in a text editor and search for keywords/formulas to find phases that are specified in database).
Step 3.8: Specify “y” so that the reactions you build will be saved to a file for later use (so you don't have to type them in again!).
Step 3.9: Enter another filename and write this one down as well.
Step 4.0: Enter another filename and writee this one down as well.
Step 4.1: Specify “1” so that plot files are not generated.

C. PHREEQC Calculations

PHREEQC takes input files that have a file extension of .pqi. These *.pqi files produce a *.pqi.out file that both contains the .pqi input and the output from the calculation when executed

in PHREEQC. PHREEQC first calculates information on the initial conditions of the solution at reaction time zero. Then it prints the results from the calculation after the reactions have reached equilibrium. The following files are the *.pqi.out files for the different experiments. These show how the calculations are setup and then how the results are printed. Even though the data shown in Chapter 4 were created using PHREEQC 2.18, these scripts have been adapted to be both PHREEQC 2.18 and 3.0.4 compatible. These output files were generated using PHREEQC 3.0.4. The following PHREEQC scripts were written to solve the different activities, pH values, and equilibria of the different solutions presented in Chapter 4.

One unique and very important caveat to PHREEQC calculations are that the solutions are solved with inputs that are the *activity* of the reactants. Since D&S equations calculate $[CO_2]$ and not $\{CO_2\}$, each PHREEQC program using $[CO_2]$ as an input is run three times. The first time with the $\log_{10}([CO_2])$ value. The second time with the $\log_{10}(\{CO_2\})$ calculated separately by taking the MacInnes γ value and multiplying it by $[CO_2]$ to get $\{CO_2\}$. The third time is to check the γ value to make sure it hasn't changed. Where possible, the input values that are to be changed are in **BOLD** and there is a bolded **#comment** on the following line describing what the **BOLD** value is.

Finally, after every PHREEQC simulation, check $[CO_2]$ in the output to make sure it matches the D&S input value. If it does not match, the calculations are not being done properly—the input activities are being calculated wrong.

To utilize these scripts, a *.pqi file should be written by including all lines between "Reading input data for simulation 1." and "Beginning of initial solution calculations. " of each of the following PHREEQC output files.

a. pH meter experiments

These experiments were completed by mixing different amounts of NaHCO3 and Na2CO3 together to tune the resultant solution to different pH's. These were assumed to be “closed” systems, that is, not at equilibrium with the atmosphere. Thus no pressure inputs were used in these calculations and [CO_2] was constrained in the system to a small value.

pH_solns.pqi.out

```
   Input file: pH_solns.pqi
  Output file: pH_solns.pqi.out
Database file: pitzer.dat

------------------
Reading data base.
------------------

        SOLUTION_MASTER_SPECIES
        SOLUTION_SPECIES
        PHASES
        PITZER
        EXCHANGE_MASTER_SPECIES
        EXCHANGE_SPECIES
        SURFACE_MASTER_SPECIES
        SURFACE_SPECIES
        END
-----------------------------------
Reading input data for simulation 1.
-----------------------------------

        PHASES
        Sodium_Carbonate
            Na2CO3 = CO3-2 + Na+ + Na+
            log_k     1.12
        CO2gas
            CO2 = CO2
            log_k     100
        SOLUTION 1
            temp      25
#if  this temperature changes, the log_k values in the SOLUTION_SPECIES section need to be
changed accordingly
            pH        7
            pe        4
            redox     pe
            units     mol/kgw
            density   1
            water    1 # kg
        EQUILIBRIUM_PHASES 1
            Nahcolite 0 0.8322
#molality of NaHCO3 in solution
            Sodium_Carbonate 0 0
#molality of Na2CO3 in solution
        SOLUTION_SPECIES
        CO2 + H2O = HCO3- + H+
            log_k     -6.345
        HCO3- = CO3-2 + H+
            log_k     -10.329
        H2O = OH- + H+
            log_k     -13.995
----------------------------------------
```

```
Beginning of initial solution calculations.
-------------------------------------------

Initial solution 1.

-----------------------------Solution composition------------------------------

        Elements           Molality       Moles

        Pure water

----------------------------Description of solution----------------------------

                                    pH  =   7.000
                                    pe  =   4.000
       Specific Conductance (uS/cm, 25 oC) = 0
                          Density (g/cm3)  =   0.99704
                               Volume (L)  =   1.00297
                      Activity of water  =   1.000
                         Ionic strength  =   1.006e-07
                     Mass of water (kg)  =   1.000e+00
                Total alkalinity (eq/kg)  =   1.158e-09
                   Total carbon (mol/kg)  =   0.000e+00
                      Total CO2 (mol/kg)  =   0.000e+00
                     Temperature (deg C)  =  25.00
                  Electrical balance (eq)  =  -1.158e-09
 Percent error, 100*(Cat-|An|)/(Cat+|An|)  =  -0.58
                               Iterations  =   3
                          Gamma iterations  =   2
                       Osmotic coefficient  =   0.99988
                          Density of water  =   0.99704
                                   Total H  = 1.110124e+02
                                   Total O  = 5.550622e+01

----------------------------Distribution of species----------------------------

                                                 MacInnes  MacInnes
                              MacInnes       Log       Log       Log    mole V
   Species          Molality    Activity  Molality  Activity     Gamma   cm3/mol

   OH-             1.012e-07   1.012e-07    -6.995    -6.995    -0.000     (0)
   H+              1.000e-07   1.000e-07    -7.000    -7.000    -0.000      0.00
   H2O             5.551e+01   1.000e+00     1.744    -0.000     0.000     18.07

------------------------------Saturation indices-------------------------------

        Phase               SI   log IAP   log K(298 K,   1 atm)

        H2O(g)           -1.50     -0.00    1.50  H2O


-----------------------------------------
Beginning of batch-reaction calculations.
-----------------------------------------

Reaction step 1.

Using solution 1.
Using pure phase assemblage 1.

-------------------------------Phase assemblage--------------------------------

                                                      Moles in assemblage
Phase               SI  log IAP  log K(T, P)   Initial       Final       Delta

Nahcolite        -0.28   -11.02    -10.74    8.322e-01           0  -8.322e-01
Sodium_Carbonate   -4.63    -3.51      1.12    0.000e+00           0   0.000e+00
```

```
-----------------------------Solution composition-----------------------------

        Elements           Molality       Moles

        C                 8.320e-01   8.322e-01
        Na                8.320e-01   8.322e-01

----------------------------Description of solution----------------------------

                                     pH  =   7.791      Charge balance
                                     pe  =   4.000      Adjusted to redox equilibrium
       Specific Conductance (uS/cm, 25 oC) = 27426
                           Density (g/cm3)  =   1.06655
                                Volume (L)  =   1.04139
                      Activity of water  =   0.975
                         Ionic strength  =   8.444e-01
                     Mass of water (kg)  =   1.000e+00
                Total alkalinity (eq/kg)  =   8.320e-01
                      Total CO2 (mol/kg)  =   8.320e-01
                    Temperature (deg C)  =  25.00
                 Electrical balance (eq)  =  -3.545e-10
 Percent error, 100*(Cat-|An|)/(Cat+|An|)  =  -0.00
                               Iterations  =  18
                          Gamma iterations  =   4
                     Osmotic coefficient  =   0.85666
                        Density of water  =   0.99704
                                 Total H  = 1.118446e+02
                                 Total O  = 5.800282e+01

----------------------------Distribution of species----------------------------

                                                 MacInnes  MacInnes
                                MacInnes       Log       Log       Log    mole V
   Species          Molality    Activity  Molality  Activity     Gamma   cm3/mol

   OH-             1.017e-06   6.087e-07    -5.993    -6.216    -0.223     (0)
   H+              2.599e-08   1.620e-08    -7.585    -7.791    -0.205      0.00
   H2O             5.551e+01   9.746e-01     1.744    -0.011     0.000     18.07
C(4)          8.320e-01
   HCO3-           8.072e-01   3.882e-01    -0.093    -0.411    -0.318     (0)
   CO2             1.239e-02   1.428e-02    -1.907    -1.845     0.061     29.09
   CO3-2           1.239e-02   1.106e-03    -1.907    -2.956    -1.049     (0)
Na            8.320e-01
   Na+             8.320e-01   5.293e-01    -0.080    -0.276    -0.196     -0.48

------------------------------Saturation indices-------------------------------

        Phase               SI   log IAP   log K(298 K,   1 atm)

        CO2(g)           -0.38     -1.85   -1.46  CO2
        CO2gas         -101.85     -1.85  100.00  CO2
        H2O(g)           -1.51     -0.01    1.50  H2O
        Nahcolite        -0.28    -11.02  -10.74  NaHCO3
        Natron           -2.80     -3.62   -0.82  Na2CO3:10H2O
        Sodium_Carbonate  -4.63     -3.51    1.12  Na2CO3
        Trona            -3.17    -14.55  -11.38  Na3H(CO3)2:2H2O
#note how all of the SI values are all negative---this means that the solution is not
supersaturated with respect to any possible mineral phase.

------------------
End of simulation.
------------------

-----------------------------------
Reading input data for simulation 2.
-----------------------------------

------------------------------
```

```
End of Run after 0.06 Seconds.
-----------------------------
```

b. High pressure NaOH solutions

These calculations were completed in two different ways. One, where $[Na^+]$ was assumed to be known ($[NaOH]=[Na^+]$ was assumed and pH.pqi was used for calculations). And two, where $[Na^+]$ was assumed to not be known. In the case of $[Na^+]$ not being known, a spreadsheet was constructed that used the charge balance equation (Equation 4.7), $[CO_2]$ from D&S, and the NMR ratio $[CO_2]/[HCO_3^-]$ to calculate $[Na^+]$ values. Since D&S depends on $[Na^+]$, the D&S calculation was done in recursion with the spreadsheet with a starting value of $[Na^+]=0$. Once charge balance gave a value for $[Na^+]$, that value was inputted into D&S which produced a new $[CO_2]$ value. A new charge balance calculation was completed which produced a new value of $[Na^+]$. This value was then put into the the D&S model---and this process repeated until $[CO_2]$ and $[Na^+]$ no longer changed (3-5 iterations). Once $[Na^+]$ was found, it was used in the activity-Na.pqi phreeqc file to calculate pH for the system, where $[Na^+]$ was input as [NaOH] with an large K value.

Here pH.pqi.out and activity-Na.pqi.out calculations are shown for the same sample JS1 ([NaOH] = 1.041 molal) at 39.35 bar of CO_2. You will notice by comparing their results that using D&S equations/charge balance to calculate $[Na^+]$ yielded a value of $[Na^+]=1.083$ molal. This is very close to the real value of 1.041 molal. In addition, the slight differences between knowing and not knowing $[Na^+]$ yielded a pH value of 6.029 for $[Na^+]$ = 1.041 molal and 6.048 for $[Na^+]$ = 1.083 molal.

pH.pqi.out

```
   Input file: pH.pqi
  Output file: pH.pqi.out
Database file: pitzer.dat

------------------
Reading data base.
------------------

        SOLUTION_MASTER_SPECIES
        SOLUTION_SPECIES
        PHASES
        PITZER
        EXCHANGE_MASTER_SPECIES
        EXCHANGE_SPECIES
        SURFACE_MASTER_SPECIES
        SURFACE_SPECIES
        END
-----------------------------------
Reading input data for simulation 1.
-----------------------------------

        SOLUTION 1
            temp      22
#temperature in C can be changed as needed. Note that if the temperature is changed, the
equilibrium constants in SOLUTION_SPECIES must be changed accordingly.
            pH        7
            pe        4
            redox     pe
            units     mol/kgw
            density   1
            water    1 # kg
        PHASES
        NaOH
            NaOH = Na+ + OH-
            analytical_expression 100 0 0 0 0 0
        Fix_CO2
                CO2 = CO2
                log_k 0
        EQUILIBRIUM_PHASES 1
            Fix_CO2  0.0125 CO2(g) 100
#0.0125 = log10({CO2}). For the first run of this script, log10([CO2]) can be used,
substituting log10({CO2}) once the activity coefficient of CO2 is known.
            -force_equality
            NaOH      0  1.041
#[Na+] in mol/kg. Here, this is the known value.
        SOLUTION_SPECIES
        CO2 + H2O = HCO3- + H+
            analytical_expression -6.345 0 0 0 0 0
        HCO3- = CO3-2 + H+
            analytical_expression -10.335 0 0 0 0 0
        H2O = OH- + H+
            analytical_expression -14.071 0 0 0 0 0
        END
-------------------------------------------
Beginning of initial solution calculations.
-------------------------------------------

Initial solution 1.

-----------------------------Solution composition------------------------------

        Elements           Molality       Moles

        Pure water

----------------------------Description of solution----------------------------
```

```
                                    pH  =   7.000
                                    pe  =   4.000
       Specific Conductance (uS/cm, 22 oC) = 0
                         Density (g/cm3)  =   0.99777
                              Volume (L)  =   1.00224
                     Activity of water  =   1.000
                        Ionic strength  =   9.249e-08
                     Mass of water (kg)  =   1.000e+00
                Total alkalinity (eq/kg)  =  -1.509e-08
                   Total carbon (mol/kg)  =   0.000e+00
                      Total CO2 (mol/kg)  =   0.000e+00
                    Temperature (deg C)  =  22.00
                 Electrical balance (eq)  =   1.509e-08
 Percent error, 100*(Cat-|An|)/(Cat+|An|)  =   8.16
                               Iterations  =  44
                          Gamma iterations  =   2
                       Osmotic coefficient  =   0.99988
                          Density of water  =   0.99777
                                   Total H  = 1.110124e+02
                                   Total O  = 5.550622e+01

----------------------------Distribution of species----------------------------

                                                 MacInnes  MacInnes
                              MacInnes       Log       Log       Log    mole V
   Species          Molality    Activity  Molality  Activity     Gamma   cm3/mol

   H+              1.000e-07   1.000e-07    -7.000    -7.000    -0.000      0.00
   OH-             8.495e-08   8.492e-08    -7.071    -7.071    -0.000     (0)
   H2O             5.551e+01   1.000e+00     1.744    -0.000     0.000     18.06

------------------------------Saturation indices-------------------------------

       Phase               SI   log IAP   log K(295 K,   1 atm)

       H2O(g)           -1.58     -0.00    1.58  H2O


----------------------------------------
Beginning of batch-reaction calculations.
----------------------------------------

Reaction step 1.

Using solution 1.
Using pure phase assemblage 1.

--------------------------------Phase assemblage--------------------------------

                                                      Moles in assemblage
Phase               SI  log IAP  log K(T, P)   Initial       Final       Delta

Fix_CO2           0.01     0.01      0.00
        CO2                is reactant       1.000e+02   9.810e+01  -1.903e+00
NaOH           -108.19    -8.19    100.00    1.041e+00           0  -1.041e+00

-----------------------------Solution composition-----------------------------

       Elements           Molality       Moles

       C                 1.903e+00   1.903e+00
       Na                1.041e+00   1.041e+00

----------------------------Description of solution----------------------------

                                    pH  =   6.029      Charge balance
                                    pe  =   4.000      Adjusted to redox equilibrium
```

```
       Specific Conductance (uS/cm, 22 oC) = 34873
                           Density (g/cm3)  =   1.09533
                                Volume (L)  =   1.11259
                          Activity of water  =   0.951
                             Ionic strength  =   1.041e+00
                         Mass of water (kg)  =   1.000e+00
                  Total alkalinity (eq/kg)  =   1.041e+00
                        Total CO2 (mol/kg)  =   1.903e+00
                       Temperature (deg C)  =  22.00
                    Electrical balance (eq)  =   1.509e-08
 Percent error, 100*(Cat-|An|)/(Cat+|An|)  =   0.00
                                Iterations  =  21
                           Gamma iterations  =   4
                       Osmotic coefficient  =   0.94726
                          Density of water  =   0.99777
                                   Total H  = 1.120534e+02
                                   Total O  = 6.035320e+01

----------------------------Distribution of species----------------------------

                                                          MacInnes  MacInnes
                                  MacInnes       Log        Log       Log    mole V
   Species          Molality      Activity  Molality  Activity     Gamma   cm3/mol

   H+              1.497e-06   9.364e-07    -5.825    -6.029    -0.204      0.00
   OH-             1.466e-08   8.624e-09    -7.834    -8.064    -0.230     (0)
   H2O             5.551e+01   9.510e-01     1.744    -0.022     0.000     18.06
C(4)          1.903e+00
   HCO3-           1.040e+00   4.723e-01     0.017    -0.326    -0.343     (0)
   CO2             8.623e-01   1.029e+00    -0.064     0.012     0.077     29.83
#note that the [CO2] concentration is the same as the D&S value.
   CO3-2           2.823e-04   2.101e-05    -3.549    -4.677    -1.128     (0)
Na            1.041e+00
   Na+             1.041e+00   7.536e-01     0.017    -0.123    -0.140     -0.50

------------------------------Saturation indices-------------------------------

       Phase               SI   log IAP   log K(295 K,   1 atm)

       CO2(g)            1.44      0.01   -1.43  CO2
       Fix_CO2           0.01      0.01    0.00  CO2
       H2O(g)           -1.60     -0.02    1.58  H2O
       Nahcolite        -0.09    -10.83  -10.74  NaHCO3
       NaOH           -108.19     -8.19  100.00  NaOH
       Natron           -4.32     -5.14   -0.82  Na2CO3:10H2O
       Trona            -4.41    -15.80  -11.38  Na3H(CO3)2:2H2O


------------------
End of simulation.
------------------

-----------------------------------
Reading input data for simulation 2.
-----------------------------------

------------------------------
End of Run after 0.06 Seconds.
------------------------------
```

activity-Na.pqi.out

```
   Input file: activity-Na.pqi
  Output file: activity-Na.pqi.out
Database file: pitzer.dat
```

```
------------------
Reading data base.
------------------

        SOLUTION_MASTER_SPECIES
        SOLUTION_SPECIES
        PHASES
        PITZER
        EXCHANGE_MASTER_SPECIES
        EXCHANGE_SPECIES
        SURFACE_MASTER_SPECIES
        SURFACE_SPECIES
        END
-----------------------------------
Reading input data for simulation 1.
-----------------------------------

        SOLUTION 1
            temp      22
#temperature in C can be changed as needed. Note that if the temperature is changed, the
equilibrium constants in SOLUTION_SPECIES must be changed accordingly.
            pH        7
            pe        4
            redox     pe
            units     mol/kgw
            density   1
            water    1 # kg
        PHASES
        NaOH
            NaOH = Na+ + OH-
            analytical_expression 100 0 0 0 0 0
        Fix_CO2
               CO2 = CO2
               log_k 0
        EQUILIBRIUM_PHASES 1
            Fix_CO2  0.01135615 CO2(g) 100
# 0.01135615 = log10({CO2}). For first run, log10([CO2]) can be used. Once the activity
coefficient for CO2 is known, replace with log10({CO2}).
            -force_equality
            NaOH      0  1.0833
#the D&S/charge balance [Na+] value in molality
        SOLUTION_SPECIES
        CO2 + H2O = HCO3- + H+
            analytical_expression -6.351 0 0 0 0 0
        HCO3- = CO3-2 + H+
            analytical_expression -10.342 0 0 0 0 0
        H2O = OH- + H+
            analytical_expression -14.085 0 0 0 0 0
        END
-------------------------------------------
Beginning of initial solution calculations.
-------------------------------------------

Initial solution 1.

-----------------------------Solution composition------------------------------

        Elements           Molality       Moles

        Pure water

----------------------------Description of solution----------------------------

                                       pH  =   7.000
                                       pe  =   4.000
       Specific Conductance (uS/cm, 22 oC) = 0
                            Density (g/cm3)  =   0.99777
                                 Volume (L)  =   1.00224
```

```
                      Activity of water  =   1.000
                         Ionic strength  =   9.114e-08
                     Mass of water (kg)  =   1.000e+00
                Total alkalinity (eq/kg)  =  -1.778e-08
                   Total carbon (mol/kg)  =   0.000e+00
                      Total CO2 (mol/kg)  =   0.000e+00
                    Temperature (deg C)  =  22.00
                  Electrical balance (eq)  =   1.778e-08
 Percent error, 100*(Cat-|An|)/(Cat+|An|)  =   9.75
                             Iterations  =  44
                        Gamma iterations  =   2
                    Osmotic coefficient  =   0.99988
                       Density of water  =   0.99777
                                Total H  = 1.110124e+02
                                Total O  = 5.550622e+01

----------------------------Distribution of species----------------------------

                                                    MacInnes  MacInnes
                               MacInnes       Log       Log       Log    mole V
   Species          Molality    Activity  Molality  Activity     Gamma   cm3/mol

   H+              1.000e-07   1.000e-07    -7.000    -7.000    -0.000      0.00
   OH-             8.225e-08   8.222e-08    -7.085    -7.085    -0.000     (0)
   H2O             5.551e+01   1.000e+00     1.744    -0.000     0.000     18.06

------------------------------Saturation indices-------------------------------

       Phase               SI   log IAP   log K(295 K,   1 atm)

       H2O(g)           -1.58     -0.00    1.58  H2O


----------------------------------------
Beginning of batch-reaction calculations.
----------------------------------------

Reaction step 1.

Using solution 1.
Using pure phase assemblage 1.

--------------------------------Phase assemblage--------------------------------

                                                      Moles in assemblage
Phase               SI  log IAP  log K(T, P)   Initial       Final       Delta

Fix_CO2           0.01     0.01      0.00
       CO2                 is reactant       1.000e+02   9.806e+01  -1.937e+00
NaOH           -108.17    -8.17    100.00    1.083e+00           0  -1.083e+00

-----------------------------Solution composition-----------------------------

       Elements           Molality       Moles

       C                 1.937e+00   1.937e+00
       Na                1.083e+00   1.083e+00

----------------------------Description of solution----------------------------

                                    pH  =   6.048      Charge balance
                                    pe  =   4.000      Adjusted to redox equilibrium
      Specific Conductance (uS/cm, 22 oC) = 35956
                         Density (g/cm3)  =   1.09868
                              Volume (L)  =   1.11360
                     Activity of water  =   0.950
                        Ionic strength  =   1.084e+00
                    Mass of water (kg)  =   1.000e+00
```

```
                Total alkalinity (eq/kg)  =   1.083e+00
                      Total CO2 (mol/kg)  =   1.937e+00
                     Temperature (deg C)  =  22.00
                  Electrical balance (eq)  =   1.778e-08
 Percent error, 100*(Cat-|An|)/(Cat+|An|)  =   0.00
                              Iterations  =  23
                         Gamma iterations  =   4
                     Osmotic coefficient  =   0.94558
                        Density of water  =   0.99777
                                 Total H  = 1.120957e+02
                                 Total O  = 6.046317e+01

----------------------------Distribution of species----------------------------

                                                    MacInnes  MacInnes
                              MacInnes       Log        Log       Log    mole V
   Species          Molality    Activity  Molality  Activity     Gamma   cm3/mol

   H+              1.431e-06   8.947e-07    -5.844    -6.048    -0.204      0.00
   OH-             1.490e-08   8.730e-09    -7.827    -8.059    -0.232     (0)
   H2O             5.551e+01   9.499e-01     1.744    -0.022     0.000     18.06
C(4)          1.937e+00
   HCO3-           1.083e+00   4.857e-01     0.034    -0.314    -0.348     (0)
   CO2             8.538e-01   1.026e+00    -0.069     0.011     0.080     29.83
#note that the [CO2] value is the same as the D&S value
   CO3-2           3.199e-04   2.293e-05    -3.495    -4.640    -1.145     (0)
Na            1.083e+00
   Na+             1.083e+00   7.823e-01     0.035    -0.107    -0.141     -0.47

------------------------------Saturation indices-------------------------------

       Phase               SI   log IAP   log K(295 K,   1 atm)

       CO2(g)            1.44      0.01   -1.43  CO2
       Fix_CO2           0.01      0.01    0.00  CO2
       H2O(g)           -1.60     -0.02    1.58  H2O
       Nahcolite        -0.05    -10.79  -10.74  NaHCO3
       NaOH           -108.17     -8.17  100.00  NaOH
       Natron           -4.25     -5.08   -0.82  Na2CO3:10H2O
       Trona            -4.31    -15.69  -11.38  Na3H(CO3)2:2H2O


------------------
End of simulation.
------------------

-----------------------------------
Reading input data for simulation 2.
-----------------------------------

------------------------------
End of Run after 0.07 Seconds.
------------------------------
```

c. High pressure and temperature pH calculations for $Mg(OH)_2$ reactions

Similarly to the NaOH calculations where [Na^+] is not known, these calculations involve D&S/charge balance to calculate [Mg^{2+}]. Here we do not know [Mg^{2+}] so there is no way to calculate error. Since the previous experiments showed that the D&S/charge balance was

accurate with the precision of D&S (7%), we will trust the values it produces. Here we use the *in situ* reaction data from sample R15, where $Mg(OH)_2$ is reacting with CO_2 in water. This data is taken from 18 hrs into the reaction, at 107 bar and 81 °C. The calculations show that [Mg2+] = 0.026 molal, $[CO_2]$ = 0.891 molal, and pH = 4.905. The output file includes an error, "WARNING: Fix_CO2, Pure phase with add formula has not converged." This error just means that the artificial Fix_CO2 phase is not fully converging with the system. This is okay and is because of the bulk extra CO2 I added in the model. It does not affect the validity of the pH results and only occurs in some of the calculations. PHREEQC often has warnings like this because it wants to make sure you don't solve for a local minimum.

activity-Mg.pqi.out

```
   Input file: activity-Mg.pqi
  Output file: activity-Mg.pqi.out
Database file: pitzer.dat

------------------
Reading data base.
------------------

        SOLUTION_MASTER_SPECIES
        SOLUTION_SPECIES
        PHASES
        PITZER
        EXCHANGE_MASTER_SPECIES
        EXCHANGE_SPECIES
        SURFACE_MASTER_SPECIES
        SURFACE_SPECIES
        END
-----------------------------------
Reading input data for simulation 1.
-----------------------------------

        SOLUTION 1
            temp      81
#change temperature in C as needed. Note that the equilibrium constants for
SOLUTION_SPECIES have been altered for this new temperature. In addition, as temperature
changes, the PHASES log_k need to be changed as well.
            pH        7
            pe        4
            redox     pe
            units     mol/kgw
            density   1
            water    1 # kg
        PHASES
        magnesite
            MgCO3 = Mg+2 + CO3-2
            log_k      -9.017
        Mg(OH)2
```

```
            Mg(OH)2 = Mg+2 + 2OH-
            log_k      -11.826
        hydromagnesite
            Mg5(CO3)4(OH)2:4H2O = 5Mg+2 + 4CO3-2 + 2OH- + 4H2O
            log_k      -42.756
        nesquehonite
            MgCO3:3H2O = Mg+2 + CO3-2 + 3H2O
            log_k      -5.247
        Fix_CO2
                CO2 = CO2
                log_k 0
        EQUILIBRIUM_PHASES 1
                Fix_CO2 -0.04607355633209 CO2(g) 100
# -0.04607355633209 = log10({CO2}). Use log10([CO2]) for first iteration, replacing with
log10({CO2}) once the activity coefficient has been calculated.
             Mg(OH)2      0          0.02605755
#the calculated molality [Mg2+] value from D&S/charge balance.
        SOLUTION_SPECIES
        CO2 + H2O = HCO3- + H+
            analytical_expression -6.267 0 0 0 0 0
        HCO3- = CO3-2 + H+
            analytical_expression -10.033 0 0 0 0 0
        H2O = OH- + H+
            analytical_expression -12.55 0 0 0 0 0
        END
-------------------------------------------
Beginning of initial solution calculations.
-------------------------------------------

Initial solution 1.

-----------------------------Solution composition------------------------------

        Elements           Molality       Moles

        Pure water

----------------------------Description of solution----------------------------

                                       pH  =   7.000
                                       pe  =   4.000
       Specific Conductance (uS/cm, 81 oC) = 0
                            Density (g/cm3)  =   0.97116
                                 Volume (L)  =   1.02970
                          Activity of water  =   1.000
                             Ionic strength  =   1.462e-06
                         Mass of water (kg)  =   1.000e+00
                 Total alkalinity (eq/kg)  =   2.723e-06
                    Total carbon (mol/kg)  =   0.000e+00
                       Total CO2 (mol/kg)  =   0.000e+00
                      Temperature (deg C)  =  81.00
                   Electrical balance (eq)  =  -2.723e-06
 Percent error, 100*(Cat-|An|)/(Cat+|An|)  = -93.15
                                Iterations  =   3
                           Gamma iterations  =   2
                        Osmotic coefficient  =   0.99947
                           Density of water  =   0.97116
                                    Total H  = 1.110124e+02
                                    Total O  = 5.550622e+01

----------------------------Distribution of species----------------------------

                                                 MacInnes  MacInnes
                                MacInnes       Log       Log       Log    mole V
   Species          Molality    Activity  Molality  Activity     Gamma   cm3/mol

   OH-             2.823e-06   2.818e-06    -5.549    -5.550    -0.001     (0)
   H+              1.002e-07   1.000e-07    -6.999    -7.000    -0.001      0.00
```

```
   H2O             5.551e+01   1.000e+00     1.744    -0.000     0.000     18.55

------------------------------Saturation indices-------------------------------

       Phase               SI   log IAP   log K(354 K,   1 atm)

       H2O(g)           -0.32     -0.00    0.32  H2O


----------------------------------------
Beginning of batch-reaction calculations.
----------------------------------------

Reaction step 1.

WARNING: Fix_CO2, Pure phase with add formula has not converged.
        SI may be a local minimum.   Residual: 5.755532e+00

WARNING: Fix_CO2, Pure phase with add formula has not converged.
        SI may be a local minimum.   Residual: 6.473280e+00

Using solution 1.
Using pure phase assemblage 1.

-------------------------------Phase assemblage--------------------------------

                                                        Moles in assemblage
Phase               SI  log IAP  log K(T, P)   Initial       Final       Delta

Fix_CO2          -0.05    -0.05      0.00
       CO2                 is reactant       1.000e+02   9.906e+01  -9.429e-01
Mg(OH)2          -5.38   -17.21    -11.83    2.606e-02           0  -2.606e-02

------------------------------Solution composition------------------------------

       Elements           Molality       Moles

       C                 9.429e-01   9.429e-01
       Mg                2.606e-02   2.606e-02

----------------------------Description of solution----------------------------

                                    pH  =   4.905      Charge balance
                                    pe  =   4.000      Adjusted to redox equilibrium
      Specific Conductance (uS/cm, 81 oC) = 5139
                         Density (g/cm3)  =   0.99469
                              Volume (L)  =   1.09505
                     Activity of water  =   0.983
                        Ionic strength  =   7.818e-02
                    Mass of water (kg)  =   1.000e+00
               Total alkalinity (eq/kg)  =   5.212e-02
                     Total CO2 (mol/kg)  =   9.429e-01
                   Temperature (deg C)  =  81.00
                Electrical balance (eq)  =  -2.723e-06
 Percent error, 100*(Cat-|An|)/(Cat+|An|)  =  -0.00
                              Iterations  =  28
                         Gamma iterations  =   5
                     Osmotic coefficient  =   0.99582
                        Density of water  =   0.97116
                                 Total H  = 1.110646e+02
                                 Total O  = 5.744421e+01

---------------------------Distribution of species----------------------------

                                                MacInnes  MacInnes
                             MacInnes       Log       Log       Log    mole V
   Species          Molality  Activity  Molality  Activity     Gamma   cm3/mol
```

```
   H+              1.660e-05   1.244e-05    -4.780    -4.905    -0.125      0.00
   OH-             3.141e-08   2.226e-08    -7.503    -7.653    -0.150      (0)
   H2O             5.551e+01   9.828e-01     1.744    -0.008     0.000     18.55
C(4)           9.429e-01
   CO2             8.908e-01   8.993e-01    -0.050    -0.046     0.004     21.89
   HCO3-           5.212e-02   3.841e-02    -1.283    -1.416    -0.133      (0)
   MgCO3           4.824e-06   4.824e-06    -5.317    -5.317     0.000    -17.08
   CO3-2           7.561e-07   1.944e-07    -6.121    -6.711    -0.590      (0)
Mg             2.606e-02
   Mg+2            2.605e-02   1.246e-02    -1.584    -1.905    -0.320    -23.17
   MgCO3           4.824e-06   4.824e-06    -5.317    -5.317     0.000    -17.08
   MgOH+           1.254e-07   9.354e-08    -6.902    -7.029    -0.127      (0)

------------------------------Saturation indices-------------------------------

       Phase               SI   log IAP   log K(354 K,   1 atm)

       Brucite          -6.89    -17.21  -10.32  Mg(OH)2
       CO2(g)            1.84     -0.05   -1.89  CO2
       Fix_CO2          -0.05     -0.05    0.00  CO2
       H2O(g)           -0.32     -0.01    0.32  H2O
       hydromagnesite   -8.95    -51.70  -42.76  Mg5(CO3)4(OH)2:4H2O
       magnesite         0.40     -8.62   -9.02  MgCO3
       Mg(OH)2          -5.38    -17.21  -11.83  Mg(OH)2
       nesquehonite     -3.39     -8.64   -5.25  MgCO3:3H2O


------------------
End of simulation.
------------------

------------------------------------
Reading input data for simulation 2.
------------------------------------

------------------------------
End of Run after 0.07 Seconds.
------------------------------
```

PHREEQC is a very useful program. Here, as described in great detail in Chapter 4, I only utilize some of its functionality. The artificial phase Fix_co2, for example, was created to keep the concentration of CO_2 in the solution constant, per the value calculated form the D&S equations. It is important to note that PHREEQC could calculate a value of [CO2] based on the temperature and pressure but is not as accurate as the D&S model because PHREEQC's [CO_2] calculations have certain limitations (see Chapter 4).

PHREEQC can also calculate [Na^+] or [Mg^{2+}] instead of using the D&S/charge balance method. I found that the PHREEQC method was more complicated and took more time to

calculate [Na^+] and [Mg^{2+}] and still had the same accuracy as the D&S/charge balance method as [CO_2] was from the D&S equations. To make PHREEQC calculate [Na^+], for instance, one needs to know initial values of [CO_2] and [HCO_3^-] and these must be calculated from D&S.

Appendix B. High pressure and temperature NMR probe design

The following two pages show two detailed designs of the high pressure yttria-stabilized zirconia reaction vessel and the supporting NMR probe infrastructure. The high pressure reaction can theoretically handle pressures up to 400 bar at 400 °C for weeks at a time.

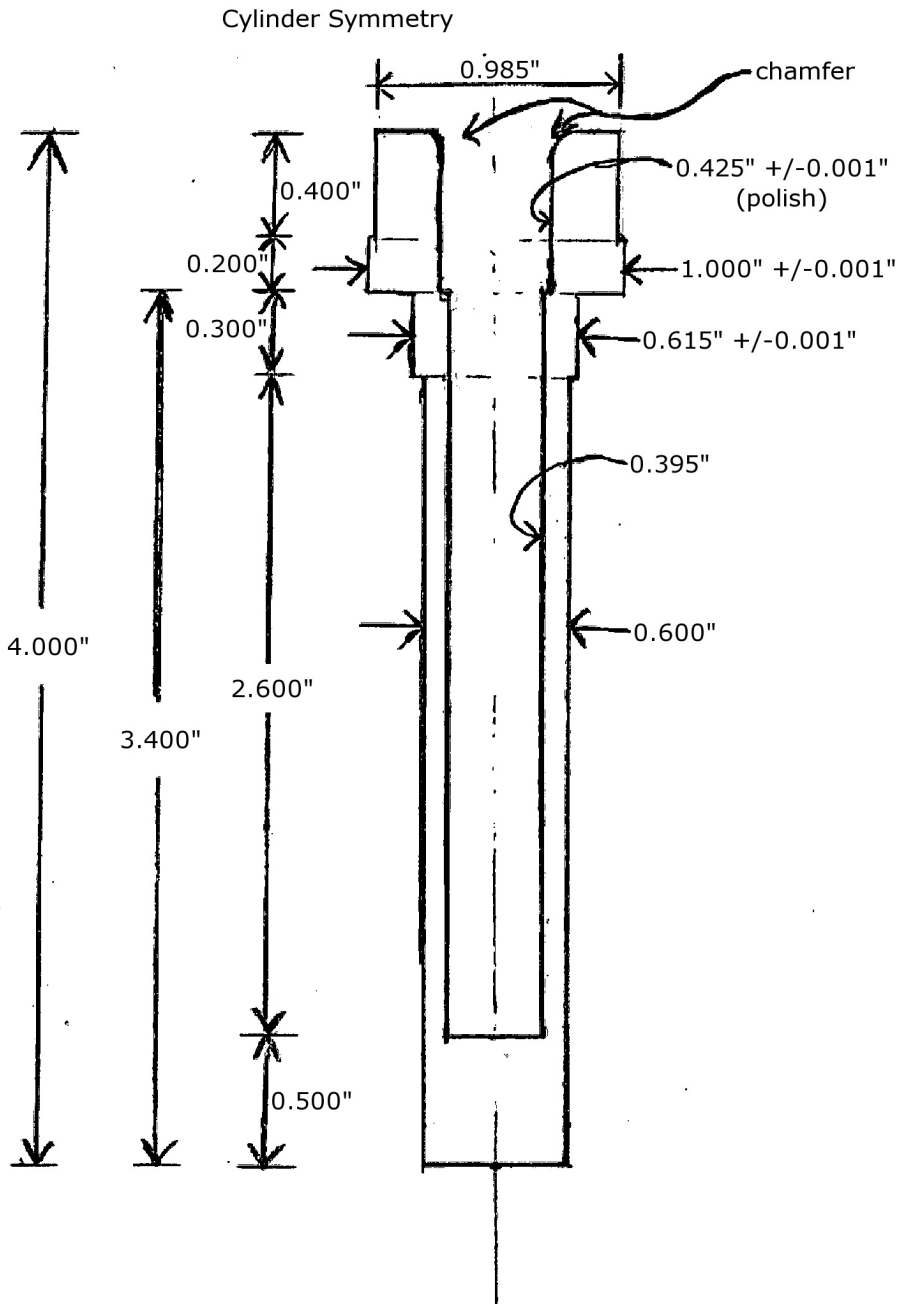
Cylinder Symmetry
0.985"
chamfer
0.425" +/-0.001"
(polish)
0.400"
0.200"
1.000" +/-0.001"
0.300"
0.615" +/-0.001"
0.395"
4.000"
0.600"
2.600"
3.400"
0.500"

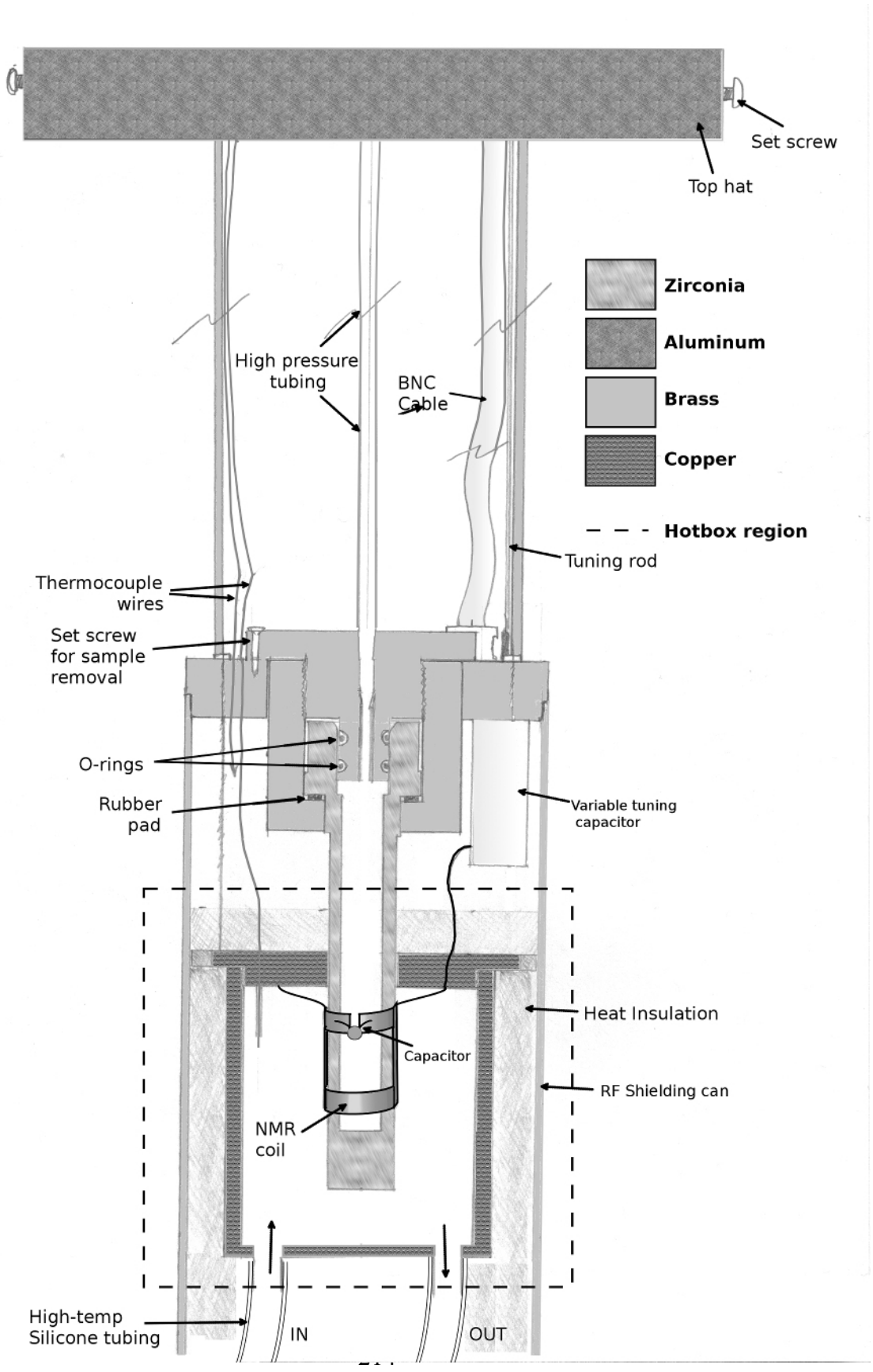
Set screw
Top hat
Zirconia
Aluminum
Brass
Copper
Hotbox region
High pressure tubing
BNC Cable
Tuning rod
Thermocouple wires
Set screw for sample removal
O-rings
Rubber pad
Variable tuning capacitor
Heat Insulation
Capacitor
RF Shielding can
NMR coil
High-temp Silicone tubing
IN
OUT

References

(1) B. Metz, O. Davidson, H.C. de Coninck, M. Loos, L. A. M. *IPCC Special Report on Carbon Dioxide Capture and Storage*; 2005; p. 205.

(2) Doney, S. C.; Fabry, V. J.; Feely, R. A.; Kleypas, J. A. Ocean Acidification: The Other CO_2 Problem. *Annu. Rev. Mar. Sci.* **2009**, *1*, 169–192.

(3) R.F. Keeling; S.C. Piper; A.F. Bollenbacher; J.S. Walker Atmospheric Carbon Dioxide Record from Mauna Loa.

(4) Florides, G. A.; Christodoulides, P. Global Warming and Carbon Dioxide through Sciences. *Environ. Int.* **2009**, *35*, 390–401.

(5) Hoegh-Guldberg, O.; Mumby, P. J.; Hooten, A. J.; Steneck, R. S.; Greenfield, P.; Gomez, E.; Harvell, C. D.; Sale, P. F.; Edwards, A. J.; Caldeira, K.; et al. Coral Reefs Under Rapid Climate Change and Ocean Acidification. *Science* **2007**, *318*, 1737–1742.

(6) Orr, J. C.; Fabry, V. J.; Aumont, O.; Bopp, L.; Doney, S. C.; Feely, R. A.; Gnanadesikan, A.; Gruber, N.; Ishida, A.; Joos, F.; et al. Anthropogenic Ocean Acidification over the Twenty-first Century and Its Impact on Calcifying Organisms. *Nature* **2005**, *437*, 681–686.

(7) Derner, J. D.; Johnson, H. B.; Kimball, B. A.; Pinter, P. J.; Polley, H. W.; Tischler, C. R.; Boutton, T. W.; Lamorte, R. L.; Wall, G. W.; Adam, N. R.; et al. Above- and Below-ground Responses of C3-C4 Species Mixtures to Elevated CO2 and Soil Water Availability. *Glob. Change Biol.* **2003**, *9*, 452–460.

(8) F.A. Bazzaz The Response of Natural Ecosystems to the Rising Global CO2 Levels. *Annu. Rev. Ecol. Syst.* **1990**, *21*, 167–196.

(9) US Energy Information Administration International Energy Statistics http://www.eia.gov/cfapps/ipdbproject/iedindex3.cfm?tid=90&pid=44&aid=8.

(10) Schmalensee, R.; Stoker, T. M.; Judson, R. A. World Carbon Dioxide Emissions: 1950–2050. *Rev. Econ. Stat.* **1998**, *80*, 15–27.

(11) Bert Metz; Ogunlade Davidson; Heleen de Coninck; Manuela Loos; Leo Meyer *IPCC Special Report on Carbon Dioxide Capture and Storage*; IPCC, 2005.

(12) Bachu, S. Screening and Ranking of Sedimentary Basins for Sequestration of CO2 in Geological Media in Response to Climate Change. *Environ. Geol.* **2003**, *44*, 277–289.

(13) Bachu, S. Sequestration of CO2 in Geological Media: Criteria and Approach for Site Selection in Response to Climate Change. *Energy Convers. Manag.* **2000**, *41*, 953–970.

(14) Rao, A. B.; Rubin, E. S. A Technical, Economic, and Environmental Assessment of Amine-Based CO_2 Capture Technology for Power Plant Greenhouse Gas Control. *Environ. Sci. Technol.* **2002**, *36*, 4467–4475.

(15) Kelemen, P. B.; Matter, J. From the Cover: In Situ Carbonation of Peridotite for CO_2 Storage. *Proc. Natl. Acad. Sci.* **2008**, *105*, 17295–17300.

(16) Matter, J. M.; Kelemen, P. B. Permanent Storage of Carbon Dioxide in Geological Reservoirs by Mineral Carbonation. *Nat. Geosci.* **2009**, *2*, 837–841.

(17) Constanz, B. R.; Andrew Youngs; Terence C. Holland Patent: CO2-sequestering Formed Building Materials. 8,006,446 B2.

(18) Wolf, G. H.; Chizmeshya, A. V. G.; Diefenbacher, J.; McKelvy, M. J. In Situ Observation of CO2 Sequestration Reactions Using a Novel Microreaction System. *Environ. Sci.*

Technol. **2004**, *38*, 932–936.
(19) Chizmeshya, A. V. G.; McKelvy, M. J.; Wolf, G. H.; Bearat, H.; Marzke, R.; Soignard, E.; Diefenbacher, J. Presentation: Development of an in Situ "Window" into Below-ground Geological Sequestration Reaction Processes **2006**.
(20) Todd Schaef, H.; McGrail, B. P.; Loring, J. L.; Bowden, M. E.; Arey, B. W.; Rosso, K. M. Forsterite [Mg2SiO4)] Carbonation in Wet Supercritical CO2: An in Situ High-pressure X-ray Diffraction Study. *Environ. Sci. Technol.* **2013**, *47*, 174–81.
(21) Surface, J. A.; Skemer, P.; Hayes, S. E.; Conradi, M. S. In Situ Measurement of Magnesium Carbonate Formation from CO(2) Using Static High-Pressure and -Temperature (13)C NMR. *Environ. Sci. Technol.* **2012**.
(22) Hoyt, D. W.; Turcu, R. V. F.; Sears, J. A.; Rosso, K. M.; Burton, D.; Felmy, A. R.; Hu, J. Z.; Burton, S. D. High-Pressure Magic Angle Spinning Nuclear Magnetic Resonance. *J. Magn. Reson.* **2011**.
(23) Diefenbacher, J.; Piwowarczyk, J.; Marzke, R. F. Note: Solution NMR Probe for the Study of CO2 Sequestration at Elevated Pressure and Temperature. *Rev. Sci. Instrum.* **2011**, *82*, 076107.
(24) Kwak, J. H.; Hu, J. Z.; Hoyt, D. W.; Sears, J. A.; Wang, C.; Rosso, K. M.; Felmy, A. R. Metal Carbonation of Forsterite in Supercritical CO_2 and H_2O Using Solid State ^{29}Si, ^{13}C NMR Spectroscopy. *J. Phys. Chem. C* **2010**, *114*, 4126–4134.
(25) Kwak, J. H.; Hu, J. Z.; Turcu, R. V. F. F.; Rosso, K. M.; Ilton, E. S.; Wang, C.; Sears, J. A.; Engelhard, M. H.; Felmy, A. R.; Hoyt, D. W. The Role of H_2O in the Carbonation of Forsterite in Supercritical CO_2. *Int. J. Greenh. Gas Control* **2011**, *5*, 1081–1092.
(26) Felmy, A. R.; Qafoku, O.; Arey, B. W.; Hu, J. Z.; Hu, M.; Todd Schaef, H.; Ilton, E. S.; Hess, N. J.; Pearce, C. I.; Feng, J.; et al. Reaction of Water-saturated Supercritical CO2 with Forsterite: Evidence for Magnesite Formation at Low Temperatures. *Geochim. Cosmochim. Acta* **2012**, *91*, 271–282.
(27) Bao, B.; Melo, L.; Davies, B.; Fadaei, H.; Sinton, D.; Wild, P. Detecting Supercritical CO(2) in Brine at Sequestration Pressure with an Optical Fiber Sensor. *Environ. Sci. Technol.* **2012**.
(28) Shao, H.; Thompson, C. J.; Qafoku, O.; Cantrell, K. J. In Situ Spectrophotometric Determination of pH Under Geologic CO(2) Sequestration Conditions: Method Development and Application. *Environ. Sci. Technol.* **2012**.
(29) Loring, J. S.; Thompson, C. J.; Wang, Z.; Joly, A. G.; Sklarew, D. S.; Schaef, H. T.; Ilton, E. S.; Rosso, K. M.; Felmy, A. R. In Situ Infrared Spectroscopic Study of Forsterite Carbonation in Wet Supercritical CO2. *Environ. Sci. Technol.* **2011**, *45*, 6204–10.
(30) Hanchen, M.; Prigiobbe, V.; Baciocchi, R.; Mazzotti, M. Precipitation in the Mg-carbonate System—effects of Temperature and CO_2 Pressure. *Chem. Eng. Sci.* **2008**, *63*, 1012–1028.
(31) Hales, M. C.; Frost, R. L.; Martens, W. N. Thermo-Raman Spectroscopy of Synthetic Nesquehonite - Implication for the Geosequestration of Greenhouse Gases. *J. Raman Spectrosc.* **2008**, *39*, 1141–1149.
(32) Smekal, A. Zur Quantentheorie der Dispersion. *Naturwissenschaften* **1923**, *11*, 873–875.
(33) Raman, C. V.; Krishnan, K. S. A New Type of Secondary Radiation. *Nature* **1928**, *121*, 501–502.

(34) Edwards, H. G. M.; Villar, S. E. J.; Jehlicka, J.; Munshi, T. FT-Raman Spectroscopic Study of Calcium-rich and Magnesium-rich Carbonate Minerals. *Spectrochim. Acta. A. Mol. Biomol. Spectrosc.* **2005**, *61*, 2273–80.
(35) Anderson, G. R. The Raman Spectra of Carbon Dioxide in Liquid Water and D2O. *J. Phys. Chem.* **1977**, *81*, 273–276.
(36) Frost, R. L.; Bahfenne, S.; Graham, J. Raman Spectroscopic Study of the Magnesium-carbonate Minerals-artinite and Dypingite. *J. Raman Spectrosc.* **2009**, *40*, 855–860.
(37) Purcell, E.; Bloembergen, N.; Pound, R. Resonance Absorption by Nuclear Magnetic Moments in a Single Crystal of CaF2. *Phys. Rev.* **1946**, *70*, 988–988.
(38) Purcell, E.; Pound, R.; Bloembergen, N. Nuclear Magnetic Resonance Absorption in Hydrogen Gas. *Phys. Rev.* **1946**, *70*, 986–987.
(39) Purcell, E.; Torrey, H.; Pound, R. Resonance Absorption by Nuclear Magnetic Moments in a Solid. *Phys. Rev.* **1946**, *69*, 37–38.
(40) Lauterbur, P. C. C13 Nuclear Magnetic Resonance Spectra. *J. Chem. Phys.* **1957**, *26*, 217.
(41) Holm, C. H. Observation of Chemical Shielding and Spin Coupling of C13 Nuclei in Various Chemical Compounds by Nuclear Magnetic Resonance. *J. Chem. Phys.* **1957**, *26*, 707.
(42) Levitt, M. H. *Spin Dynamics : Basics of Nuclear Magnetic Resonance*; Wiley: Hoboken, N.J., 2008.
(43) Alderman, D. W.; Grant, D. M. An Efficient Decoupler Coil Design Which Reduces Heating in Conductive Samples in Superconducting Spectrometers. *J. Magn. Reson. 1969* **1979**, *36*, 447–451.
(44) Etesse, P.; Zega, J. A.; Kobayashi, R. High Pressure Nuclear Magnetic Resonance Measurement of Spin–lattice Relaxation and Self-diffusion in Carbon Dioxide. *J. Chem. Phys.* **1992**, *97*, 2022.
(45) Abbott, T. M.; Buchanan, G. W.; Kruus, P.; Lee, K. C. ^{13}C Nuclear Magnetic Resonance and Raman Investigations of Aqueous Carbon Dioxide Systems. *Can. J. Chem.* **1982**, *60*, 1000–1006.
(46) Jakobsen, J. P.; Krane, J.; Svendsen, H. F. Liquid-Phase Composition Determination in CO_2 −H_2O−Alkanolamine Systems: An NMR Study. *Ind. Eng. Chem. Res.* **2005**, *44*, 9894–9903.
(47) Fulmer, G. R.; Miller, A. J. M.; Sherden, N. H.; Gottlieb, H. E.; Nudelman, A.; Stoltz, B. M.; Bercaw, J. E.; Goldberg, K. I. NMR Chemical Shifts of Trace Impurities: Common Laboratory Solvents, Organics, and Gases in Deuterated Solvents Relevant to the Organometallic Chemist. *Organometallics* **2010**, *29*, 2176–2179.
(48) Gallagher, F. A.; Kettunen, M. I.; Day, S. E.; Hu, D.-E.; Ardenkjaer-Larsen, J. H.; Zandt, R. in ’T; Jensen, P. R.; Karlsson, M.; Golman, K.; Lerche, M. H.; et al. Magnetic Resonance Imaging of pH in Vivo Using Hyperpolarized 13C-labelled Bicarbonate. *Nature* **2008**, *453*, 940–3.
(49) Mani, F.; Peruzzini, M.; Stoppioni, P. CO2 Absorption by Aqueous NH3 Solutions: Speciation of Ammonium Carbamate, Bicarbonate and Carbonate by a 13C NMR Study. *Green Chem.* **2006**, *8*, 995.

(50) Lauterbur, P. Anisotropy of the C^{13} Chemical Shift in Calcite. *Phys. Rev. Lett.* **1958**, *1*, 343–344.
(51) Papenguth, H. W. W.; Kirkpatrick, R. J. J.; Montez, B.; Sandberg, P. A. A. ^{13}C MAS NMR Spectroscopy of Inorganic and Biogenic Carbonates. *Am. Miner.* **1989**, *74*, 1152–1158.
(52) Vinegar, H. J.; Tutunjian, P. N.; Edelstein, W. A.; Roemer, P. B. Determining Carbonate Content of Cores by 13C NMR. In *SCA Conference Paper*; Society of Core Analysts, 1989.
(53) Harris, R. K.; Becker, E. D.; de Menezes, S. M. C.; Goodfellow, R.; Granger, P. NMR Nomenclature. Nuclear Spin Properties and Conventions for Chemical shifts(IUPAC Recommendations 2001). *Pure Appl. Chem.* **2001**, *73*, 1795–1818.
(54) Nebel, H.; Neumann, M.; Mayer, C.; Epple, M. On the Structure of Amorphous Calcium Carbonate–a Detailed Study by Solid-state NMR Spectroscopy. *Inorg. Chem.* **2008**, *47*, 7874–9.
(55) Feng, J. Observation of Bicarbonate in Calcite by NMR Spectroscopy. *Am. Miner.* **2006**, *91*, 957–960.
(56) Mason, H. E.; Kozlowski, A.; Phillips, B. L. Solid-State NMR Study of the Role of H and Na in AB-Type Carbonate Hydroxylapatite. *Chem. Mater.* **2008**, *20*, 294–302.
(57) Case, D. H.; Wang, F.; Giammar, D. E. Precipitation of Magnesium Carbonates as a Function of Temperature, Solution Composition, and Presence of a Silicate Mineral Substrate. *Environ. Eng. Sci.* **2011**, *28*, 881–889.
(58) Giammar, D. E.; Bruant, R. G.; Peters, C. A.; Bruant Jr., R. Forsterite Dissolution and Magnesite Precipitation at Conditions Relevant for Deep Saline Aquifer Storage and Sequestration of Carbon Dioxide. *Chem. Geol.* **2005**, *217*, 257–276.
(59) Wang, F.; Giammar, D. E. Forsterite Dissolution in Saline Water at Elevated Temperature and High CO(2) Pressure. *Environ. Sci. Technol.* **2012**.
(60) Hanchen, M.; Prigiobbe, V.; Storti, G.; Seward, T.; Mazzotti, M. Dissolution Kinetics of Fosteritic Olivine at 90–150°C Including Effects of the Presence of CO_2. *Geochim. Cosmochim. Acta* **2006**, *70*, 4403–4416.
(61) Kelemen, P. B.; Matter, J. M.; Streit, L.; Rudge, J. F.; Curry, W. B.; Blusztajn, J. S.; Streit, E. E. Rates and Mechanisms of Mineral Carbonation in Peridotite: Natural Processes and Recipes for Enhanced, in Situ CO_2 Capture and Storage. *Annu. Rev. Earth Planet. Sci.* **2010**, *39*, 545–576.
(62) Miller, Q. R. S.; Thompson, C. J.; Loring, J. S.; Windisch, C. F.; Bowden, M. E.; Hoyt, D. W.; Hu, J. Z.; Arey, B. W.; Rosso, K. M.; Schaef, H. T. Insights into Silicate Carbonation Processes in Water-bearing Supercritical CO2 Fluids. *Int. J. Greenh. Gas Control* **2013**, *15*, 104–118.
(63) Béarat, H.; McKelvy, M. J.; Chizmeshya, A. V. G.; Gormley, D.; Nunez, R.; Carpenter, R. W.; Squires, K.; Wolf, G. H. Carbon Sequestration via Aqueous Olivine Mineral Carbonation: Role of Passivating Layer Formation. *Environ. Sci. Technol.* **2006**, *40*, 4802–4808.
(64) Harrison, A. L.; Power, I. M.; Dipple, G. M. Accelerated Carbonation of Brucite in Mine Tailings for Carbon Sequestration. *Environ. Sci. Technol.* **2013**, *47*, 126–34.
(65) Rosenbauer, R. J.; Koksalan, T.; Palandri, J. L. Experimental Investigation of

CO_2–brine–rock Interactions at Elevated Temperature and Pressure: Implications for CO_2 Sequestration in Deep-saline Aquifers. *Fuel Process. Technol.* **2005**, *86*, 1581–1597.
(66) Spycher, N.; Pruess, K.; Ennis-King, J. CO_2-H_2O Mixtures in the Geological Sequestration of CO_2. I. Assessment and Calculation of Mutual Solubilities from 12 to 100°C and up to 600 Bar. *Geochim. Cosmochim. Acta* **2003**, *67*, 3015–3031.
(67) Barnes, D. a.; Bacon, D. H.; Kelley, S. R. Geological Sequestration of Carbon Dioxide in the Cambrian Mount Simon Sandstone: Regional Storage Capacity, Site Characterization, and Large-scale Injection Feasibility, Michigan Basin. *Environ. Geosci.* **2009**, *16*, 163–183.
(68) Benson, S. M.; Cole, D. R. CO2 Sequestration in Deep Sedimentary Formations. *Elements* **2008**, *4*, 325–331.
(69) Oelkers, E. H.; Gislason, S. R.; Matter, J. Mineral Carbonation of {CO2}. *Elements* **2008**, *4*, 333–337.
(70) Edsall, J. T. Carbon Dioxide , Carbonic Acid , and Bicarbonate Ion : Physical Properties and Kinetics of Interconversion.
(71) Gibbons, B. H.; Edsall, J. T. Rate of Hydration of Carbon Dioxide and Dehydration of Carbonic Acid At 25 Degrees. *J. Biol. Chem.* **1963**, *238*, 3502–7.
(72) Harned, H.; Davis, R. The Ionization Constant of Carbonic Acid in Water and the Solubility of Carbon Dioxide in Water and Aqueous Salt Solutions from 0 to 50. *J. Am. Chem. Soc.* **1943**, *206*.
(73) Tossell, J. a H_2CO_3 and Its Oligomers: Structures, Stabilities, Vibrational and NMR Spectra, and Acidities. *Inorg. Chem.* **2006**, *45*, 5961–70.
(74) Rasul, C.; Reddy, V. P.; Zdunek, L. Z.; Prakash, G. K. S.; Olah, C. A. Carbonic Acid and Its Mono- and Diprotonation : NMR, Ab Initio, and IGLO Investigation. *J. Am. Chem. Soc.* **1993**, *115*, 2236–2238.
(75) Olah, G. A.; White, A. M. Stable Carbonium Ions. LXIX. Protonation of Ureas, Guanidines, and Biotin in Super Acid Solution. *J. Am. Chem. Soc.* **1968**, *90*, 6087–6091.
(76) Dai, L.; Douglas, E. P.; Gower, L. B. Compositional Analysis of a Polymer-induced Liquid-precursor (PILP) Amorphous CaCO3 Phase. *J. Non-Cryst. Solids* **2008**, *354*, 1845–1854.
(77) Schaef, H. T.; Windisch, C. F.; McGrail, B. P.; Martin, P. F.; Rosso, K. M. Brucite [Mg(OH2)] Carbonation in Wet Supercritical CO2: An in Situ High Pressure X-ray Diffraction Study. *Geochim. Cosmochim. Acta* **2011**, *75*, 7458–7471.
(78) White, M. D.; McGrail, B. P.; Schaef, H. T.; Hu, J. Z.; Hoyt, D. W.; Felmy, A. R.; Rosso, K. M.; Wurstner, S. K. Multiphase Sequestration Geochemistry: Model for Mineral Carbonation. *Energy Procedia* **2011**, *4*, 5009–5016.
(79) Fathi, A.; Mohamed, T.; Claude, G.; Maurin, G.; Mohamed, B. A. Effect of a Magnetic Water Treatment on Homogeneous and Heterogeneous Precipitation of Calcium Carbonate. *Water Res.* **2006**, *40*, 1941–50.
(80) Turner, J. V. Kinetic Fractionation of Carbon-13 During Calcium Carbonate Precipitation. *Geochim. Cosmochim. Acta* **1982**, *46*, 1183–1191.
(81) Xiang, Q.; Fang, M.; Yu, H.; Maeder, M. Kinetics of the Reversible Reaction of CO(2) (aq) and HCO(3)(-) with Sarcosine Salt in Aqueous Solution. *J. Phys. Chem. A* **2012**, *116*, 10276–84.

(82) Mills, G.; Urey, H. The Kinetics of Isotopic Exchange Between Carbon Dioxide, Bicarbonate Ion, Carbonate Ion and Water1. *J. Am. Chem. Soc.* **1940**, *814*.
(83) Ho, C.; Sturtevant, J. M. The Kinetics of the Hydration of Carbon Dioxide at 25°C. *J. Biol. Chem.* **1963**, *238*, 3499–3501.
(84) Pascale, F.; Tosoni, S.; Zicovich-Wilson, C.; Ugliengo, P.; Orlando, R.; Dovesi, R. Vibrational Spectrum of Brucite, Mg(OH)2: a Periodic Ab Initio Quantum Mechanical Calculation Including OH Anharmonicity. *Chem. Phys. Lett.* **2004**, *396*, 308–315.
(85) Duffy, T. S.; Meade, C.; Fei, Y.; Mao, H.-K.; Hemley, R. J. High-pressure Phase Transition in Brucite, Mg(OH) 2. *Am. Miner.* **1995**, *80*, 222–230.
(86) Yi, Y.; Liska, M.; Unluer, C.; Al-Tabbaa, A. Carbonating Magnesia for Soil Stabilisation. *Can. Geotech. J.* **2013**.
(87) Béarat, H.; McKelvy, M. J.; Chizmeshya, A. V. G.; Sharma, R.; Carpenter, R. W. Magnesium Hydroxide Dehydroxylation/Carbonation Reaction Processes: Implications for Carbon Dioxide Mineral Sequestration. *J. Am. Ceram. Soc.* **2004**, *85*, 742–748.
(88) Fricker, K. J.; Alissa Park, A.-H. Effect of H2O on Mg(OH)2 Carbonation Pathways for Combined CO2 Capture and Storage. *Chem. Eng. Sci.* **2012**.
(89) Butt, D. P.; Lackner, K. S.; Wendt, C. H.; Conzone, S. D.; Kung, H.; Lu, Y.-C.; Bremser, J. K. Kinetics of Thermal Dehydroxylation and Carbonation of Magnesium Hydroxide. *J. Am. Ceram. Soc.* **1996**, *79*, 1892–1898.
(90) Lackner, K. S.; Wendt, C. H.; Butt, D. P.; Joyce, E. L.; Sharp, D. H. Carbon Dioxide Disposal in Carbonate Minerals. *Energy* **1995**, *20*, 1153–1170.
(91) Fagerlund, J.; Zevenhoven, R. An Experimental Study of Mg(OH)2 Carbonation. *Int. J. Greenh. Gas Control* **2011**, *5*, 1406–1412.
(92) Sipilä, J.; Teir, S.; Zevenhoven, R. Carbon Dioxide Sequestration by Mineral Carbonation Literature Review Update 2005 – 2007 Carbon Dioxide Sequestration by Mineral Carbonation Literature Review Update 2005 – 2007. *Environ. Prot.* **2008**.
(93) Zhao, L.; Sang, L.; Chen, J.; Ji, J.; Teng, H. H. Aqueous Carbonation of Natural Brucite: Relevance to CO2 Sequestration. *Environ. Sci. Technol.* **2010**, *44*, 406–11.
(94) Pronost, J.; Beaudoin, G.; Tremblay, J.; Larachi, F.; Duchesne, J.; Hébert, R.; Constantin, M. Carbon Sequestration Kinetic and Storage Capacity of Ultramafic Mining Waste. *Environ. Sci. Technol.* **2011**, *45*, 9413–20.
(95) Hövelmann, J.; Putnis, C. V.; Ruiz-Agudo, E.; Austrheim, H. Direct Nanoscale Observations of CO2 Sequestration During Brucite [Mg(OH)2] Dissolution. *Environ. Sci. Technol.* **2012**, *46*, 5253–60.
(96) Pokrovsky, O. S.; Schott, J. Experimental Study of Brucite Dissolution and Precipitation in Aqueous Solutions: Surface Speciation and Chemical Affinity Control. *Geochim. Cosmochim. Acta* **2004**, *68*, 31–45.
(97) Wang, Y.; Liu, W.; Huang, F.; Zou, T.; Lin, Z. The “jump of Size” Phenomenon in Aqueous-nanoparticle Reaction System: Phase Transformation from nano-Mg(OH)2 to Bulk MgCO3·3H2O. *CrystEngComm* **2012**, *14*, 7165.
(98) K.Mader, U. H2O-CO2 Mixtures: A Review of P-V-T-X Data Point of Vivew and an Assessment from a Phase-equilibrium. *Can. Miner.* **1991**, *29*, 767–790.
(99) Jun, Y.-S.; Giammar, D. E.; Werth, C. J. Impacts of Geochemical Reactions on Geologic Carbon Sequestration. *Environ. Sci. Technol.* **2013**, *47*, 3–8.

(100) Van Noort, R.; Spiers, C. J.; Drury, M. R.; Kandianis, M. T. Peridotite Dissolution and Carbonation Rates at Fracture Surfaces Under Conditions Relevant for in Situ Mineralization of CO2. *Geochim. Cosmochim. Acta* **2013**, *106*, 1–24.
(101) Carroll, S. a; McNab, W. W.; Dai, Z.; Torres, S. C. Reactivity of Mount Simon Sandstone and the Eau Claire Shale Under CO2 Storage Conditions. *Environ. Sci. Technol.* **2013**, *47*, 252–61.
(102) Davies, P. J.; Bubela, B. The Transformation of Nesquehonite into Hydromagnesite. *Chem. Geol.* **1973**, *12*, 289–300.
(103) WU, Y.-L. Study on Crystals Transformation Process of Magnesium Carbonate Hydrate Based on the Salt Lake Magnesium Resource Utilization.
(104) Ballirano, P.; De Vito, C.; Mignardi, S.; Ferrini, V. Phase Transitions in the Mg-CO2-H2O System and the Thermal Decomposition of Dypingite, Mg5(CO3)4(OH)2·5H2O: Implications for Geosequestration of Carbon Dioxide. *Chem. Geol.* **2012**, *5*.
(105) Prigiobbe, V.; Mazzotti, M. Precipitation of Mg-carbonates at Elevated Temperature and Partial Pressure of CO2. *Chem. Eng. J.* **2013**.
(106) Raade, G. Dypingite, a New Hydrous Basic Carbonate of Magnesium, from Norway. *Am. Miner.* **1970**, *55*, 1457–1465.
(107) Canterford, J. H. Some Observations on the Properties of Dypingite, $Mg_5(CO_3)_4(OH)_2{\cdot}5H_2O$, and Related Minerals. *Miner. Mag.* **1984**, *48*, 437–442.
(108) Halasz, I. Single-Crystal-to-Single-Crystal Reactivity: Gray, Rather Than Black or White. *Cryst. Growth Des.* **2010**, *10*, 2817–2823.
(109) Stebbins, J. F. Magnesium Site Exchange in Forsterite : A Direct Measurement by High-temperature 25Mg NMR Spectroscopy. *Am. Miner.* **1996**, *81*, 1315–1320.
(110) Chopelas, A. Single Crystal Raman Spectra of Forsterite, Fayalite, and Monticellite. *Am. Miner.* **1991**, *76*, 1101–1109.
(111) Steel, K. M.; Alizadehhasari, K.; Balucan, R. D.; Ba\vsić, B. Conversion of CO2 into Mineral Carbonates Using a Regenerable Buffer to Control Solution pH. *Fuel* **2013**.
(112) Duan, Z.; Sun, R. An Improved Model Calculating CO2 Solubility in Pure Water and Aqueous NaCl Solutions from 273 to 533 K and from 0 to 2000 Bar. *Chem. Geol.* **2003**, *193*, 257–271.
(113) Meyssami, B.; Balaban, M. O.; Teixeira, A. A. Prediction of pH in Model Systems Pressurized with Carbon Dioxide. *Biotechnol. Prog.* **1992**, *8*, 149–154.
(114) King, H. E.; Putnis, C. V. Direct Observations of the Influence of Solution Composition on Magnesite Dissolution. *Geochim. Cosmochim. Acta* **2013**.
(115) Wilson, S. a; Barker, S. L. L.; Dipple, G. M.; Atudorei, V. Isotopic Disequilibrium During Uptake of Atmospheric CO2 into Mine Process Waters: Implications for CO2 Sequestration. *Environ. Sci. Technol.* **2010**, *44*, 9522–9.
(116) Saldi, G. D.; Schott, J.; Pokrovsky, O. S.; Gautier, Q.; Oelkers, E. H. An Experimental Study of Magnesite Precipitation Rates at Neutral to Alkaline Conditions and 100–200 °C as a Function of pH, Aqueous Solution Composition and Chemical Affinity. *Geochim. Cosmochim. Acta* **2012**, *83*, 93–109.
(117) Liu, X.; Wang, Z. A.; Byrne, R. H.; Kaltenbacher, E. a; Bernstein, R. E. Spectrophotometric Measurements of pH In-situ: Laboratory and Field Evaluations of

Instrumental Performance. *Environ. Sci. Technol.* **2006**, *40*, 5036–44.
(118) Bates, R. G. *The Determination of pH: Theory and Practice*; 1973.
(119) Kaszuba, J. P.; Janecky, D. R.; Snow, M. G. Carbon Dioxide Reaction Processes in a Model Brine Aquifer at 200 C and 200 Bars : Implications for Geologic Sequestration of Carbon. *Science* **2003**, *18*, 1065–1080.
(120) Patterson Jr., A.; Ettinger, R. Nuclear Magnetic Resonance Studies of the Carbon Dioxide-Water Equilibrium. *Z. Elektrochmie Berichte Bunsenges. Phys. Chem.* **1960**, *64*, 98–110.
(121) Moret, S.; Dyson, P. J.; Laurenczy, G. Direct, in Situ Determination of pH and Solute Concentrations in Formic Acid Dehydrogenation and CO(2) Hydrogenation in Pressurised Aqueous Solutions Using (1)H and (13)C NMR Spectroscopy. *Dalton Trans. Camb. Engl. 2003* **2013**, 1–4.
(122) Yang, J.; Singh, S.; Shen, J. 13C Saturation Transfer Effect of Carbon Dioxide-bicarbonate Exchange Catalyzed by Carbonic Anhydrase in Vivo. *Magn. Reson. Med. Off. J. Soc. Magn. Reson. Med. Soc. Magn. Reson. Med.* **2008**, *59*, 492–8.
(123) HOFFMAN, D.; HENKENS, R. The Rates of Fast Reactions of Carbon Dioxide and Bicarbonate in Human Erythrocytes Measured by Carbon-13 NMR. *Biochem. Biophys. Res. Commun.* **1987**, *143*, 67–73.
(124) Duan, Z.; Hu, J.; Li, D.; Mao, S. Densities of the CO 2 –H 2 O and CO 2 –H 2 O–NaCl Systems Up to 647 K and 100 MPa. *Energy Fuels* **2008**, *22*, 1666–1674.
(125) Li, D.; Duan, Z. The Speciation Equilibrium Coupling with Phase Equilibrium in the H2O–CO2–NaCl System from 0 to 250 °C, from 0 to 1000 Bar, and from 0 to 5 Molality of NaCl. *Chem. Geol.* **2007**, *244*, 730–751.
(126) Mao, S.; Duan, Z.; Hu, W. A Vapor–liquid Phase Equilibrium Model for Binary CO2–H2O and CH4–H2O Systems Above 523K for Application to Fluid Inclusions. *J. Supercrit. Fluids* **2009**, *50*, 13–21.
(127) Duan, Z.; Sun, R.; Zhu, C.; Chou, I.-M. An Improved Model for the Calculation of CO2 Solubility in Aqueous Solutions Containing Na+, K+, Ca2+, Mg2+, Cl−, and SO42−. *Mar. Chem.* **2006**, *98*, 131–139.
(128) Johnson, J. W.; Oelkers, E. H.; Helgeson, H. C. SUPCRT92: A Software Package for Calculating the Standard Molal Thermodynamic Properties of Minerals, Gases, Aqueous Species, and Reactions from 1 to 5000 Bar and 0 to 1000°C. *Comput. Geosci.* **1992**, *18*, 899–947.
(129) Parkhurst, D. L.; Appelo, C. A. *User's Guide to PHREEQC (version 2) - A Computer Program for Speciation, Batch-Reaction, One-Diemnsional Transport, and INverse Geochemical Calculations*; Water-Resources Investigations Report 99-4259: Denver, CO, 1999.
(130) Duan, Z.; Møller, N.; Weare, J. H. An Equation of State for the CH4-CO2-H2O System: I. Pure Systems from 0 to 1000°C and 0 to 8000 Bar. *Geochim. Cosmochim. Acta* **1992**, *56*, 2605–2617.
(131) Duan, Z.; Møller, N.; Greenberg, J.; Weare, J. H. The Prediction of Methane Solubility in Natural Waters to High Ionic Strength from 0 to 250°C and from 0 to 1600 Bar. *Geochim. Cosmochim. Acta* **1992**, *56*, 1451–1460.
(132) Pitzer, K. S. Thermodynamics of Electrolytes. I. Theoretical Basis and General

Equations. *J. Phys. Chem.* **1973**, *77*, 268–277.
(133) Duan, Z.; Sun, Y. Thermodynamic Models in the Duan Research Group.
(134) Peng, D.-Y.; Robinson, D. B. A New Two-Constant Equation of State. *Ind. Eng. Chem. Fundam.* **1976**, *15*, 59–64.
(135) Plummer, L. N.; Parkhurst, D. L.; Fleming, G. W.; Dunkle, S. A. *A Computer Program Incorporating Pitzer's Equations for Calculation of Geochemical Reactions in Brines*; Water-Resources Investigations Report; pp. 88–4153.
(136) Morrow, J. S.; Keim, P.; Gurd, F. R. CO2 Adducts of Certain Amino Acids, Peptides, and Sperm Whale Myoglobin Studied by Carbon 13 and Proton Nuclear Magnetic Resonance. *J. Biol. Chem.* **1974**, *249*, 7484–94.
(137) Holmes, P. E.; Naaz, M.; Poling, B. E. Ion Concentrations in the CO 2 −NH 3 −H 2 O System from 13 C NMR Spectroscopy. *Ind. Eng. Chem. Res.* **1998**, *37*, 3281–3287.
(138) Gottlieb, H. E.; Kotlyar, V.; Nudelman, A. NMR Chemical Shifts of Common Laboratory Solvents as Trace Impurities. *J. Org. Chem.* **1997**, *62*, 7512–7515.
(139) Pocker, Y.; Bjorkquist, D.; Schaffer, W.; Henderson, C. Reversible Hydration of Pteridine. General Acid-base Catalysis, Solvent Deuterium Isotope Effects, and Transition State Characterization. *J. Am. Chem. Soc.* **1975**, *97*, 5540–5546.
(140) Hickel, B.; Corfitzen, H.; Sehested, K. Measurement of the Rate Constants of the Reactions $OH + OH^- \rightleftarrows O^- + H_2O$ and $OD + OD^- \rightleftarrows O^- + D_2O$ in Forward and Reverse Directions. Kinetic Determination of the p *K*'s of OH and OD Radicals. *J. Phys. Chem.* **1996**, *100*, 17186–17190.
(141) Salomaa, P.; Schaleger, L. L.; Long, L. A. Solvent Deuterium Isotope Effects on Acid-Base Equilibria. *J. Am. Chem. Soc.* **1964**, *86*, 1–7.
(142) Pocker, Y.; Bjorkquist, D. W. Comparative Studies of Bovine Carbonic Anhydrase in H_2O and D_2O. Stopped-flow Studies of the Kinetics of Interconversion of CO_2 and HCO_3^-. *Biochemistry (Mosc.)* **1977**, *16*, 5698–5707.
(143) Hikita, H.; Asai, S.; Takatsuka, T. Absorption of Carbon Dioxide into Aqueous Sodium Hydroxide and Sodium Carbonate-bicarbonate Solutions. *Chem. Eng. J.* **1976**, *11*, 131–141.
(144) Garcia, D. J.; Shao, H.; Hu, Y.; Ray, J. R.; Jun, Y.-S. Supercritical CO2–brine Induced Dissolution, Swelling, and Secondary Mineral Formation on Phlogopite Surfaces at 75–95 °C and 75 Atm. *Energy Environ. Sci.* **2012**, *5*, 5758.
(145) Battino, R. The Ostwald Coefficient of Gas Solubility. *Fluid Phase Equilibria* **1984**, *15*, 231–240.
(146) Liger-Belair, G.; Prost, E.; Parmentier, M.; Jeandet, P.; Nuzillard, J.-M. Diffusion Coefficient of CO(2) Molecules as Determined by (13)C NMR in Various Carbonated Beverages. *J. Agric. Food Chem.* **2003**, *51*, 7560–3.
(147) Fordham, E. .; Gibbs, S. .; Hall, L. . Partially Restricted Diffusion in a Permeable Sandstone: Observations by Stimulated Echo PFG NMR. *Magn. Reson. Imaging* **1994**, *12*, 279–284.
(148) Callaghan, P. T.; Godefroy, S.; Ryland, B. N. Use of the Second Dimension in PGSE NMR Studies of Porous Media. *Magn. Reson. Imaging* **2003**, *21*, 243–248.
(149) Woessner, D. E. Effects of Diffusion in Nuclear Magnetic Resonance Spin-Echo Experiments. *J. Chem. Phys.* **1961**, *34*, 2057–2061.

(150) Sinnaeve, D. The Stejskal-Tanner Equation Generalized for Any Gradient Shape-an Overview of Most Pulse Sequences Measuring Free Diffusion. *Concepts Magn. Reson. Part* **2012**, *40A*, 39–65.
(151) Stejskal, E. O.; Tanner, J. E. Spin Diffusion Measurements: Spin Echoes in the Presence of a Time-Dependent Field Gradient. *J. Chem. Phys.* **1965**, *42*, 288–292.
(152) Tanner, J. E. Use of the Stimulated Echo in NMR Diffusion Studies. *J. Chem. Phys.* **1970**, *52*, 2523.
(153) Stallmach, F.; Galvosas, P. Spin Echo NMR Diffusion Studies. In *Annual Reports on NMR Spectroscopy*; G.A. Webb, Ed.; Academic Press, 2007; Vol. Volume 61, pp. 51–131.
(154) Lamb, D.; Grandinetti, P.; Jonas, J. Fixed Field Gradient NMR Diffusion Measurements Using Bessel Function Fits to the Spin-echo Signal. *J. Magn. Reson. 1969* **1987**.
(155) Fleury, M.; Berne, P.; Bachaud, P. Diffusion of Dissolved CO2 in Caprock. *Energy Procedia* **2009**, *1*, 3461–3468.
(156) Holz, M.; Weingartner, H. Calibration in Accurate Spin-echo Self-diffusion Measurements Using 1H and Less-common Nuclei. *J. Magn. Reson. 1969* **1991**, *92*, 115–125.
(157) Holz, M.; Heil, S. R.; Sacco, A. Temperature-dependent Self-diffusion Coefficients of Water and Six Selected Molecular Liquids for Calibration in Accurate 1H NMR PFG Measurements. *Phys. Chem. Chem. Phys.* **2000**, *2*, 4740–4742.
(158) Easteal, A. J.; Price, W. E.; Woolf, L. A. Diaphragm Cell for High-temperature Diffusion Measurements. Tracer Diffusion Coefficients for Water to 363 K. *J. Chem. Soc. Faraday Trans. 1 Phys. Chem. Condens. Phases* **1989**, *85*, 1091–1097.
(159) Albright, J. G.; Mathew, R.; Miller, D. G. Measurement of Binary and Ternary Mutual Diffusion Coefficients of Aqueous Sodium and Potassium Bicarbonate Solutions at 25C. *J. Phys. Chem.* **1987**, *91*, 210–215.
(160) Hinshaw, W. S.; Lent, A. H. An Introduction to NMR Imaging: From the Bloch Equation to the Imaging Equation. *Proc. Ieee* **1983**, *71*, 338–350.
(161) Frydman, L.; Chingas, G. C.; Lee, Y. K.; Grandinetti, P. J.; Eastman, M. A.; Barrall, G. A.; Pines, A. Variable-angle Correlation Spectroscopy in Solid-state Nuclear Magnetic Resonancea). *J. Chem. Phys.* **1992**, *97*, 4800.
(162) Lee, Y.; Vold, R.; Hoatson, G.; Lin, Y. Y.; Pines, A. Linear Prediction with Singular-Value Decomposition for Removing Phase Artifacts in 2D VACSY Spectra. *J. Magn. Reson. A* **1995**, *112*, 112–117.
(163) Fang, Z. Accomplishment of VACSY Experimental Set-up and Its Application to Investigate Molecular Orientation Distrubiution of Solid-State Polymers, 1999.
(164) Bénézeth, P.; Saldi, G. D.; Dandurand, J.-L.; Schott, J. Experimental Determination of the Solubility Product of Magnesite at 50 to 200°C. *Chem. Geol.* **2011**, *286*, 21–31.
(165) Sandengen, K.; Jø sang, L. O.; Kaasa, B. Simple Method for Synthesis of Magnesite ($MgCO_3$). *Ind. Eng. Chem. Res.* **2008**, *47*, 1002–1004.
(166) Sayles, F. L.; Fyfe, W. S. The Crystallization of Magnesite from Aqueous Solution. *Geochim. Cosmochim. Acta* **1973**, *37*, 87–99.
(167) Sevelsted, T. F.; Herfort, D.; Skibsted, J. 13C Chemical Shift Anisotropies for Carbonate Ions in Cement Minerals and the Use of 13C, 27Al and 29Si MAS NMR in Studies of

Portland Cement Including Limestone Additions. *Cem. Concr. Res.* **2013**, *52*, 100–111.
(168) Stueber, D.; Grant, D. M. The 13C Chemical Shift Tensor Principal Values and Orientations in Dialkyl Carbonates and Trithiocarbonates. *Solid State Nucl. Magn. Reson.* **2002**, *22*, 439–57.
(169) Pines, A. ^{13}C Chemical Shielding Anisotropy in Solids. CS_2 and $CaCO_3$. *J. Chem. Phys.* **1971**, *54*, 5438.
(170) Bol, W.; Gerrits, G. J. A.; van Panthaleon Eck, C. L. The Hydration of Divalent Cations in Aqueous Solution. An X-ray Investigation with Isomorphous Replacement. *J. Appl. Crystallogr.* **1970**, *3*, 486–492.
(171) P. R. Smirnov; Trostin, V. N. Structural Parameters of Hydration of Be2+ and Mg2+ Ions in Aqueous Solutions of Their Salts. *Russ. J. Gen. Chem.* **2008**, *78*, 1643–1649.
(172) Dong, M.; Li, Z.; Mi, J.; Demopoulos, G. P. Solubility and Stability of Nesquehonite ($MgCO_3 \cdot 3H_2O$) in Mixed NaCl + $MgCl_2$, NH_4Cl + $MgCl_2$, LiCl, and LiCl + $MgCl_2$ Solutions. *J. Chem. Eng. Data* **2009**, *54*, 3002–3007.
(173) Ferrini, V.; De Vito, C.; Mignardi, S. Synthesis of Nesquehonite by Reaction of Gaseous CO2 with Mg Chloride Solution: Its Potential Role in the Sequestration of Carbon Dioxide. *J. Hazard. Mater.* **2009**, *168*, 832–837.
(174) Akao, M.; Marumo, F.; Iwai, S. The Crystal Structure of Hydromagnesite. *Acta Crystallogr. B* **1974**, *30*, 2670–2672.
(175) Murdoch, J. Unit Cell of Hydromagnesite. *Am. Miner.* **1954**, *39*, 24–29.
(176) Wang, D.; Li, Z. Gas − Liquid Reactive Crystallization Kinetics of Hydromagnesite in the MgCl 2 − CO 2 − NH 3 − H 2 O System : Its Potential in CO 2 Sequestration. **2012**.
(177) Coleyshaw, E. E.; Crump, G.; Griffith, W. P. Vibrational Spectra of the Hydrated Carbonate Minerals Ikaite, Monohydrocalcite, Lansfordite and Nesquehonite. *Spectrochim. Acta. A. Mol. Biomol. Spectrosc.* **2003**, *59*, 2231–2239.
(178) Stephan, G. W.; MacGillavry, C. H. The Crystal Structure of Nesquehonite, MgCO3.3H2O. *Acta Crystallogr. B* **1972**, *28*, 1031–1033.
(179) Akao, M.; Iwai, S. The Hydrogen Bonding of Hydromagnesite. *Acta Crystallogr. B* **1977**, *33*, 1273–1275.
(180) Jujin Suzuki, M. I. A New Magnesium Carbonate Hydrate Mineral, Mg5(CO3)4 (OH)2•8H2O, from Yoshikawa, Aichi Prefecture, Japan. *J. Jpn. Assoc. Miner. Pet. Econ. Geol.* **1973**, 353–361.
(181) Zhang, Z.; Zheng, Y.; Ni, Y.; Liu, Z.; Chen, J.; Liang, X. Temperature- and pH-Dependent Morphology and FT−IR Analysis of Magnesium Carbonate Hydrates. *J. Phys. Chem. B* **2006**, *110*, 12969–12973.
(182) Arvidson, R. S.; Mackenzie, F. T. Temperature Dependence of Mineral Precipitation Rates Along the CaCO3–MgCO3 Join. *Aquat. Geochem. 6*, 249–256.
(183) SCHEUBEL, W.; ZIMMERMANN, H.; HAEBERLEN, U. High-resolution 1H, 2H, and 13C Solid-state NMR of Dimethylmalonic Acid. Detection of a New Mode of Hydrogen Motion. *J. Magn. Reson. 1969* **1988**, *80*, 401–416.
(184) J. T. Kloprogge, W. N. Martens, L. Nothdurft, L. V. D.; Webb, G. E. Low Temperature Synthesis and Characterization of Nesquehonite. *J. Mater. Sci. Lett.* **2003**, *22*, 825 – 829.
(185) Giester, G.; Lengauer, C. L.; Rieck, B. The Crystal Structure of Nesquehonite, MgCO3·3H2O, from Lavrion, Greece. *Miner. Pet.* **2000**, *70*, 153–163.

(186) Kamenetsky, V. S.; Kamenetsky, M. B.; Weiss, Y.; Navon, O.; Nielsen, T. F. D.; Mernagh, T. P. How Unique Is the Udachnaya-East Kimberlite? Comparison with Kimberlites from the Slave Craton (Canada) and SW Greenland. *Lithos* **2009**, *112*, 334–346.
(187) H. Shiba; T. Watanabe Les Structures Des Cristaux de Northupite, de Northupite Bromee et de Tychite. *Comptes Rendus Hebd. Seances Acad. Sci.* **1931**, *193*, 1421–1423.
(188) Koller, H.; Engelhardt, G.; Kentgens, A. P. M.; Sauer, J. 23Na NMR Spectroscopy of Solids: Interpretation of Quadrupole Interaction Parameters and Chemical Shifts. *J. Phys. Chem.* **1994**, *98*, 1544–1551.
(189) Harris, R. K.; Nesbitt, G. J. Cross Polarization for Quadrupolar nuclei—Proton to Sodium-23. *J. Magn. Reson. 1969* **1988**, *78*, 245–256.
(190) Johnson, B.; Goldburg, W. Nuclear-Magnetic-Resonance Spin-Lattice Relaxation in High and Low Fields. *Phys. Rev.* **1966**, *145*, 380–390.
(191) Dusek, M.; Chapuis, G.; Meyer, M.; Petricek, V. Sodium Carbonate Revisited. *Acta Crystallogr. B* **2003**, *59*, 337–352.
(192) Jones, A. R.; Winter, R.; Greaves, G. N.; Smith, I. H. ^{23} Na, ^{29} Si, and ^{13} C MAS NMR Investigation of Glass-Forming Reactions Between Na_2CO_3 and SiO_2. *J. Phys. Chem. B* **2005**, *109*, 23154–23161.
(193) Sass, R. L.; Scheuerman, R. F. The Crystal Structure of Sodium Bicarbonate. *Acta Crystallogr.* **1962**, *15*, 77–81.
(194) Morcombe, C. R.; Zilm, K. W. Chemical Shift Referencing in MAS Solid State NMR. *J. Magn. Reson.* **2003**, *162*, 479–486.
(195) Riddell, F. G.; Arumugam, S.; Harris, K. D. M.; Rogerson, M.; Strange, J. H. A Carbon-13 CP/MAS NMR Study of a Double Tert-butyl Group Rotation in the Solid State Using T1.rho. and Line Shape Measurements. *J. Am. Chem. Soc.* **1993**, *115*, 1881–1885.
(196) Witkowski, S.; Paradowska, K.; Wawer, I. 13C CP/MAS NMR Studies of Vitamin E Model Compounds. *Magn. Reson. Chem.* **2004**, *42*, 863–869.
(197) Power, I.; Wilson, S. Biologically Induced Mineralization of Dypingite by Cyanobacteria from an Alkaline Wetland Near Atlin, British Columbia, Canada. *Geochem. Ldots* **2007**.
(198) Haurie, L.; Lacasta, a M.; Ciudad, a.; Realinho, V.; Velasco, J. I. Addition of Flame Retardants in Epoxy Mortars: Thermal and Mechanical Characterization. *Constr. Build. Mater.* **2013**, *42*, 266–270.
(199) Haurie, L.; Fernández, A. I.; Velasco, J. I.; Chimenos, J. M.; Lopez Cuesta, J.-M.; Espiell, F. Synthetic Hydromagnesite as Flame Retardant. Evaluation of the Flame Behaviour in a Polyethylene Matrix. *Polym. Degrad. Stab.* **2006**, *91*, 989–994.
(200) Power, I. M.; Wilson, S. A.; Thom, J. M.; Dipple, G. M.; Gabites, J. E.; Southam, G. The Hydromagnesite Playas of Atlin, British Columbia, Canada: A Biogeochemical Model for CO2 Sequestration. *Chem. Geol.* **2009**, *260*, 286–300.
(201) Alderman, A. R.; Von Der Borch, C. C. Occurrence of Hydromagnesite in Sediments in South Australia. *Nature* **1960**, *188*, 931–931.
(202) Russell, M. J.; Ingham, J. K.; Zedef, V.; Maktav, D.; Sunar, F.; Hall, A. J.; Fallick, A. E. Search for Signs of Ancient Life on Mars: Expectations from Hydromagnesite Microbialites, Salda Lake, Turkey. *J. Geol. Soc.* **1999**, *156*, 869–888.
(203) Botha, A.; Strydom, C. A. DTA and FT-IR Analysis of the Rehydration of Basic

Magnesium Carbonate. *J. Therm. Anal. Calorim.* **2003**, *71*, 987–996.
(204) King, H. E.; Plümper, O.; Putnis, A. Effect of Secondary Phase Formation on the Carbonation of Olivine. *Environ. Sci. Technol.* **2010**, *44*, 6503–9.
(205) Herzfeld, J.; Berger, A. E. Sideband Intensities in NMR Spectra of Samples Spinning at the Magic Angle. *J. Chem. Phys.* **1980**, *73*, 6021.
(206) Sachleben, J. R. Bayesian and Information Theory Analysis of MAS Sideband Patterns in Spin 1/2 Systems. *J. Magn. Reson.* **2006**, *183*, 123–133.